

Jordan Journal of Mechanical and Industrial Engineering (JJMIE)

JJMIE is a high-quality scientific journal devoted to fields of Mechanical and Industrial Engineering. It is published by Hashemite University in corporation with the Jordanian Scientific Research Support Fund.

EDITORIAL BOARD

Editor-in-Chief

Dr. Ali M. Jawarneh

Assistant Editor

Dr. Faris M. AL-Oqla

Dr. Akram S. ALSukker

Editorial board

Prof. **Mohammad Ahmad Hamdan**
University of Jordan

Prof. **Naser Al-Huniti**
University of Jordan

Prof. **Amin Al Robaidi**
Al Balqa Applied University

Prof. **Mohammad Hayajneh**
Jordan University of Science and Technology

Prof. **Mohammad Al-Tahat**
The university of Jordan

Prof. **Suhil Kiwan**
The Jordan University of Science and Technology

THE INTERNATIONAL ADVISORY BOARD

Abu-Qudais, Mohammad
Jordan University of Science & Technology, Jordan

Jaber, Jamal
Al- Balqa Applied University, Jordan

Abu-Mulaweh, Hosni
Purdue University at Fort Wayne, USA

Jubran, Bassam
Ryerson University, Canada

Afaneh Abdul-Hafiz
Robert Bosch Corporation, USA

Kakac, Sadik
University of Miami, USA

Afonso, Maria Dina
Institute Superior Tecnico, Portugal

Khalil, Essam-Eddin
Cairo University, Egypt

Badiru, Adedji B.
The University of Tennessee, USA

Mutoh, Yoshiharu
Nagaoka University of Technology, Japan

Bejan, Adrian
Duke University, USA

Pant, Durbin
Iowa State University, USA

Chalhoub, Nabil G.
Wayne State University, USA

Riffat, Saffa
The University of Nottingham, U. K

Cho, Kyu-Kab
Pusan National University, South Korea

Saghir, Ziad
Ryerson University, Canada

Dincer, Ibrahim
University of Ontario Institute of Technology,
Canada

Sarkar, MD. Abdur Rashid
Bangladesh University of Engineering &
Technology, Bangladesh

Douglas, Roy
Queen's University, U. K

Siginer, Dennis
Wichita State University, USA

El Bassam, Nasir
International Research Center for Renewable
Energy, Germany

Sopian, Kamaruzzaman
University Kebangsaan Malaysia, Malaysia

Haik, Yousef
United Arab Emirates University, UAE

Tzou, Gow-Yi
Yung-Ta Institute of Technology and Commerce,
Taiwan

EDITORIAL BOARD SUPPORT TEAM

Language Editor

Dr. Baker M. Bani-khair

Publishing Layout

Eng. Ali Abu Salimeh

SUBMISSION ADDRESS:

Dr. Ali M. Jawarneh, Editor-in-Chief
Jordan Journal of Mechanical & Industrial Engineering,
Hashemite University,
PO Box 330127, Zarqa, 13133 , Jordan
E-mail: jjmie@hu.edu.jo



Hashemite Kingdom of Jordan



Hashemite University

Jordan Journal of
Mechanical and Industrial Engineering

JJMIE

An International Peer-Reviewed Scientific Journal
Financed by Scientific Research Support Fund

<http://jjmie.hu.edu.jo/>

ISSN 1995-6665

Jordan Journal of Mechanical and Industrial Engineering (JJMIE)

JJMIE is a high-quality scientific journal devoted to fields of Mechanical and Industrial Engineering. It is published by The Jordanian Ministry of Higher Education and Scientific Research in corporation with Hashemite University.

Introduction: The Editorial Board is very committed to build the Journal as one of the leading international journals in mechanical and industrial engineering sciences in the next few years. With the support of the Ministry of Higher Education and Scientific Research and Jordanian Universities, it is expected that a heavy resource to be channeled into the Journal to establish its international reputation. The Journal's reputation will be enhanced from arrangements with several organizers of international conferences in publishing selected best papers of the conference proceedings.

Aims and Scope: *Jordan Journal of Mechanical and Industrial Engineering* (JJMIE) is a refereed international journal to be of interest and use to all those concerned with research in various fields of, or closely related to, mechanical and industrial engineering disciplines. *Jordan Journal of Mechanical and Industrial Engineering* aims to provide a highly readable and valuable addition to the literature which will serve as an indispensable reference tool for years to come. The coverage of the journal includes all new theoretical and experimental findings in the fields of mechanical and industrial engineering or any closely related fields (Materials, Manufacturing, Management, Design, Thermal and Fluid, Energy, Control, Mechatronics, and Biomedical). The journal also encourages the submission of critical review articles covering advances in recent research of such fields as well as technical notes.

Guide for Authors

Manuscript Submission:

High-quality submissions to this new journal are welcome now and manuscripts may be either submitted online or email.

Online: For online and email submission upload one copy of the full paper including graphics and all figures at the online submission site, accessed via <http://jjmie.hu.edu.jo>. The manuscript must be written in MS Word 2010 Format. All correspondence, including notification of the Editor's decision and requests for revision, takes place by e-mail and via the Author's homepage, removing the need for a hard-copy paper trail.

Submission address and contact:

Dr. Ali M. Jawarneh
Editor-in-Chief
Jordan Journal of Mechanical & Industrial Engineering,
Hashemite University,
PO Box 330127, Zarqa, 13115, Jordan
E-mail: jjmie@hu.edu.jo

Types of contributions: Original research papers and Technical reports

Corresponding author: Clearly indicate who is responsible for correspondence at all stages of refereeing and publication, including post-publication. Ensure that telephone and fax numbers (with country and area code) are provided in addition to the e-mail address and the complete postal address. Full postal addresses must be given for all co-authors.

Original material: Submission of an article implies that the work described has not been published previously (except in the form of an abstract or as part of a published lecture or academic thesis), that it is not under consideration for publication elsewhere, that its publication is approved by all authors and that, if accepted, it will not be published elsewhere in the same form, in English or in any other language, without the written consent of the Publisher. Authors found to be deliberately contravening the submission guidelines on originality and exclusivity shall not be considered for future publication in this journal.

Withdrawing: If the author chooses to withdraw his article after it has been assessed, he shall reimburse JJMIE with the cost of reviewing the paper.

Manuscript Preparation:

General: Editors reserve the right to adjust style to certain standards of uniformity. Original manuscripts are discarded after publication unless the Publisher is asked to return original material after use. Please use MS Word 2010 for the text of your manuscript.

Structure: Follow this order when typing manuscripts: Title, Authors, Authors title, Affiliations, Abstract, Keywords, Introduction, Main text, Conclusions, Acknowledgements, Appendix, References, Figure Captions, Figures and then Tables. Please supply figures imported into the text AND also separately as original graphics files. Collate acknowledgements in a separate section at the end of the article and do not include them on the title page, as a footnote to the title or otherwise.

Text Layout: Use 1.5 line spacing and wide (3 cm) margins. Ensure that each new paragraph is clearly indicated. Present tables and figure legends on separate pages at the end of the manuscript. If possible, consult a recent issue of the journal to become familiar with layout and conventions. All footnotes (except for table and corresponding author footnotes) should be identified with superscript Arabic numbers. To conserve space, authors are requested to mark the less important parts of the paper (such as records of experimental results) for printing in smaller type. For long papers (more than 4000 words) sections which could be deleted without destroying either the sense or the continuity of the paper should be indicated as a guide for the editor. Nomenclature should conform to that most frequently used in the scientific field concerned. Number all pages consecutively; use 12 or 10 pt font size and standard fonts.

Corresponding author: Clearly indicate who is responsible for correspondence at all stages of refereeing and publication, including post-publication. The corresponding author should be identified with an asterisk and footnote. Ensure that telephone and fax numbers (with country and area code) are provided in addition to the e-mail address and the complete postal address. Full postal addresses must be given for all co-authors. Please consult a recent journal paper for style if possible.

Abstract: A self-contained abstract outlining in a single paragraph the aims, scope and conclusions of the paper must be supplied.

Keywords: Immediately after the abstract, provide a maximum of six keywords (avoid, for example, 'and', 'of'). Be sparing with abbreviations: only abbreviations firmly established in the field may be eligible.

Symbols: All Greek letters and unusual symbols should be identified by name in the margin, the first time they are used.

Units: Follow internationally accepted rules and conventions: use the international system of units (SI). If other quantities are mentioned, give their equivalent in SI.

Maths: Number consecutively any equations that have to be displayed separately from the text (if referred to explicitly in the text).

References: All publications cited in the text should be presented in a list of references following the text of the manuscript.

Text: Indicate references by number(s) in square brackets in line with the text. The actual authors can be referred to, but the reference number(s) must always be given.

List: Number the references (numbers in square brackets) in the list in the order in which they appear in the text.

Examples:

Reference to a journal publication:

[1] M.S. Mohsen, B.A. Akash, "Evaluation of domestic solar water heating system in Jordan using analytic hierarchy process". Energy Conversion & Management, Vol. 38 (1997) No. 9, 1815-1822.

Reference to a book:

[2] Strunk Jr W, White EB. The elements of style. 3rd ed. New York: Macmillan; 1979.

Reference to a conference proceeding:

[3] B. Akash, S. Odeh, S. Nijmeh, "Modeling of solar-assisted double-tube evaporator heat pump system under local climate conditions". 5th Jordanian International Mechanical Engineering Conference, Amman, Jordan, 2004.

Reference to a chapter in an edited book:

[4] Mettam GR, Adams LB. How to prepare an electronic version of your article. In: Jones BS, Smith RZ, editors. Introduction to the electronic age, New York: E-Publishing Inc; 1999, p. 281-304

Free Online Color : If, together with your accepted article, you submit usable color and black/white figures then the journal will ensure that these figures will appear in color on the journal website electronic version.

Tables: Tables should be numbered consecutively and given suitable captions and each table should begin on a new page. No vertical rules should be used. Tables should not unnecessarily duplicate results presented elsewhere in the manuscript (for example, in graphs). Footnotes to tables should be typed below the table and should be referred to by superscript lowercase letters.

Notification: Authors will be notified of the acceptance of their paper by the editor. The Publisher will also send a notification of receipt of the paper in production.

Copyright: All authors must sign the Transfer of Copyright agreement before the article can be published. This transfer agreement enables Jordan Journal of Mechanical and Industrial Engineering to protect the copyrighted material for the authors, but does not relinquish the authors' proprietary rights. The copyright transfer covers the exclusive rights to reproduce and distribute the article, including reprints, photographic reproductions, microfilm or any other reproductions of similar nature and translations.

Proof Reading: One set of page proofs in MS Word 2010 format will be sent by e-mail to the corresponding author, to be checked for typesetting/editing. The corrections should be returned within **48 hours**. No changes in, or additions to, the accepted (and subsequently edited) manuscript will be allowed at this stage. Proofreading is solely the author's responsibility. Any queries should be answered in full. Please correct factual errors only, or errors introduced by typesetting. Please note that once your paper has been proofed we publish the identical paper online as in print.

Author Benefits:

No page charges: Publication in this journal is free of charge.

Free offprints: One journal issues of which the article appears will be supplied free of charge to the corresponding author and additional offprint for each co-author. Corresponding authors will be given the choice to buy extra offprints before printing of the article.

PAGES	PAPERS
69 - 75	Energy Performance Assessment of a Non-domestic Service Building in Jordan <i>Mohamad I. Al-Widyan, Ibrahim A. Soliman, Ahmed A. Alajlouni, Omar I. Al Zu'bi, Amal I. Jaradat</i>
77 - 91	Optimization of a Closed Loop Green Supply Chain using Particle Swarm and Genetic Algorithms <i>Mojtaba Rahimi , Hamed Fazlollahtabar</i>
93– 98	Sensorless Control System Design of a Small Size Vertical Axis Wind Turbine <i>Mayouf Messaoud, Bakhti Hadi , Dahmani Aissa</i>
99– 107	Pulsating Nanofluid Jet Impingement onto a Partially Heated Surface Immersed in a Porous Layer <i>Iman Zahmatkesh, Seyyed Ali Naghedifar</i>
109– 116	Design Approach of Shell and Tube Vaporizer for LNG Regasification <i>Ganesh Prasad, Amlan Das</i>
117– 122	The Effect of NanoParticle Coating on Anticorrosion Performance of Centrifugal Pump Blades <i>Somayeh Kouhi, Bahram Ghamari, Reza Yeganeh</i>
123– 129	Experimental Study to Investigate the Effect of Dust, Wind Speed and Temperature on the PV Module Performance <i>Maher Al-Maghalseh</i>
131– 139	Effect of Transverse Steady Magnetic Field on MHD Flow Under Free Convection Conditions in Vertical Microchannels <i>Mohammad A. Hamdan , Anwar H. Al-Assaf , Mohammad A. Al-Nimr</i>
141– 151	Domains of Magnetic Moments of Two onboard Coils with Stable Damping of Microsatellite Angular Velocities <i>V.V. Lyubimov, S.V. Podkletnova</i>
153– 159	Embedded Wireless Testing System Applied in Coal Cutting Experiment <i>Chenxu Luo, Shuangxi Jing , Yu LIU, xiaoming HAN</i>

Energy Performance Assessment of a Non-domestic Service Building in Jordan

Mohamad I. Al-Widyan^{*}, Ibrahim A. Soliman, Ahmed A. Alajlouni
Omar I. Al Zu'bi, Amal I. Jaradat

Department of Mechanical Engineering - Jordan University of Science and Technology, Irbid 22110,
Jordan

Received JAN 13 2018

Accepted Aug 24 2018

Abstract

This work assessed the energy performance of a non-residential service building in Jordan. A comprehensive energy audit was conducted through which building systems were investigated including the building envelope, HVAC, and lighting systems. Multiple site surveys were conducted using standard audit instruments to record different operating conditions. Energy analysis, consumption trends, and system specifications were all examined, additionally, retrofit solutions were proposed to enhance the efficiency of each system. Results indicated that replacing all the single glazed windows with double-glazed thermally broken windows could yield a reduction in total energy consumption by 9%. Moreover, installing LED fixtures instead of the existing fluorescent fixtures can lower the total annual energy consumption by 4%. Also, in this particular building, separating the building's first floor balcony terrace from the ground floor can reduce the total annual energy consumption by 13%. Additionally, using all proposed retrofit solutions can reduce the building total annual energy consumption by more than 33%.

© 2018 Jordan Journal of Mechanical and Industrial Engineering. All rights reserved

Keywords: Energy performance assessment, Energy efficiency, Energy audit, Non-domestic service buildings, Jordan.

1. Introduction

The continuous use of fossil fuels over the last 100 years had detrimental environmental impacts that manifested itself in global warming among other consequences [1]. In addition, the ever-diminishing fossil fuel sources caused a giant leap in the interest in assessing the energy performance and efficiency in buildings. As such, many studies worldwide addressed the impact of various retrofit measures on energy consumption in buildings [2-4]. Findings showed that thermal improvements in buildings can result in substantial energy savings in excess of 40% [5, 6], as well as a reduction in cooling loads of up to 80% [7]. Other studies involved implementing energy audits for existing commercial office buildings and resulted in an average energy utilization index (EUI) of about 235 kWh/m²/year [8]. Susorova et al. [9] examined commercial office buildings under six climate zones in the USA and showed that fenestration improvements can yield up to 14% reduction in building total energy consumption in hot climates.

Jordan, like many other developing countries, imports more than 97% of its energy needs [10], leading to vital socio-economic consequences [11]. Also, Jordan's primary energy demand is forecast to grow by 62% by the year 2025 [12]. In response, a national energy efficiency strategy was launched in 2005 that included a wide range

of energy efficiency measures [13, 14]. This strategy marked the first systematic governmental and, to a much less extent, research community's interest in the energy issue in the country.

Several local sporadic research efforts tackled energy efficiency and building energy performance in Jordan. Overall, most studies investigated the feasibility of incorporating energy efficient measures to various types of existing buildings [15-21]. Alzoubi, and Al-Zoubi [22] conducted a simulation study on the impact of different shading devices and configurations on daylight quality and building energy performance. Results showed that internal luminance can be maximized with minimum solar heat gain by utilizing vertical shading devices. Also, energy and exergy utilization in Jordan were investigated by Al-Ghandour [23] who utilized the end-use models to perform the required energy analysis. Al-Ghandour found that Jordan's energy efficiency amounted to about 48%, and energy efficiency to 23% and further reported that the industrial sector is the most energy efficient amongst others [23].

Based on our literature search, it was evident that, compared to other world regions, there is a serious lack in systematic studies on energy performance and efficiency in buildings in Jordan and the region. Therefore, this work was initiated to assess, in a comprehensive and integrated manner, energy performance of the building of Irbid Chamber of Commerce through an extensive energy audit

* Corresponding author e-mail: widyan@just.edu.jo

and investigate implementing an upgrade to existing systems to assess the potential enhancement of the building's energy efficiency and performance.

2. Materials and Methods

This study was conducted at the building of the Chamber of Commerce (Figure 1) of the City of Irbid, located in the Northwestern part of the country. The exact geographical location of the building is 32.5441° N, 35.8596° E.



Figure 1: The building of Irbid Chamber of Commerce (ICC).

2.1. Building Information

Detailed energy assessments were conducted on the building envelope, HVAC system, and the lighting system as they make up almost the total energy consumption in the building.

As the building layout sketches were initially not available, they were reproduced using Pro/ENGINEER CAD (Figure 2). Wall orientations and fenestration components were recorded from true North using a smart phone accelerometer chip. Then, building information was gathered on major energy consuming devices, fenestrations, shading techniques, HVAC, existing abnormalities (viz., apparent leakages, broken lights), and occupant's attitude toward energy consumption. These notes formed the basis of the follow up extensive audit of the building.

The building was erected in 1996 and consists of an underground and ground floors, and three more levels. Its main entrance is facing southwest with a large tinted

glass façade that has a vestibule entrance with two gates; internal and external that are about 2.0 m apart.

2.2. Instruments used

A measuring tape, Lux meter (Lutron LM-8010), temperature and humidity meter (Di-

Log DL7102), and an IR thermometer (Raytek Raynger MX 4KM98) were used.

2.3. Systems considered and approaches used

2.3.1. The building envelope.

The parameters considered here were wall and window dimensions and orientation along with the specifications of envelope component. For windows, the overall heat transfer coefficient (U), solar heat gain coefficient (SHGC), visible transmittances (VT), and air leakage were examined. For walls, types of layers, their thicknesses, thermal conductivities and resistances, and overall heat transfer coefficient (U) were recorded. Data on thermal properties of some envelope components were obtained from local codes.

2.3.2. The HVAC system.

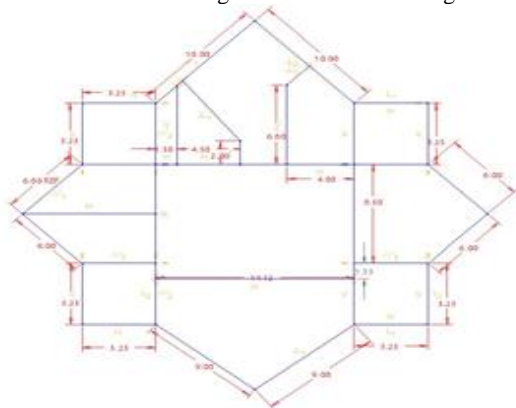
The building heating system consists of a diesel-fired boiler (RIELLO type - RL70), while the cooling system consists of a 150-kW electric water-cooled chiller (BITZER type). The assessment of the HVAC system started with air distribution units.

Temperatures of supply air, room air temperature, and radiators were recorded.

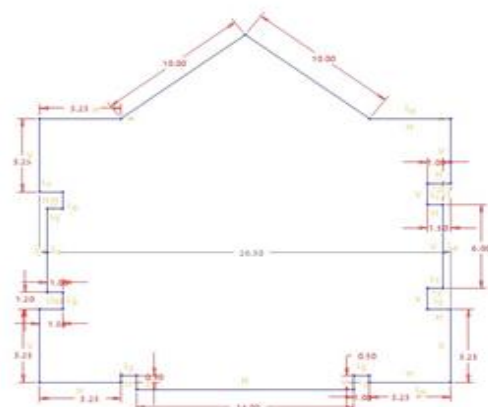
Energy consumption of the heating system was estimated from the equation [24]:

$$Qh = (UA_{glaze} + UA_{window} + UA_{frame}) \cdot \Delta T + \frac{1}{2} V C_p \rho \Delta T \quad (1)$$

where, U is the overall heat loss coefficient, A is the total floor area, ΔT is temperature difference, V is the floor volume, C_p is the specific heat of air, and ρ is air density. Cooling energy consumption was calculated using the formula [24, 25]



(a) First floor



(b) Second and third floors

Figure 2.: The general layout of the building of Irbid Chamber of Commerce.

$$Qc = \left[(UA_{glaze} + UA_{window} + UA_{frame}) \cdot \Delta T \right] + \left[\frac{1}{2} V C_p \rho \Delta T \right] + [N \cdot M] + [A_{glaze} \cdot SHGC \cdot G \cdot \cos\theta] \quad (2)$$

where N is the number of people per floor, SHGC is the solar heat gain coefficient, G is the solar insolation (assumed 800 W/m²), and θ is the solar altitude angle (approx. 83° altitude for local summer), M is the metabolism heat generation (100 W per person) [25]. The second term in Equations 1 and 2 is the air change per hour (assumed 0.5 to account for infiltration) [25].

Finally, additional heating/cooling loads due to human-related factors such as energy misconducts were estimated using the following equation which is an alteration of the air change method infiltration formula [26]:

$$Q_{\text{losses}} = \text{hr} \cdot P\% \cdot \rho \cdot Q \cdot C_p \cdot \Delta T \quad (3)$$

where hr is the working hours per year, P% is the percent of misconducts that represents the percentage of the working hours during which human related losses are imposed (estimated around 10% of the working day), and Q volume flow rate, assumed to be about 5 m³ per hour for the building [26]. In this work, the temperature difference between indoor and outdoor were assumed to be 20 °C for winter and 14 °C for summer.

2.3.3. The lighting system.

Notes were taken on fixture specification, count, and distribution, in addition to lux data. Also, Luminaire Dirt Depreciation (LDD) and Lamp Lumen Depreciation (LLD) data were considered. The visual comfort probability (VCP) was assessed by performing a survey on building occupants in terms of lighting glare, and work environment lighting quality while the Color Rendering Index (CRI) was determined from the datasheets.

Finally, internal shading in each room was accounted for.

2.3.4. Appliances.

These included mostly computers and printers. It was assumed that computers operate 5 hours a day; the mean loading is 75%, and 25% for computers and printers, respectively.

3. Results and Discussion

3.1. Building Envelope

The gross area of the building walls was about 1370 m². The walls consisted of several layers including limestone, insulation, hollow block, and plaster. Table 1 outlines the specifications of wall layers (thermal conductivity, k, and overall heat transfer coefficient, U).

Table 1: Specifications of wall components.

Layer	Thickness	Thermal conductivity	Thermal resistance	U-factor
	m	W/m ² .K	m ² K/W	W/m ² .K
Limestone	0.3	0.95	0.3158	
Insulation	0.05	0.04	1.25	0.6*
Hollow-Block	0.1	1	0.1	
Plaster	0.02	1.4	0.0143	

*Makes about 100% of the wall's total U-value.

The gross window area in the building was about 490 m². All windows were single glazed (U of 2.1 W/ m².K) with aluminum frames (U of 2.4 W/ m².K) and overall U factor of 4.5 W/ m².K. South-facing windows in the ground and first floors, although tinted, they admit substantial amount of daylight due to their large areas. In contrast, north-facing windows can better reduce lighting load by benefiting from daylight. However, these windows were small and heavily shaded all day. As such, folding the shades can enable more access to ambient day lighting.

3.2. Heating and cooling loads

Figure 3 shows that the peak heat load was about 18 MWh and that heating load in December 2016 was only 10% of the corresponding load in 2015 due to utilizing the PV in the heating mode. The mean heating load in 2016 was about 60% of that in 2015, which was due to utilizing the PV system. Figure 3 also compares the “ideal” heat load (zero losses), with the actual measured data indicating that losses impose a 30% increase in heating load.

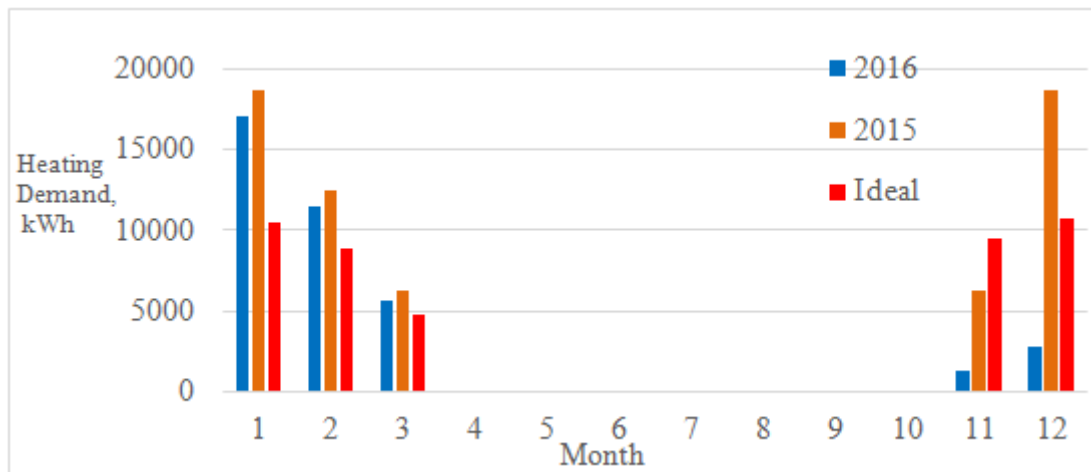


Figure 3: Actual and ideal monthly heating loads for the ICC building for 2015 and 2016.

Figure 4 shows that cooling load peaks (12 MWh) in August and cooling loads were similar for 2015 and 2016 due to similar weather conditions. Figure 4 also reveals that the actual cooling load would be 10% higher than the ideal goal as there had been no infiltration or heat gains.

3.3. Lighting and appliance loads

Lighting specifications in each floor are outlined in Table 2.

Lighting types used were CFL, F15T8, and LED with several fixtures that were either

broken, at the end of their life cycle, or with high dirt depreciation. As for glare, the survey results revealed a 70% rate of satisfaction among employees. (IES). Table 3 outlines the

performance of existing lighting in the building relative to recommended values Illuminating Engineering Society IES [27].

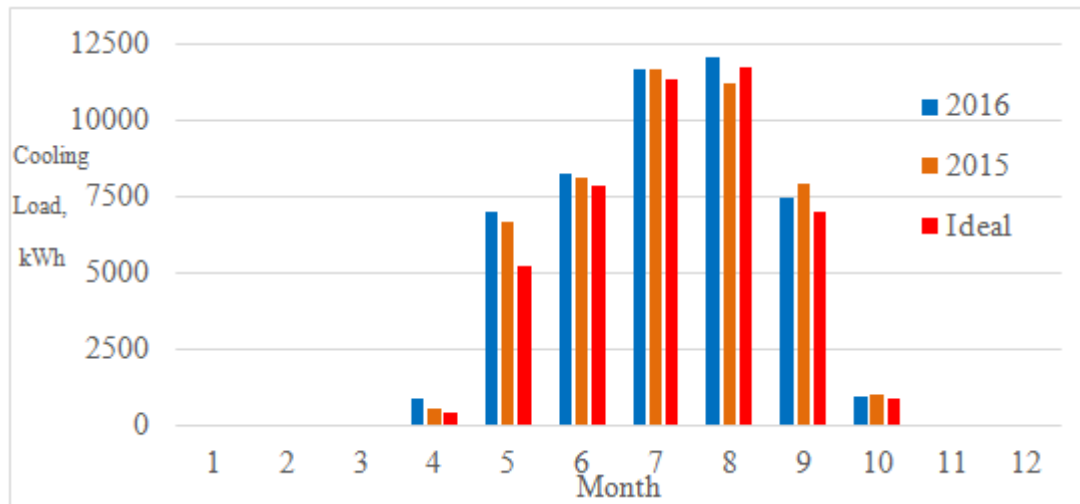


Figure 4: Actual and ideal monthly cooling loads for the ICC building for 2015 and 2016

Table 2: General specifications of existing lighting.

Floor	Lighting type	Number of fixtures	Wattage	Total power peak load	Lighting peak load
Ground	CFL	9	24	576 W	11892 W
	F15T8	6 (4×)	15		
First	CFL	4	24	3760 W	
	F15T8	29 (4×)	15		
	LED	52	37		
Second	CFL	20	24	2276 W	
	F15T8	25 (4×)	15		
Third	LED	8	37	5280 W	
	CFL	10	24		
	F15T8	84 (4×)	15		

Table 3: Performance indices of existing buildings and nominal values.

Performance index	Lux	Uniformity	Glare	CRI
Actual values	Offices and labs: 350	insufficient light distribution	Mean VCP: 70%	80+
Nominal values	500	Uniform on work-plane	VCP: 80+	Excellent: 90+

As far as appliances are concerned, relevant data showed that, at the time of this study, the building had 56 computer units rated at 130 W and 22 printers rated at 30 W. This made the average daily energy consumption by appliances around 28.6 kWh.

3.4. Electricity and diesel consumption

Figure 5 shows electricity consumption (kWh) for the years 2015 and 2016. It should be noted that the difference in consumption between the two years is due to the fact that there is an underground floor that was vacant in 2015, but has been rented to a medical center in June 2016. The medical center was factored out from assessment. Electric load in winter was substantially lower than that in summer because heating was performed by a diesel-fired boiler.

The peak, average, and base electricity loads for the year 2016 are depicted in Figure 6 which shows a peak load in August at around 16 MWh which is due to high electric cooling loads. Moreover, the dip in Figure 6 around September is ascribed to the installation of a 50-kW PV system that carries part of the cooling/heating load via an integrated boiler and absorption cycles. The average electricity load was 9.5 MWh while the base load was 3.2 MWh.

Figure 7 shows that diesel consumption was maximum in January where heating load was maximum, whereas a significantly lower diesel consumption in November and

December of 2016 was noted, which is attributed to using the PV system in heating mode. As evident from Figure 7, the solar system contribution is vividly evident when comparing December 2015 to 2016 where diesel consumption was reduced by 3.65 m³.

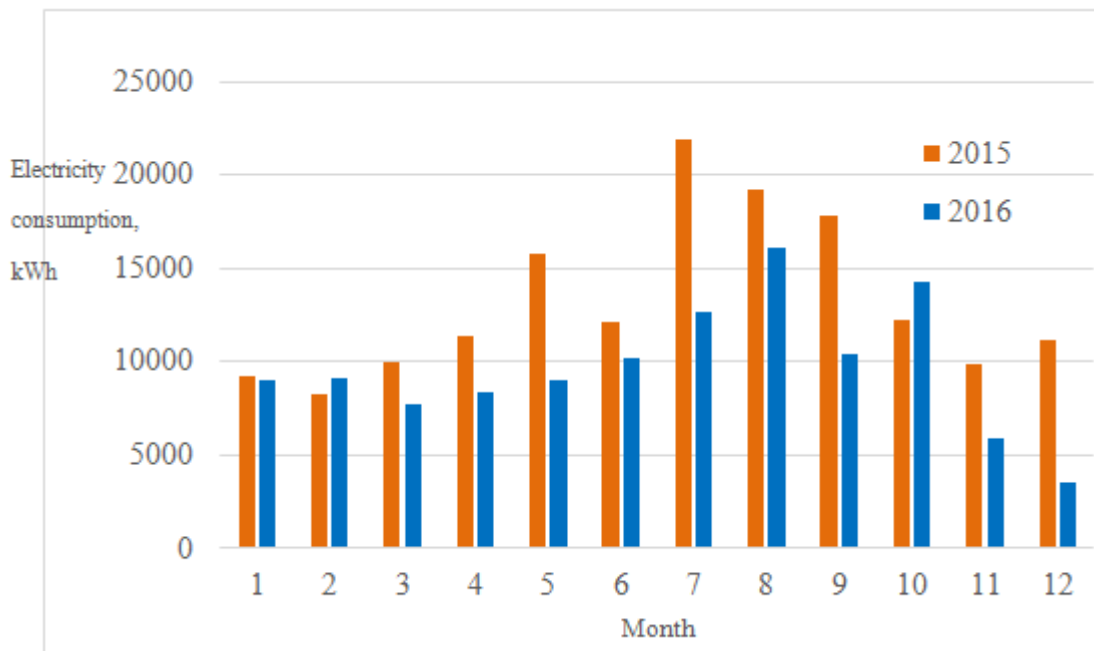


Figure 5: Monthly electricity consumption for the ICC building for 2015 and 2016.

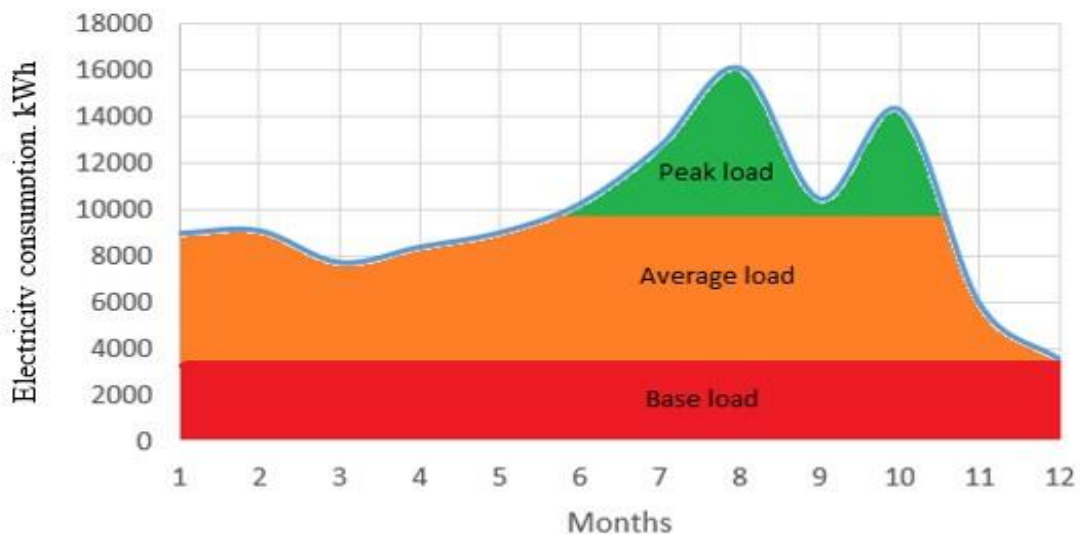


Figure 6: Peak, average, and base loads for the ICC building for 2016.

3.5. Building energy performance

Table 4 outlines electricity and diesel consumption for 2015 and 2016. Based on carbon emission data by electricity generating facilities in Jordan, 724 g of CO₂ are emitted per kWh of electricity [28], compared to about 277 g CO₂/kWh of energy generated by diesel fuel [29].

The annual heating load is higher than the cooling load, which is a consequence of heating degree days, HDD, and cooling degree days, CDD, which are, respectively, 2190 and 660 for the year 2016 [30].

3.6. Energy misconducts

Misconducts included such practices as setting heating thermostat at excessively high values. In contrast to a comfort heating temperature of 27 °C, temperatures of airflow

in some offices were 46 °C. Moreover, it was noted that leaving the doors open to the

unconditioned staircase which is open to the whole building and adjacent to the building envelope across four floors is common practice. Both misconducts caused substantial conditioning energy losses.

3.7. Proposed energy saving measures and their potential impacts

Based on the findings, major proposed measures involve switching to double-glazed and

LED lights, avoiding excessive heat loss, dealing with energy misconducts and conducting

awareness campaigns. The potential impact of the individual and all proposed measures are shown in Figure 8 which readily shows that implementing all proposed measures can yield up to 33% reduction in annual energy consumption.

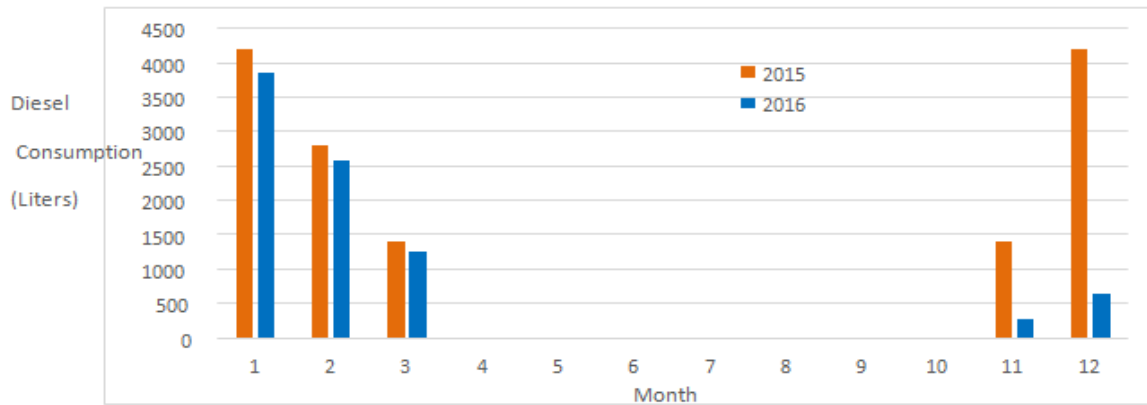


Figure 7: Annual diesel consumption for the ICC building in 2015 and 2016.

Table 4: outlines electricity and diesel consumption for 2015 and 2016.

Year	Energy Source	Total Consumption		Annual Cost	Consumption Index	Emissions
		(kWh)	(GJ)			
2015	Electricity	159013	572.45	39172	217.66	115.13
	Diesel		548.8	4855	208.67	42.26
	Total		549.37		426.33	157.39
2016	Electricity	116138	418	28766	158.94	84.08
	Diesel		671.58	5792	255.35	51.71
	Total		671.98		414.29	135.79

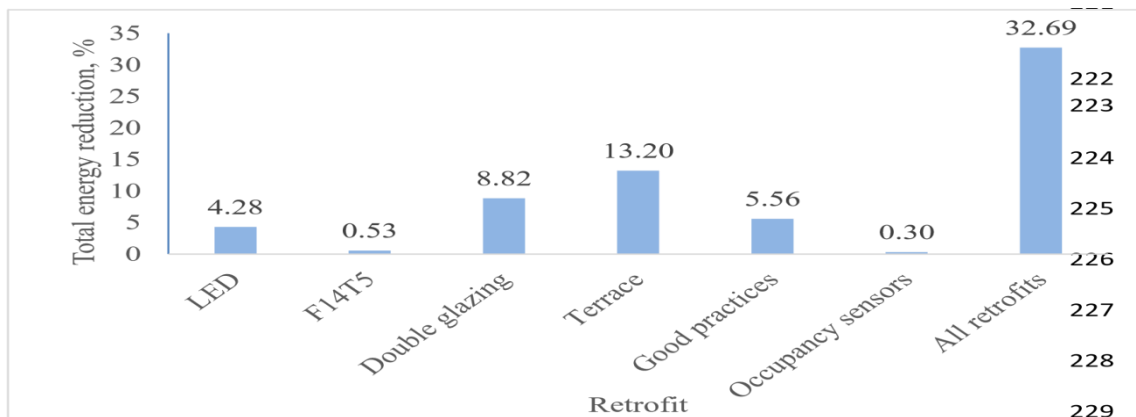


Figure 8: Existing system and proposed retrofit annual total energy consumption.

4. Conclusion

Based on the findings of this study, it may be concluded that in a country like Jordan that relies heavily on imported energy, a substantial potential does exist not only for reducing energy consumption, but also for simultaneously improving the level of human comfort in service buildings. Also, in such buildings, the envelope, HVAC, and lighting systems make up almost the total energy consumption and thus energy management efforts should focus on them. In addition, this work indicated that a reduction of 33% is achievable by implementing common retrofits to the existing building systems considered here. Also, this study revealed that, at the national level, there is a serious deficiency in energy audit efforts and hence there is a genuine need for systematic awareness campaigns and audit effort in this respect. Finally, implementing renewable energy projects, particularly, PV systems, can make substantial savings in energy consumption in buildings. Therefore, national incentive programs to this end should be re-examined and expanded.

References

- [1] Al-Widyan, M.I., Al-Muhtaseb, M.T., 2009. Institutional Aspects of Regional Energy
- [2] Systems. Renewable Energy in the Middle East NATO Science for Peace and Security Series C: Environmental Security 177–195. doi:10.1007/978-1-4020-9892-5_10. London, UK.
- [3] Geng Y, Ji W, Lin B, Hong J, Zhu Y. Building energy performance diagnosis using energy bills and weather data. *Energy and Buildings*. 2018 Aug 1;172:181-91.
- [4] Lee P, Lam PT, Lee WL. Performance risks of lighting retrofit in Energy Performance Contracting projects. *Energy for Sustainable Development*. 2018 Aug 1;45:219-29.
- [5] Carlson K, Pressnail KD. Value impacts of energy efficiency retrofits on commercial office buildings in Toronto, Canada. *Energy and Buildings*. 2018 Mar 1;162:154-62.
- [6] Aste, N.C.B., Pero, C.D., 2012. Energy retrofit of commercial buildings: case study and applied methodology. *Energy Efficiency* 6, 407–423. doi:10.1007/s12053-012-9168-4.
- [7] Nazi, W.I., Royapoor, M., Wang, Y., Roskilly, A.P., 2017. Office building cooling load reduction using thermal analysis method – A case study. *Applied Energy* 185, 1574–1584. doi:10.1016/j.apenergy.2015.12.053.
- [8] Huang, Y., Niu, J.-L., Chung, T.M., 2013. Study on performance of energy-efficient retrofitting measures on commercial building external walls in cooling-dominant cities. *Applied Energy* 103, 97–108. doi:10.1016/j.apenergy.2012.09.003.
- [9] Jing, R., Wang, M., Zhang, R., Li, N., Zhao, Y., 2017. A study on energy performance of 30 commercial office buildings in Hong Kong. *Energy and Buildings* 144, 117–128. doi:10.1016/j.enbuild.2017.03.042.
- [10] Susorova, I., Tabibzadeh, M., Rahman, A., Clack, H.L., Elnimeiri, M., 2013. The effect of geometry factors on fenestration energy performance and energy savings in office buildings. *Energy and Buildings* 57, 6–13. doi:10.1016/j.enbuild.2012.10.035.
- [11] Key World Energy Statistics 2016. Key World Energy Statistics 2016. doi:10.1787/key_eng_stat-2016-en.
- [12] Energy Sector in Jordan 2, Crude Oil and Non-Renewable Resources, Jordan: Jordan Independent Economy Watch, 2015.
- [13] Energy 2016 - Facts and figures, Jordan: Ministry of Energy and Mineral Resources, 2016. [13] Updated Master Strategy Of Energy Sector In Jordan For The Period (2007-2020), Jordan:
- [14] Royal Commission, 2007.
- [15] The Demographic Opportunity in Jordan, Jordan: Higher Population Council, 2009.
- [16] Hammad M, Ebaid MS, Al-Hyari L. Green building design solution for a kindergarten in Amman. *Energy and Buildings* 2014;76:524–37. doi:10.1016/j.enbuild.2014.02.045.
- [17] Hassouneh K, Al-Salaymeh A, Quossous J. Energy audit, an approach to apply the concept of green building for a building in Jordan. *Sustainable Cities and Society* 2015;14:456–62. doi:10.1016/j.scs.2014.08.010.
- [18] Jaber S, Ajib S. Optimum, technical and energy efficiency design of residential building in Mediterranean region. *Energy and Buildings* 2011;43:1829–34. doi:10.1016/j.enbuild.2011.03.024.
- [19] Sharaf FM, Al-Salaymeh A. A comparative study of the use of energy conservation techniques in office building: Passive and solar energy applications: The case of Jordan.
- [20] *Sustainable Cities and Society* 2012;5:16–22. doi:10.1016/j.scs.2012.08.001.
- [21] Hassouneh K, Alshboul A, Al-Salaymeh A. Influence of windows on the energy balance of apartment buildings in Amman. *Energy Conversion and Management* 2010;51:1583–91. doi:10.1016/j.enconman.2009.08.037.
- [22] Hasan Jarad and "Moh'd Sami" Ashhab. Energy Savings in the Jordanian Residential Sector.
- [23] *Jordan Journal of Mechanical and Industrial Engineering* 2017;11:51-59.
- [24] Al-Hinti, I. and H. Al-Sallami. Potentials and Barriers of Energy Saving in Jordan's Residential Sector through Thermal Insulation. *Jordan Journal of Mechanical and Industrial Engineering* 2017;11:141-145.
- [25] Alzoubi HH, Al-Zoubi AH. Assessment of building façade performance in terms of daylighting and the associated energy consumption in architectural spaces: Vertical and horizontal shading devices for southern exposure facades. *Energy Conversion and Management* 2010;51:1592–9. doi:10.1016/j.enconman.2009.08.039.
- [26] Al-Ghandoor A. Evaluation of energy use in Jordan using energy and exergy analyses.
- [27] *Energy and Buildings* 2013;59:1–10. doi:10.1016/j.enbuild.2012.12.035.
- [28] McQuiston FC. Heating, ventilation and air conditioning. New York: Wiley; 2004.
- [29] Ventilation for acceptable indoor air quality: ASHRAE standard. Atlanta, GA: American Society of Heating, Refrigerating and Air-Conditioning Engineers; 2013.
- [30] Thumann A, Mehta DP. Handbook of energy engineering. Lilburn, GA: Fairmont Press; 2013.
- [31] Rea MS. The IESNA lighting handbook: reference & application. New York, NY: IESNA, Publ. Dep.; 2000.
- [32] Mojaheed Elsagheer. The Energy Situation in Jordan. Ministry of Planning and International Cooperation, July 2013.
- [33] U.S. Energy Information Administration - EIA - Independent Statistics and Analysis. How much carbon dioxide is produced when different fuels are burned? - FAQ - US Energy Information Administration (EIA). <https://www.eia.gov/tools/faqs/faq.php?id=73&t=11> (accessed March 19, 2017).
- [34] Custom Degree Day Data. Degree Days Net. <http://www.degree-days.net/> (accessed March 19, 2017).

Optimization of a Closed Loop Green Supply Chain using Particle Swarm and Genetic Algorithms

Mojtaba Rahimi^a, Hamed Fazlollahtabar^{b,*}

^aDepartment of Industrial Engineering, Mazandaran University of Science and Technology, Babol, Iran

^bDepartment of Industrial Engineering, School of Engineering, Damghan University, Damghan, Iran

Received OCT 20 2017

Accepted SEP 01 2018

Abstract

Nowadays, due to increase of environmental hazards and legislation in this context by governments and also restriction of manufacturing resources, researchers paid special attention to the design of closed-loop green supply chain network. To establish better coordination between the components of the supply chain and gain more profits in the network, special decisions are required during the product lifecycle. The network presented in this study consists of four layers in the forward chain including suppliers, manufacturers, distribution centers and customer markets, and it also includes three facilities containing collection, dismantler and disposal centers in reverse chain. A mixed integer linear programming model proposed to optimize closed-loop green supply chain by considering the level of quality for constituent components of manufacturing parts along with the pricing policy and product life cycles to maximize profits. Genetic algorithm and particle swarm optimization are used to find the optimal solutions. Having analyzed the results and due to the relative percentage deviation and solution time, it was found that genetic algorithm performs better compared with the particle swarm optimization.

© 2018 Jordan Journal of Mechanical and Industrial Engineering. All rights reserved

Keywords: Closed-loop supply chain (CLSC); Green supply chain (GrSC); Mathematical programming; Particle swarm optimization (PSO); Genetic algorithm (GA).

1. Introduction

Recently, much research in the field of closed-loop and green supply chain is done. A closed-loop logistics model for remanufacturing has been studied by Jayaraman et al. (1999) in which decisions relevant to shipment and remanufacturing of a set of products, as well as establishment of facilities to store the remanufactured products, were taken into consideration. The model was in the form of a 0–1 integer programming formulation and minimizes a total cost function of shipment, remanufacturing, and inventory. Fleischmann et al. (2001) considered a reverse logistics (RL) network design problem in which they analyzed the impact of product return flows on logistics networks. Krikke et al. (2003) considered minimization of facility set-up, processing, and distribution costs in the CLSC network design, while designing a GrSC with support from both product design and logistics networks. Sarkis (2003) provided a strategic decision framework with the help of an analytical network process for making decisions within the GrSC. Debo et al. (2006) studied the effects of new and remanufacturing products in the same market over the life cycle. In addition, they examined the production system when demand for new and remanufactured products is segmented into same and secondary markets. Ko and Evans (2007) presented a mixed-integer nonlinear programming (MINLP) model to configure forward and

return networks. Moreover, they utilized genetic algorithm to solve the problem. Salema et al. (2007) presented a general model for reverse logistics network where capacity limits, multiproduct management, and uncertainty on product demands and returns exist.

While reverse logistic activities in a CLSC can improve the competence of enterprises, customer service level, and reduce the production costs, they should also provide a green image to the enterprises by increasing the demand of conscious customers for their products (Demirel and Gokcen 2008). Selim and Ozkarahan (2008) proposed a fuzzy goal programming approach for a reverse logistics (RL) network. The uncertainty in demand and decision makers' aspiration levels for the goals are taken into account. Lee et al. (2009) proposed a model for minimizing shipment costs of a CLSC and opening costs of disassembly centers and processing centers. In other words, the model can determine the optimal numbers of disassembly and processing centers. But, it does not include inventory costs such as holding costs. In addition, the model is designed for single supplier. Guide and Van Wassenhove (2009) categorized product returns according to product life cycle. Besides, they linked product return types to specific recovery activities. However, they did not examine the effects of returns pair on network configuration. Commercial returns are products that are returned by consumers within a certain period of time (for instance, 60 days after buying). These returned products often are repaired. End-of-use returns happen when a

* Corresponding author e-mail: hfazl@du.ac.ir;
hfazl@alumni.iust.ac.ir.

functional product is replaced by a technological upgrade. The majority of these products are remanufactured. End-of-life returns are available when the product becomes technically obsolete or no longer contains any utility for the current user. The option of recycling is more suitable for this kind of return. Cell phone industry is a good example of three types of returns.

Pishvae et al. (2010) developed a bi-objective MILP model to minimize the total costs and maximize the responsiveness of a logistics network. They applied a memetic algorithm. El-Sayed et al. (2010) proposed a multi-period forward and reverse logistics network. They considered both deterministic and stochastic demands. Paksoy et al. (2010) emphasized the reuse of recovered and recycled material while considering the minimization of carbon emissions of transporting vehicles through multi-objective mixed integer linear programming problems. Kannan et al. (2010) proposed a multi-period closed loop supply chain network for the optimum usage of recovered material in terms of lead recovered from lead-acid batteries. Their purpose was to develop a multi-echelon, multi-period, and multi-product CLSC to determine optimum distribution and inventory level decisions through a heuristics-based genetic algorithm (GA).

Pishvae et al. (2011) proposed a robust optimization model for handling the inherent uncertainty of input data in a CLSC network problem. While first, a deterministic mixed integer programming model is developed for designing the CLSC network, finally the robust counterpart of the proposed model was presented by using the recent extensions in robust optimization theory. Shi et al. (2011) studied a production-planning problem for a multi-product closed-loop system, in which the manufacturer has two channels for supplying products: producing brand-new products and remanufacturing returns into as-new ones. The problem is to maximize the manufacturer's expected profit by jointly determining the production quantities of brand-new products, the quantities of remanufactured products, and the acquisition prices of the used products, subject to a capacity constraint. Ramezani et al. (2013) proposed a stochastic multi-objective model for the integrated forward and reverse supply chain network under uncertain environments. In their study, uncertainty referred to the return rate of used products. They aimed at maximization of profits, customer service levels in both forward and reverse networks, and sigma quality levels by minimizing defects in raw materials. Ozkır and Baslıgil (2013) proposed a multi-period, multi-commodity and capacitated CLSC network design with the help of a multi-objective optimization model.

Devika et al. (2014) proposed a mixed integer linear programming model to design a CLSC network to capture the triple bottom line of the sustainability. They considered recovering, remanufacturing, recycling, and disposal facilities under treatment centers of the reverse logistics network. Ozceylan et al. (2014) proposed an integrated

model that jointly optimizes the strategic and tactical decisions of a closed-loop supply chain (CLSC). The strategic level decisions relate to the amounts of goods flowing on the forward and reverse chains. The tactical level decisions concern balancing disassembly lines in the reverse chain. The objective is to minimize costs of transportation, purchasing, refurbishing, and operating the disassembly workstations. A nonlinear mixed integer programming formulation is described for the problem. Soleimani and Kannan (2015) proposed a hybrid algorithm based on particle swarm optimization (PSO) and genetic algorithm (GA) for a CLSC network design problem. Accorsi et al. (2015) provided a tool to assess the enabling economic, environmental, and transport geography conditions to design sustainable closed-loop networks for the management of a generic product along its life-cycle. The proposed tool is built through a mixed-integer linear programming (MILP) model for the strategic design of a multi-echelon closed-loop network. The model minimizes a cost-based and a carbon-based function to determine the optimal geographic location of the nodes of the network and the allocation of transport flows. On the other hand, Diabat et al. (2015) address the single echelon case for both the forward and backward logistics of a closed-loop location-inventory problem, but develop an exact two phase Lagrangian relaxation to solve it. Garg et al. (2015) proposed a multi-objective mixed integer nonlinear programming model that extending the traditional supply chain to a closed-loop supply chain for to control the environmental issues has been achieved in terms of increased transport activities and to solve it offered an interactive multi-objective approach and Lingo software.

Zohal and Soleimani (2016) developed a model for green closed-loop supply chain in a gold industry. A green approach based on the CO₂ emission function was regarded in the proposed model. A new ant colony optimization algorithm was proposed to solve generated and real instances.

Soleimani et al. (2017) addressed a design problem of a closed-loop supply chain regarding various echelons of a supply chain. Sustainability and green approaches were considered in the modeling and solving the proposed closed-loop supply chain. Fuzzy type of uncertainty was regarded for customer demands. A developed genetic algorithm was also proposed in order to solve the presented model.

Ghomi-Avili et al. (2018) presented a bi-objective model for green closed-loop supply chain network design considering disruption and operational risks with a fuzzy price-dependent demand. Also, environmental issues by minimizing CO₂ emission in production process were addressed and a bi-level programming method was applied to model Stackleberg game in the problem.

To sum up, an overview of the most significant past works' contributions and the gap handled by this paper are summarized in Table 1.

Table 1: Summary of past works and research gap

	Authors	Year	Topic	Approach
1	Demirel and Gokcen	2008	remanufacturing in reverse logistics environment	mixed integer programming
2	El-Sayed et al.	2010	forward-reverse logistics network design	Mathematical programming
3	Abdallah et al	2012	Green supply chains with carbon trading	Mathematical formulation
4	Amin and Zhang	2012a	closed-loop supply chain configuration	Multi-objective
5	Demirel et al.	2014	closed-loop supply chain network	genetic algorithm
6	Garg et al.	2015	environmental issues in closed loop supply chain network	multi-criteria optimization
7	Zohal and Soleimani	2016	green closed-loop supply chain network	ant colony
8	Soleimani et al.	2017	sustainable and green closed-loop supply chain network	Fuzzy multi-objective and GA
9	Ghomi-Avili et al.	2018	green competitive closed-loop supply chain	Game theory and fuzzy optimization
10	The proposed problem	-	Green closed loop supply chain (considering quality, life cycle and pricing)	GA and PSO

As it is concluded from the reviewed past works the emphasis on more tactical and strategic levels of CLSC were neglected. Most of the reviewed works concentrated on operational variables of supply chain in mathematical formulations. Also, other works mainly used an evolutionary algorithm and the comparison of the methods to find the most efficient one was not investigated. In this paper, we intend to present a mixed integer linear programming model for a green closed-loop supply chain network design problem with respect of pricing, quality of the components and products life cycle that are effective tactical and strategic level decisions, under certain conditions of demand and rate of return. Furthermore, two evolutionary algorithms are adapted for the problem and their performance to find solutions are compared and analyzed.

The remainder of the paper is organized as follows. Next, the proposed problem is described and justified. In Section 3, the corresponding mathematical formulations are given. In Section 4, particle swarm optimization (PSO) and genetic algorithm (GA) are implemented to optimize the proposed mathematical model as solution approaches. Results for implementation and discussions are presented in Section 5. We conclude in Section 6.

2. Problem description

We configured a closed-loop green supply chain (CLGSC) network as shown in Figure 1. Network facilities can be classified into two groups namely, forward supply chain and reverse supply chain facilities. The forward supply chain, which is the same as the traditional supply chain consists of raw material supplier facilities, manufacturing facilities, and distribution centers to serve their end customers. The reverse supply chain consists of three facilities: collection centers, dismantling centers and the disposal site location. The forward supply chain begins with the procurement of raw material from suppliers. Plant facilities are well equipped with required technology and responsible for manufacturing various components and then assembling them into products. From there, finished products move towards the end customers via distribution centers and customer zones. In the reverse chain of the proposed CLGSC network, returned products are collected from their users through a take back scheme. Users will be paid incentives for returning their end of life (EOL) and end of use (EOU) consumed products at the company operated collection center. Returned products collected

will be transferred to the dismantling centers. There separated components will be inspected based on their quality and classified into two categories namely reusable and non-reusable components. The first category is that their use is terminated but due to possession of good and acceptable quality being used again and returned to manufacturing centers. The second category is considered to be waste and transferred to the disposal site. In this supply chain three types of products are produced that are called grade 1, grade 2, and grade 3. Grade 1 products are such products that it's all constituent components and raw materials are original and directly procured from suppliers. Then, the components produced and assembled in manufacturing centers. Finally, the product grade 1 is delivered to the customer. In the second grade products, all its constituent parts are the reusable components that are sent to the manufacturing centers through the reverse chain and the dismantling centers. These components are then assembled and form product grade 2. In the third grade products, the components are a combination of original and reusable components.

Seeing all these issues, a mixed integer linear programming model, depicting the requirement of the proposed CLGSC is formulated. A model corresponding to the proposed multi-echelon CLGSC is configured for a multi type product and a multi period to determine the optimum flow of material, product and component in the network, while maximizing the total profit. Moreover, during the course of model formulation, the following assumptions are postulated:

1. Demand at customer end is deterministic; there is no shortage.
2. Facility locations are known a priori and they are fixed.
3. The flow of products, parts, and materials can occur only in between two consecutive stages; inter stage flow is not allowed.
4. All cost parameters are deterministic and all operations of CLSC are to be carried under capacity limitations.
5. Set-up cost of facilities is considered to be a part of the operations cost of the respective facilities.
6. Quality testing is done in the dismantling center and operational expense of this center, including the cost of the test is also.
7. Products quality grade 2 and grade 3 is different from the grade 1. Therefore, the selling price is considered to be different.
8. Demand and the rate of return for each type of product are considered to be different.

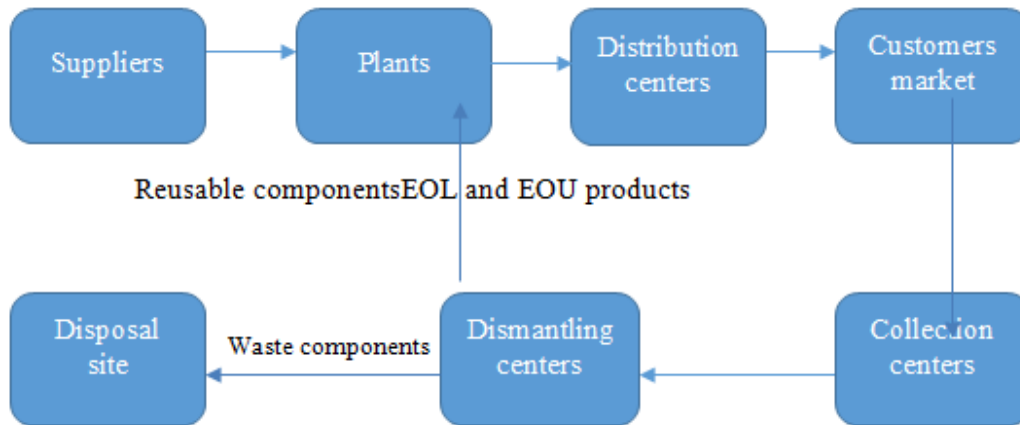


Figure 1: Closed loop green supply chain network

3. Mathematical formulation

Here, the mathematical notations proposed for the mathematical presentation of the problem are listed and defined.

Sets:

I : Set of raw material supplier, indexed by $i, i=1, 2, \dots, I$

J : Set of manufacturing plant, indexed by $j, j=1, 2, \dots, J$

K : Set of distribution center, indexed by $k, k=1, 2, \dots, K$

L : Set of customer market, indexed by $l, l=1, 2, \dots, L$

C : Set of collection centers, indexed by $c, c=1, 2, \dots, C$

p : Set of dismantling centers, indexed by $p, p=1, 2, \dots, P$

f : Set of disposal sites, indexed by $f, f=1, 2, \dots, F$

T : Set of time period, indexed by $t, t=1, 2, \dots, T$

R : Set of raw materials, indexed by $r, r=1, 2, \dots, R$

M : Set of components, indexed by $m, m=1, 2, \dots, M$

$$Q = \begin{cases} 1 & \text{quality of reusable components} \\ 2 & \text{quality of wastes components} \end{cases}$$

Cost parameters:

Pur_{ijt}^r Per unit purchasing cost of r th material from i th supplier for j th plant in period t

HA_{mjt} Production cost of m th component at j th plant in period t

HM_{jt} Assembling cost of a product at j th plant in period t

OP_{kt} Per unit operating cost at k th distribution center in period t

KB_t Incentive paid for a return in period t (fixed regardless of the condition)

PC_{pt} Dismantling cost of a returned product at p th dismantling center in period t

HD_{ft} Disposal cost of a f th disposal site for each component in period t

TC_{it}^{ij} Cost of transporting of r th raw material from i th supplier to j th plant in period t

TC_t^{jk} Cost of transporting a unit of product from j th plant to k th distribution center in period t

TC_t^{kl} Cost of transporting a unit of product from k th distribution center to l th customer in period t

TC_t^{cp} Cost of transporting a unit of returned product from c th collection center to p th dismantling center in period t

TC_{mt}^{pj} Cost of transporting a unit of m th component from p th dismantling center to j th plant in period t

TC_{mt}^{pf} Cost of transporting a unit of m th component from p th dismantling center to f th disposal site in period t

Other parameters:

D_{lt} Demand of customer l for grade1 product in period t

D'_{lt} Demand of customer l for grade2 product in period t

D''_{lt} Demand of customer l for grade3 product in period t

α_{lt} Rate of return for grade1 product from customer l in period t

α'_{lt} Rate of return for grade2 product from customer l in period t

α''_{lt} Rate of return for grade3 product from customer l in period t

β_m Utilization rate of m th component in the product

μ_r^m Utilization rate of r th material per unit of m th component

MI Great number

Q'_{lt} Unit selling price of grade1 product for the customer market l in period t

Q''_{lt} Unit selling price of grade2 product for the customer market l in period t

Q'''_{lt} Unit selling price of grade3 product for the customer market l in period t

Cap_i^r Capacity of i th supplier for supplying r th material

Cap_j Production capacity of plant j

Cap_k Capacity of k th distribution center

δ_t Rate of return for reusable components from dismantling centers in period t

Decision variables:

X_{ijrt} Quantity of raw material r shipped from supplier i to plant j in period t

X_{mjt} Quantity of m th original component that is produced at plant j in period t

X_{jkt} Quantity of grade1 product shipped from plant j to distribution center k in period t

X'_{jkt} Quantity of grade2 product shipped from plant j to distribution center k in period t

X''_{jkt} Quantity of grade3 product shipped from plant j to distribution center k in period t

X_{klt} Quantity of grade1 product shipped from distribution center k to customer market l in period t

X'_{klt} Quantity of grade2 product shipped from distribution center k to customer market l in period t

X''_{klt} Quantity of grade3 product shipped from distribution center k to customer market l in period t

X_{lct} Quantity of used product returned from customer market l to collection center c in period t

X_{ct} Quantity of product shipped from collection center c to dismantler centers in period t

X_{mpjqt} Quantity of m th component with quality $q=1$ that considered reusable components and shipped from dismantler center p to plant j in period t

X_{mpfqt} Quantity of m th component with quality $q=2$ that considered waste components and shipped from dismantler center p to disposal center f in period t

$A_{lc} = \begin{cases} 1 & \text{if collection center } c \text{ is opened to collect return goods from costumer market } l \\ 0 & \text{otherwise} \end{cases}$

$B_{kl} = \begin{cases} 1 & \text{if costumer market } l \text{ to be catered by distribution center } k \\ 0 & \text{otherwise} \end{cases}$

In terms of the sets indices, parameters, and decision variables defined above, the multi-echelon, multi-product and multi-period green closed loop supply chain design problem can be formulated as follows.

Objective functions:

The objective is to maximize the total profit generated in the CLGSCN. The profit is to be obtained by subtracting the total cost incurred to the system from the income earned in the network. The sources of income in the CLSC network are the customer market where the finished products with each type are to be sold. The mathematical representation of total income generated in the CLSC is:

$$\sum_k \sum_l \sum_t (Q'_{lt} * X_{klt} + Q''_{lt} * X'_{klt} + Q'''_{lt} * X''_{klt}) \quad (I)$$

In equation (I), the first term shows the multiplication of unit selling price of grade1 product to quantity of grade1 product leading to the earned income from product grade 1. The second and the third terms are also the earned income from grade 2 and 3 products, respectively.

Various costs borne by the company including the costs of maintaining effective functioning of each facility and the flow between the facilities need to be considered. Thus the total cost includes operational costs and transportation costs. Furthermore, the operational costs incurred in the forward chains are due to the purchasing of raw material, the production of original components, product assembly and on-time delivery of the products to their customers. The reverse chain requires the company to pay incentives to their customers under a take back scheme for returning EOU and EOL products, and the company also bears various costs in the reverse chain such as dismantling cost that including quality testing, and disposal cost. The mathematical representation of operational costs incurred in the network follows in equation (II).

Equation (III) represents the transportation cost which includes the cost of transporting material from suppliers to plants, products from plants to distribution centers and distribution centers to customers market in the forward chain, the cost of shipping returned products from collection centers to the dismantling centers, and the cost of shipping components from the dismantlers to plants and disposal centers.

$$\begin{aligned}
& \sum_r \sum_j \sum_i \sum_t Pur_{ijt}^r * X_{ijrt} + \sum_m \sum_j \sum_t HA_{mjt} * X_{mjt} \\
& + \sum_j \sum_k \sum_t HM_{jt} * (X_{jkt} + X'_{jkt} + X''_{jkt}) + \sum_k \sum_l \sum_t OP_{kt} * (X_{klt} + X'_{klt} + X''_{klt}) \\
& + \sum_l \sum_c \sum_t KB_t * X_{lct} + \sum_p \sum_c \sum_t PC_{pt} * X_{ct} + \sum_p \sum_f \sum_m \sum_t HD_{ft} * X_{mpfq2t}
\end{aligned} \tag{II}$$

$$\begin{aligned}
& \sum_r \sum_j \sum_i \sum_t TC_{rt}^{ij} * X_{ijrt} + \sum_j \sum_k \sum_t TC_t^{jk} * (X_{jkt} + X'_{jkt} + X''_{jkt}) \\
& + \sum_k \sum_l \sum_t TC_t^{kl} * (X_{klt} + X'_{klt} + X''_{klt}) + \sum_p \sum_c \sum_t TC_t^{cp} * X_{ct} \\
& + \sum_p \sum_j \sum_m \sum_t TC_{mt}^{pj} * X_{mpjq1t} + \sum_p \sum_f \sum_m \sum_t TC_{mt}^{pf} * X_{mpfq2t}
\end{aligned} \tag{III}$$

Therefore, the objective function is (I)-(II)-(III):

$$\begin{aligned}
MaxZ = & \sum_k \sum_l \sum_t (QF_{lt} * X_{klt} + Q'F_{lt} * X'_{klt} + Q''F_{lt} * X''_{klt}) \\
& - (\sum_r \sum_j \sum_i \sum_t Pur_{ijt}^r * X_{ijrt} + \sum_m \sum_j \sum_t HA_{mjt} * X_{mjt} \\
& + \sum_j \sum_k \sum_t HM_{jt} * (X_{jkt} + X'_{jkt} + X''_{jkt}) + \sum_k \sum_l \sum_t OP_{kt} * (X_{klt} + X'_{klt} + X''_{klt}) \\
& + \sum_l \sum_c \sum_t KB_t * X_{lct} + \sum_p \sum_c \sum_t PC_{pt} * X_{ct} + \sum_p \sum_f \sum_m \sum_t HD_{ft} * X_{mpfq2t} \\
& + \sum_r \sum_j \sum_i \sum_t TC_{rt}^{ij} * X_{ijrt} + \sum_j \sum_k \sum_t TC_t^{jk} * (X_{jkt} + X'_{jkt} + X''_{jkt}) \\
& + \sum_k \sum_l \sum_t TC_t^{kl} * (X_{klt} + X'_{klt} + X''_{klt}) + \sum_p \sum_c \sum_t TC_t^{cp} * X_{ct} \\
& + \sum_p \sum_j \sum_m \sum_t TC_{mt}^{pj} * X_{mpjq1t} + \sum_p \sum_f \sum_m \sum_t TC_{mt}^{pf} * X_{mpfq2t})
\end{aligned}$$

Constraints:

Constraints under which we need to optimize the above objective are as follows.

$$\sum_i X_{ijrt} = \sum_m \mu_r^m * X_{mjt} \quad \forall j, r, t \tag{1}$$

Constraint (1) represents the quantity of each raw material shipped from suppliers to plant, and it depends on the number of components manufactured there.

$$\sum_j X_{ijrt} \leq Cap_i^r \quad \forall r, i, t \tag{2}$$

Constraint (2) shows that the total quantity of each raw material shipped from any supplier cannot exceed the supplier's supplying capacity.

$$\sum_j X_{jkt} = \sum_l X_{klt} \quad \forall k, t \tag{3}$$

$$\sum_j X'_{jkt} = \sum_l X'_{klt} \quad \forall k, t \tag{4}$$

$$\sum_j X''_{jkt} = \sum_l X''_{klt} \quad \forall k, t \tag{5}$$

Constraints (3)-(5) represents that for each type of the product the flow entering each distribution center is equal to the flow exiting from the distribution center.

$$\sum_l (X_{klt} + X'_{klt} + X''_{klt}) \leq Cap_k \quad \forall k, t \tag{6}$$

Constraint (6) ensures that the flow of the product exiting from each distribution center does not exceed the capacity of the distribution center.

$$\sum_k X_{jkt} * \beta_m \leq X_{mjt} \quad \forall m, j, t \tag{7}$$

Constraint (7) shows the quantity of the original components that are required for the production of the grade1 product.

$$\sum_k X'_{jkt} * \beta_m \leq \sum_p X_{mpjq1(t-1)} \quad \forall m, j, t \tag{8}$$

Constraint (8) shows the quantity of the reusable components that are required for the production of the grade2 product.

$$\sum_k X'_{jkt} * \beta_m \leq \left(X_{ijt} - \left(\sum_k X'_{jkt} * \beta_m \right) \right) + \left(\sum_p X_{mpjq1(t-1)} - \left(\sum_k X'_{jkt} * \beta_m \right) \right) \forall m, j, t \quad (9)$$

Constraint (9) shows the quantity of the original and reusable components that are required for the production of the grade3 product.

$$\sum_k (X_{jkt} + X'_{jkt} + X''_{jkt}) \leq Cap_j \quad \forall j, t \quad (10)$$

Constraint (10) ensures that the flow of the product exiting from each plant does not exceed of the production capacity of the plant.

$$\sum_k X_{klt} \geq D_{lt} \quad \forall l, t \quad (11)$$

$$\sum_k X'_{klt} \geq D'_{lt} \quad \forall l, t \quad (12)$$

$$\sum_k X''_{klt} \geq D''_{lt} \quad \forall l, t \quad (13)$$

Constraints (11)-(13) ensures no shortages of each type of the product at demand point.

$$\sum_c X_{lct} = (\alpha_{lt} * D_{lt}) + (\alpha'_{lt} * D'_{lt}) + (\alpha''_{lt} * D''_{lt}) \quad \forall l, t \quad (14)$$

Constraint (14) describes the relationship between the demand and quantity of return products transferred from customers to collection centers.

$$X_{ct} = \sum_l X_{lct} \quad \forall c, t \quad (15)$$

Constraint (15) calculates the quantity of the total returned product at each collection center in each period.

$$\sum_p \sum_j X_{mpjq1t} = \sum_c \delta_t * X_{ct} * \beta_m \quad \forall t, m \quad (16)$$

Constraint (16) shows the quantity of the total reusable components that flow of each component exiting from dismantling center to plant in each period.

$$\sum_p \sum_f X_{mpfq2t} = \sum_c (1 - \delta_t) * X_{ct} * \beta_m \quad \forall t, m \quad (17)$$

Constraint (17) shows the quantity of the waste components that flow of each component exiting from dismantling center to disposal center in each period.

$$(X_{klt} + X'_{klt} + X''_{klt}) \leq MI * B_{kl} \quad \forall k, l, t \quad (18)$$

$$X_{lct} \leq MI * A_{lc} \quad \forall l, c, t \quad (19)$$

Constraint (18) represents that a distribution center can only serve the customers market assigned to it. Similarly, Constraint (19) says that a collection center can only collect the returned product from the customer market assigned to it.

$$B_{kl}, A_{lc} \in \{0, 1\} \quad \forall k, l, c \quad (20)$$

$$(X_{ijrt}, X_{mjrt}, X_{jkt}, X'_{jkt}, X''_{ikt}, X_{klt}, X'_{lct}, X''_{lct}, X_{lct}, X_{ct}, X_{mpjq1t}, X_{mpfq2t}) \geq 0 \quad (21)$$

and Integer $\forall i, j, k, l, c, p, f, m, r, q, t$

Constraints (20) and (21) impose the binary, non-negativity and integer restrictions on the corresponding decision variables.

4. Proposed algorithms

4.1. Particle Swarm Optimization (PSO)

PSO is a population based stochastic optimization technique developed by Eberhart and Kennedy(1995), inspired by the social behavior of bird flocking or fish schooling. The algorithm was further developed (Poli et al., 2007). The system is initialized with a population of random solutions and searches for optima by updating generations. However, unlike the GA, the PSO has no evolution operators such as crossover and mutation. PSO is one of the swarm intelligent techniques. In the idea of PSO, each particle in the swarm has the same characteristics and behaviors. However, each particle has a random of the position and velocity parameter. The position of particles is explained by a possibility that is a solution of the optimization problem. In this algorithm, each bird is a possible answer in the search space of the problem. At first by a group of birds that have been produced randomly, the algorithm begins searching to obtain the best solution. At each step of the iteration, the bird moves to the better position. The next opportunity for each bird is to consider the two values: the first value is the best position so far that bird has got (*pbest*) and the second value is the best position that all birds have won (*gbest*). In other words, *gbest* can be considered the best *pbest* in the whole group. This process continues until the algorithm reaches the termination condition. Termination condition in the algorithm tends the birds speed to zero or the number of repetitions that have been considered. According to *pbest* and *gbest* values, each bird uses the following formula to determine the next location:

$$v_i^{k+1} = wv_i^k + c_1 rand_1 \times (pbest_i - s_i^k) + c_2 rand_2 \times (gbest - s_i^k) \quad (22)$$

$$s_i^{k+1} = s_i^k + v_i^{k+1} \quad (23)$$

where v_i^k is the current velocity of particle i at iteration k , v_i^{k+1} the new velocity of particle i at iteration k , c_1 the adjustable cognitive acceleration constant, c_2 the adjustable social acceleration constant, $rand_{1,2}$ the random number between 0 and 1, s_i^k the current position of particle i at iteration k , s_i^{k+1} the new position of particle i at iteration k , $pbest_i$ the personal best of particle i , and

gbest is the global best of population. Note that, *pbest_i* is the best location of individual particle while *gbest* is the best location of the swarm.

4.2. Genetic Algorithm (GA)

Genetic Algorithms (GAs) are adaptive heuristic search algorithms based on the evolutionary ideas of natural selection and genetic processes. The basic principles of GAs were first proposed by John Holland (1975), inspired by the mechanism of natural selection where stronger individuals are likely the winners in a competing environment. The GA assumes that the potential solution to any problem is an individual and can be represented by a set of parameters. These parameters are regarded as the genes of a chromosome and can be structured by a string of values in binary form. A positive value, generally known as a fitness value, is used to reflect the degree of "goodness" of the chromosome for solving the problem, which is highly related with its objective value. A GA starts with a random population of solutions (called chromosomes) and then tries to improve solutions through many iterations called generations. Each solution's performance is evaluated by a fitness function corresponding to the objective function of the optimization problem. Following parental selection, crossover and mutation operators are applied. Crossover combines materials from parents to produce children. On the other hand, mutation makes small local changes in feasible solutions to provide population diversity for a wider exploration of feasible solutions. The mutation operator is defined to ensure that generated solutions are not trapped in some local optima. As the final solution is independent of initial solutions, the basic population is randomly generated in most cases (Michalewicz, 1996).

4.2.1. Chromosome structure

In this algorithm, based on the type of facilities available for the proposed network and the relationships

between them, showing the chromosome is composed of seven parts. All these sectors of a multidimensional matrix and elements with real value in the interval [0,1] are formed. Together they create a solution to the problem that the values of the variables and objective function are calculated accordingly. The following matrix (Table 2) displays dimensions of each section.

For example, the first part of a four-dimensional matrix with dimensions (K*L*Q*T) has been formed. This section determines that each customer in each period will receive the required product with any level of quality from each distributor. Suppose in a sample with 3 customers and 2 distributors, first part of chromosome for product with quality level 1 in period 2 is as shown in Table 3.

In this section of the chromosomes, to assign each customer demand to distributor, the element assignment with the highest value is begun. In this case, the element regarding to customer 1 and distributor 2 is the highest and thus customer's demand 1 is supplied through distributor 2, and the assigned demand is reduced from distribution's capacity. If one distribution's capacity was less than the corresponding customer's demand, then that distributor devotes its capacity and the remainder is supplied by another distributor.

4.2.2. Crossover operator

Crossover operator employed in this algorithm is based on a guide matrix. This matrix has binary elements and for each individual element the chromosome size is the same. In this way, to select parents cross over operator is applied using roulette wheel. Thus, for each of the elements in each of the four sections of chromosomes a corresponding element of the guide matrix exists. In order to generate new offspring, if the value of the corresponding element in the guide matrix is 1, the corresponding element value is changed between two parents; otherwise, the element is left unchanged. Figure 2 implies a small example of this approach.

Table2: Matrix dimensions of each section

Section1	Section2	Section3	Section4	Section5	Section6	Section7
$K \times L \times Q \times T$	$J \times K \times Q \times T$	$I \times J \times R \times T$	$L \times C \times T$	$C \times P \times T$	$P \times J \times T$	$P \times F \times T$

Table3: An example of the first part of chromosome structure

	Customer			
Distributor		1	2	3
1		0.27	0.81	0.46
2		0.99	0.46	0.17

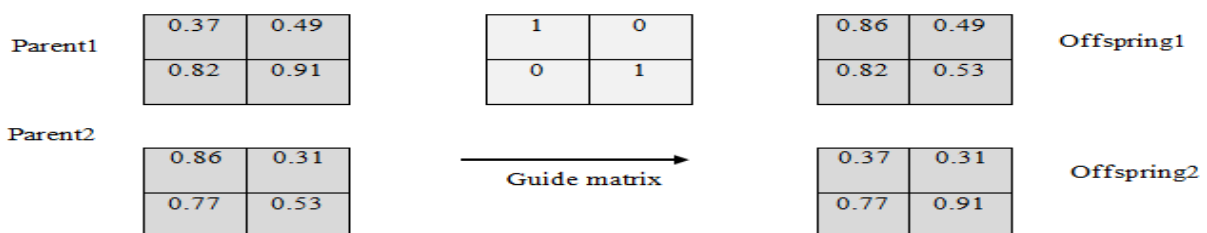


Figure 2: Proposed Crossover operator

4.2.3. Mutation operator

In this algorithm, for mutation in each section of chromosome, randomly two rows or two columns are chosen and the elements are pasted between them upside down. For parts of chromosomes that have more than one dimension, the operation is applied for all of them. Figure 3 shows how to apply mutation operator.

4.3. Parameters setting

Performance of any meta-heuristic algorithm is directly influenced by parameters and operators setting, so that the wrong choice of algorithm parameters will lead to ineffectiveness of the solutions. Based on past studies and experimental considerations, the parameters are defined as shown in Tables 4 and 5 for GA and PSO algorithms, respectively.

5. Results of the proposed algorithms

In this section, a total of 30 sample problems were selected and each problem is repeated 5 times. Dimensions of sample problems are presented in Table 6.

Table 4: GA Parameters

Population size	Number of iterations	Crossover Rate	Mutation Rate	Elitism Rate
350	150	0.9	0.1	0.1

Table 5: PSO Parameters

Population size	Number of iterations	v	w	C ₁	C ₂
350	150	0.9	0.75	2	2

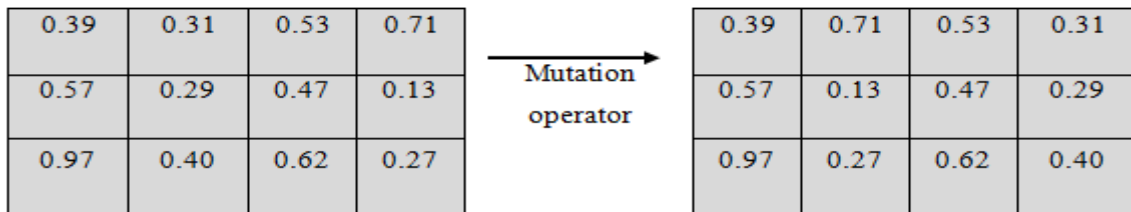


Figure 3: Proposed Mutation operator

Table 6: Dimensions of sample problems

problem size	suppliers	Manufacturers	distribution centers	Customers market	period	collection centers	dismantling centers	disposal site	components	Raw material
1	3	2	2	4	2	4	1	1	4	10
2	3	2	2	5	2	4	1	1	4	10
3	3	3	2	5	2	5	1	1	4	10
4	4	3	2	5	2	5	1	1	4	10
5	4	3	3	6	2	5	1	1	4	10
6	4	4	3	6	2	5	1	1	4	10
7	5	2	2	5	3	5	2	1	4	10
8	5	3	3	4	3	4	2	1	4	10
9	5	3	4	6	3	6	2	1	4	10
10	5	4	3	5	2	4	1	1	4	10
11	5	4	4	6	3	6	2	1	4	10
12	5	5	4	5	3	5	2	1	4	10
13	5	5	4	6	3	5	1	1	4	10
14	6	5	4	5	3	5	2	1	4	10
15	6	4	4	5	4	5	2	1	4	10
16	6	4	4	6	4	6	2	1	4	10
17	6	4	4	7	4	6	2	1	4	10
18	6	5	4	7	4	7	3	2	4	10
19	7	5	5	7	4	7	3	2	4	10
20	7	6	5	7	4	7	3	2	4	10
21	7	6	6	7	5	7	3	2	4	10
22	7	6	5	8	5	7	3	2	4	10
23	8	6	5	8	5	8	3	2	4	10
24	8	6	6	8	6	8	4	2	4	10
25	8	7	5	8	5	8	3	2	4	10
26	8	7	5	9	5	8	4	2	4	10
27	8	7	5	9	6	9	4	3	4	10
28	9	7	6	9	6	9	4	3	4	10
29	9	8	6	10	6	9	4	3	4	10
30	9	8	6	10	6	10	4	3	4	10

The values of the parameters used in the model are randomly generated based on the given probability distribution functions in the following table (Table 7) and is used in each stage.

Table7: Parameter values in the model

Parameter Number	Parameter	probability functions
1	QF_{lt}	U[1955,11700]
2	$Q'F_{lt}$	U[1562,11500]
3	$Q''F_{lt}$	U[1750,11755]
4	D_{lt}	U[1120,1210]
5	D'_{lt}	U[0,148]
6	D''_{lt}	U[0,190]
7	α_{lt}	U[0.52,0.75]
8	α'_{lt}	U[0.28,0.56]
9	α''_{lt}	U[0.47,0.68]
10	Pur_{ijt}^r	U[4,18]
11	HA_{mjt}	U[40,58]
12	HM_{jt}	U[40,50]
13	OP_{kt}	U[45,55]
14	KB_t	U[95,105]
15	PC_{pt}	U[35,44]
16	HD_{ft}	U[51,61]
17	TC_{rt}^{ij}	U[20,35]
18	TC_t^{jk}	U[20,33]
19	TC_t^{kl}	U[20,33]
20	TC_t^{cp}	U[20,32]
21	TC_{mt}^{pj}	U[20,32]
22	TC_{mt}^{pf}	U[20,32]
23	Cap_i^r	U[61300,130200]
24	Cap_j	U[13450,16250]
25	Cap_k	U[13000,15000]
26	δ_t	U[0.43,0.57]

5.1. Measures of algorithm performance

To study the effectiveness of the proposed algorithms and compare them with each other, a measure of the relative percentage deviation (RPD) used that is calculated by the following equation:

$$RPD_{ab} = \left| \frac{(Mean_{sol})_{ab} - Best_{sol}}{Best_{sol}} \right| \quad (24)$$

where $Best_{sol}$ is the best result for a problem between all performances of the problem and $(Mean_{sol})_{ab}$ is the mean of the best results for a problem in an algorithm. Obviously, a lower value of (RPD) represents the algorithm has better performance. It is also known that an important feature of each algorithm is the computational time. Clearly, the proper use of meta-heuristic algorithm reduces the computational time for a problem. In Table 8 the results of the two algorithms are shown.

Table8: The results of the GA algorithm and PSO algorithms

Problem number	GA algorithm				PSO algorithm			
	Mean	Best	Time	RPD	Mean	Best	Time	RPD
1	25727176.8	25728321	108.8207	0.0471	26613903	26998222	162.9818	0.0142
2	27533283.8	27726698	124.1821	0.007	27205304.2	27644764	203.6378	0.0188
3	9081762	9116236	154.2433	0.1132	9975214.4	10240851	530.0432	0.0259
4	26529593.7	26569450	211.408	0.0381	26952338	27581159	350.6616	0.0228
5	-2344434.2	-1898141	257.4556	0.2351	-2222085.2	-2097766	457.3326	0.1707
6	11732358.9	12097469	299.743	0.0849	11997137.2	12821131	508.9971	0.0643
7	-1608452.6	-1355601	276.9875	0.4116	-1354632.3	-1139461	478.0214	0.1888
8	29336463.6	29605973	345.59	0.066	30449607.6	31410818	853.2278	0.0306
9	78485567.6	78877074	514.1089	0.0195	77349956.2	80048327	697.574	0.0337
10	9333445.8	9710196	406.3376	0.2724	10814956.2	12828595	712.0418	0.157
11	56793521.4	57442661.6	568.0022	0.05	58471076.7	59784232.3	829.1311	0.022
12	29983902.7	31362475.6	1058.045	0.044	29016879.6	31269455	837.8348	0.0748
13	54815452	55484178.3	1871.012	0.0121	53045156.2	55300421	893.5983	0.044
14	35166080.7	35517962.3	931.0291	0.0955	37623726.5	38879316	928.1525	0.0323
15	97649910	98706250	3821.869	0.02	96964262.5	99643729	1066.032	0.0269
16	25087706.1	26229566	862.7388	0.0435	18752074.3	20385899	1242.021	0.2851
17	30476547.4	31817281	915.8037	0.0421	22536321.4	23841114	1336.709	0.2916
18	143653590	144095563	1057.302	0.0031	138624146	143276556	1719.556	0.038
19	195785782	78779223	1228.755	0.0041	193338178	194259465	1748.414	0.0166
20	76168864.6	78779223	1426.445	0.0331	69261453.5	71516008.3	1950.664	0.1208
21	193426387	195292564	2290.256	0.0096	185913567	188937311	2442.267	0.048
22	-8106671.6	-6728674	2281.183	0.2048	-23279928	-20904265	2670.729	2.4598
23	103144435	103949997	2187.646	0.0077	90706818.2	94289903	2551.266	0.1274
24	144808109	147738949	2792.341	0.0198	137857166	141438086	3636.245	0.0669
25	117983938	122360844	2538.078	0.0358	110521973	113351132	3181.979	0.0968
26	185026377	187772817.6	2580.784	0.0146	176280127.4	179896662.3	3159.592	0.0612
27	277832644	282025518.5	3402.463	0.0149	268122134.2	269976107.7	4330.511	0.0493
28	216991612	222083769	3851.312	0.229	196093058	205698700	4460.662	0.117
29	123408828	126849792	4504.353	0.0271	109017654	113135257	5402.177	0.1406
30	62046948.7	70148233	4528.834	0.1155	4717958.6	53718567	5652.2	0.3274

In Table 8 by “the best” we mean the best solution among the optimum solutions for each algorithm and the “mean”, “time” and “RPD” stand for average optimum solutions, time and calculated RPD to 5 times run of any problem, respectively. Figure 4 shows solution for problem 27 in replication 1 (27-1).

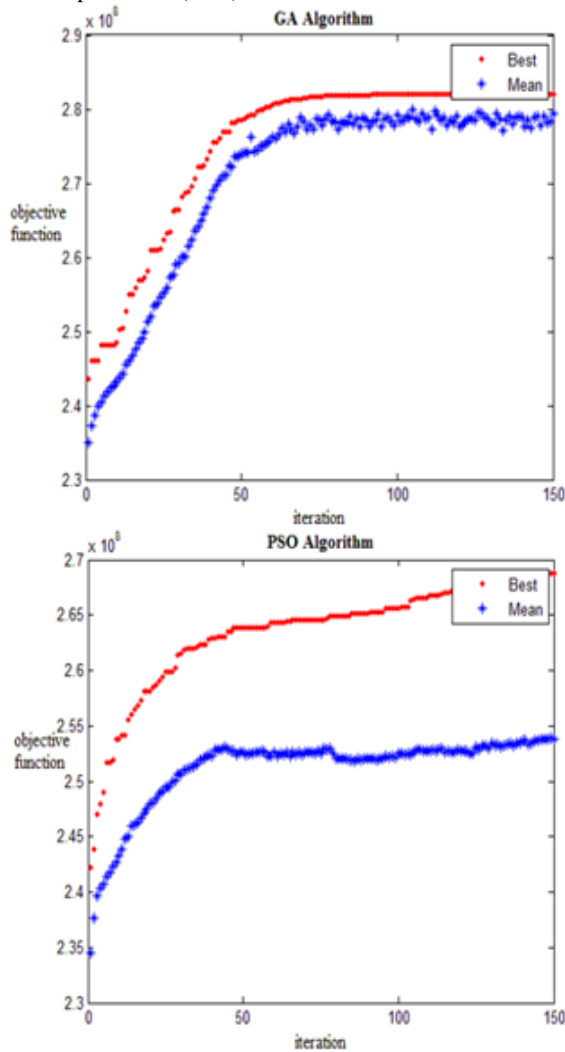


Figure 4: Solution graph for problem 27-1 using GA and PSO algorithms

As mentioned in the past section, to check the performance of the proposed algorithm RPD criterion is used. Supply chain issues are usually more sensitive in specific variables. In this study, the efficiency of algorithms is analyzed for closer examination of these issues with respect to variables including suppliers, manufacturers, distribution centers, customers and periods. RPD graph is drawn. For example, in the graph shown below (Figure 5) by changing the number of suppliers the analysis is performed. When the number of suppliers is between 3 and 9, supplier RPD variations for both algorithms are depicted.



Figure 5: Algorithms RPD graph with the different number of suppliers

As it is clear from Figure 5, for problems until 5 suppliers, the PSO algorithm's RPD is less. But by increasing the number of suppliers, GA algorithm outperforms PSO with respect to RPD and therefore has a better performance.

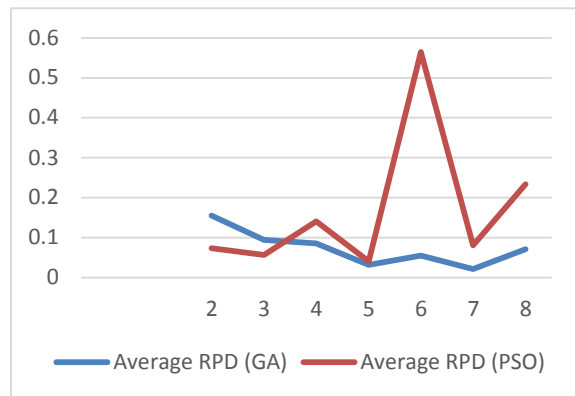


Figure 6: RPD graph with the different number of manufacturers

As it is clear from Figure 6, for problems until 3 manufacturers, the PSO algorithm's RPD is less. But by increasing the number of manufacturers, GA performs better.

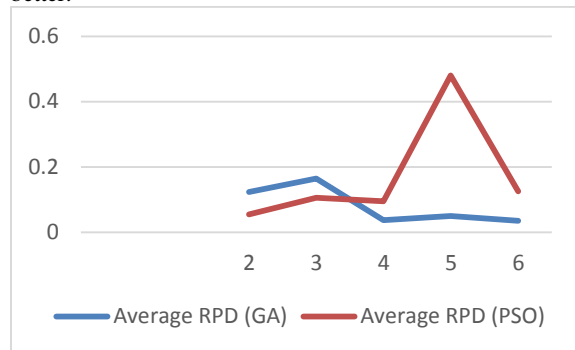


Figure 7: RPD graph with the different number of distribution centers

According to Figure 7, for problems until 3 distribution centers, the PSO algorithm's RPD is less. But by increasing the number of distribution centers, GA performs better.

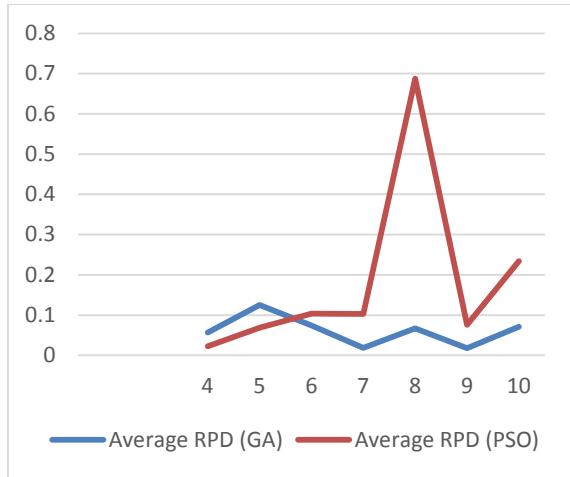


Figure 8. RPD graph with the different number of customers

As it is clear from Figure 8, for problems until 5 customers, the PSO algorithm's RPD is less. But by increasing the number of customers, GA performs better.

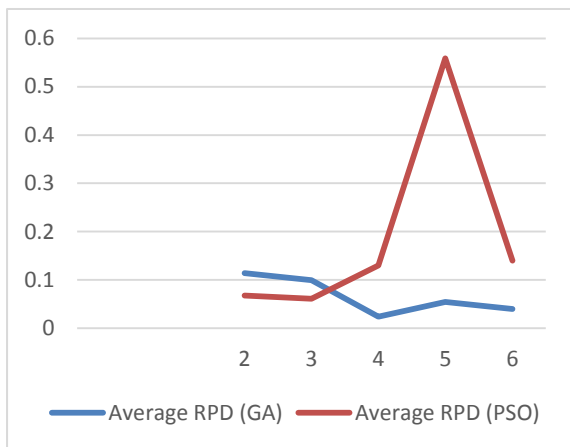


Figure 9. RPD graph in different time periods

As it is clear from Figure 9, for problems until 3 periods, the PSO algorithm's RPD is less. But by increasing the number of periods, GA performs better.

Another measure to evaluate the performance of the proposed algorithms is solution time. In Figure 10 the solution time comparison of GA versus PSO with respect to different problem sizes is depicted.

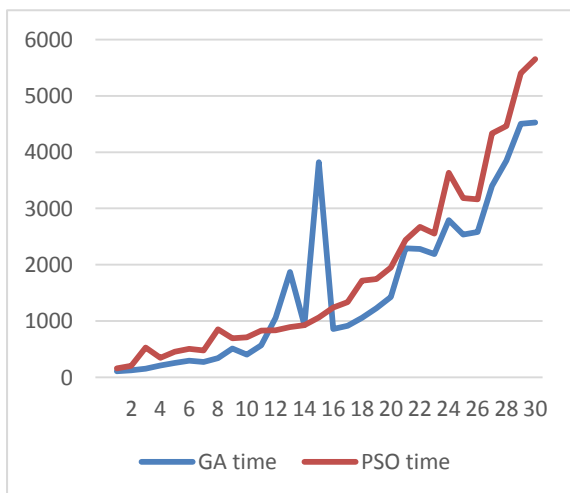


Figure 10. The proposed algorithms solution times graphs

According to the solution time, it is implied that except in instances 13, 14, and 15, GA needs shorter solution time in comparison with PSO.

According to the results of algorithms and analyzes made by the RPD and solution time graphs it can be interpreted that genetic algorithm has better performance and the results obtained are more efficient compared with particle swarm optimization algorithm.

6. Conclusions

Product life cycle development and products return through a reverse logistic network provide reduction in wastes and job opportunities. Design of a closed-loop supply chain network enforces enterprises to decide about end of life or end of use products. In this research, a four-layer forward supply chain and a three-layer reverse one is considered. A mixed integer linear mathematical model is proposed to maximize the total profit with respect to product quality classification, pricing policy and product life cycle. As solution approaches GA and PSO were proposed and implemented. The required modifications and parameters adjustment with respect to the proposed problem and mathematical formulations were performed. Two criteria of RPD and computational time were considered for comparing GA and PSO for different problem settings. RPD was handled separately for suppliers, manufacturers, distribution centers and customers. The results show better performance of GA in different problem sizes considering the solution time and relative percentage deviation.

As for future research directions, the following are suggested; Considering uncertainty in parameters like demand and rate of return could help the decision makers to include uncertainty of real world cases; including inventory and warehouse issues in the model lead to a more comprehensive problem which is complex and need to develop efficient solution methods; More emphasis on environmental aspect of green supply chain by including gas emission parameters in the model makes the problem more environment friendly; Considering game theory based pricing strategies for pricing segment of the model helps to develop a competitive model for the peers in each stage of the supply chain.

References

- [1] Abdallah, T., Farhat, A., Diabat, A., Kennedy, S., (2012). Green supply chains with carbon trading and environmental sourcing: formulation and life cycle assessment. *Appl. Math. Model.* 36 (9), 4271-4285.
- [2] Abdallah, T., Diabat, A., Simchi-Levi, D., (2011). Sustainable supply chain design: a closed-loop formulation and sensitivity analysis. *Prod. Plan. Control* 23 (2e3), 120-133.
- [3] Abdallah, T., Diabat, A., Rigter, J., (2013). Investigating the option of installing small scale {PVs} on facility rooftops in a green supply chain. *Int. J. Prod. Econ.* 146 (2), 465-477.
- [4] Accorsi, R., Manzini, R., Pini, Ch., Penazzi, S. (2015). "On the design of closed-loop networks for product life cycle management: Economic, environmental and geography considerations". *Journal of Transport Geography* 48; 121-134.
- [5] Al Zaabi, S., Al Dhaheri, N., Diabat, A., (2013). Analysis of interaction between the barriers for the implementation of

- sustainable supply chain management. *Int. J. Adv. Manuf. Technol.* 68 (1-4), 895-905.
- [6] Amin, S.H. Zhang, G. (2012a). An integrated model for closed-loop supply chain configuration and supplier selection: Multi-objective approach. *Expert Systems with Applications* 39, 6782-6791.
- [7] Amin, S.H., Zhang, G. (2012b). A proposed mathematical model for closed-loop network configuration based on product life cycle. *Int. J. Adv. Manuf. Technol.* 58 (5); 791-801.
- [8] Brandenburg, M., Govindan, K., Sarkis, J., Seuring, S., (2014). Quantitative models for sustainable supply chain management: developments and directions. *Eur. J. Oper. Res* 233 (2), 299-312.
- [9] Debo L, Toktay B, Van Wassenhove LN, (2006). Joint life-cycle dynamics of new and remanufactured products. *Prod Oper Manag* 15(4):498-513.
- [10] Demirel, N.O., Gokcen, H., (2008). A mixed integer programming model for remanufacturing in reverse logistics environment. *International Journal of Advanced Manufacturing Technology*, 39 (11-12), 1197-1206.
- [11] Demirel, N., Özceylan, T., Paksoy, and H. Gökçen, (2014). A genetic algorithm approach for optimising a closed-loop supply chain network with crisp and fuzzy objectives. *International Journal of Production Research*, 52(12): 3637-3664.
- [12] Devika, K., Jafarian, A., Nourbakhsh, V., (2014). Designing a sustainable closed loop supply chain network based on triple bottom line approach: a comparison of metaheuristics hybridization techniques. *Eur. J. Oper. Res.* 235 (3), 594-615.
- [13] Diabat, A., Abdallah, T., Henschel, A., (2015). A closed-loop location-inventory problem with spare parts consideration. *Comput. Oper. Res.* 54 (0), 245-256.
- [14] Du F, Evans GW (2008). A bi-objective reverse logistics network analysis for post-sale service. *Comput Oper Res* 35(8):2617-2634.
- [15] El-Sayed M, Afia N, El-Kharbotly A. (2010). A stochastic model for forward-reverse logistics network design under risk. *Comput Ind Eng* 58(3):423-431.
- [16] Fahimnia, B., Sarkis, J., Dehghanian, F., Banhashemi, N., Rahman, S., (2013). The impact of carbon pricing on a closed-loop supply chain: an Australian case study. *J. Clean. Prod.* 59, 210-225.
- [17] Fleischmann, M., et al., (2001). The impact of product recovery on logistics network design. *Production & Operations Management*, 10 (3), 156-173
- [18] Francas, D., Minner, S. (2009). Manufacturing network configuration in supply chains with product recovery. *Omega* 37(4):757-769.
- [19] Garg, K., Kannan, D., Diabat, A., Jha, P.C. (2015). A multi-criteria optimization approach to manage environmental issues in closed loop supply chain network design. *Journal of Cleaner Production*, 100, 297-314.
- [20] Guide VDR Jr, Van Wassenhove LN, (2009). The evolution of closed-loop supply chain research. *Oper Res* 57(1):10-18.
- [21] Jayaraman, V., Guide Jr, V.D.R., and Srivastava, R., (1999). A closed-loop logistics model for remanufacturing. *Journal of the Operational Research Society*, 50 (5), 497-508.
- [22] Jindal, A., Sangwan, K.S., (2013). Development of an interpretive structural model of drivers for reverse logistics implementation in Indian industry. *Int. J. Bus. Perform. Supply Chain Model.* 5 (4), 325-342.
- [23] Kannan, G., Noorul Haq, A., Devika, M., (2009). Analysis of closed loop supply chain using genetic algorithm and particle swarm optimisation. *Int. J. Prod. Res.* 47 (5), 1175-1200.
- [24] Kannan, G., Sasikumar, P., Devika, K., (2010). A genetic algorithm approach for solving a closed supply chain model: a case of battery recycling. *Appl. Math. Model.* 34, 655-670.
- [25] Kannan D, Diabat A, Alrefaei M, Govindan K, Yong G. (2012). A carbon footprint based reverse logistics network design model, Resources, conservation and recycling, 67, 75-79.
- [26] Kim, K, Song, I, Kim, J, Jeong, B. (2006). Supply planning model for remanufacturing system in reverse logistics environment. *Comput Ind Eng* 51(2):279-287.
- [27] Ko HJ, Evans GW, (2007). A genetic algorithm-based heuristic for the dynamic integrated forward/reverse logistics network for 3PLs. *Comput Oper Res* 34(2):346-366.
- [28] Krikke, H., Bloemhof-Ruwaard, J., Wassenhove, V., (2003). Concurrent product and closed-loop supply chain design with an application to refrigerators. *Int. J. Prod. Res.* 41 (16), 3689-3719.
- [29] Labatt, S., White, R., (2007). *Carbon Finance: the Financial Implications of Climate Change*. Wiley, New York.
- [30] Lee DH, Dong M, (2009). Dynamic network design for reverse logistics operations under uncertainty. *Transp Res Part E Logist Transp Rev* 45(1):61-71.
- [31] Lee JE, Gen M, Rhee KG, (2009). Network model and optimization of reverse logistics by hybrid genetic algorithm. *Comput Ind Eng* 56(3):951-964.
- [32] Lin, C., Choy, K. L., Ho, G. T., Chung, S., & Lam, H. (2014). Survey of green vehicle routing problem: Past and future trends. *Expert Systems with Applications*. 41(4). P 1118-1138.
- [33] Listes O, (2007). A generic stochastic model for supply-and-return network design. *Comput Oper Res* 34(2):417-442.
- [34] Özceylan, E., T. Paksoy, and T. Bektas, (2014). Modeling and optimizing the integrated problem of closed-loop supply chain network design and disassembly line balancing. *Transportation Research Part E: Logistics and Transportation Research Review*, 61: 142-164.
- [35] Ozkır, V., Bas, İlgil, H., (2013). Multi-objective optimization of closed-loop supply chains in uncertain environment. *J. Clean. Prod.* 41, 114-125.
- [36] Paksoy, T., Özceylan, E., Weber, G.W., (2010). A multi objective model for optimization of a green supply chain network. *Glob. J. Technol. Optim.* 2 (1).
- [37] Paksoy, T., Bektas, T., Özceylan, E., (2011). Operational and environmental performance measures in a multi-product closed-loop supply chain. *Transp. Res. Part E: Logist. Transp. Res.* 47 (4), 532-546.
- [38] Pati, K.R., Vrat, P., Kumar, P., (2008). A goal programming model for paper recycling system. *Omega* 36 (3), 405-417.
- [39] Pishvae MS, Farahani RZ, Dullaert W (2010). A memetic algorithm for bi-objective integrated forward/reverse logistics network design. *Comput Oper Res* 37(6):1100-1112.
- [40] Pishvae, M.R., Rabbani, M., and Torabi, S.A., (2011). A robust optimization approach to closed-loop supply chain network design under uncertainty. *Applied Mathematical Modeling*, 35 (2), 637-649.
- [41] Ramezani, M., Bashiri, M., Tavakkoli-Moghaddam, R., (2013). A new multi-objective stochastic model for a forward/reverse logistic network design with responsiveness and quality level. *Appl. Math. Model.* 37 (1), 328-344.
- [42] Salema MIG, Barbosa-Povoa AP, Novais AQ, (2007). An optimization model for the design of a capacitated multi-product reverse logistics network with uncertainty. *Eur J Operat Res* 179(3):1063-1077.
- [43] Sarkis, J., (2003). A strategic decision framework for green supply chain management. *J. Clean. Prod.* 11 (4), 397-409.
- [44] Selim H, Ozkarahan I, (2008). A supply chain distribution network design model: an interactive fuzzy goal programming-based solution approach. *Int J Adv Manuf Technol* 36(3-4):401-418.
- [45] Shi, J., Zhang, G., and Sha, J., (2011). Optimal production planning for a multi-product closed loop system with

- uncertain demand and return. *Computers & Operations Research*, 38 (3), 641–658
- [46] Soleimani, H., Kannan G., (2015). A hybrid particle swarm optimization and genetic algorithm for closed-loop supply chain network design in large-scale networks. *Applied Mathematical Modelling*. 39, 3990-4012.
- [47] Srivastava, S. K. (2007). Green supply-chain management: A state-of-the-art literature review. *International Journal of Management Review*, 9(1), 53-80.
- [48] Wang, H., Hsu, H. (2010). A closed-loop logistic model with a spanning-tree based genetic algorithm. *Comput. Oper. Res.* 37, 376-389.
- [49] Winkler, H., (2011). Closed-loop production systems_A sustainable supply chain approach. *CIRP J. Manuf. Sci. Technol.* 4 (3), 243-246.
- [50] Soleimani, H., Govindan, K., Saghafi, H., Jafari, H. (2017). Fuzzy multi-objective sustainable and green closed-loop supply chain network design. *Computers & Industrial Engineering*, 109, 191-203.
- [51] Zohal, M., and Soleimani, H. (2016). Developing an ant colony approach for green closed-loop supply chain network design: a case study in gold industry. *Journal of Cleaner Production*, 133, 314-337.
- [52] Ghomi-Avili, M., Jalali Naeini, S.G., Tavakkoli-Moghaddam, R. and Jabbarzadeh, A. (2018). A fuzzy pricing model for a green competitive closed-loop supply chain network design in the presence of disruptions. *Journal of Cleaner Production*, 188, 425-442.
- [53] Kennedy, J. and Eberhart, R.C. (1995). Particle swarm optimization. *Proceedings of the 1995 IEEE International Conference on Neural Networks*, Vol. 4, p. 1942-1948, Perth, Australia.
- [54] Poli, R., Kennedy, J. and Blackwell, T. (2007). Particle swarm optimization: An overview. *Swarm Intelligence*. 1(1), 33–57.
- [55] Holland, J. H. (1975). *Adaptation in Natural and Artificial Systems*. University of Michigan Press, USA.
- [56] Michalewicz, Z. (1996), *Genetic Algorithms + Data Structures = Evolution Programs*. Third edition. New York: Springer-Verlag.

Sensorless Control System Design of a Small Size Vertical Axis Wind Turbine

Mayouf Messaoud^{*,a}, Bakhti Hadi^a, Dahmani Aissa^b

^aDepartment of Electrical Engineering, Faculty of Technology, University of Mohamed Boudiaf, M'sila, Algeria

^bDepartment of Electrical Engineering, Faculty of Engineering Sciences, University of Elhadj Lakhdar, Batna, Algeria

Received JAN 12 2018

Accepted JULY 25 2018

Abstract

This paper describes control system design of a small size vertical axis wind turbine for battery charging, using permanent magnet synchronous generator (PMSG). The direct drive PMSG is connected to the battery through a switch mode rectifier where a DC-DC buck converter is used to optimize the wind power. The use of speed sensor to the control system design complicates and adds more costs to the system. To resolve this problem, a sensorless maximum power-tracking algorithm is proposed to calculate the current command that corresponds to maximum power output of the turbine. The DC-DC converter uses this current command to calculate the duty cycle which is necessary to control the pulse width modulated (PWM) active switching device. The system overview and modeling is presented, including characteristics of wind turbine, generator, batteries, power converter, control system, and supervisory system. A simulation of the system is performed using MATLAB/SIMULINK.

© 2018 Jordan Journal of Mechanical and Industrial Engineering. All rights reserved

Keywords: Battery charging, Permanent magnet synchronous generator (PMSG), vertical axis wind turbine, maximum power point tracking (MPPT), PWM DC-DC buck converter.

1. Introduction

Most wind generation systems use horizontal axis turbine, they are often designed to be connected to electric grid[1]. For small size systems, vertical wind turbines have a great potential to generate electricity for applications in rural areas, such as residences far from a power grid, telecommunication towers, monitoring stations. Its main advantage is the lower connection wind speed[2].

Direct drive permanent magnet synchronous generator for vertical axis wind turbines has received much attention in wind energy application because of their property of self-excitation, which allows an operation at a high power factor and high efficiency [3].

A wind energy conversion system with PMSG can be used basically in three distinct applications: standalone systems, hybrid systems, and grid connected systems. Previous publications related to PMSG based variable speed wind turbine are mostly concentrated on grid connected system [4]. Despite the abundance of renewable energies along isolated areas, electricity supply is one of the biggest obstacles to the population because of the cost and difficulty of connecting to electrical grid.

To resolve this problem, direct-drive permanent magnet synchronous generator for battery charging, using vertical axis wind turbine is very useful for low power applications. However, for large power applications, the

cost-effectiveness of such wind systems requires additional design costs[5].

The direct battery charging through a rectifier bridge represents a simple solution adopted by some manufacturers because of its simplicity and robustness [6]. Despite these advantages, several problems associated with this solution result, such as the reduction of batteries useful life and increase of power losses, and also, the wind turbine does not operate at its maximum electrical power in all operating conditions. Therefore, it is necessary to provide variable speed wind generation systems that allow the use of turbine for its maximum power coefficient in a large range of wind speed, optimizing the use of the available energy[7]. This is possible by inserting a DC-DC converter between the rectifier output and the battery to adapt the generator voltage to the battery bank voltage. Several papers have been published in this topic. For example in [8], the topology proposed uses DC-DC boost converter to regulate the battery bank current using different control strategies. The concept of the control strategy of power maximization used in paper [9] is based on the calculating of the differential power from the power-frequency curve tracking the inflexion point to reach the maximum power point.

This paper proposes a sensorless wind power topology that employs a DC-DC buck converter for battery charging using simple control algorithm; which calculates battery current reference and introduces losses in the global behavior of the system.

* Corresponding author e-mail: mayouf71@yahoo.fr

2. System Modeling

The proposed system is shown in Figure 1. It is composed of a vertical axis wind turbine connected to a permanent magnet synchronous generator (PMSG). The generator is cascaded with a battery charger composed by three-phase rectifier and DC-DC buck converter. In the aim to know the global behavior of the production system, we suppose that the batteries are composed of an ideal electric supply source E_{bat} in series with a resistance R_{bat} . The battery charger operates to obtain maximum power transferred to the batteries and can also limit voltage levels of the battery bank. The converter duty cycle is changed in accordance with control system, which receives a reference signal from the supervisory system.

2.1. Wind Turbine Performance

The proposed model is based on the steady state characteristics of the vertical axis wind turbine. The output mechanical power available from a wind turbine can be expressed as follows [10].

$$p_m = \frac{1}{2} \cdot \rho \cdot S \cdot C_p(\lambda) \cdot V_w^3 \quad (1)$$

$$\lambda = \frac{R \cdot \omega}{V_w} \quad (2)$$

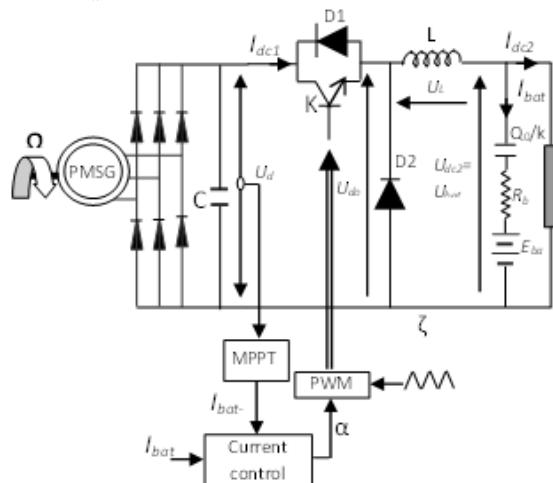


Figure1. General scheme of the proposed system

Where, ρ is the air density (typically 1.225 Kg/m^3 at sea level with standard conditions, i.e. temperature of 15°C and atmospheric pressure of 101.325 Kpa , S is the area swept by the rotor blades (in m^2), V_w is the wind speed (in m/s) and C_p is the so-called "power coefficient" of the wind turbine (dimensionless), with R being the radius of the turbine blades (in m) and ω being the angular speed of the turbine rotor (in rad/s).

As can be derived from Eq. 1, the power coefficient C_p is a nonlinear function of the tip-speed ratio (TSR) λ (dimensionless). Therefore, if the air density, swept area, and wind speed are constant, the output power of the turbine will be a function of power coefficient of the turbine. A generic equation is used to model the power coefficient $C_p(\lambda)$, based on the modeling vertical axis turbine characteristics used in [11]:

$$C_p = -0.2121\lambda^3 + 0.0856\lambda^2 + 0.2539\lambda \quad (3)$$

The characteristic function C_p vs. λ , is illustrated in Figure 2. As can be seen from Figure 2, at TSR-opt , C_p has its maximum value which results in the optimum efficiency, therefore, maximum power is captured from wind by the wind turbine. Figure 3 illustrates the output power of a wind turbine versus rotor speed while speed of wind changed from V_1 to V_n ($V_n > V_1$).

It can be observed that, for each wind speed, there exists a specific point in the wind generator power characteristic, this point is known maximum power point.

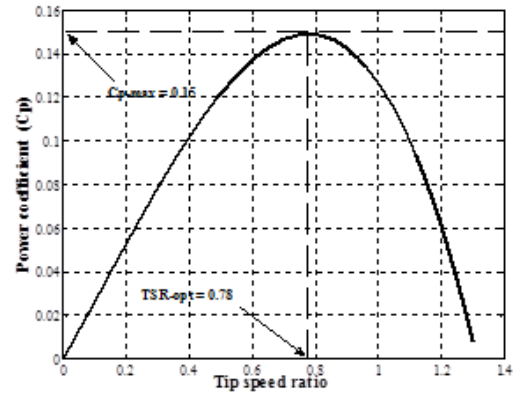


Figure2. Power coefficient versus tip-speed ratio

Thus, the control of the wind energy conversion system load results in a variable-speed operation of the turbine rotor, such that the maximum power is extracted continuously from the wind. The target optimum power from a wind turbine can be written as:

$$P_{m-opt} = \frac{1}{2} \cdot \rho \cdot S \cdot C_{p-opt} \cdot \left(\frac{R \cdot \Omega_{opt}}{\lambda_{opt}} \right)^3 = K_{opt} \cdot \Omega_{opt}^3 \quad (4)$$

Where:

$$K_{opt} = \frac{1}{2} \cdot \rho \cdot S \cdot C_{p-opt} \cdot \left(\frac{R}{\lambda_{opt}} \right)^3 \quad (5)$$

$$\Omega_{opt} = \frac{\lambda_{opt}}{R} \cdot V \quad (6)$$

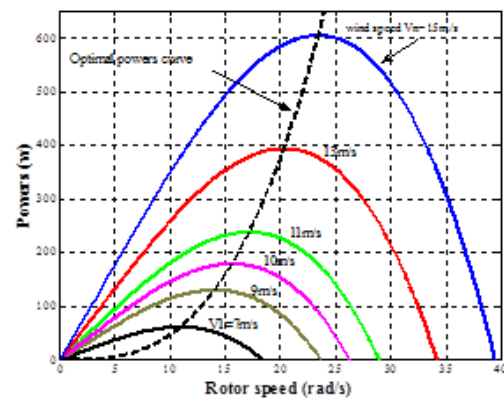


Figure 3. Power versus rotor speed at various wind speeds

2.2. Permanent Magnet synchronous Generator

The wind turbine driven PMSG can be represented in the rotor reference frame by the following model [12],[13]:

$$\begin{cases} V_d = -R_s I_d - L_d \frac{d}{dt} I_d + \omega L_q I_q \\ V_q = -R_s I_q - L_q \frac{d}{dt} I_q - \omega L_d I_d + \omega \psi_f \end{cases} \quad (7)$$

Where:

L_d : Stator inductance in direct axis(H).

L_q : Stator inductance in quadrature axis (H).

R_s : Stator phase winding resistance (Ω).

ψ_f : Amplitude of the flux linkages (v.s/rad).

I_d : direct axis current (A)

I_q : quadrature axis current (A)

The electromagnetic torque is expressed by[12], [13]:

$$C_{em} = \frac{3}{2} P[(L_q - L_d)i_d i_q + i_q \psi_f] \quad (8)$$

Where, P is PMSG number of pairs of poles.

The dynamics of the machine is given by the following mechanical equation:

$$C_m - C_{em} - f\Omega = J \frac{d\Omega}{dt} \quad (9)$$

Where:

C_m : Motor torque developed by the turbine shaft (Nm)

C_{em} : Electromagnetic torque developed by the generator (Nm)

$f\Omega$: Friction torque

J : Moment of inertia referred to generator shaft (Kgm^2)

f : Friction coefficient.

Ω : mechanical angular velocity of the turbine (rad/s).

The relation between the rotor angular velocity of the generator ω and the mechanical angular velocity of the wind turbine rotor Ω is expressed as[12], [13]:

$$\omega = P\Omega \quad (10)$$

2.3. Three phases diode bridge rectifier

The diode rectifier is the most commonly used topology in power electronic applications. For a three phase system, it is consisting of six diodes. The diode rectifier can only be used in one quadrant, it is simple and it is not possible to control it. The DC voltage and current output depend on the generator voltage and current as following[14]:

$$U_{dc} = \frac{3}{\pi} E_{ab}^{\max} = \frac{3\sqrt{6}}{\pi} E_a^{\text{eff}} \quad (11)$$

$$I_{dc} = \frac{\pi}{\sqrt{6}} I_a \quad (12)$$

Where:

U_{dc} and I_{dc} : Medium output voltage and current of rectifier.

E_a and I_a : Output voltage and current of generator (phase a).

2.4. Battery Model and State of Charge

The battery model is inspired from Ford batteries model. It is formed by an ideal voltage supply E_{bat} in series with resistance R_{bat} and capacity Q (Ah) as illustrated in

Figure 1. The electrical model is given by the following expression [15]:

$$V_{dc2} = E_{bat} - K \frac{\int I_{bat} dt}{Q_0} - R_{bat} I_{bat} \quad (13)$$

Where:

K is a constant depends on the battery.

$\frac{\int I_{bat} dt}{Q_0}$ Is a term that indicates the state of discharge.

2.5. DC-DC Buck Converter Model

The standard unidirectional topology of the DC-DC buck converter of the Figure. 1, consists of a switching-mode power device containing basically two semiconductor switches (a rectifier diode D2 and a power transistor K with its corresponding anti-parallel diode D1) and an inductor L. The output DC voltage is produced at a level lower than its input DC voltage. This converter acts as an interface between the full-wave rectifier bridge and the battery bank, by employing pulse-width modulation (PWM) control techniques. Operation of the DC-DC converter in the continuous (current) conduction mode (CCM), i.e. the current which is flowing continuously in the inductor during the entire switching cycle, facilitates the development of the state-space model because only two switch states are possible during a switching cycle, namely, (i) the power switch K is on and the diode D2 is off; or (ii) K is off and D2 is on.

Electric equations that describe the dynamics of the DC-DC buck converter over a commutation period are given by:

$$U_{do} = \alpha U_{dc1} \quad (14)$$

$$U_{do} = U_{bat} + U_L \quad (15)$$

$$U_{do} = E_{bat} + R_{bat} I_{bat} + L \frac{dI_{bat}}{dt} \quad (16)$$

Where, I_{bat} is the converter output current (battery current charging), U_{bat} is the output voltage, U_{dc1} is the buck converter input voltage, U_L and U_{d0} are respectively, inductor (L) and diode rectifier (D2) voltages.

3. Control of DC-DC buck converter with maximum power extraction

The battery current charging can be controlled by controlling the duty cycle of the switch (K) at any wind speed to extract maximum power from the wind turbine. Figure 4shows the control block diagram of DC-DC buck converter. Since the battery current charging I_{bat} depends on the power of the battery P_{bat} , we can consider this power as reference stat variable according to following relation:

$$I_{bat}^{ref} = \frac{P_{bat}^{ref}}{U_{bat}} \quad (17)$$

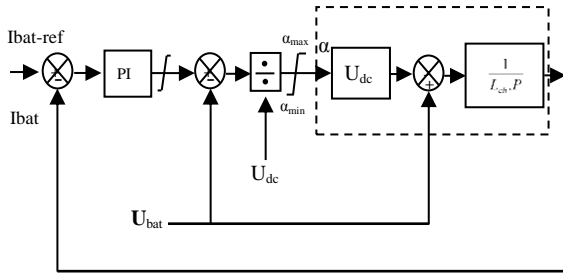


Figure 4. Control block diagram of dc-dc buck converter

3.1. MPPT

The senseless control strategy proposed in this work is based on the indirect piloting of the battery current charging. This can simplify wind power conversion system and minimize its cost, without reducing the energizing efficiency. We consider that the rotor speed picture is given by the PMSG electromotive force; both parameters are then bound to output rectifier voltage. The mechanical speed sensor can be suppressed and replaced by a simple voltage measure which can be assimilated to the rotation speed according to following equation:

$$U_{dc}(\Omega) = \frac{3}{\pi} \cdot E_{ab}^{\max} = \frac{3 \cdot \sqrt{6}}{\pi} \cdot \psi_{f-eff} \cdot P \cdot \Omega = \mu \cdot \Omega \quad (18)$$

Where, μ is a constant given by:

$$\mu = \frac{3 \cdot \sqrt{6}}{\pi} \cdot \psi_{f-eff} \cdot P \quad (19)$$

Therefore, the target optimum battery current charging can be given by:

$$I_{bat}^{ref} = \frac{K_{opt}}{U_{bat}} \cdot \Omega^3 = \frac{K_{opt}}{U_{bat}} \cdot \left(\frac{U_{dc}}{\mu}\right)^3 = \frac{\sigma \cdot (U_{dc})^3}{U_{bat}} \quad (20)$$

$$\sigma = \eta \cdot K_{opt} \cdot \left(\frac{\pi}{3 \cdot \sqrt{6} \cdot \psi_{f-eff} \cdot P}\right)^3 \quad (21)$$

The maximal power of the battery is given therefore by:

$$P_{bat}^{\max} = f(U_{dc}) = \sigma \cdot (U_{dc})^3 \quad (22)$$

The MPPT device gotten is illustrated therefore on Figure 5.

$$U_{dc} [K] \longrightarrow \frac{P_{bat}^{\max} = f(U_{dc})}{U_{bat}} [K] \longrightarrow I_{bat}^{ref} [K + 1]$$

Figure 5. Control algorithm of the battery current

The control algorithm includes then, the following steps:

- Measure output diode rectifier voltage.
- Determine the reference current charging of the battery.

3.2. Compatibility of the Proposed Structure opposite the Battery Voltage

For an optimal working régime, the output rectifier voltage value can be determined according to the wind speed by the following expression:

$$U_{dcl} = \frac{3 \cdot \sqrt{3}}{\pi} \cdot p \cdot \psi_{f-max} \cdot \frac{\lambda_{opt}}{R} \cdot V_v \quad (23)$$

While neglecting losses, the output rectifier voltage can be written according to the battery voltage U_{bat} and duty cycle α by:

$$U_{dcl} = \frac{U_{bat}}{\alpha} \quad (24)$$

According to the wind system application conditions, the simple DC-DC buck converter imposes some limitations. The converter input voltage possesses minimal and maximal stops, determined by the battery voltage U_{bat} and duty cycle stops α_{min} and α_{max} .

The minimum input voltage of DC-DC buck converter is defined by:

$$U_{dcl}^{\min} = \frac{U_{bat}}{\alpha_{max}} \quad (25)$$

Therefore, the minimal wind speed can be calculated according to the battery voltage:

$$V_v^{\min} = \frac{\sqrt{3} \cdot \pi \cdot R}{9 \cdot p \cdot \psi_{f-max} \cdot \lambda_{opt} \cdot \alpha_{max}} \cdot U_{bat} \quad (26)$$

Admitting that the duty cycle maximal value equal to 0.99, it is possible to find the minimal speed of wind assuring the good functioning of the wind power conversion system for different battery voltages. For the duty cycle lower limit that is supposed equal to 0.1, there is no problem posed, because the wind values gotten are very big.

4. Results and discussions

The model of the PMSG based variable speed wind turbine system of Figure 1 is built using Matlab/Simpower dynamic system simulation software. The parameters of the Turbine and PMSG used are given in Table 1. The power converter and the control algorithm are also implemented and included in the model. The wind profile input data used during this study are shown in Figure 6. In the aim to know the load voltage effect on the system behavior, three different batteries are used during this 120-s simulation period as shown in Figure 7. As shown in Figure 8, the peak power follows the wind speed profile, and it is close to the actual maximum power for each variation of wind speed. Figure 9 represented the power coefficient which is kept almost constant and very close to the maximum value $C_p\text{-max}=0.15$. And since global losses are proportional to the current, measured power illustrated in Figure 8 is less important for low voltages as shown after 80 seconds, and follows closely the power reference for high voltages. As the wind speed decreased or increased, the controller tracks maximum power by varying the duty cycle over the whole range of input wind conditions as shown in Figure 9. It seems that with increase in battery voltage, the sensorless controller increases the duty cycle which directly controls the modulation index of the PWM DC-DC converter. In that case, the charging current decreases and the output power increases. Figure 11 shows optimum power versus wind speed, where connection wind speed V_{cut-in} is very low (about 2.7m/s), and battery voltage variation effect is

observed in the form of peaks. The integrated value of the maximum power at the end of the simulation is the maximum energy available from the wind with this wind energy conversion system. Simulation results show that the

overall energy captured is optimized by the control strategy throughout the range of wind speed as can be seen in Figure12

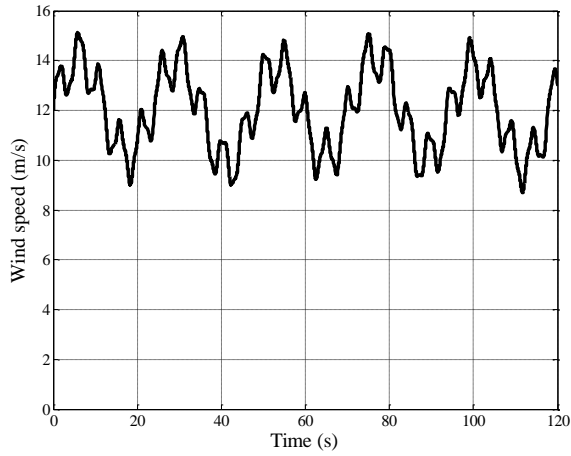


Figure 6. Wind speed profile

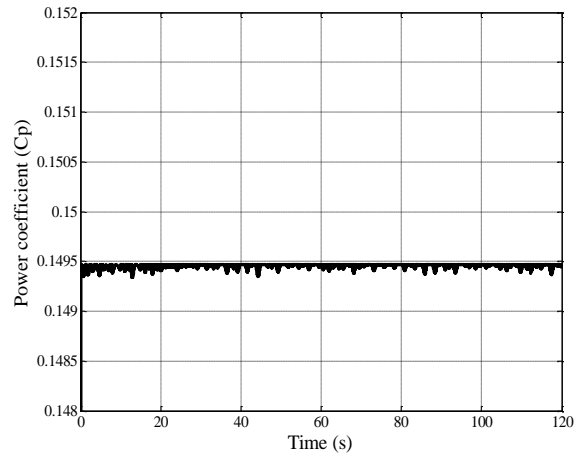


Figure 9. Power coefficient

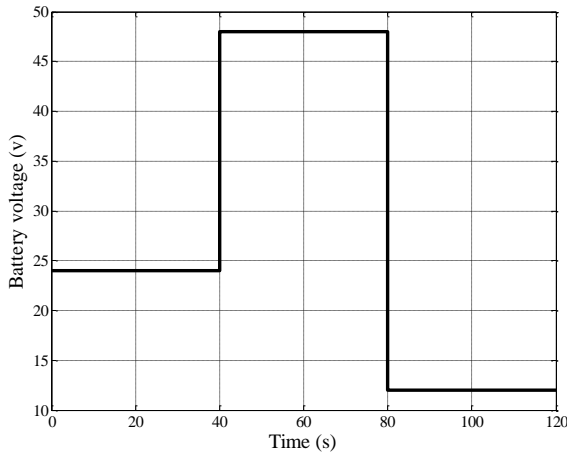


Figure 7. Battery voltages

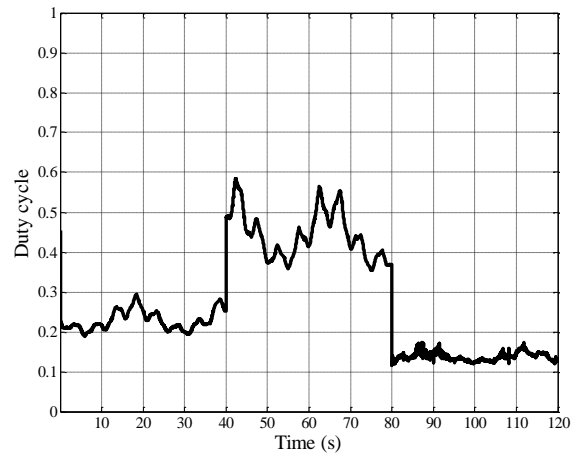


Figure 10. Duty cycle

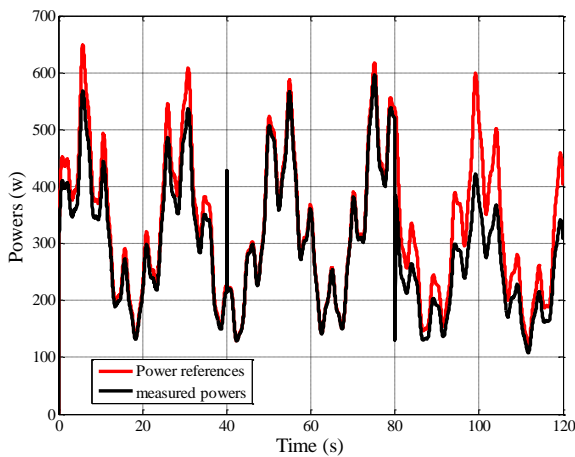


Figure 8. Optimal and maximized powers

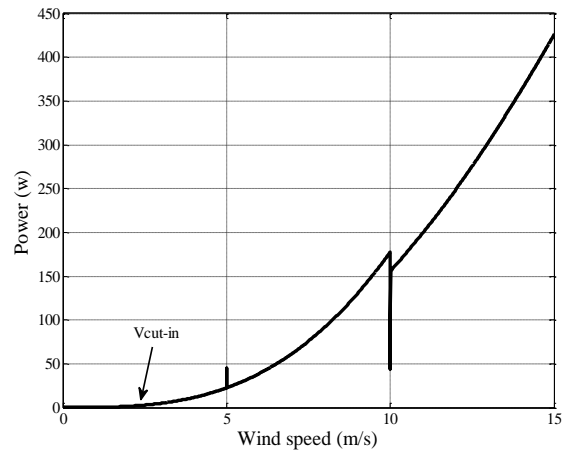


Figure 11. Power versus wind speed

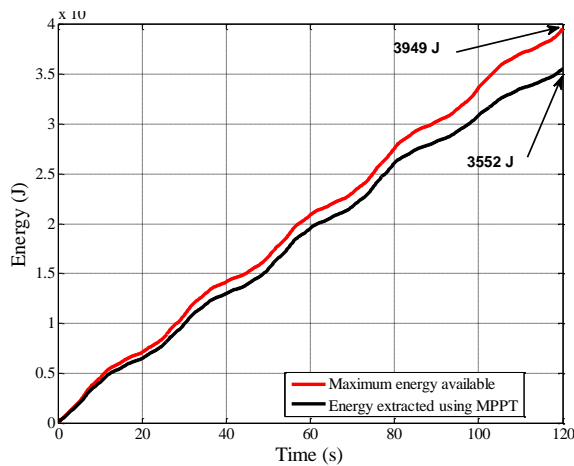


Figure 12. Optimal and maximized energies

Conclusion

A simple sensorless control strategy applied in small size wind generator systems for charging batteries has been proposed. A complete modeling and simulation of turbine, generator, converter, and battery was developed. The MPPT system was designed and studied via simulated results. The main target of the proposed system is the exploitation of the available wind energy at low speeds in an optimum operating point without compromising the efficiency at higher wind speeds. The algorithm control of DC-DC buck converter is designed with reduced overall cost which improves its use in domestic life with a large safety margin because it is designed to be connected with low voltage batteries.

Table 1. Wind energy system parameters

Wind turbine	
Density of air	1.225 Kg/m ³
Area swept by blades, S	2 m ²
Optimum coefficient, K _{opt}	0.0474 Nm/(rd/s) ²
PMSG	
No. of poles	34
Rated current	4.8 A
Rated voltage	90 V
Armature resistance, R _s	1.137 Ω
Magnet flux linkage	0.15 Wb
Stator inductance, L _s	2.7 mH
Rated power	600 W
Inertia	0.1 Kg·m ²
DC-DC buck converter	
filtering voltage capacity	3.3 mF
Smoothing inductance	2.5 mH
Cutting frequency	5 kHz
Diode threshold voltage	0.65 V
Transistor threshold voltage	0 V
Diode conduction resistance	20.7e-3 Ω
Transistor conduction resistance	85e-3 Ω

Acknowledgements

The authors of this article thank the Director of the Electrical Engineering Laboratory (LEB) of the

engineering Sciences Faculty of Batna University for his support in carrying out this research work.

References

- [1] H. Li, Z. Chen, "Overview of different wind generator systems and their comparisons", IET Renewable Power Generation, Vol. 2, No. 2, 2008, 123-138.
- [2] C.N.Bhende, S.Mishra, S.G.Malla, S.Ganesh. "Permanent magnet synchronous generator-based standalone wind energy supply system". IEEE Transactions on Sustainable Energy, Vol. 2, No.4, 2011, 361-373.
- [3] S.Sharma, B.Singh, B. "Control of permanent magnet synchronous generator-based stand-alone wind energy conversion system". IET Power Electronics, Vol. 5, No.8, 2012, 1519-1526.
- [4] M.Yin, G.Li, M.Zhou, "Modeling of the wind turbine with a permanent magnet synchronous generator for integration". In Power Engineering Society General Meeting, IEEE, 2007, 1-6.
- [5] M.Herminio, F.Oliveira, S.Demercil, R.P.T. Bascopé, C.E.A. Silva, G.J.Almeida, "On the study of wind energy conversion system applied to battery charging using multiblade turbine", Power Electronics Conference, IEEE, Bonito, Brazil, 2009.
- [6] T.Tafticht, K.Agbossou, A.Chériti, M.L.Doumbia, "Output power maximization of a permanent magnet synchronous generator based stand-alone wind turbine". IEEE International Symposium on Industrial Electronics, Vol. 3, 2412-2416, 2006, Montreal, Que., Canada.
- [7] S.Vijayalakshmi, S.Saikumar, S.Saravanan, R.V.Sandip, V. Sridhar, "Modeling and control of a Wind Turbine using Permanent Magnet Synchronous Generator". International Journal of Engineering Science and Technology (IJEST), Vol. 3, No. 3, 2011, 2377-2384.
- [8] M.Mayouf, D.Aissa, "New Control strategies of a Small Size Wind Generation System for Battery Charging", 4th International Conference on Electrical Engineering, Boumerdes, Algeria, 2015.
- [9] K.Y.Lo, Chen, Y.M.Chen, Y.R.Chang, "MPPT battery charger for stand-alone wind power system". IEEE transactions on power electronics, Vol. 26, No.6, 2011, 1631-1638.
- [10] G.L.Johnson, D.Gary, (2001). Wind Turbine Power, Energy and Torque. Electrical ed. Prentice-Hall Englewood Cliffs. 2001
- [11] A.Mirecki, X.Roboam, F.Richardeau, "Comparative Study of Maximum Power Strategy in Wind Turbines" IEEE International Symposium on Industrial Electronics, Vol. 2, 2004, 993-998
- [12] M.Mayouf, Rachid Abdessemed, " Modeling and optimization of wind turbine driving permanent magnet synchronous generator", Jordan journal of mechanical and industrial engineering (JJMIE), Vol.5, No. 6, 2011
- [13] A.Rolan, A.Luna, G.Vazquez, D. Aguilar, G.Azevedo, "Modeling of a variable speed wind turbine with a permanent magnet synchronous generator". IEEE International Symposium on Industrial Electronics, Seoul, South Korean, 2009
- [14] F.Blaabjerg, M. Liserre, K.Ma, "Power electronics converters for wind turbine systems". IEEE Transactions on industry applications, Vol. 48, No.2, 2012, 708-719.
- [15] D.Rekioua, Z. Roumila, T.Rekioua, "Etude d'une centrale hybride photovoltaïque, éolien, diesel", Revue des énergies renouvelables. Vol. 11, No. 4, 2004, 623-633.

Pulsating Nanofluid Jet Impingement onto a Partially Heated Surface Immersed in a Porous Layer

Iman Zahmatkesh*, Seyyed Ali Naghedifar

Department of Mechanical Engineering, Mashhad Branch, Islamic Azad University, Mashhad, Iran

Received JAN 12 2018

Accepted JULY 25 2018

Abstract

Laminar forced convection heat transfer during pulsating nanofluid jet impingement onto a partially heated surface immersed in a porous layer is presented in this study. For this purpose, the Brinkman–extended Darcy model is adopted. The base fluid and the nanoparticles are taken to be in local thermal equilibrium with the same velocities and temperatures. The local thermal equilibrium is also assumed between the nanofluid and the porous matrix. Simulation results are validated thoroughly. Thereafter, the consequences of the pulsation frequency and amplitude, the Reynolds number, the Darcy number, the medium porosity, the nanoparticles fraction, and the geometric ratio on thermal performance of the system are analyzed. It is found that direct relations exist between the heat transfer rate and the pulsation amplitude, the medium porosity, the Darcy number, the nanoparticles fraction, and the geometric ratio whereas the pulsation frequency contributes neutrally. The presented results demonstrate that superimposing pulsation on the mean flow augments heat transfer as compared to an equivalent steady case.

© 2018 Jordan Journal of Mechanical and Industrial Engineering. All rights reserved

Keywords: Forced convection, Nanofluid, Porous media, Jet impingement, Pulsating flow.

Nomenclature		t	time (s)
A	pulsation amplitude	T	temperature (K)
C	specific heat (J/(kg K))	u, v	velocity components along x and y axes, respectively (m/s)
d	half of the width of the jet inlet (m)	U, V	dimensionless velocity components, u/V_0 and v/V_0
Da	Darcy number, κ/L^2	V_0	mean inlet velocity (m/s)
f	pulsation frequency (Hz)	w	half of the width of the solution domain (m)
h	height of the solution domain (m)	x, y	Cartesian coordinates (m)
h	heat transfer coefficient (W/(m ² K))	X, Y	dimensionless Cartesian coordinates, x/L and y/L
k	thermal conductivity (W/(m K))	<i>Greek Symbols</i>	
L	half of the heat source length (m)	θ	dimensionless temperature, $(T - T_C)/(T_H - T_C)$
Nu	local Nusselt number, hL/k_f	κ	permeability (m ²)
\overline{Nu}	space-averaged Nusselt number	μ	dynamic viscosity (Pa.s)
$\langle \overline{Nu} \rangle$	time-space-averaged Nusselt number	ρ	density (kg/m ³)
p	pressure (Pa)	τ	dimensionless time, tV_0/L
P	dimensionless pressure, $p/(\rho_f V_0^2)$		
Pe	Peclet number, $Pe = Re Pr$		
Pr	Prandtl number, $\mu_f C_f/k_f$		
Re	Reynolds number, $\rho_f V_0 L/\mu_f$		

* Corresponding author e-mail: zahmatkesh5310@mshdiau.ac.ir

ϕ	porosity
χ	nanoparticles fraction
ψ	stream function (m^2/s)
Ψ	dimensionless stream function, ψ/V_0L
ω	vorticity ($1/\text{s}$)
Ω	dimensionless vorticity, $\omega L/V_0$

Subscripts

C	cold
f	base fluid
H	hot
nf	nanofluid
p	nanoparticle
s	solid matrix
$stag$	stagnation point

1. Introduction

As a consequence of high rates of heat and mass transfer, impinging jets are widely used in industrial processes. Examples include cooling of electronic equipments and turbine blades, annealing of sheet metals, drying of paper, textile, and glass, and anti-icing systems. Thermal performance of impinging jets can be modified if one superimposes pulsation on the mean flow. This occurs since the pulsation redevelops and breaks up the boundary layers within each oscillation period, which may lead to thinner boundary layers as compared to an equivalent steady case. Previous studies indicate that there is a lack of consensus about the impact of flow pulsation on jet impingement heat transfer. Both improvement and deterioration of heat transfer due to creation of unsteady flows have been reported in the scientific literature. Additional studies are thereby required to examine the correlation between flow pulsation and heat transfer in impinging jets.

Addition of nanoparticles to conventional fluids is a recent way to improve cooling/heating performance. Physical reasoning for this behavior is the fact that thermal properties of the resulting fluid (nanofluid) are more proper than those of conventional fluids. Looking at the previous literature shows some recent interests on jet impingement heat transfer together with flow pulsation (e.g., [1–5]) or nanoparticles addition (e.g., [6–8]), separately. However, the combined effects have not been discussed thoroughly. The available work goes back to the study of Selimefendigil and Oztop [9]. They simulated pulsating jet impingement of an Al_2O_3 –water nanofluid, and they studied the effects of the pulsation frequency along with the Reynolds number, and the nanoparticles fraction on the heat transfer characteristics. Their results led to the conclusion that in some cases, the combined effects of the flow pulsation and the inclusion of the nanoparticles may not be favorable for heat transfer augmentation.

Convective flows in porous media have been extensively analyzed in the past since many practical applications can be modeled with transport phenomena in porous media [10,11]. So, some researchers have discussed jet impingement cooling of heated surfaces immersed in porous media in the regimes of forced convection [12–14] and mixed convection [15–17]. Recently, thermal performance of jets impinging onto a solid heat source immersed in a porous layer has been analyzed by Saeid [18]. Meanwhile, Lam and Prakash [19] have studied jet impingement onto an array of heat sources mounted on a target surface with/without a porous layer. Local thermal non-equilibrium effects during jet impingement cooling of a constant-heat-flux plate have been considered by Buonomo et al. [20]. Oscillatory mixed convection in the jet impingement cooling of a horizontal surface immersed in a nanofluid-saturated porous medium has been simulated and discussed by Zahmatkesh and Naghedifar [21]. More recently, Chinige et al. [22] have reported an optimized configuration of multijets impinging through porous passages.

Although previous achievements are important, the combined effects of flow pulsation, nanoparticles addition, and porous media in jet impingement heat transfer have not been analyzed yet. In the present contribution, laminar forced convection heat transfer during pulsating nanofluid jet impingement onto a partially heated surface immersed in a porous layer is simulated. Thereafter, the consequences of the pertinent parameters on thermal performance of this complex system are discussed. The current parameters include the pulsation frequency and amplitude, the Reynolds number, the Darcy number, the medium porosity, the nanoparticles fraction, and the geometric ratio.

2. Mathematical Modeling

2.1. Physical model

As depicted in Fig. 1, the present computational domain consists of a channel including two parallel plates separated with a distance h . A nanofluid jet from a slot on the top adiabatic plate with a width of $2d = 0.5L$ flows through a saturated porous layer and impinges onto the bottom plate that is partially heated. Subsequently, it flows out through the outlets, which are located at $2w = 25L$ far from each other along the plates. The pulsating inlet jet has a time dependent velocity distribution while its temperature (T_C) is smaller than that of the heated section of the channel (T_H). It is assumed that temperature difference between the incoming fluid and the isothermal plate is not significant. Therefore, buoyancy effects are ignored. Additionally, the nanofluid properties are taken temperature-independent.

2.2. Nanofluid description

In this study, the basefluid is water with Al_2O_3 nanoparticles which are added in 1, 4, and 8 percent by volume. The nanofluid flow is assumed to be Newtonian, incompressible, and laminar with negligible viscous dissipation. The base fluid and the nanoparticles are taken to be in local thermal equilibrium with the same velocities

and temperatures. The local thermal equilibrium is also assumed between the nanofluid and the porous matrix. Consequently, a single-phase approach is used for the simulation of the flow field. Thermophysical properties of the base fluid and the nanoparticles are kept constant at 300K with the numerical values reported in [23]. Effective properties of the nanofluid are determined as follows:

Density:

$$\rho_{nf} = (1 - \chi)\rho_f + \chi\rho_p \quad (1)$$

Specific heat:

$$(\rho C)_{nf} = (1 - \chi)(\rho C)_f + \chi(\rho C)_p \quad (2)$$

Dynamic viscosity [24]:

$$\mu_{nf} = \frac{\mu_f}{(1 - \chi)^{2.5}} \quad (3)$$

Thermal conductivity [25]:

$$\frac{k_{nf}}{k_f} = \frac{(k_p + 2k_f) - 2\phi(k_f - k_p)}{(k_p + 2k_f) + \phi(k_f - k_p)} \quad (4)$$

2.3. Governing equations

Governing equations for the problem at hand are [26]:

Continuity equation:

$$\frac{\partial u}{\partial x} + \frac{\partial v}{\partial y} = 0 \quad (5)$$

Momentum equations:

$$\rho_{nf} \left[\frac{1}{\phi} \frac{\partial u}{\partial t} + \frac{1}{\phi^2} \left(u \frac{\partial u}{\partial x} + v \frac{\partial u}{\partial y} \right) \right] = -\frac{\partial p}{\partial x} + \frac{\mu_{nf}}{\phi} \left(\frac{\partial^2 u}{\partial x^2} + \frac{\partial^2 u}{\partial y^2} \right) - \frac{\mu_{nf}}{\kappa} u \quad (6)$$

$$\rho_{nf} \left[\frac{1}{\phi} \frac{\partial v}{\partial t} + \frac{1}{\phi^2} \left(u \frac{\partial v}{\partial x} + v \frac{\partial v}{\partial y} \right) \right] = -\frac{\partial p}{\partial y} + \frac{\mu_{nf}}{\phi} \left(\frac{\partial^2 v}{\partial x^2} + \frac{\partial^2 v}{\partial y^2} \right) - \frac{\mu_{nf}}{\kappa} v \quad (7)$$

Energy equation:

$$(\rho C)_{nf} \left(\frac{\partial T}{\partial t} \right) + (\rho C)_{nf} \left(u \frac{\partial T}{\partial x} + v \frac{\partial T}{\partial y} \right) = k_{nf} \left(\frac{\partial^2 T}{\partial x^2} + \frac{\partial^2 T}{\partial y^2} \right) \quad (8)$$

Here, the Forchheimer term has been ignored in the momentum equations. The following parameters are used to make the above equations dimensionless:

$$\tau = \frac{t}{L/V_0} \quad X = \frac{x}{L} \quad Y = \frac{y}{L} \quad U = \frac{u}{V_0} \quad (9)$$

$$V = \frac{v}{V_0} \quad P = \frac{p}{\rho_f V_0^2} \quad \theta = \frac{T - T_c}{T_H - T_c}$$

The resulting momentum equations are thereafter cross-differentiated and then subtracted. So that, the pressure terms are removed. Consequently, one obtains the dimensionless governing equations in terms of stream function (Ψ) and vorticity (Ω) as:

Continuity equation:

$$\frac{\partial^2 \Psi}{\partial X^2} + \frac{\partial^2 \Psi}{\partial Y^2} = -\Omega \quad (10)$$

Momentum equation:

$$\frac{1}{\phi} \frac{\partial \Omega}{\partial \tau} + \frac{1}{\phi^2} \left(\frac{\partial \Psi}{\partial Y} \frac{\partial \Omega}{\partial X} - \frac{\partial \Psi}{\partial X} \frac{\partial \Omega}{\partial Y} \right) = \frac{1}{\phi} \frac{\rho_f \mu_{nf}}{Re \rho_{nf} \mu_f} \left(\frac{\partial^2 \Omega}{\partial X^2} + \frac{\partial^2 \Omega}{\partial Y^2} \right) - \frac{1}{Re Da} \frac{\rho_f \mu_{nf}}{\rho_{nf} \mu_f} \Omega \quad (11)$$

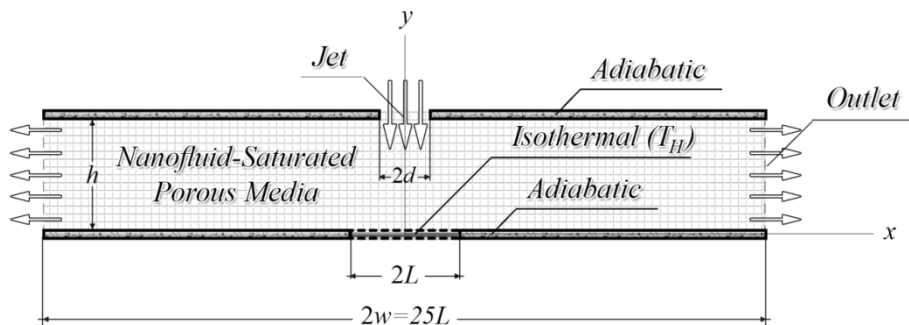


Figure 1: Schematic of the jet impingement problem.

Energy equation:

$$\frac{\partial \theta}{\partial \tau} + \frac{\partial \Psi}{\partial Y} \frac{\partial \theta}{\partial X} - \frac{\partial \Psi}{\partial X} \frac{\partial \theta}{\partial Y} = \frac{1}{Re Pr_f} \frac{k_{nf}}{k_f} \frac{(\rho C)_f}{(\rho C)_{nf}} \left(\frac{\partial^2 \theta}{\partial X^2} + \frac{\partial^2 \theta}{\partial Y^2} \right) \quad (12)$$

with:

$$Re = \frac{\rho_f V_0 L}{\mu_f} \quad Da = \frac{\kappa}{L^2} \quad Pr_f = \frac{\mu_f C_f}{k_f} \quad (13)$$

2.4. Boundary conditions

The current flow problem is symmetric about the yaxes. So, the right side of Fig. 1 is selected as the computational domain. The incoming nanofluid is assumed to have a uniform but time-dependent velocity profile with the form of $V = 1 + A \sin(2\pi f\tau)$ and a constant temperature. Moreover, the fully-developed condition is prescribed at the outlet for the velocity and temperature. The associated boundary conditions are:

At the inlet ($0 < X < d/L, Y = h/L$):

$$\Psi = X[1 + A \sin(2\pi f\tau)] \quad \Omega = -\frac{\partial^2 \Psi}{\partial Y^2} \quad \theta = 0 \quad (14a)$$

At the outlet ($X = w/L, 0 < Y < h/L$):

$$\frac{\partial \Psi}{\partial X} = 0 \quad \frac{\partial \Omega}{\partial X} = 0 \quad \frac{\partial \theta}{\partial X} = 0 \quad (14b)$$

At the symmetry axis ($X = 0, 0 < Y < h/L$):

$$\frac{\partial \Psi}{\partial Y} = 0 \quad \frac{\partial \Omega}{\partial X} = 0 \quad \frac{\partial \theta}{\partial X} = 0 \quad (14c)$$

At the upper adiabatic surface ($d/L \leq X \leq w/L, Y = h/L$):

$$\Psi = \frac{d}{L} = 0.25 \quad \Omega = -\frac{\partial^2 \Psi}{\partial Y^2} \quad \frac{\partial \theta}{\partial Y} = 0 \quad (14d)$$

At the heater ($0 < X < 1, Y = 0$):

$$\Psi = 0 \quad \Omega = -\frac{\partial^2 \Psi}{\partial Y^2} \quad \theta = 1 \quad (14e)$$

At the lower adiabatic surface ($1 \leq X \leq w/L, Y = 0$):

$$\Psi = 0 \quad \Omega = -\frac{\partial^2 \Psi}{\partial Y^2} \quad \frac{\partial \theta}{\partial Y} = 0 \quad (14f)$$

To ensure that the lower surface is large enough to satisfy the fully-developed boundary condition at the outlet, the computational domain is doubled in the longitudinal direction. Inspection of the results demonstrates that such a change may not bring substantial variations in the simulation results.

2.5. Nusselt number

In this paper, heat transfer performance of the pulsating nanofluid jet is evaluated using the Nusselt number. To this aim, the local Nusselt number, the space-averaged Nusselt number, and the time-space-averaged Nusselt number are employed. The local Nusselt number is defined as:

$$Nu = -\frac{k_{nf}}{k_f} \left(\frac{\partial \theta}{\partial Y} \right)_{Y=0} \quad (15)$$

The space-averaged Nusselt number at each time instant is obtained after integrating the local Nusselt number along the heater:

$$\overline{Nu} = \int_0^1 Nu. dX \quad (16)$$

One arrives at the time-space-averaged Nusselt number by applying time-averaging to the space-averaged Nusselt number, i.e.,

$$\langle \overline{Nu} \rangle = \frac{1}{\tau} \int_0^{\tau} \overline{Nu}. d\tau \quad (17)$$

3. Solution procedure

3.1. The CFD code

Solution of the unsteady governing equations is accomplished using an implicit finite-difference approach. The diffusion terms are discretized by a second-order central-difference method while a second-order upwind scheme is applied to the convective terms. A computer

code was developed in FORTRAN to perform the current calculations.

Schematic of the current non-uniform grid system is depicted in Fig. 2. Notice that the grid points are clustered at the proximity of the header as well as the upper and lower surfaces.

To undertake a grid independency study, the lower plate is maintained at a constant temperature while the remaining parameters are assumed to be $Re = 100$, $\chi = 0.06$, $Da = \infty$, and $\phi = 1$. Thereafter, numerical values of the local Nusselt number for different grid systems including 80×27 , 120×40 , 180×60 , 270×90 , and 405×105 are compared. It is found that a 270×90 grid system provides acceptable results since difference in the values of \overline{Nu} employing 270×90 and 405×105 grids remains below 2%.

In order to find suitable time-step, results in terms of temporal variations of the Nusselt number at the stagnation point for different time-steps are compared in Fig. 3. It is obvious that the cases with $\Delta\tau \leq 0.5 \times 10^{-4}$ lead to nearly identical results. So, $\Delta\tau = 0.5 \times 10^{-4}$ is chosen for our forthcoming calculations.

3.2. Validation study

The current computational code is a modified version of an in-house code built and validated in the previous works [27–29]. In order to validate this code for the simulation of the current jet impingent problem, we compare our results with those of Wong and Saeid [16] and Sivasamy et al. [17] in Figs. 4 and 5, respectively. The study of Sivasamy et al. [17] has considered a constant-heat-flux heater in unsteady regime while Wong and Saeid [16] have simulated an isothermal heater in steady conditions. To validate the current nanofluid model in porous media, simulation results for natural convection of an Al_2O_3 -water nanofluid with $\chi = 0.1$ are compared with those of Bourantas et al. [30] in Fig. 6 for two different Darcy numbers. The obvious agreement between the results of the current code and those of the previous studies assures us that the current mathematical model and solution procedure are accurate and lends confidence into the simulation results to be presented subsequently.

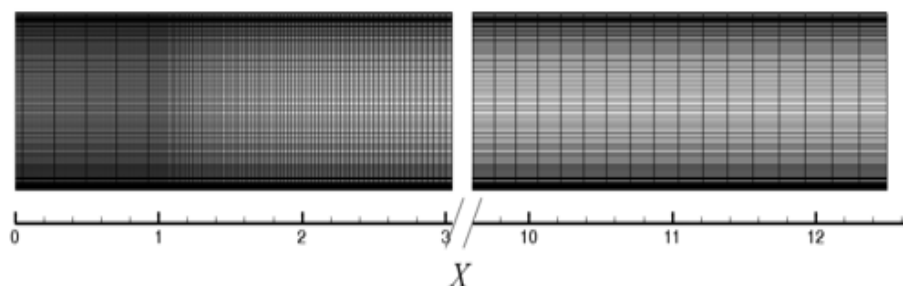


Figure 2: Distribution of the grid points in the solution domain.

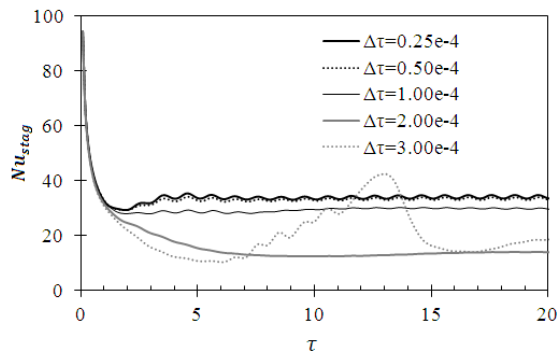


Figure 3: Time-step study ($Re = 400, Da = \infty, \chi = 0.06, \phi = 1.0$).

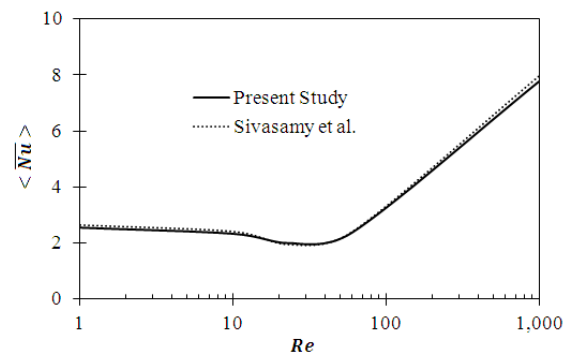


Figure 5: Comparing the present results with those of Sivasamy et al. [17]

4. Simulation results

In this section, simulation results are presented and discussed. To provide a picture about the consequences of the pertinent parameters, computations are undertaken for a range of the pulsation frequency and amplitude ($1 \leq f \leq 2$ and $0.5 \leq A \leq 1$), the Reynolds number ($200 \leq Re \leq 800$), the medium porosity ($0.6 \leq \phi \leq 0.8$), the Darcy number ($10^{-5} \leq Da \leq 10^{-1}$), the nanoparticles fraction ($0.01 \leq \chi \leq 0.08$), and the geometric ratio ($0.5 \leq L/h \leq 2.0$). In all cases, a constant Prandtl number is assumed for the base fluid with $Pr_f = 6.2$. Moreover, *Base Case* is considered as $f = 0$ (steady-state), $Re = 400$, $\phi = 0.7$, $Da = 10^{-3}$, $\chi = 0.04$, and $L/h = 1$ in order to be compared with other results.

4.1. Effects of the pulsation frequency and amplitude

Firstly, the effects of the pulsation frequency and amplitude on thermal behavior of the current flow problem are analyzed. To this aim, computations are undertaken for different values of these parameters maintaining other pertinent parameters identical to the base case. Results in terms of temporal variations of \overline{Nu} for $45 \leq \tau \leq 50$ are plotted in Fig. 7. The corresponding time-space-averaged Nusselt numbers are also reported in Table 1. The present selection of the time interval ensures us to reach stable oscillations.

Inspection of the presented results indicates that duplicating the pulsation amplitude leads to about 6% elevation in $\langle \overline{Nu} \rangle$. This trend is consistent with previous results of Demircan and Turkoglu [1] and Geng

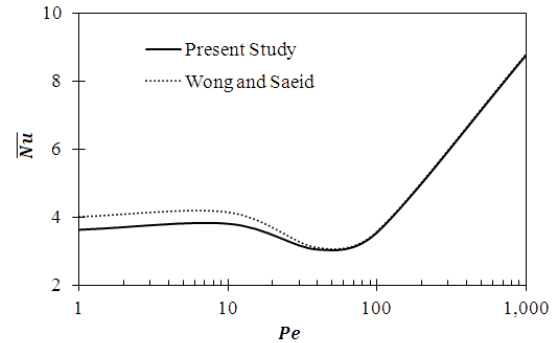


Figure 4: Comparing the present results with those of Wong and Saeid [16]

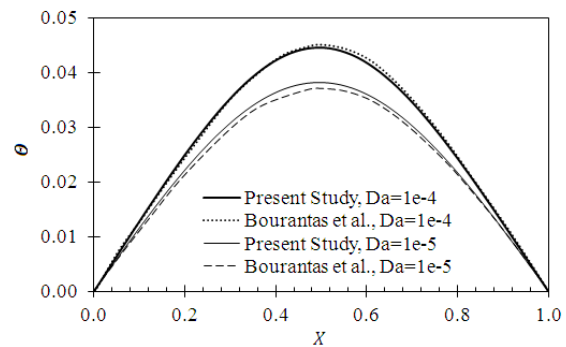


Figure 6: Comparing the present results with those of Bourantas et al. [29]

et al. [3]. Notice also that increase in the pulsation frequency, in spite of changing the oscillation pattern, has not produced noticeable rise in the time-space-averaged Nusselt number under the current circumstances.

Comparing the results of the pulsating cases with those of the base case (i.e., steady-state) indicates that, in the present cases, the sinusoidal inlet velocity provides higher heat transfer rates. This is attributed to the fact that the flow pulsation redevelops and breaks up the boundary layers in a continuous manner. So, thinner boundary layers with higher heat transfer coefficients establish in a pulsating case as compared to an equivalent steady one.

4.2. Effect of the Reynolds number

Next, the impact of the Reynolds number is assessed. Accordingly, simulation results in terms of numerical values of $\langle \overline{Nu} \rangle$ for different Reynolds numbers are provided in Table 2. The presented results correspond to $A = 0, 0.5$, and 1 . Results investigation clearly indicates that the jet impingement heat transfer is a strong function of the Reynolds number. This is in accord with the results of Jeng and Tzeng [12] and is expected since Re is directly related to the flow momentum. Closer scrutiny of the presented results demonstrates up to about 63% rise in heat transfer as a consequence of passing from $Re = 400$ to $Re = 800$. This allows one to conclude that the consequence of the Reynolds number is more prominent than that of the pulsation frequency and amplitude. Notice also that, the effect of A on $\langle \overline{Nu} \rangle$ becomes more remarkable as the Reynolds number increases. Heat transfer improvements as a result of

duplication of A are about 3, 6, and 9 percent for the Reynolds numbers of 200, 400, and 800, respectively.

4.3. Effect of the medium porosity

Table 3 is constructed to show the effect of the medium porosity on the time-space-averaged Nusselt number. Here, three values of the porosity (i.e., $\phi = 0.6, 0.7,$ and 0.8) are compared. Clearly, the rise of porosity from 0.7 to 0.8 has increased the Nusselt values up to about 8%. The trend of the Nusselt rise due to increase in the medium porosity has been previously reported by Wong and Saeid [16] and occurs due to reduction in the thickness of thermal boundary layer.

4.4. Effect of the Darcy number

It is interesting to investigate the consequences of the Darcy number on the heat transfer performance of the impinging jet. To this aim, temporal variations of \overline{Nu} for different Darcy numbers are shown in Fig. 8. The figure indicates heat transfer enhancement as a result of increase in the Darcy number. This is expected due to decrease in the frictional resistance of the medium. It is noteworthy that at the smallest Darcy number (i.e., $Da = 10^{-5}$), the results coincide with those of $Da = 10^{-3}$. So, they are omitted from the figure for the sake of brevity.

4.5. Effect of the nanoparticles fraction

Effect of the nanoparticles fraction on the heat

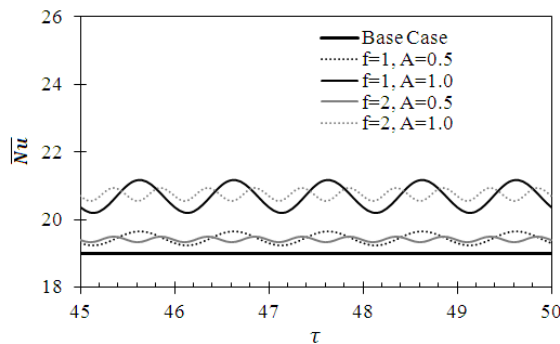


Figure 7: Effects of the pulsation frequency and amplitude on the temporal variations of the space-averaged Nusselt number.

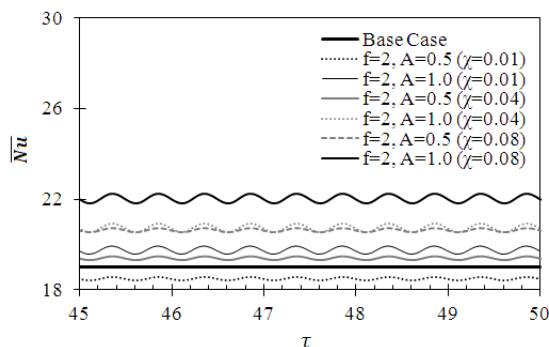


Figure 9: Effect of the nanoparticles fraction on the temporal variations of the space-averaged Nusselt number.

transfer performance is demonstrated in Fig. 9. The figure indicates that increase in the nanoparticles fraction enhances the jet impingement heat transfer. This occurs as a consequence of improvement in thermophysical properties of the nanofluid and is in agreement with previous evidences of Dutta et al. [6], Torshizi and Zahmatkesh [7], and Lam and Prakash [8].

4.6. Effect of geometric ratio

Geometric ratio is defined here as the proportion of the half of the heater length to the jet-to-plate spacing (i.e., L/h). So, increase in L/h can be interpreted as narrowing the distance between the jet and the target surface. Figure 10 shows the effect of this parameter on temporal variations of the space-averaged Nusselt number. Notice that as the geometric ratio increases, the numerical values of \overline{Nu} enhance. The observed behavior is in accord with previous findings of Saeid and Mohamad [15] and Sivasamy et al. [17]. Substantial increase in the pulsation amplitude appears in the highest geometric ratio (i.e., $L/h = 2$). For $L/h = 0.5$, however, the oscillations are roughly disappeared and the Nusselt numbers decrease. This occurs since under this circumstance, the pulsating jet and the target surface are far apart that decreases the velocity magnitudes and the flow pulsation at the proximity of the heater. Closer scrutiny of the figure demonstrates that in the case with $L/h = 0.5$, the heat transfer of the pulsating jet is even weaker than that of the base case (i.e., steady-state jet with $L/h = 1$).

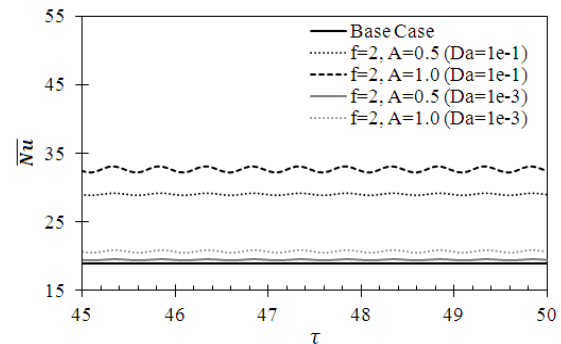


Figure 8: Effect of the Darcy number on the temporal variations of the space-averaged Nusselt number.

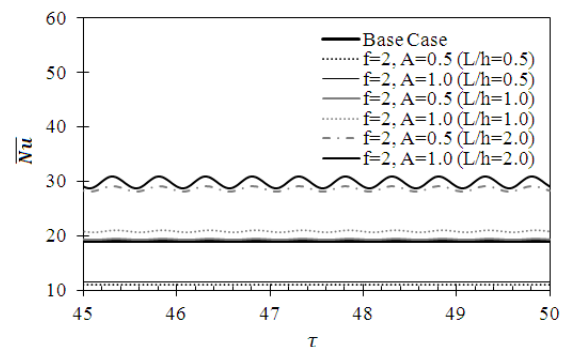


Figure 10: Effect of the geometric ratio on the temporal variations of the space-averaged Nusselt number.

Table 1. Effects of the pulsation frequency and amplitude on the time-space-averaged Nusselt number.

f	A	$\langle \overline{Nu} \rangle$
0	0	19.9
1	0.5	20.3
1	1	21.5
2	0.5	20.3
2	1	21.6

Table 2. Effect of the Reynolds number on the time-space-averaged Nusselt number.

f	A	Re	$\langle \overline{Nu} \rangle$
0	0	400	19.9
2	0.5	200	13.9
2	1	200	14.3
2	0.5	400	20.3
2	1	400	21.6
2	0.5	800	32.0
2	1	800	35.4

Table 3. Effect of the medium porosity on the time-space-averaged Nusselt number.

f	A	ϕ	$\langle \overline{Nu} \rangle$
0	0	0.7	19.9
2	0.5	0.6	19.5
2	1	0.6	20.4
2	0.5	0.7	20.3
2	1	0.7	21.6
2	0.5	0.8	21.5
2	1	0.8	23.3

5. Concluding remarks

Based on the presented results, the following conclusions may be drawn:

1. Superimposing pulsation on the mean flow augments heat transfer as compared to an equivalent steady case.
2. Increase in the pulsation amplitude leads to heat transfer improvement, especially in higher Reynolds numbers.
3. Growth of the pulsation frequency, in spite of changing the oscillation pattern, may not produce noticeable rise in the time-space-averaged Nusselt number.
4. With increase in the Reynolds number, the medium porosity, the Darcy number, the nanoparticles fraction, and the geometric ratio, higher cooling performance can be achieved.

References

- [1] T. Demircan, H. Turkoglu, "The numerical analysis of oscillating rectangular impinging jets". Numerical Heat Transfer, Part A, Vol. 58(2010)146–161.
- [2] S. Alimohammadi, D.B. Murray, T. Persoons, "On the numerical-experimental analysis and scaling of convective

- heat transfer to pulsating impinging jets". International Journal of Thermal Sciences, Vol. 98 (2015)296–311.
- [3] L. Geng, C. Zheng, J. Zhou, "Heat transfer characteristics of impinging jets: The influence of unsteadiness with different waveforms". International Communications in Heat and Mass Transfer, Vol. 66 (2015) 105–113.
- [4] G. Eschmann, A. Kuntze, W. Uffrecht, E. Kaiser, S. Odenbach, "Experimental and numerical investigation of heat transfer coefficients in gaseous impinging jets—First test of a recent sensor concept for steady and unsteady flow". International Journal of Thermal Sciences, Vol. 96 (2015) 290–304.
- [5] S. Ghadi, K. Esmailpour, M. Hosseinalipour, M. Kalantar, "Dynamical study of pulsed impinging jet with time varying heat flux boundary condition". Heat Transfer—Asian Research, Vol. 45 (2016) 85–100.
- [6] E. Torshizi, I. Zahmatkesh, "Comparison between single-phase, two-phase mixture, and Eulerian–Eulerian models for the description of jet impingement of nanofluids". Journal of Applied & Computational Sciences in Mechanics, Vol. 27(2016) 55–70.
- [7] P. Naphon, L. Nakharintr, S. Wiriyasart, "Continuous nanofluids jet impingement heat transfer and flow in a micro-channel heat sink". International Journal of Heat and Mass Transfer, Vol. 126 (2018) 924–932.
- [8] F. Selimefendigil, H.F. Oztop, "Analysis and predictive modeling of nanofluid–jet impingement cooling of an isothermal surface under the influence of a rotating cylinder". International Journal of Heat and Mass Transfer, Vol. 121 (2018) 233–245.
- [9] F. Selimefendigil, H.F. Oztop, "Pulsating nanofluids jet impingement cooling of a heated horizontal surface". International Journal of Heat and Mass Transfer, Vol. 69 (2014) 54–65.
- [10] S.R. Kumar, "The effect of the couple stress fluid flow on MHD peristaltic motion with uniform porous medium in the presence of slip effect". Jordan Journal of Mechanical and Industrial Engineering, Vol. 9 (2015) 269–278.
- [11] K. Singh, M. Kumar, "The effect of chemical reaction and double stratification on MHD free convection in a micropolar fluid with heat generation and Ohmic heating". Jordan Journal of Mechanical and Industrial Engineering, Vol. 9 (2015) 279–288.
- [12] T.M. Jeng, S.C. Tzeng, "Numerical study of confined slot jet impinging on porous metallic foam heat sink". International Journal of Heat and Mass Transfer, Vol. 48 (2005) 4685–4694.
- [13] D.R. Graminho, M.J.S. de Lemos, "Laminar confined impinging jet into a porous layer". Numerical Heat Transfer, Part A, Vol. 54 (2008) 151–177.
- [14] M.J.S. de Lemos, C. Fischer, "Thermal analysis of an impinging jet on a plate with and without a porous layer". Numerical Heat Transfer, Part A, Vol. 54 (2008) 1022–1041.
- [15] N.H. Saeid, A.A. Mohamad, "Jet impingement cooling of a horizontal surface in a confined porous medium: Mixed convection regime". International Journal of Heat and Mass Transfer, Vol. 49 (2006)3906–3913.
- [16] K.C. Wong, N.H. Saeid, "Numerical study of mixed convection on jet impingement cooling in a horizontal porous layer using Brinkman–extended Darcy model". International Journal of Thermal Sciences, Vol. 48 (2009) pp. 96–104.
- [17] A. Sivasamy, V. Selladurai, P.R. Kanna, "Mixed convection on jet impingement cooling of a constant heat flux horizontal porous layer". International Journal of Thermal Sciences, Vol. 49 (2010) pp. 1238–1246.
- [18] N.H. Saeid, "Mixed convection jet impingement cooling of a rectangular solid heat source immersed in a porous layer". Journal of Porous Media, Vol. 18 (2015)pp. 401–413.

- [19] P.A.K. Lam, K.A.P. Prakash, "A numerical investigation of heat transfer and entropy generation during jet impingement cooling of protruding heat sources without and with porous medium". *Energy Conversion & Management*, Vol. 89 (2015) pp. 626–643.
- [20] B. Buonomo, G. Lauriat, O. Manca, S. Nardini, "Numerical investigation on laminar slot-jet impingement in a confined porous medium in local thermal non-equilibrium". *International Journal of Heat and Mass Transfer*, Vol. 98 (2016) pp. 484–492.
- [21] I. Zahmatkesh, S.A. Naghedifar, "Oscillatory mixed convection in the jet impingement cooling of a horizontal surface immersed in a nanofluid-saturated porous medium". *Numerical Heat Transfer, Part A*, Vol. 72 (2017) 401–416.
- [22] S.K. Chinige, N. Ghanta, A. Pattamatta, "Multiobjective optimization study of jet impingement heat transfer through a porous passage configuration". *Numerical Heat Transfer, Part A*, Vol. 73 (2018) 446–465.
- [23] I. Zahmatkesh, "On the suitability of volume-averaging approximation for the description of thermal expansion coefficient of nanofluids". *Proceedings of the Institution of Mechanical Engineering, Part C: Journal of Mechanical Engineering Science*, Vol. 229 (2015) pp. 2835–2841.
- [24] H.C. Brinkman, "The viscosity of concentrated suspensions and solutions". *Journal of Chemical Physics*, Vol. 20 (1952) pp. 571–581.
- [25] J.C. Maxwell-Garnett, "Colours in metal glasses and in metallic films". *Philosophical Transactions of the Royal Society of London, Series A*, Vol. 203 (1904) 385–420.
- [26] Nield DA, Bejan A. *Convection in porous media*. 4th ed. New York; Springer-Verlag, 2013.
- [27] I. Zahmatkesh, "On the importance of thermal boundary conditions in heat transfer and entropy generation for natural convection inside a porous enclosure". *International Journal of Thermal Sciences*, Vol. 47 (2008) 339–346.
- [28] I. Zahmatkesh, "Effect of a thin fin on natural convection heat transfer in a thermally stratified porous layer". *Emirates Journal for Engineering Research*, Vol. 19 (2014) 57–64.
- [29] I. Zahmatkesh, "Heatline visualization for buoyancy-driven flow inside a nanofluid-saturated porous enclosure". *Jordan Journal of Mechanical and Industrial Engineering*, Vol. 9 (2015) 149–157.
- [30] G.C. Bourantas, E.D. Skouras, V.C. Loukopoulos, V.N. Burganos, "Heat transfer and natural convection of nanofluids in porous media". *European Journal of Mechanics B/Fluids*, Vol. 43 (2014) 45–56.

Design Approach of Shell and Tube Vaporizer for LNG Regasification

Ganesh Prasad^a, Amlan Das^{*b}

^aDesign Engineer, Precision Equipments (Chennai) Pvt. Ltd., Chennai 600096, India,

^bResearch Scholar, Metallurgical and Materials Engineering Department, National Institute of Technology, Rourkela, Odisha, India,

Received OCT 23 2017

Accepted JULY 26 2018

Abstract

Natural Gas as a fossil fuel has been an emerging source of renewable energy in the last decade. It is converted to liquefied form (LNG) by keeping in a cryogenic state and transported via pressure vessels. We have considered the use of shell and tube heat exchanger which is appropriate for high pressure applications. Turbulent heat transfer conditions are utilised in the design calculations. The design of TEMA (BJ21M) type heat exchanger was modelled with the consideration that, tube side fluid is LNG and two different shell side fluids are ethylene and propylene glycol water. Design and comparison was carried out in relevance to cases of with and without twisted tape turbulators. Heat Transfer Research Inc. (HTRI) software was used to perform the thermal design. It was found that heat exchangers with twisted tape turbulators operating with L/D ratio of 18 gave better heat transfer co-efficient on both shell and tube side compared to heat exchangers without turbulators. Further with optimization of tube side parameters and tube length, it was noted that the heat transfer rate increased in both shell and tube side considerably for both the cases of ethylene and propylene glycol water on shell side. For the given design constraints, it was seen that the working of the vaporiser with ethylene glycol water and turbulators in shell side was efficient and better compared to propylene glycol water and turbulators in shell side. The authors have aimed at reducing the space and cost constraints of regasification equipment. The software results are in good agreement with analytical and numerical outputs.

© 2018 Jordan Journal of Mechanical and Industrial Engineering. All rights reserved

Keywords: Thermal design, LNG Regasification, Shell and Tube Heat Exchanger, HTRI, Turbulators.

1. Introduction

Natural gas can be referred as a hydrocarbon gas mixture comprising predominantly of methane, and containing variable extents of other higher alkanes along with minute amounts of carbon dioxide, nitrogen and hydrogen sulphide. It assumes popularity due to its low environmental impact. The low density characteristic makes natural gas challenging for storage and transportation. The feasible way is to liquefy it in a liquefaction plant where it is super cooled to -162°C . This operation leads to a reduction in volume by more than 600 times, which makes it efficiently practical to store and transport. LNG is vaporized for further use at receiving terminals by superheating the high-pressure LNG. The vaporization process is accomplished by means of shell and tube heat exchanger. The liquefaction process eliminates the odour from the gas which necessitates that the gas must be odorized before exiting the vaporizer. Figure 1 depicts a flow diagram of the regasification process. The intention behind selecting a shell and tube heat exchanger is that it can provide enhanced heat transfer, wide variation of pressure and pressure drops,

inexpensive accommodation of thermal stresses, easy cleaning and repair, considerable flexibility concerning materials of construction to manage corrosion and other concerns.

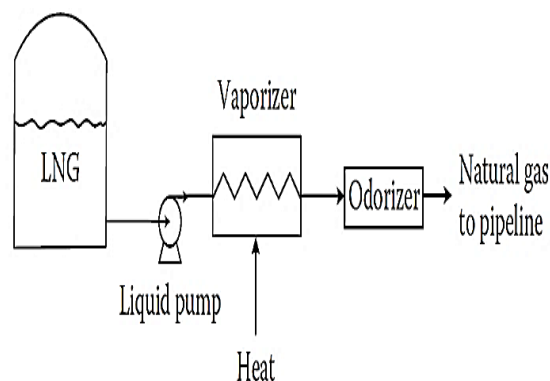


Figure 1. Simplified flow diagram of a typical LNG regasification system.

Allocation of the fluid is done based on the considerations shown in the Table 1.

* Corresponding author e-mail: amlandas08@gmail.com.

Table 1: Parameters for allocation of fluid

PARAMETERS	DESCRIPTION
Corrosion	Tube side is selected to carry more corrosive fluid.
Fouling	Tube side is designated to carry more fouling fluid.
Fluid Temperature	Hotter fluid in the tube side if temperatures are high enough that require special alloys.
Operating Pressure	Tubes are comparatively cheaper than shells for high pressure conditions.
Viscosity	High viscous material in the shell side, if it can provide turbulence. The value of Critical Reynolds number for turbulent flow in the shell ranges around 2300. We can consider transferring the fluid to the tubes if the shell fails to pronounce desired turbulence.
Flow rate	Economical design of the vessel demands that the shell should accommodate the fluids with lowest flow-rate.
Pressure drop	It is necessary that the shell side should put up with the fluid having lowest acceptable pressure drop.

The structure of the heat exchanger is made on the basis of TEMA standards which are shown in Figure 2. The figure represents the different types of stationary head, shell and rear head type. Configuration of the shell and tube heat exchanger assembly is based on different combination of stationary head, shell and rear head types.

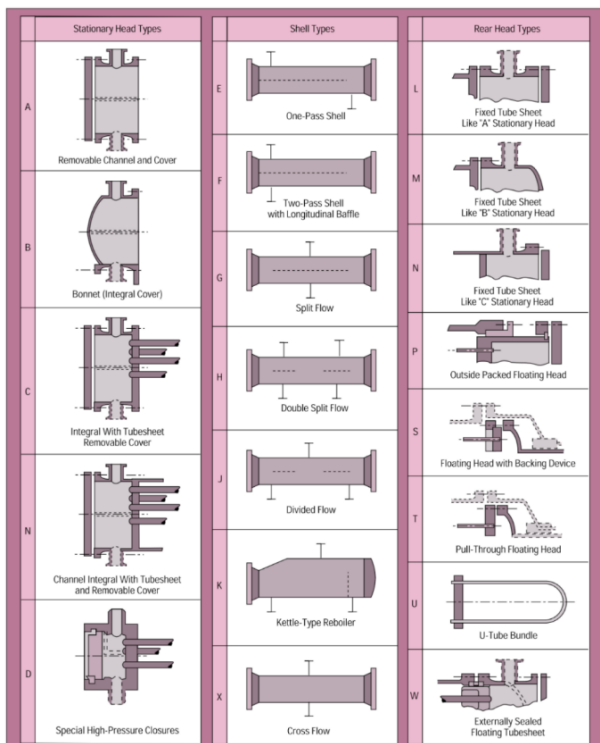


Figure 2: TEMA configurations of Heat Exchangers© 1988 by Tubular Exchanger Manufacturers Association [26]

This paper discusses about the thermal design and optimization of the shell and tube heat exchanger for LNG gasification. Shell and tube heat exchanger with and without turbulators were considered for the present design and study. Figure 3 shows the appearance of the heat exchangers with the incorporation of turbulators.

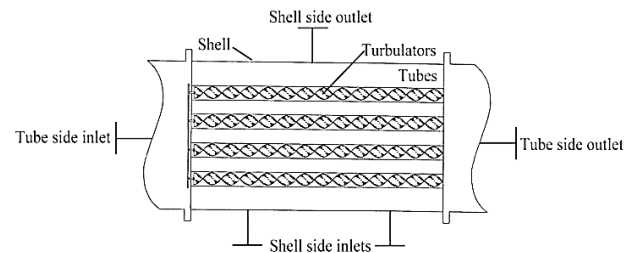


Figure 3: Schematics of Heat Exchanger with Turbulators

2. LITERATURE REVIEW

Shinji Egashira [1] explained clearly the concept of LNG vaporization in his paper. The author showed the different trends in receiving terminal, structures and features of LNG vaporizer for primary and secondary receiving terminals, and different types of vaporizers, such as floating storage re-gasification unit, open Rack Vaporizers, intermediate fluid vaporizers, submerged combustion vaporizers, and intermediate fluid vaporizers with air heat source..etc, along with their features, development of vaporizers with air heat-source and the future development of the LNG vaporizers.

Michelle Michot Foss [4] published a paper, where the author briefly explains about the LNG industry and growing role LNG may play in the energy future. The paper briefly informs us about the LNG safety and security, the role of LNG in developing countries natural Gas supply and demand, and it also addresses details on LNG operations and market place.

Brian Eisentrout, Steve Winter Corn and Barbara Weber [5] presented a paper where a study was conducted on six systems to provide an evaluation of each system in conjunction with the conditions that might influence its viability. The re-gasification systems evaluated in this study are fixed heaters with intermediate fluid, submerged combustion vaporizers, sea water vaporizers, heating towers with intermediate fluids, gas turbine generators with WHR, and steam turbine generator cycle.

Patel et al. [6] mentioned the guidelines necessary to choose a LNG vaporization design appropriate for present day terminals according to the site's climatic conditions. Conventionally, base load re-gasification terminals are categorised into two types: 70% utilities are in the form of Open Rack Vaporizer (ORV), 25% see the use of Submerged Combustion Vaporizer (SCV) and 5% use Intermediate Fluid Vaporizer (IFV). This paper showcases the results of LNG vaporization Screening Study for LNG re-gasification facilities located in warm climate and cold climate regions of the world.

Favi and Olt Livorno [7] gave a clear concept of FSRU's on their paper. The FSRU's are the LNG receiving terminals and the special feature in this type is that they are placed offshore and in event of disaster, loss to public can be evaded. They also gave a detailed outline of construction of the LNG tanks and Terminals and also the measures for pitching and rolling of the hull, as it works on offshore.

Rajiv Mukerjee [8] elucidates on the theory of thermal design which involves the topics on STHE components and their description according to their construction and service. He

provides an overall idea to carry out an optimum design of heat exchangers. The paper also describes the fundamental principles related to thermal design of heat exchangers and effective use of software tools. He also briefly explains the components, classification, design data, configurations, and optimization in design etc.

Yusuf Ali Kara and Ozbilen Guraras [9] composed a computerized approach to achieve a pilot design of shell and tube heat exchanger with single phase fluid both shell and tube side. They stated that the present approach can provide a methodical variation in exchanger parameters. The model defines the overall dimensions of the shell, the tube bundle and optimum heat transfer surface area. They also explained that if minimum shell side pressure drop is considered as a criterion for optimum design then the presence of cold fluid in shell side is advantageous than hot fluid as shell as it causes lower shell side pressure drop and has small heat transfer area requirement. In general, it is advisable to have the stream with lower mass flow rate on shell side because of the baffle spacing.

Andre L.H. Costa, Eduardo M. Queiroz [10] have presented an optimization technique based on the minimization of the thermal surface area for a certain service. The proposed algorithm deals with the concept of tube count table search. It is necessary to consider discrete decision variables for optimisation. They have considered the inclusion of important additional constraints which were overlooked earlier in order to estimate the solution to the design practice. They attained minimum computational costs owing to the use of variable bounds, feasibility tests and fathoming procedures.

Than, Lin and Mon [11] presented the design process for an oil cooler in relevance to shell and tube heat exchanger. Their aim was to achieve a high heat transfer rate without exceeding the allowable pressure drop. They used numerical and software tools to serve their purpose. The spoke of limitations occurring in the program and how to eliminate them.

G. Hima Bharati [12] has gone through different types of vaporizer which is suitable for climatic conditions of India, and also explains the details of different types of vaporizers used by different organizations and which they are going to install on the proposed site.

Cong Dinh, Joseph Cho and Jay Jang [13] proposed novel re-gasification methods that use Multi-Temperature Level (MTL) air heaters to achieve less economy and also to be environment friendly. This paper also describes how LNG can be heated and vaporized using cold Heat Transfer Fluid (HTF).

The various literatures available on the topic suggest that sufficient amount of work has been carried out in relation to Open Rack Vaporizers, Floating storage regasification unit, Submerged combustion Vaporizer, and Intermediate fluid vaporizer. It is observed that regasification techniques through shell and tube heat exchanger have been given inadequate outlook. With the increase in demand of natural gas it is quite essential that better methodologies should be employed to carry out regasification process. Hence it is an area which can be explored and valuable amount of research can be conducted. This project is an initiative to understand and work on the above area so that scientific benefit can be achieved.

3. METHODOLOGY

The design procedure is initiated with an analytical approach by implementing the **Kern method** which is described below:

- **Step 1:** Initially, we have to find out the required thermo-physical properties of hot and cold fluids at the caloric temperature or arithmetic mean temperature. Calculation of these properties at the caloric temperature is essential if the variation of viscosity with temperature is large. The comprehensive approach can be derived from "Process Heat" Transfer by Kern.
- **Step 2:** Perform energy balance and find out the heat duty (Q) of the exchanger.
- **Step 3:** Assume a reasonable value of overall heat transfer coefficient ($U_{o,assm}$). The value of $U_{o,assm}$ with respect to the process hot and cold fluids can be taken from the Heat and Mass Transfer Data hand books.
- **Step 4:** Decide tentative number of shell and tube passes (N_p). Determine the LMTD and the correction factor F_T . F_T normally should be greater than 0.75 for the steady operation of the exchangers. Otherwise it is required to increase the number of passes to obtain higher F_T values.
- **Step 5:** Calculate heat transfer area (A) required:

$$A = \frac{Q}{U_{o,assm}.LMTD.F_T} \quad (1)$$

- **Step 6:** Select tube material, decide the tube diameter ($ID = d_i$, $OD = d_o$), its wall thickness (in terms of BWG or SWG) and tube length (L). Calculate the number of tubes (N_t) required to provide the heat transfer area (A):

$$N_t = \frac{A}{\pi d_o L} \quad (2)$$

$$\text{Calculate tube side fluid velocity, } u = \frac{4m \left(\frac{N_p}{N_t} \right)}{\pi \rho d_i^2} \quad (3)$$

$$\text{If } u < 1 \text{ m/s, fix } N_o p \text{ so that, } Re = \frac{4m \left(\frac{N_p}{N_t} \right)}{\pi d_i \mu} \geq 10^4 \quad (4)$$

where, m, ρ and μ are mass flow rate, density and viscosity of tube side fluid. However, this is subject to allowable pressure drop in the tube side of the heat exchanger.

- **Step 7:** Decide type of shell and tube exchanger (fixed tube sheet, U-tube etc.). Select the tube pitch (P_T), determine inside shell diameter (D_s) that can accommodate the calculated number of tubes (N_t). Use the standard tube counts table for this purpose. Tube counts are available in standard text books.
- **Step 8:** Assign fluid to shell side or tube side. Select the type of baffle (segmental, doughnut etc.), its size (i.e. percentage cut, 25% baffles are widely used), spacing (B) and number. The baffle spacing is usually chosen within 0.2 D_s to D_s .
- **Step 9:** Determine the tube side film heat transfer coefficient (h_i) using the suitable form of Sieder-Tate equation in laminar and turbulent flow regimes. Estimate the shell-side film heat transfer coefficient (h_o) from:

$$Nu = 0.36 (Re)^{0.55} (Pr)^{0.33} (\mu / \mu_w)^{0.14} \quad (5)$$

$$h_o = (Nu \times K) / De \quad (6)$$

You may consider, $\frac{\mu}{\mu_w} = 1.0$

Select the outside tube (shell side) dirt factor (R_{do}) and inside tube (tube side) dirt factor (R_{di}). Calculate overall heat transfer coefficient ($U_{o,cal}$) based on the outside tube area (you may neglect the tube-wall resistance) including dirt factors:

$$U_{o,cal} = \left[\frac{1}{h} + R_{do} + \frac{A_o}{A_i} \left(\frac{d_o - d_i}{2k_w} \right) + \frac{A_o}{A_i} \left(\frac{1}{h_i} \right) + \frac{A_o}{A_i} R_{di} \right]^{-1} \quad (7)$$

- **Step 10:** If, $0 < \frac{U_{o,cal} - U_{o,assm}}{U_{o,assm}} < 30\%$, go the next **step 11**. Otherwise go to **step 5**, calculate heat transfer area (A) required using $U_{o,cal}$ and repeat the calculations starting

from step 5. If the calculated shell side heat transfer coefficient (h_o) is too low, assume closer baffle spacing (B) close to 0.2 Ds and recalculate shell side heat transfer coefficient. However, this is subject to allowable pressure drop across the heat exchanger.

- **Step 11:** Calculate % overdesign. Overdesign represents extra surface area provided beyond that required to compensate for fouling. Typical value of 10% or less is acceptable.

$$\% \text{ Overdesign} = \frac{A - A_{\text{reqd}}}{A_{\text{reqd}}} \times 100 \quad (8)$$

A = design area of heat transfer in the exchanger; A_{reqd} = required heat transfer area.

- **Step 12:** Calculate the tube-side pressure drop (ΔP_T): (i) pressure drop in the straight section of the tube (frictional loss) (ΔP_f) and (ii) return loss (ΔP_{rt}) due to change of direction of fluid in a “multi-pass exchanger”.

$$\text{Total tube side pressure drop: } \Delta P_T = \Delta P_f + \Delta P_{rt} \quad (9)$$

- **Step 13:** Calculate shell side pressure drop (ΔP_S): (i) pressure drop for flow across the tube bundle (frictional loss) (ΔP_s) and (ii) return loss (ΔP_{rs}) due to change of direction of fluid.

$$\text{Total shell side pressure drop: } \Delta P_S = \Delta P_s + \Delta P_{rs} \quad (10)$$

If the tube-side pressure drop exceeds the allowable pressure drop for the process system, decrease the number of tube passes or increase number of tubes per pass. Go back to **step 6** and repeat the calculations steps. If the shell-side pressure drop exceeds the allowable pressure drop, go back to **step 7** and repeat the calculations steps.

The thermal design of shell and tube heat exchanger for LNG re-gasification is carried out using Heat Transfer Research Inc. (HTRI) software. Based upon the design requirement as shown below, shell and tube heat exchanger with two inlets and one outlet on shell side and single tube pass (BJ21M) was designed as per TEMA standard which is shown in Figure 4. Design requirement involves:

- Maximum length of heat exchanger should not exceed 15 meters.
- Mounting of the vaporizer should be vertical.
- Two inlets and one outlet should be on shell side.
- Heat exchanger tube side should have single pass and
- Maximum weight of heat exchanger should not exceed 60,000 kgs.

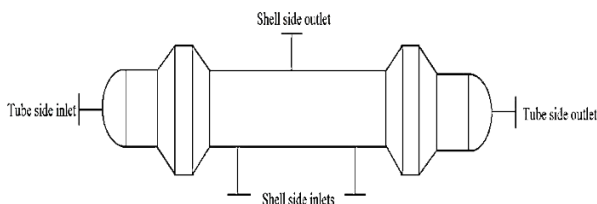


Figure 4: TEMA BJ21M Heat Exchanger with One Tube Pass© 1988 by Tubular Exchanger Manufacturers Association [26]

Design pressure of a heat exchanger is the gage pressure at the top of the vessel. This pressure is used to determine the minimum wall thickness of the various pressure parts. The IS: 4503 specifies that the design pressure should at least 5% greater than the maximum allowable working pressure. Usually a 10% higher value is used. The design temperature is used to determine the minimum wall thickness of various parts of the exchanger for a specified design pressure. It is normally 10°C greater than the maximum allowable temperature. All materials

used construction of shell and heat exchangers for pressure parts must have the appropriate specification as given in IS: 4503 Appendix C. The materials of construction should be compatible with process fluids and others parts of materials and should be cost effective.

Based on design requirements, the working methodology involves assessment of input parameters which are suitably given to the software to initiate processing as given in Table 2.

Table 2: Input Parameter Datasheet

LNG VAPORIZER DATA SHEET					
		SHELL SIDE		TUBE SIDE	
		INLET	OUTLET	INLET	OUTLET
Fluid Name		WATER ETHLENE GLYCOL/WATER PROPYLENE GLYCOL		LNG	
Total Fluid	kg/hr.	1439648	1439648	109664	109664
Total Liquid	kg/hr.	1439648	1439648	109664	-
Total Vapour	kg/hr.	-	-	-	109664
Temperature	°c	16	2	-150	6
Inlet Pressure	bar	1.5	-	84.6	-
Allow. Pressure Drop	bar	0.7		2	
Design Pressure	bar	10		145	
Design Temperature	°c	65		65	
Fouling Factor	m ² c/w	0.00035		0.00018	
Heat Exchanged	kw	20.142			
Material of Construction		Stainless Steel			

The nominal diameter (outside diameter in millimetres rounded is to the nearest integer) of the heat exchanger is specified in IS: 2844-1964 in case of shells manufactured from flat sheet. The following diameters (in mm) should be preferably used in the case of cylindrical pipe shell: 159, 219, 267, 324, 368, 419, 457, 508, 558.8, 609.6, 660.4, 711.2, 762, 812.8, 863.6, 914.4 and 1016. The minimum shell thickness should be decided in compliance with the nominal shell diameter including the corrosion allowance as specified by IS: 4503.

The software yields corresponding output values, which help us in generalizing the design. Optimization was carried out by iterative process till the obtained design suits the given requirements and process. Further the design process was carried out using turbulators as tube inserts for increasing the heat transfer rate in both shell and tube side operating fluids with an L/D ratio of 18 thus increasing the performance of the complete heat exchanger system. A comparative study between shell side operating fluid as ethylene glycol water and out which gives us an initial design of the vaporizer. It was found

that the initial design did not fulfil the design requirements, hence continuous iteration process in HTRI software was carried out using the initial values until a satisfactory optimum design of the shell and tube heat exchanger is made to give maximum heat transfer rate on both shell and tube side. The analytical results were validated with the results obtained from HTRI software. Propylene glycol water was carried out for both the cases of with and without turbulators. The HTRI software was operated in Design mode and the above values (Table 1) were filled in respective areas. Table 3 contains the values which are required to be checked in outputs.

Table 3: Parameters to be checked in outputs

Sl. No.	Properties	Units	Range
1	Over Design	%	6 to 8
2	Pressure Drop Liquids (Shell Side , Tube Side)	kg/cm ²	< 0.7
3	Pressure Drop High Viscous Liquid (Shell Side , Tube Side)	kg/cm ²	> 0.7
4	Pressure Drop Gas side (Shell Side , Tube Side)	kg/cm ²	0.05 to 0.2
5	Tube Velocity	m/s	1 to 3
6	Baffle Cut Single Segmental	%	15 to 45
7	Baffle Cut Double Segmental	%	25-35
8	Baffle Spacing	mm	shell id/5 to shell id
9	A Stream Flow Fraction On Shell Side	%	< 10
10	B Stream Flow Fraction On Shell Side	%	> 40
11	C Stream Flow Fraction On Shell Side	%	< 10
12	E Stream Flow Fraction On Shell Side	%	< 15
13	F Stream Flow Fraction On Shell Side	%	< 10
14	Rho V2 Shell Side (Inlet , Outlet)	kg/m s ²	< 4500
15	Rho V2 Tube Side (Inlet , Outlet)	kg/m s ²	< 8938
16	Rho V2 Bundle (Entry , Exit)	kg/m s ²	< 5953
17	Ratio Of Cross Velocity To Window Velocity Ntiw (NoTubes In Window) Baffles	≤ 3	
18	Ratio Of Cross Velocity To Window Velocity (Others)	1 to 1.2	
19	Bundle Weight	kg	≤ 20000
20	Bundle Dia	mm	≤ 1500
21	Tube Length	m	4 to 12

The selection of material is done according to the ASME standards (ASME Section VIII, Div. 1 & 2). The ASME

standard offers material sustainability for different temperatures and pressures. For this case, we selected stainless steel, because it can withstand the temperature and pressure constraints and it is comparatively cheaper. Once again the program is executed and the output values are checked for small variations. The parameters are re-iterated till optimum values are obtained.

4. RESULTS AND DISCUSSION

The design of Shell and Tube Vaporizer is attempted through manual process by implementing D. Q. Kern Method. The solution converges after 3 iterations. This study contains the output of final iteration.

4.1. Given data:

Hot fluid inlet temperature (T_1) = 16°C
 Hot fluid outlet temperature (T_2) = 2°C
 Cold fluid inlet temperature (t_1) = -150°C
 Cold fluid outlet temperature (t_2) = 6°C
 Fouling factor of hot fluid (R_h) = 0.00035 (for ethylene glycol water)
 Fouling factor of cold fluid (R_c) = 0.00018 (for LNG)
 P_{inlet} (for hot fluid) = 1.5 bar
 P_{inlet} (for cold fluid) = 84.5 bar
 Δp_{max} (for hot fluid) = 0.7 bar
 Δp_{max} (for cold fluid) = 2 bar
 Mass flow rate of hot fluid (m_h) = 66.66 kg/s
 Mass flow rate of cold fluid (m_c) = 10.154 kg/s

4.1.1. LMTD Calculation

ΔT_{lmtd} = 43.38°C
 R = 0.08974
 S = 0.93975
 F_T = 0.93

4.1.2. Energy Balance

Assuming no heat loss to the surroundings,
 $Q_h = m_h \times C_p \times \Delta T = 3353.466$ kW

4.1.3. Calculation of heat transfer area and tube numbers

The iteration is started assuming 1 shell and 1 tube pass shell and tube exchanger with following dimensions and considerations.

Fixed tube sheet
 19.05 mm OD tubes (d_o) on 25.4 mm square pitch (P_T)
 Outer diameter of tube = 19.05 mm
 Tube length (L_t) = 8534 mm
 Tube ID (d_i) = 14.85 mm
 Fluid arrangement = LNG is placed in tube side.

Assuming overall heat transfer coefficient value as $U_{o,assm} = 217$ W/m²°C

$A = 382.1202$ m²
 $N_t = 1502.3$

The next standard number of tubes is 1560 and corresponding shell ID is 1.16 m

4.1.4. Calculation of Heat transfer coefficient of Shell side and Tube side

$A_s = 0.0783$ m²
 $G_s = 851.3410$ kg/m²-s
 $D_e = 0.0241$ m
 $R_c = 7404.6$

$P_r = 22.3452$
 $N_u = 155.3411$
 $h_o = 2.8719 \text{ W/m}^2\text{C}$

In a similar way we have to find out tube side Heat Transfer Coefficient,

$A_{tp} = 0.2702\text{m}^2$
 $G_s = 37.5811 \text{ kg/m}^2\text{-s}$
 $R_e = 4493.4$
 $P_r = 2.117$
 $h_{o,i} = 334.6041 \text{ W/m}^2\text{C}$

Similarly for vapour, $h_{o,v} = 319.9942 \text{ W/m}^2\text{C}$

We have to calculate 2 phase heat transfer coefficient using Kandlikar correlation.

$h_{TP} = 443.1122 \text{ W/m}^2\text{C}$
 $h_i = 365.9035 \text{ W/m}^2\text{C}$

4.1.5. Overall Heat transfer coefficient calculation

$U_{o,cal} = 217.7135 \text{ W/m}^2\text{C}$

The above results bear similar results when run through MATLAB program. Figure 5 depicts a small part of the MATLAB program used for the calculations.

```
% program for Design of SNT Vaporizer by Kern Method%
clc;
fprintf('Given Data ');
Mh = input('Enter the hot fluid mass flow rate in kg/s: ');
Mc = input('Enter the cold fluid mass flow rate in kg/s: '); % mass flow rate in kg/s
th1 = input('Enter the hot fluid inlet temperature in degrees: '); % in degrees
th0 = input('Enter the hot fluid outlet temperature in degrees: '); % in degrees
tc1 = input('Enter the cold fluid inlet temperature in degrees: '); % in degrees
tc0 = input('Enter the cold fluid outlet temperature in degrees: '); % in degrees
rfh = 0.00035 % Fouling resistance of hot fluid in m^2/kw
rfc = 0.00018 % Fouling resistance of cold fluid in m^2/kw
Np = 1 % No of passes
RhoH = 1064.5 % Density of hot fluid in kg/m^3
RhoC = 463.47 % Density of cold fluid at inlet in kg/m^3
RhoCV = 99.925 % Density of cold fluid at outlet in kg/m^3
Vish = 0.0027675 % Viscosity of hot fluid in kg/m-s
ViscL = 0.0001242 % Viscosity in cold fluid inlet in kg/m-s
ViscV = 0.0000136 % Viscosity in cold fluid outlet in kg/m-s
Cph = 3593 % Specific heat of hot fluid in J/kg-C
Cpcl = 2945.6 % Specific heat of cold fluid inlet in J/kg-C
Cpcv = 3437.1 % Specific heat of cold fluid outlet in J/kg-C
Kh = 0.445 % Thermal conductivity of hot fluid in W/m-C
Kcl = 0.1728 % Thermal conductivity of cold fluid inlet in W/m-C
Kcv = 0.0431 % Thermal conductivity of cold fluid outlet in W/m-C
Tw1 = (th1-th0)
Tw2 = (tc1-tc0)
Q = Mh*Cph*Tw2
DelT = ((th1-tc1)-(tc0-th0))/log((th1-tc1)/(tc0-th0))
Uas = input('Enter the value of Assumed Overall Heat Transfer Coefficient: ');
```

Figure 5: MATLAB Code for Kern Method

Figure 6 shows the results obtained from HTRI software after several iterations carried out to optimize the performance of the heat exchanger. The values obtained includes shell inner diameter (ID), number of tubes, tube outer diameter (OD), thickness, pitch and length to obtain maximum heat transfer from the heat exchanger. The maximum heat transfer rate in both the shell and tube side are also obtained from the HTRI software result for the optimized design as mentioned earlier.

Ethylene Glycol Water As Shell Side Fluid (Case Type 1)									
Description	Shell ID (Mm)	No. Of Tubes	Tube OD (mm)	Tube Thickness (mm)	Tube Pitch (mm)	Tube Length (mm)	Tube Layout Angle	Shell Side h (w/m2k)	Tube Side h (w/m2k)
Without Turbulators	1200	1640	19.05	2.11	25.4	8534	90°	2324.5	350.61
With Turbulators	1100	1380	19.05	2.11	25.4	7315	90°	2585.6	711.83

Propylene Glycol Water As Shell Side Fluid (Case Type 2)									
Description	Shell ID (Mm)	No. Of Tubes	Tube OD (mm)	Tube Thickness (mm)	Tube Pitch (mm)	Tube Length (mm)	Tube Layout Angle	Shell Side h (w/m2k)	Tube Side h (w/m2k)
Without Turbulators	1200	1640	19.05	2.11	25.4	8700	90°	1432.3	356.58
With Turbulators	1100	1380	19.05	2.11	25.4	8000	90°	1524.5	588.9

Figure 6: HTRI results

From Figure 6, it is clear that the heat transfer rate in both shell and tube side is maximum with the usage of turbulators compared to without turbulators for the given design constraints. This is because in the former case, the inlet fluid enters with high pressure and goes out randomly in plain tubes i.e. without turbulators thus resulting in low heat transfer rate. In the case of latter with the use of turbulators, the velocity of the fluid flow gets reduced and creates turbulence so that the heat transfer rate increases thus increasing the efficiency of the heat exchanger. Various comparisons with respect to shell side fluid operation with and without turbulators for the optimization of the results and maximum heat transfer rate are discussed below.

4.2. Comparison of Shell ID:

Figure 7 shows the comparison of shell inner diameter (ID) values obtained from HTRI software between the case type of with and without turbulators. It is notable that the shell ID has been considerably decreased from 1200mm to 1100mm in the case type of with turbulators which is cost effective.

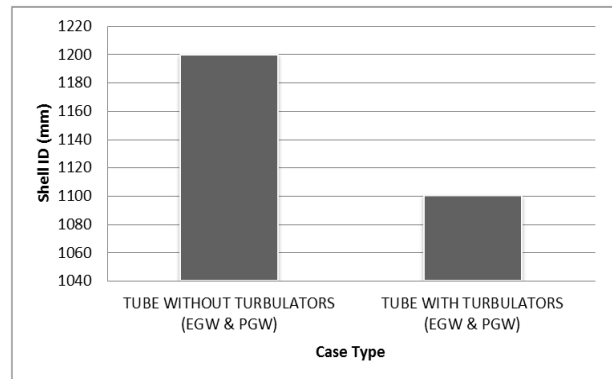


Figure 7: Comparison of shell ID

4.3. Comparison of Tube Length and Number of Tubes:

With the use of turbulators as tube inserts with constant shell and tube outside diameter (OD), pitch and thickness, it is seen that the heat transfer rate on both shell and tube side is considerably increasing. Further the length of the tubes and tube count decrease substantially even for high heat transfer rate in both shell and tube side. The comparison of the tube length and the number of tubes for different case types is shown in Figure 8. Therefore, with the use of turbulators as tube inserts, increase in heat transfer rate and decrease in weight and cost of the heat exchanger is achieved.

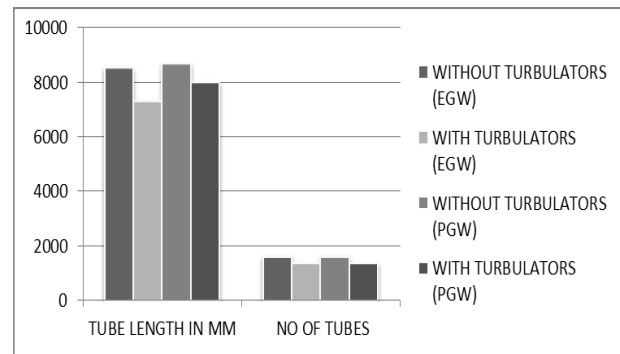


Figure 8: Comparison of Tube length and Number of Tubes

4.4. Comparison of Shell Side Heat Transfer Rate:

Figure 9 shows the comparison of shell side heat transfer rate for both the case types of with and without turbulators using ethylene and propylene glycol water mixture on shell side. It is observed that for both the case types, the heat transfer rate increases with the usage of turbulators with the decrease in tube length and tube count as discussed earlier.

4.5. Comparison of Tube Side Heat Transfer Rate:

The comparison of tube side heat transfer rate with and without turbulators for both ethylene and propylene glycol water case types is shown in Figure 10. As in the case of shell side heat transfer rate, it was found that the heat transfer rate in tube side also increased considerably with the use of turbulators.

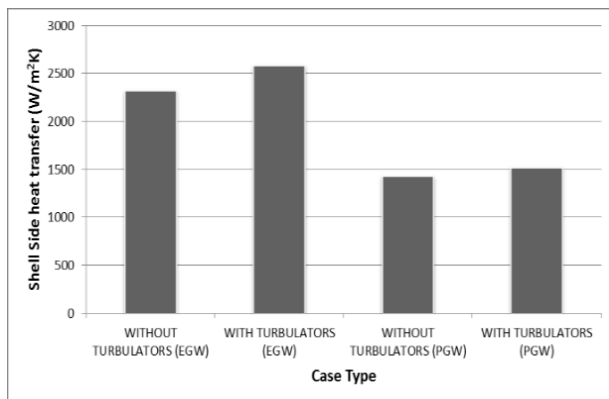


Figure 9: Comparison of Shell Side Heat Transfer Rate

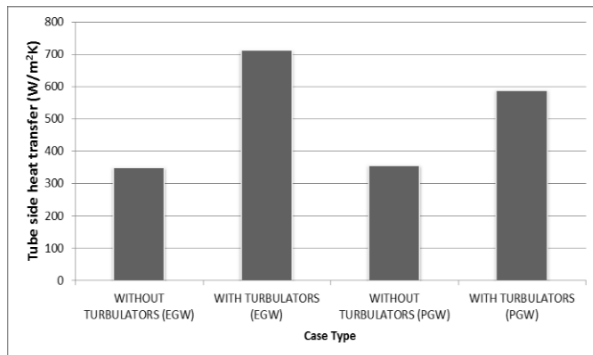


Figure 10: Comparison of Tube Side Heat Transfer Rate

Therefore, from the above comparisons, it is evident that the use of turbulators plays an important role in the heat transfer rate in both shell and tube side. The shell ID has considerably reduced with the use of turbulators. Considering tube length for the case types of ethylene glycol water and propylene glycol water as shell side fluid, the tube length has decreased from 8534 mm to 7315 mm in the former and 8700 mm to 8000 mm with the use of turbulators. The number of tubes has also decreased from 1640 to 1380 in both the case types with the use of turbulators. The shell and tube side heat transfer rate has also increased at a higher rate with the use of turbulators as shown in Table 2 for both the case types. Thus it is also evident that the use of ethylene glycol water as shell side fluid has much better performance compared to the use of propylene glycol water as tube side fluid with and without turbulators.

5. CONCLUSION

Thermal design of TEMA (BJ21M) type shell and tube heat exchanger was carried out for LNG regasification as per given design constraints. LNG is used as a tube side fluid due to its high pressure and ethylene and propylene glycol water is used as a shell side fluid. Design and optimization of this heat exchanger was carried out using HTRI software. Further the case types of without and with turbulators was considered for performance analysis. The major highlights are as follows:

1. The use of turbulators increases the performance of the heat exchanger and decreases the number of tubes and tube length thus making it cost effective.
2. The performance of the heat exchanger with the use of ethylene glycol water was considerably efficient compared to propylene glycol water as shell side fluid.
3. The heat transfer rate at shell and tube side of heat exchanger consisting of ethylene glycol water with turbulators was much better than that of propylene glycol water with turbulators thus increasing the overall performance of the heat exchanger.
4. Thus for the given design constraints, shell and tube heat exchanger operating with ethylene glycol water as shell side fluid with tabulators is much efficient and preferred compared to heat exchanger with propylene glycol water with turbulators.

REFERENCES

- [1] Egashira, S. LNG Vaporizer for LNG Re-gasification Terminal. *Kobelco Tech. Rev.*, 32, 64-69 (2013).
- [2] Kim, H., & Lee, J. Design and Construction of LNG Regasification Vessel. *Proceedings of GASTECH*(2005).
- [3] Kawamoto, H. Natural gas regasification technologies. *Coast Guard Journal of Safety & Security at Sea, Proceedings of the Marine Safety & Security Council*, 65 (4) (2008).
- [4] Michelle Michot Foss. Offshore LNG Terminals. *Centre for Energy Economics*, Texas University (2006).
- [5] Eisentrout, B., Wintercorn, S., & Weber, B. Study focuses on six LNG regasification systems. *LNG journal*, 21-22 (2006)
- [6] Patel, D., Mak, J., Rivera, D., & Anguaco, J. LNG vaporizer selection based on site ambient conditions. *Proceedings of the LNG*, 17, 16-19 (2013).
- [7] Favi. And OLT Livorno,FSRU's: An innovative solution for oil and gas industry. *Convegno Tematici ATI-2012*, Sesto San Giovanni (MI) (2012).
- [8] Mukharji, R. Effective design of shell and tube heat exchanger. *American Institute of Chemical Engineering*(1988).
- [9] Kara, Y. A., & Güraras, Ö. A computer program for designing of shell-and-tube heat exchangers. *Applied Thermal Engineering*, 24(13), 1797-1805 (2004).
- [10] Costa, A. L., & Queiroz, E. M. Design optimization of shell-and-tube heat exchangers. *Applied Thermal Engineering*, 28 (14), 1798-1805 (2008).
- [11] Than, S. T. M., Lin, K. A., & Mon, M. S. Heat exchanger design. *World Academy of Science, Engineering and Technology*, 46, 604-611(2008).
- [12] G. Hima Bharathi. Comparative Study of LNG Vaporizers in India. *International Oil and Gas Conference, Petrotech*, New Delhi (2012).
- [13] Cong Dinh, Joseph Cho, Jay Yang, *Cost Effective LNG Regasification with Multi-Temperature Level Air Heaters*. SK Engineering and Construction co., Texas, USA.
- [14] Kakac, S., Liu, H., & Pramuanjaroenkij, A. *Heat exchangers: selection, rating, and thermal design*. CRC Press (2012).
- [15] Perry, R. H., & Green, D. W. *Perry's chemical engineers' handbook*. McGraw-Hill Professional(1999).

- [16] Kandlikar, S. G. A general correlation for saturated two-phase flow boiling heat transfer inside horizontal and vertical tubes. *ASME J. Heat Transfer*, 112(1), 219-228 (1990).
- [17] Shah, M. M. Chart correlation for saturated boiling heat transfer: equations and further study. *ASHRAE Trans.:(United States)*, 88 (CONF-820112) (1982).
- [18] Bell, K. J., & Mueller, A. C. Condensation Heat Transfer and Condenser Design. *AI Ch. E. Today's Series*(1971).
- [19] Butterworth, D. Condensers and their design. In *Two-Phase Flow Heat Exchangers* Springer Netherlands (pp. 779-828) (1988).
- [20] Breber, G. E. O. R. G. E. Condenser design with pure vapor and mixture of vapors. *Heat Transfer Equipment Design*, 477(1988).
- [21] Indian Standard (IS: 4503-1967): *Specification for Shell and Tube Type Heat Exchangers*, BIS (2007).
- [22] Sinnott, R. K. *Chemical engineering design: SI Edition*. Elsevier (2009).
- [23] Kern, D. Q. *Process heat transfer*. Tata McGraw-Hill Education (1950).
- [24] Dutta, B. K. *Heat transfer: principles and applications*. PHI Learning Pvt. Ltd.(2000).
- [25] Couper, J. R., Penney, W. R., & Fair, J. R. *Chemical process equipment revised 2E: selection and design*. Gulf Professional Publishing (2009).
- [26] R. Brogan, SHELL AND TUBE HEAT EXCHANGERS, in: A-to-Z Guide to Thermodynamics, Heat and Mass Transfer, and Fluids Engineering, Begellhouse, n.d. doi:10.1615/AtoZ.s.shell_and_tube_heat_exchangers.

The Effect of NanoParticle Coating on Anticorrosion Performance of Centrifugal Pump Blades

Somayeh Kouhi, Bahram Ghamari*, Reza Yeganeh

Department of Mechanical Engineering of Biosystems, Faculty of Agriculture, Ilam University, Ilam 69315-516, Iran

Received April 29 2018

Accepted 21 June 2018

Abstract

A common problem in the production of a centrifugal pump is the corrosion caused by fluid communication. The use of nano-coatings is one of the most effective methods for preventing and postponing corrosion. Nano-coatings have a higher thermal expansion coefficient, higher hardness and toughness, and more resistance to corrosion, abrasion and erosion. The purpose of this study was to investigate the effect of TiO₂ nano-particle coating on the construction of corrosion resistant blades of centrifugal pumps. Thin layers of titanium dioxide nano-particles were created in two separate steps on GG25 gray cast iron samples with specific dimensions and characteristics using the sol-gel process and immersion method. After each step, heat treatment was performed to stabilize the nano-coating. The thickness of applied coatings was measured by scanning electron microscopy (SEM). In order to measure the corrosion rate, the samples were exposed to petrochemical wastewater. The corrosion rate was measured by atomic absorption spectrometry method. The experiments were carried out in a factorial arrangement in a completely randomized design with three temperature levels of 40, 50 and 60 °C and four thicknesses. The results showed that coating of titanium dioxide nano-particles increased the corrosion resistance of GG25 gray cast iron. With an increase in temperature from 40 to 60 °C, the corrosion rate of all samples increased by 46.6%. Coated samples with thicknesses of 440-550, 840-970, and 1030-1330nm reduced corrosion rates by 39.1%, 67.8% and 73.6%, respectively.

© 2018 Jordan Journal of Mechanical and Industrial Engineering. All rights reserved

Keywords: *Corrosion; Centrifugal pump; Nano-particle coating; Titanium dioxide.*

1. Introduction

Corrosion causes the destruction of materials through a chemical reaction with the environment. The corrosion phenomenon occurs in all major categories of materials, including metals, ceramics, polymers and composites, but its occurrence in metals is much higher [1-2]. One of the most important issues facing the industry, especially the oil industry and its related industries, is the presence of corrosion problems [3]. Centrifugal pumps are widely used in various industries, including petrochemicals, refineries, military, power plants, and agricultural industries[4]. The most important performance problem of these types of pumps is the appearance of corrosion and abrasion. The major effects of corrosion in the blades and shells of the centrifugal pumps appear in the forms of performance drop, noise, and unwanted vibrations, resulting in a great deal of damage [5].

Studies have shown that corrosion costs and damages are estimated to be about 2-4% of gross national product, of which 21 to 51% is reduced by appropriate methods [6-8]. Nowadays, new technologies with the application of various materials, including metals and alloys, plastics,

tires, ceramics, corrosion protection coatings, and so forth are trying to reduce the corrosion damage. Among the methods of preventing and postponing corrosion, the use of coatings is considered as an effective method [1].

Studies on nano-coatings show that the properties of nano-coated materials are significantly improved in comparison with the conventional coatings [9]. Better appearance, higher chemical resistance, less permeability to corrosive environments, easy surface cleaning, good adhesion of coating, and scratch resistance are among the prominent features of nano-coatings [10]. Among these types of coatings, the use of ceramic nano-structured coatings such as titanium dioxide (TiO₂) has attracted the attention of researchers because of their electrical and thermal properties, oxidation and corrosion and abrasion resistance. Shanghi et al. [11] investigated the corrosion properties of TiO₂ nano-particles applied on the simple carbon steel using a sol-gel process by immersion method. They stated that the quality of the applied coating depends on the speed of the immersion process, the drying time, the heat treatment, and the number of applied layers. In another study, Curkovic et al. [12] examined the corrosion behavior of a thin layer of titanium dioxide nano-particles on steel AISI 304. In order to examine the effect of the

* Corresponding author e-mail: bahramghamary@gmail.com

number of layers on the degree of corrosion, coating was carried out in one and three layers on the surface of the samples. The corrosion properties of the applied coatings were investigated in sodium chloride solution 3% by electrochemical method. Based on the results, with increasing the number of layers of titanium dioxide nano-particles, the amount of cracks and roughness of the surface decreased and caused the potential defects in the surface to be discarded. According to the results of this study, after corrosion tests, it was found that by increasing the number of layers, the corrosion of coating of titanium dioxide nano-particles applied on the surface of AISI 304 steel was reduced. Baghal Nezhad et al. [13] investigated the effect of titanium dioxide nano-particles on the corrosion behavior of nano-composite coatings of chromium, titanium dioxide and pure chromium by potentiodynamic polarization and electrochemical impedance spectroscopy. The results showed that the titanium dioxide nano-particles deposited in the coating increased in corrosion resistance and reduced the corrosion rate of chromium coatings in salt and alkaline solutions. Khaledinia et al. [14] investigated the application of nano-particle coatings in the production of corrosion-resistant machinery components against agricultural pesticides. The results showed that the coating of titanium dioxide on high-carbon steel surface significantly contributes to its corrosion resistance against agricultural pesticides.

The current study aimed at providing anticorrosion blades for centrifugal pumps. Hence, the performance of GG25 gray cast iron coated by TiO₂ nano-particles was investigated using immersion and electron microscopy methods.

2. Materials and Methods

2.1. Samples preparation

In this study, 36 GG25 gray cast iron samples with the dimensions of 30 x 15 x 4mm were used to apply the coating of titanium dioxide nano-particles on. Table 1 shows the weight percent of GG25 gray cast iron components.

Table 1: Specification of gray cast iron GG25

Element	Fe	Cr	S	P	Mn	Si	C
Weight percent	93.63	0.04	0.11	0.12	0.5	2.2	3.4

In order to apply the coating of titanium dioxidenano-particles, the operation of working on metal coupons was done in several steps. First, the coupons were polished with Silicium Carbide and washed with distilled water. Then, they were polished with Aluminum Oxide and washed with distilled water. The coupons were washed by Acetone for 10 minutes before exposure to ultrasonic in degreasing process. Finally, the samples surface was activated by soaking them in Hydrochloric acid for 3 minutes.

2.2. Preparation of titanium dioxide solution

The steps for preparing the titanium dioxide solution are shown in Fig. 1. After preparing the titanium solution and preparing the samples, immersion method was used to apply nano-particle coating on steel surfaces. Three samples were deposited randomly in each step. The difference in thermal expansion coefficient in metal samples and nano-coatings cause cracks and defects in the surface of the samples[11]. To solve this problem, the coating operation was carried out in two separate steps (i.e. primary and secondary steps). Performing the initial coating minimizes the thermal expansion coefficient variation and increases the final quality and properties of metal samples [12]. After the initial coating, the samples were subjected to heat treatment as in Fig. 2.

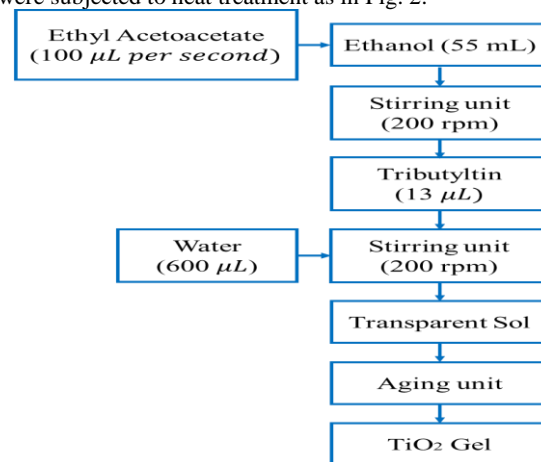


Figure 1: Steps for preparing a titanium dioxide solution.

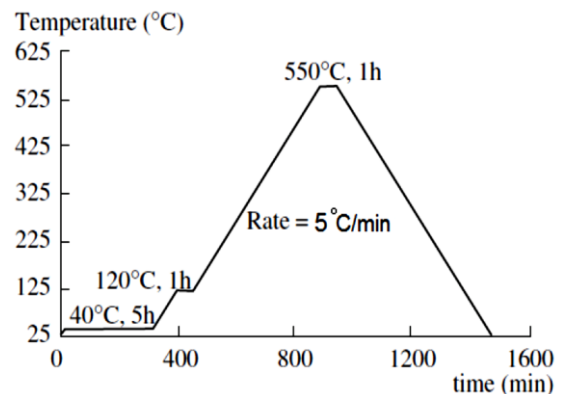


Figure 2: Applied Heat Treatment Cycle

After initial deposition of the thin layer, the samples were washed in distilled water, acetone and ethanol in ultrasonic apparatus and prepared for final coating. To create the final coatings at different thicknesses, the samples were coated in three groups with speeds of 30, 60, 120 mm / min. In each group, the samples were carefully immersed in the solution and after 5 minutes, they were removed at the same initial rate. The coated samples were again subjected to the mentioned heat treatment. The thickness of the coatings was measured using a scanning electron microscope (Fig. 3). The thickness of the coated samples at three speeds of 30, 60 and 120 mm / min was in the range of 440-550, 870-970, and 1350-1030 nm, respectively.

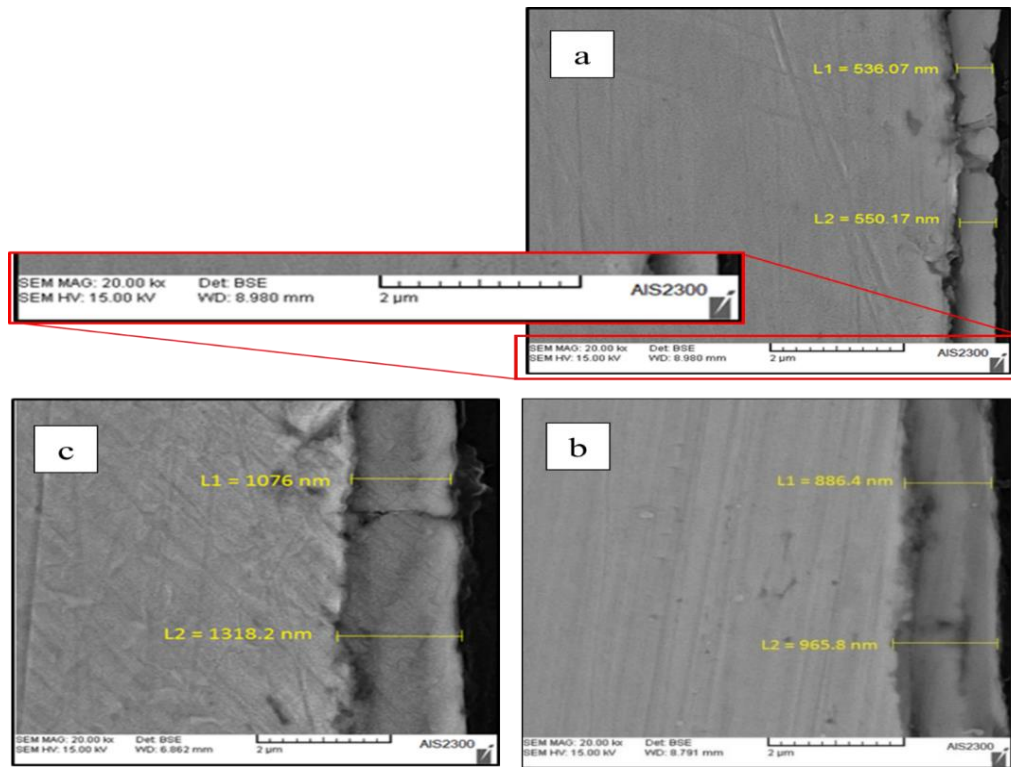


Figure: The thickness of the coatings a) coating at 30 mm / min; (b) coating at 60 mm / min; (c) coating at 120 mm / min.

2.3. Providing Petrochemical Wastewater

Petrochemical wastewater was used to evaluate the corrosion rate of cast iron samples. The wastewater was produced from Ilam Petrochemical Complex. Wastewater characteristics are given in Table 2.

Table 2. The properties of the wastewater.

Parameter	Unit	Value
Conductivity	µS/Cm	1412
Turbidity	NTU	3
P-Alkalinity	ppm	NIL
M-Alkalinity, AS CaCO ₃	ppm	44
Ca-H, AS CaCO ₃	ppm	100
Total Phosphate	ppm	8
O- Phosphate	ppm	5
Organic Phosphate	ppm	3
Zinc	ppm	1.8
Total Hardness	ppm	<1200
Chloride (Cl ⁻)	ppm	...
T.SS	ppm	...
Free chlorine	ppm	0.2-0.5
Totalchlorine	ppm	0.7-1
pH	ppm	7

2.4. Testing corrosion rate

The corrosion rate of samples was measured by atomic absorption spectrometry (AAS). AAS is the measurement of absorption of radiation by free atoms. The total amount of absorption depends on the number of free atoms present and the degree to which the free atoms absorb the

radiation. At the high temperature of the atomic absorption flame, the sample is broken down into atoms and it is the concentration of these atoms that is measured. To measure the corrosion rate of samples, a factorial test was used in a completely randomized design. Variables in these experiments were the thickness of the nano-coating (D) at four levels (i.e. $d_0=0$, $d_1=440-550$, $d_2=840-970$, $d_3=1050-1330$) and corrosive fluid temperature (T) at three levels (i.e. $t_1=40$, $t_2=50$, $t_3=60$).

2.5. Corrosion tests

In order to conduct a corrosion test, three WISD Heater stirrer devices, a closed Erlenmeyer flask and a magnet--- for generating flow in a flame---were used. The heater stirrer device was adjustable (up to 550 °Temperatures), rotary speed (up to 1500 rpm) and time. The GG25 gray cast iron samples were tested in the wastewater by adjusting the device at a specified temperature, rotational speed and time. A specific volume (200 ml for all samples) of petrochemical wastewater was poured inside a closed Erlenmeyer flask and then the cast iron samples were immersed in a solution at a certain height (i.e. 15 mm for all samples). A magnet was used to create fluid flow in the Erlenmeyer. In this way, the magnet rotation inside the fluid caused fluid circulation and rotational movement of the cast iron sample. The rotational speed at all stages was the same and about 1000 rpm. For all thicknesses, each sample was exposed to fluids for 72 hours.

After the prescribed time, the sample was removed from the fluid and the solution was examined by an automated compact spectrometer (novAA 400P, Analytik Jena AG, Germany) to determine the corrosion rate. The results were used to report corrosion rate in ppm scale. The results present the amount of corrosion in ppm. According

to this method, the samples should be soluble. The petrochemical wastewater that was in contact with the cast iron samples was evaluated to determine the absorbed amount of the metal. To obtain the concentration of the examined sample in the spectroscopy, the relationship between the amount of absorbed light by the sample and the concentration of the sample was used. The electrons of the atoms with certain wavelength absorption energy can go to higher levels of energy and come to the excited state for a short time. This amount of energy is different for each atom in comparison with other atoms. When the excited atom returns to the base state, it emits a certain wavelength. By measuring the absorbance of the sample and drawing the calibration curve, the unknown value was determined in the sample. Each test was repeated three times to minimize the test errors. As a whole, 36 tests were performed, and the data were then analyzed.

3. Results and discussion

3.1. Effect of temperature and coating thickness on corrosion rate

The results of ANOVA test for the effect of temperature and thickness of nano coating are given in Table 3. As it can be seen, the effect of temperature, nano coating thickness and interaction of these factors on corrosion rate were significant with a probability of 99%. Significance at a 99% probability level indicates a significant difference in the levels of the factors.

Table 3: Analysis of variance of the effect of temperature and thickness of the nano coating on the corrosion rate (ppm)

Source of variance	Degree of freedom	Sum of squares	Mean squares	F
Temperature	2	12.37	6.18	248.96**
Thickness	3	55.52	18.50	745.00**
Temperature×Thickness	6	0.97	0.16	6.15**
Error Total	24	0.59	0.02	-
Corrected Total	35	69.46	-	-

Considering the significance of the interaction between temperature and coating thickness, it can be concluded that these two factors have not worked independently on their own levels.

3.2. Effect of temperature on corrosion

The Duncan multidimensional test was used to examine and compare the mean of the temperature effect on the corrosion rate (Table 4). According to Table 4, there was a significant difference between corrosion rates of different temperatures. The maximum and minimum corrosion rates were at 60 and 40 °C, respectively. With an increase in temperature from 40 to 60 °C, the mean corrosion rate increased from 1.64 to 3.7 ppm. As the temperature rises, the speed of reactions and interactions increases, which increases the level of corrosion at the surface of the GG25 gray cast iron samples.

Table 4: Duncan test results of comparing the mean of the temperature effect on the corrosion rate

Temperature (°C)	corrosion rate (ppm)
40	1.64 ^c
50	2.43 ^b
60	3.07 ^a

With increasing temperature from 40 to 60 °C, the corrosion rate increased in all uncoated (d₀) and coated samples with different thickness of d₁, d₂ and d₃ (Fig. 4).

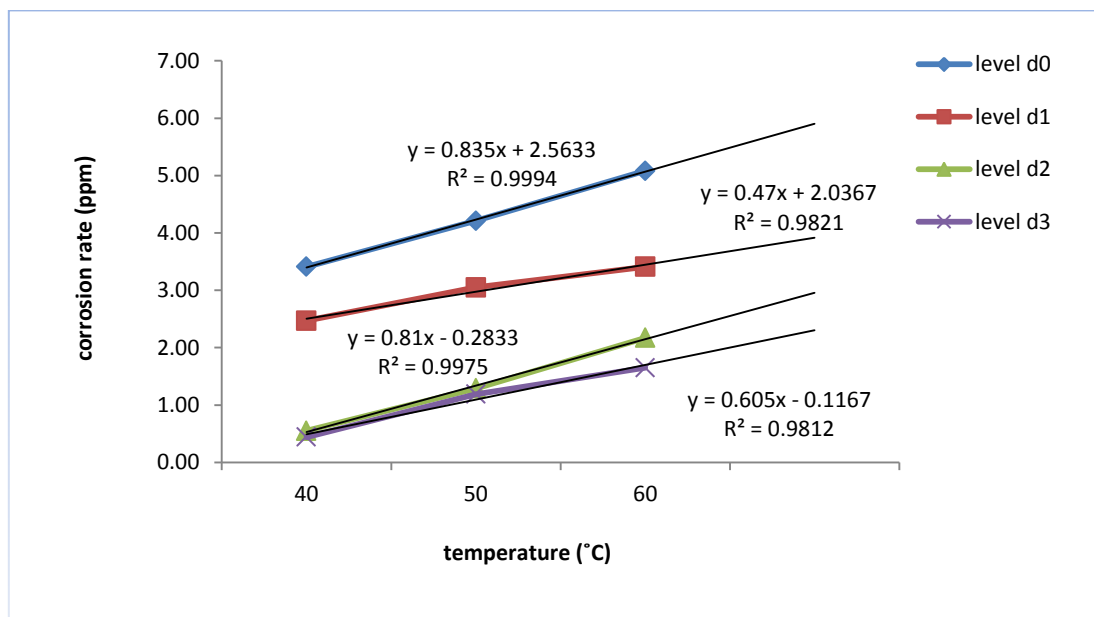


Figure 4: Changes of corrosion rate with different coating thicknesses.

It is noted that the correlation between the corrosion rate and the temperature was linear, so the corrosion could be predicted at an acceptable accuracy at any point outside the measured range. Also, line slope in the graph of the corrosion rate for uncoated samples was greater than the coated ones. This means that the effect of increased temperature on the corrosion rate of the uncoated samples (d0) was greater than that of the coated ones with d1, d2 and d3 thicknesses and uncoated samples tended to be more sensitive to temperature rise. The gentler slope in the coated samples than the uncoated ones indicated that the coating prevented rapid corrosion changes when the temperature rose. Therefore, the corrosion rate in coated samples was more consistent than that in the uncoated ones.

To reduce corrosion in the petrochemical industry and other industries using centrifugal pumps, it is possible to reduce the temperature of the fluid. To compare the thickness effect of TiO₂ nano-particle coating on the corrosion rate, Duncan test was used and the results were shown in Table 5.

According to the results of Duncan's classification test (Table 5), there was a significant difference between the corrosion values of four different coating thicknesses. The results showed that the corrosion rate in all samples was significantly different from each other. The results also showed that the corrosion resistance of samples coated with nano-particles of titanium dioxide was higher than that of uncoated samples against reacting with petrochemical wastewater. According to Table 5, the corrosion rate was decreasing with increasing coating thickness from 550-440 to 1350- 1050 nm. Corrosion rate in the thickness of d₃ was 3.8, 2.72, and 1.22 times less than that for d₀, d₁, and d₂, respectively.

Table 5. The results of the Duncan's test to compare the mean effect of coating thickness on corrosion rate (ppm)

coating thickness(nm)	corrosion rate (ppm)
d ₀	4.13 ^a
d ₁	2.97 ^b
d ₂	1.33 ^c
d ₃	1.9 ^d

The variation in the corrosion rate in proportion to the thickness of nano-coating at various temperatures was shown in Figures 5 and 6. According to Fig. 5, the corrosion rate of the uncoated samples (d₀) was higher than other thicknesses. By applying coatings of titanium dioxide nano-particles in different thicknesses, the corrosion rate was strongly reduced at all temperatures as well as with increasing in thickness of coating, the corrosion rate in all samples decreased.

At first, the slope of the line at different temperatures is very high which then decreases (Fig. 5). This shows that the coating of titanium dioxide nano-particles acts as a barrier to develop corrosion at the surface of the samples, and causes a lower corrosion rate [16]. The coating of TiO₂ nano-particles applied by the sol-gel method had a good adhesion, and by reducing the surface defects of the field on a molecular scale by creating a smooth (e.g. low roughness on a nanometer scale), non-cracking, water-resistant and abrasion-resistant surface increased the resistance to corrosion. Other researchers reported the same results for using Titanium Dioxide nano-coatings [11,12, 14-17]. By increasing the thickness of the nano-particle coating to a range of 1050-1330 nm, the corrosion rate significantly decreased. The coatings produced in two immersion stages with a 120 mm / min deposition rate had the highest corrosion resistance and the best performance. This was observed by Shanaghi et al. [18] in using TiO₂ nanostructure coatings on mild steel.

By increasing the coating thickness from 550-440 to 1350-1030 nm, the corrosion rate reduced at different temperatures (Fig. 6). Corrosion rate also increased with increasing degree in the wastewater temperature. In general, the corrosion rate was significantly reduced by increasing the thickness of the coating and reducing the temperature of the wastewater.

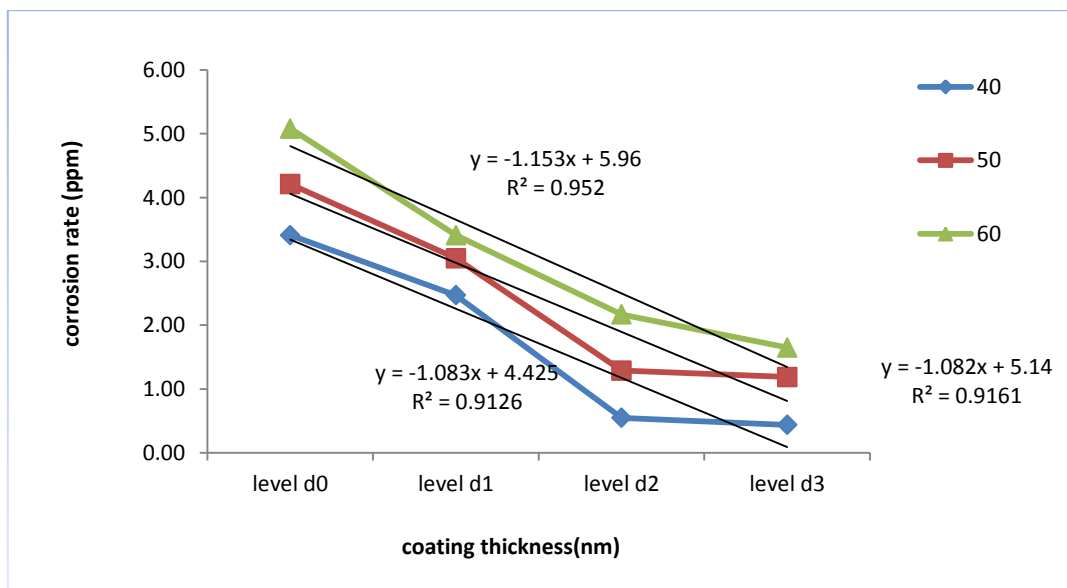


Figure 5: The chart of corrosion rate with coating thickness at different temperatures

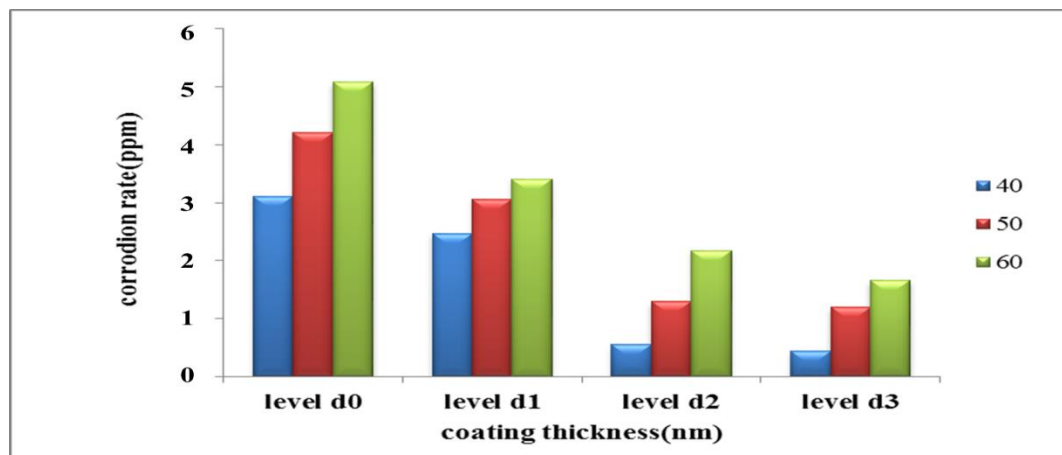


Figure 6: The effect of coating thickness at different temperatures on corrosion

4. Conclusion

In this study, coating of titanium dioxide nano-particles was applied on GG25 gray cast iron using the sol-gel method and in three different thicknesses. The corrosion rate of the coated samples was compared with the uncoated ones at three different temperatures.

By analyzing and investigating the data obtained by atomic absorption spectroscopy and measuring the corrosion rate of all samples, the results are reported as follows:

1. The coating of titanium dioxide nano-particles improved the corrosion resistance of GG25 gray cast iron against reacting with petrochemical wastewater.
2. With an increase in the temperature of the petrochemical wastewater from 40 to 60 °C, the corrosion rate of all samples increased by 46.6%.
3. The samples coated with titanium dioxide nano-particles with thicknesses of 440-550, 840-970, and 1050-1330 nm reduced the corrosion rate by 39.1%, 67.8% and 73.6%, respectively.
4. By increasing the coating thickness, the corrosion rate of all samples decreased. The best performance among the samples in terms of corrosion resistance is from a sample with a thickness of 1050- 1330 nm.

References

- [1]. R. Zamanian. Corrosion and Its Control. Tehran: University of Tehtan. In Persian. 1991.
- [2]. E. Vannan, P. Vizhian, "Corrosion Characteristics of Basalt Short Fiber Reinforced with Al-7075 Metal Matrix Composites". JJMIE, Vol. 9, 2015, 121-128.
- [3]. N. Zubkov, V. Poptsov, S. Vasiliev, "Surface Hardening by Turning without Chip Formation". JJMIE, Vol. 11, 2017, 13-19.
- [4]. M.A. Deyab, S.T. Keera, "Effect of nano-TiO₂ particles size on the corrosion resistance of alkyd coating". Materials Chemistry and Physics, Vol. 146, 2014, 406-411.
- [5]. M. Farzam. Corrosion and Protection of Materials Engineering. Tehran: Yadvareh Ketab. (In Persian). 2011.
- [6]. H. Wang, D. Zuo, G. Chen, G. Sun, X. Li, X. Cheng, "Hot corrosion behaviour of low Al NiCoCrAlY cladded coatings reinforced by nano-particles on a Ni-base super alloy". Corrosion Science, Vol. 52, 2010, 3561-3567.
- [7]. M. Salah, "Laboratory Automotive Suspension Test Rig: Design, Implementation and Integration". JJMIE, Vol. 11, 2017, 67-71.
- [8]. M. Ali, B. Suppiah, Z. Muayaduldeen, "Preparation and Corrosion Behavior of Bronze -40%w Composite". JJMIE, Vol. 10, 2016, 141-147.
- [9]. A. Al Robaidi, "Crystallization behavior of iPP/LLDPE blend filled with nano kaolin particles". JJMIE, Vol. 7, 2013, 35-39.
- [10]. Gh. Shiravand, "Application of Nano Coatings in Aircraft Industry". Journal of Chemical Sciences and Technology, Vol. 22, 2013, 29-33.
- [11]. A. Shanaghi, A. S. Rouhaghdam, S. A. Tabatabaei, M. Shariatpanahi, A. Rastgoo, A. K. Yousefi, M. Samadzadeh, "An experimental investigation of corrosion resistance of mild steel by sol-gel process using TiO₂ nanostructure coating and prediction of optimal parameters". Journal of Nanoengineering and Nanosystems, Vol. 227, 2013, 105-111.
- [12]. L. Curkovic, H. O. Curkovic, S. Salopek, M. M. Renjo, S. Segota, "Enhancement of corrosion protection of AISI 304 stainless steel by nanostructured sol-gel TiO₂ films". Corrosion Science, Vol. 77, 2013, 176-184.
- [13]. M. Baghalnejad, M. Farzad, A. Najafi bergani, "Electrochemical Impedance Spectrometry and Corrosion Function and Corrosion Function of nano-Composite Coatings of Chromium Dioxide Titanium". The First National Conference on Gas Technology and Development, Firoozabad, Iran, 2014.
- [14]. M. Khaledinia, B. Ghamari, M. Roshani, "Application of nano - Particles coating in making of corrosion resistance parts against agricultural pesticides". Iranian Journal of Biosystem Engineering, Vol. 3, 2015, 245-253.
- [15]. N. Barati, M.A.F. Sani, H. Ghasemi, Z. Sadeghian, S.M.M. Mirhoseini, "Preparation of uniform TiO₂ nanostructure film on 316L stainless steel by sol-gel dip coating". Applied Surface Science, Vol. 225, 2009, 8328-8333.
- [16]. M. Ali, S. Falih, "Synthesis and Characterization of Aluminum Composites Materials Reinforced with TiC Nano-Particles". JJMIE, Vol. 8, 2014, 257-264.
- [17]. G. X. Shen, Y. C. Chen, L. Lin, C. J. Lin, D. Scantlebury, "Study on a hydrophobic nano-TiO₂ coating and its properties for corrosion protection of metals". Electrochimica Acta, Vol. 50, No. 25, 2005, 5083-5089.
- [18]. A. Shanaghi, A. R. Sabour, T. Shahrabi, M. Aliofkhaeze, "Corrosion protection of mild steel by applying TiO₂ nanoparticle coating via sol-gel method". Protection of Metals and Physical Chemistry of Surfaces, Vol. 45, 2009, 305-311.

Experimental Study to Investigate the Effect of Dust, Wind Speed and Temperature on the PV Module Performance

Maher Al-Maghalseh^{a,b*}

^aCollege of Engineering, Palestine Polytechnic University, Hebron, Palestine

^bFaculty of Engineering and Environment, Northumbria University, Newcastle, UK

Received Dec 29 2017

Accepted 31 July 2018

Abstract

This paper investigates the environmental effects (temperature, wind speed and dust) on photovoltaic module (mono-crystalline) performance. The degradation of the PV performance owing to an increase of temperature and dust density is investigated. A series of experiments were conducted in order to study the effect of these parameters on the PV performance. First, a test of the PV module at standard test conditions (STC) was analyzed. Then, the effects of temperature, wind speed and several type of dust accumulation on the PV performance were examined. The depositions of red soil, sand and white soil dust were used in the study. I-V characteristics were determined for various intensities of dust. The evolutions of the short circuit current, the open circuit voltage, and the maximum power for the several cases were examined. The experimental results show that the PV voltage and power is affected significantly by pollutant type and deposition level. However, a larger reduction in the PV performance was observed in the case of white soil dust, owing to its smaller particles, than sand or red soil.

© 2018 Jordan Journal of Mechanical and Industrial Engineering. All rights reserved

Keywords: *The PV performance, Dust, Red soil, White dust.*

1. Introduction

Solar energy is one of the most important renewable energy sources on account of its easy availability, cleanness and cheapness. Nowadays a number of solar energy approaches are being pursued and photovoltaic cells are being given more attention by electrical power engineers, owing to rapid development in the world and society. More recent attention has focused on the use of PV power systems on the distribution networks as well as the degradation effects of PV on the distribution system stability, power losses and reliability. Al-Maghalseh [1-5] investigated the differential impact of renewable energy distribution generation on the system performance and stability. PV system performance can be affected by several conditions such as temperature, weather conditions, dust, wind speed. However, There is a large volume of published studies have investigated the effect of dust and climate conditions on the PV performance. Mani and Pillai [6] reviewed the literature from the period to evaluate the impact of dust on PV performance. The research has been conducted into two phases for two time periods. Drawing on an extensive range of sources, the authors identifies the challenges of future research and the appropriate cleaning/maintenance cycle of the PV systems. Batra et al [7], investigate the effects of Badarpur, fly ash, and rice husk on the PV performance. He found that the rice husk has the highest effects on the PV performance.

El-Shobokshy and Hussein[3, 4]carried out both experimental and numerical study in order to investigate the effect of dust on PV performance. The study has shown that the short circuit current was reduced significantly with dust deposition. Further, the finer particles have a greater effect on the PV performance compared to that of courser particle. Kymakis et al.[5] examined the effect of dust deposition on the power losses of a grid connected PV park. The system has a peak power of 171.36 kWp and it indicated that the annual loss is about 5.86% due to the dust deposition. Kaldellis et al.[6]conducted an outdoor experiment to study the impact of temperature and wind speed on the PV performance. It was found that the PV efficiency has reduced by 0.3%-0.45% per the increase of temperature (C). Schwingshackl et al.[7] numerically investigated the effect of wind on the PV Module temperature. Several techniques are investigated, and it was found that the wind cooling effects plays an important role for the power estimation.

The performance of a photovoltaic cell depends on manufacturing technology and the operating conditions under Standard Test Conditions (STC)[8]. The photovoltaic cell of terrestrial solar power modules is tested in order to measure and explain its I-V curve characteristic and to compare the performance of different solar power modules under uniform operating conditions. These performance conditions are at incident sunlight of 1000 W/m², a cell temperature of 25°C (77°F) and an AM (air mass) of 1.5. The air mass determines the radiation

* Corresponding author e-mail: maherm@ppu.edu.

impact and the spectral combination of the light arriving on the earth's surface [8]. With the increasing use of the PV systems, it is vital to know the effects that active meteorological parameters such as humidity, dust, temperature, wind speed have on their efficiency. This paper investigates the effect of temperature and dust on the PV system performance and parameters such as light intensity or irradiation, tracking angle, temperature, air velocity and dust. Through the photovoltaic parameters like open circuit voltage, short circuit current, maximum output power, fill factor and efficiency are generally affected by the above environmental parameters.

A temperature experiment of the PV by Chander et al. [9] studied the effect of cell temperature on the photovoltaic parameters of a monocrystalline silicon solar cell. The experiment was carried out employing a solar cell simulator with varying temperatures in the range of 25–60°C at constant light intensities of 215–515 W/m². The results show that cell temperature has a significant effect on the photo voltaic parameters and controls the quality and performance of the solar cells. The open circuit voltage of the solar cell is highly sensitive to cell temperature. The open circuit voltage, fill factor and maximum output power decrease with an increase in temperature, while short circuit current increases with an increase in temperature. Therefore, the temperature coefficient of the open circuit voltage, fill factor and maximum output is negative, yet positive for the short circuit current. A relative change study of photovoltaic parameters with temperature was also undertaken.

Sulaiman et al. [10] made a study of the effect of dust accumulation on the PV panels. The study used a solar panel (50W) under constant light radiation provided by two spotlights, each giving 500W. An artificial dust of two kinds (dried mud, talcum powder) was used instead of real dust. The dust was spread on a plastic sheet. To measure the dust accumulation on the plastic sheet, a Scanning Electron Microscope (SEM) was used. The power of the solar panel was measured under four conditions: with no plastic sheet, with a clear plastic sheet, with dried mud on the plastic sheet, and with talcum on the plastic sheet. The result showed that the highest peak power occurred when the panel was not covered by a layer of dust or a plastic sheet. If the dust had accumulated on the plastic sheet, the reduction of power generated could be up to 18%. Thus the clean plastic and solar the PV panel without plastic gave the highest efficiency owing to the absence of dust on its surface. Conversely if the dust appeared on the surface of the photovoltaic solar panel it could reduce the system's efficiency by up to 50%.

In this paper, the influence of different values of temperature and the accumulation of dust types on the efficiency of solar the PV panels is assessed by using artificial materials. A constant radiation condition is used by a sun simulator to overcome the variation of the sunlight.

2. Experiment set-up

Basically, the system comprised a multi-crystalline photovoltaic module. This module is a 10W, 21.08V, 0.59A, 1.5 kg and 415×268×22m³ the PV module. The PV module is connected to the sun simulator to control the

radiation by autotransformer. The performances of the PV module are monitored by digital multimeters, temperature sensors and dust sensors. In this research, indoor experiments are conducted to investigate the effect of uniform dust, wind speed and temperature on the PV performance, so the experiments are divided into four sections: (i) The PV module at STC, (ii) the impact of temperature on the PV performance, (iii) the impact of uniform dust on the PV performance, and (iv) the impact of wind speed on the PV module. Fig. 1 shows the experimental block diagram and procedure.

Firstly, in order to determine the impact of the different selected dust (red soil, sand, white soil) on the PV module performance, an experimental procedure was carried out in order to compare the voltage output of the PV module under different dust deposition conditions at constant radiation (1000W/m²) and a temperature of 30°C. The experimental procedure was carried out indoors and at least 30 measurements were recorded within the time period 110s. The experimental analysis was conducted in the Renewable Energy Laboratory located at the Palestine Polytechnic University in Hebron, Palestine. The dust deposition density was measured in mg/m³ by using dust sensor GP2Y1010AU0F. Then different types of dust were monitored by an Arduino controller to record the values on an Excel sheet and draw the curves. The dust was uniformly distributed on the PV surface using a fan. Secondly, to determine the effect of temperature on the PV module, the experimental procedure was carried out indoors at a constant radiation (1000W/m²), varying the value of temperature from 25°C to 55°C, and then taking the mean value of 50 measurements for each value of temperature. In this section, the Arduino microcontroller was connected with the temperature sensor to observe and record its values. In the wind speed effects on the PV experiments, an anemometer was used to measure the value of wind speeds. Also, we used a multispeed fan in order to obtain several wind speed values.

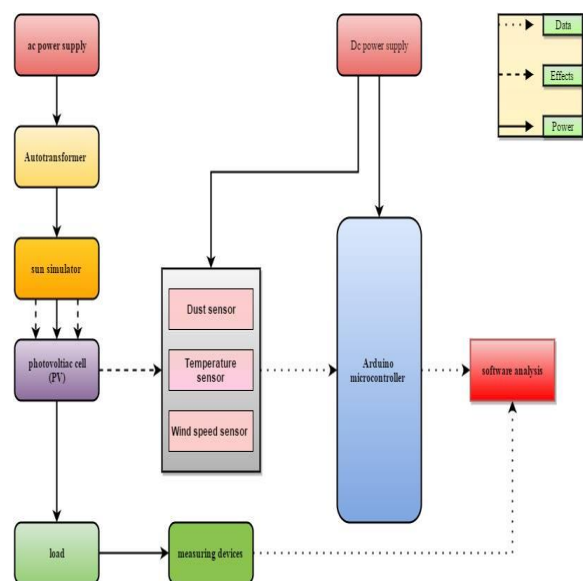


Figure 1: Experiment Block diagram and procedure

3. Results and discussions

3.1. Photovoltaic module at standard test conditions.

Fig. 2 illustrates the I-V and P-V curves for the PV cell under STC conditions (1000W/m², 25°C, A.M 1.5). In this case, the short circuit current (I_{sc}) was 0.6A and open circuit voltage 20.7V. Under STC the maximum power that could be obtained from the PV module was 9.352W and the efficiency was 9.396 %.

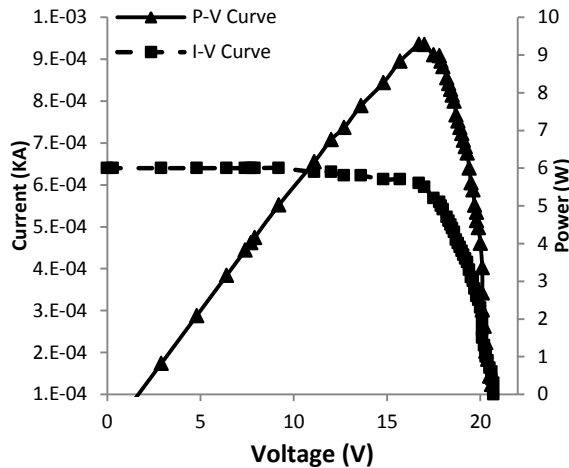


Figure 2: I-V and P-V curves of the PV module at STC.

3.2. The effect of temperature change on the PV module.

In this section, the performance of the PV module at different temperature levels was investigated. The analysis considers the effect of temperature on the open circuit voltage (V_{oc}), the short circuit current (I_{sc}), maximum power and efficiency of the PV module. Figures 3 and 4 illustrate the I-V and P-V curves at different temperatures of the PV. It can be seen that when the temperature of the PV increased to 30, 35, 40, 45, 50 and 55°C, the open circuit voltage (V_{oc}) decreased to 20, 18.9, 18, 17.4, 16.4 and 16.1V respectively. While the short circuit current (I_{sc}) increased slightly to 0.61, 0.62, 0.64, 0.65, 0.66 and 0.67A respectively. In other words, V_{oc} was decreased by 3.89% per 5 °C above 25°C and I_{sc} was increased by 2% per 5°C above 25°C.

The P-V curves of the PV showed that maximum power (P_{Max}) that could be generated from the PV decreased to 9.263, 8.584, 8.208, 7.611, 7.02 and 6.786W, when the temperature of the PV was raised to 30, 35, 40, 45, 50 and 55°C. Also, the efficiency of the PV decreased to 9.263%, 8.584%, 8.208%, 7.611%, 7.02% and 6.786% respectively. From these results it can be concluded that P_{Max} and η were decreased by 5% per 5°C above 25 °C (STC). In case of the temperature of the PV below 25°C, V_{oc} increased to 21 V and I_{sc} was decreased to 0.56 A. The maximum output power (P_{Max}) and the efficiency (η) generated from the PV was decreased to 8.823W and 8.86%, respectively. The results agreed well the previous work of [11-14].

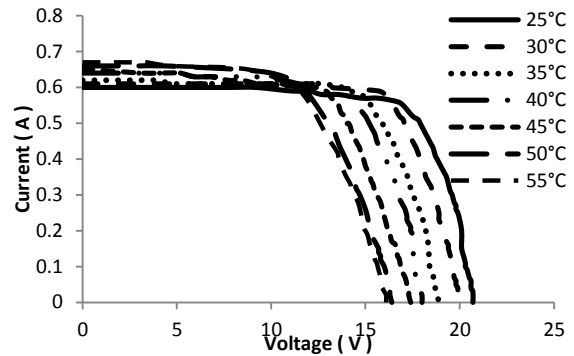


Figure 3: I-V curves of the PV module at different temperature.

The effect of temperature change on maximum output power of the PV module is demonstrated in Fig. 5. From the figure below we can obtain a mathematical expression that describes the relation between P_{Max} and temperature of the PV (T). The P_{Max} of the PV is a function of temperature is drawn below:

$$P_{Max}(T) = -0.09398T + 11.88, \quad T \geq 25^\circ\text{C} \quad (1)$$

$$P_{Max}(T) = 0.092T + 7.029, \quad T \leq 25^\circ\text{C} \quad (2)$$

where: P_{Max} is the maximum output power that can be generated from the PV module (W), and T is the temperature of the PV module (°C).

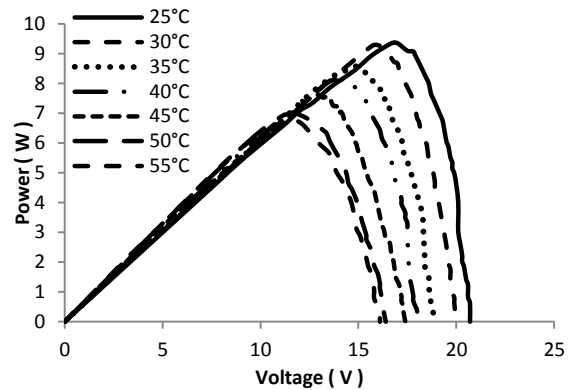


Figure 4: P-V curves of the PV module at different temperature.

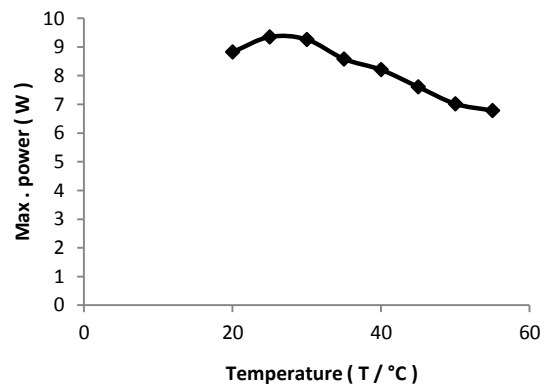


Figure 5: The maximum output power of the PV module at different temperature.

3.3. The effects of dust density on the PV module

In this section, the effect of several types of dust on the PV performance was investigated. Three types of dust were used in the experiment. These were red soil, sand and white soil. It was found that the short circuit current (I_{sc}) was strongly decreased as the dust density increased. Also maximum output power and efficiency decreased significantly as the dust density increased. However, different dust types with different densities did not vary greatly in their effect on the open circuit voltage (V_{oc}).

3.3.1. Effect of red soil dust on the PV module

Figures 6-8 show the effect of red dust on the I-V curve, power, and efficiency of the PV module. The results show that the short circuit current (I_{sc}) was decreased from 0.61 to 0.56, 0.64 and 0.48 A for red dust densities of 25, 30 and 35 mg/m³, respectively, while the open circuit voltage (V_{oc}) was slightly increased to 20.1 and 20.3V for red dust densities of 30 and 35 mg/m³. In other words, I_{sc} was decreased by 2.4% and V_{oc} increased by 0.15% per 5 mg/m³ of red dust density. Furthermore, the P_{Max} of the PV module was decreased as the red dust densities increased. It can be seen that without any dust on the PV module, the maximum power was 9.263W, but where red dust densities were 25, 30 and 35 mg/m³, the maximum power varied between 8.036, 7.56 and 7.26W respectively. It can be concluded that the maximum power of the PV is decreased by 13.24%, 18.38%, and 21.62% for the cases of 25, 30, 35 mg/m³ respectively. In other words, the maximum power of the PV was decreased by 3% per 5 mg/m³ of red dust. Similar observation was made for the effect of red soil density on the PV efficiency (Figure 8). The results agreed well with the results of [2, 15-17].

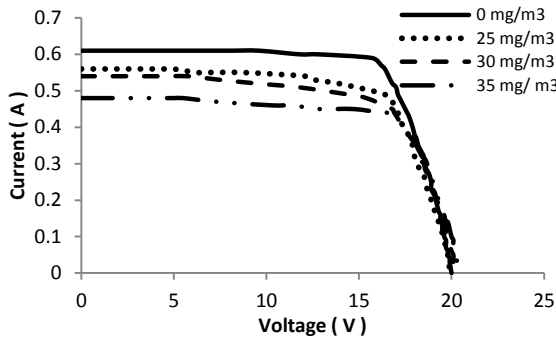


Figure 6: I-V curves at 30°C and different red soil dust densities.

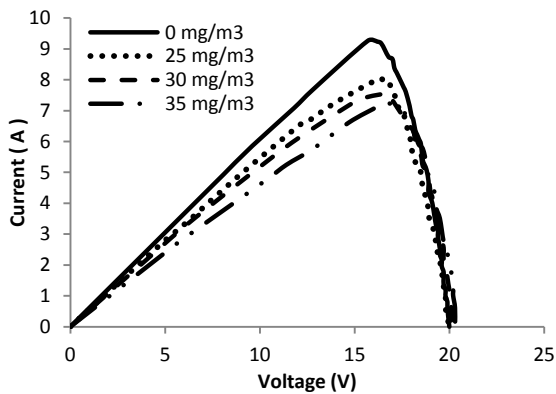


Figure 7: P-V curves at 30°C and different red soil dust density.

3.3.2. Effect of sand dust on the PV module

Figures 9–11 show the effect of sand dust on the I-V curve, power, and efficiency of the PV module. The experimental results show that without any dust on the PV, the short circuit current (I_{sc}) and open circuit voltage (V_{oc}) were 0.61A and 20V respectively. But when the PV was subjected to sand dust with densities of 25, 30 and 35 (mg/m³) the short circuit current (I_{sc}) was decreased to 0.59, 0.58 and 0.55A respectively. But the V_{oc} increased to 20, 20.5 and 20.8V for sand densities of 25, 30 and 35 mg/m³ respectively. Which mean that I_{sc} decreased by 3.27%, 4.91% and 9.83% for the cases of 25, 30 and 35 mg/m³. And for 30 and 35 mg/m³, V_{oc} increased by 2.5%, 4% and sequentially. In general, V_{oc} increased by 0.5% (5mg/m³) but I_{sc} decreased by 1.02% (5mg/m³).

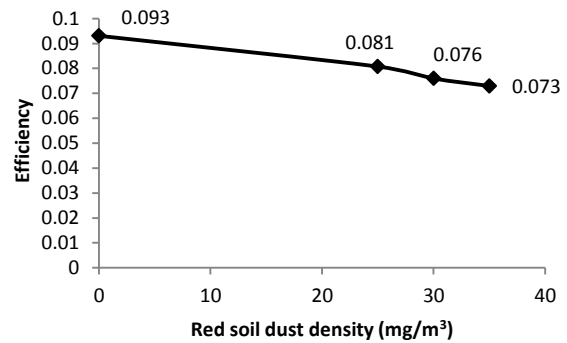


Figure 8: The efficiency of the PV module at different red soil dust densities.

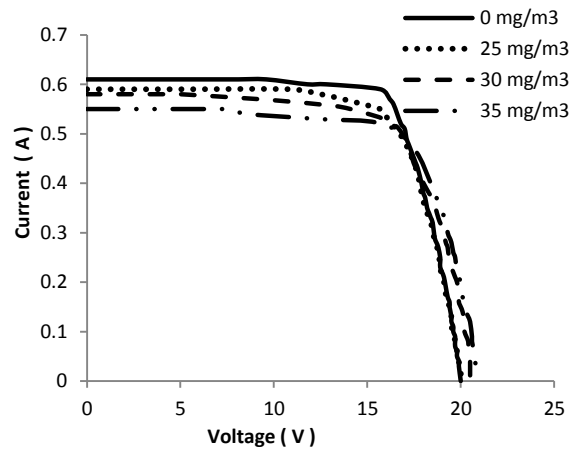


Figure 9: I-V curves of the PV module at different sand dust densities.

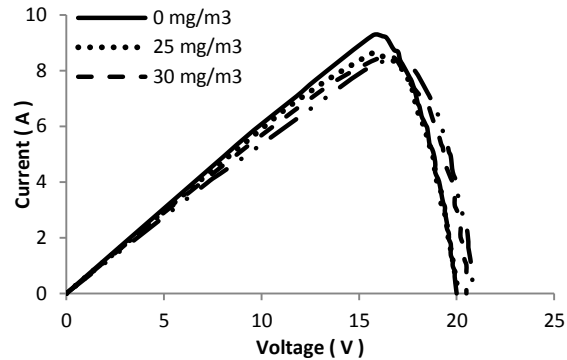


Figure 10: P-V curves of the PV module at different sand dust densities.

The maximum output power obtained from the PV module at different sand densities was measured. It was found that the maximum power when the PV was clean was 9.263W. But with sand dust on the PV at densities of 25, 30 and 35mg/m³, the maximum power was decreased to 8.635, 8.528 and 8.225W, ie by 6.77%, 7.93% and 11.2% sequentially. Beside this, for 5mg/m³ of sand dust, the maximum power of the PV module decreased by 1.5 %. Also the efficiency of the PV at different dust densities decreased by the same percentage as maximum power decreased. These results agreed well with the results of [17-20].

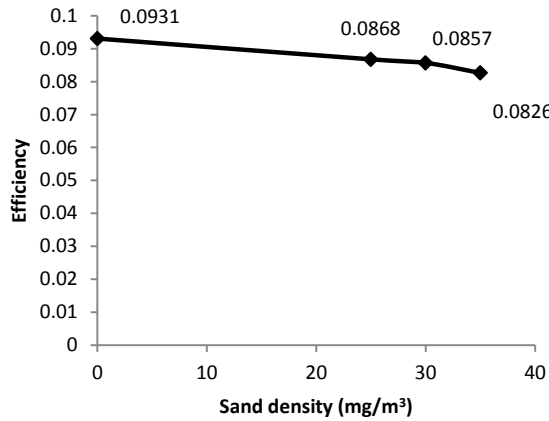


Figure 11: The efficiency of the PV at different sand density.

3.3.3. Effect of white soil dust on the PV module

Figures 12–14 show the effect of white dust density on the PV module. It can be seen that the white dust has a significant effect on the short circuit current (I_{sc}). However, in case of clean the PV module (without any dust), the short circuit current was 0.61A and open circuit voltage (V_{oc}) was 20 V. When the PV was covered with white dust the short circuit current (I_{sc}) was decreased to 0.53, 0.51 and 0.43A for the white dust densities of 20, 30 and 40 mg/m³ respectively. Conversely, the open circuit voltage (V_{oc}) was increased to 20.7, 20.8 and 20.9 for 20, 30 and 40 mg/m³ densities. For 20, 30 and 40 mg/m³ of dust density, it was found that the short circuit current (I_{sc}) is decreased by 13.11%, 16.39% and 29.5% respectively, but open circuit voltage (V_{oc}) was increased by 3.5%, 4% and 4.5% respectively. However, it was found that V_{oc} increased by 0.54% per 5 mg/m³ and I_{sc} decreased by 3.4% per 5 mg/m³ of white soil dust. Further, the maximum power when the PV was without any dust was 9.263W, and decreased to 7.701, 7.425, and 6.498W for the cases of 20, 30, and 40 mg/m³ of dust density respectively. Thus the maximum power and efficiency of the PV were decreased by 16.86%, 19.84%, and 29.84% for the cases of 20, 30, 40 mg/m³ respectively. However, it was found that the maximum power was decreased by 3.6% per 5mg/m³ of white dust (3.6 % / 5mg/m³). Similar results were found for the effect of white dust on the PV efficiency (Figure 14). These results agreed well with the results of [1, 21, 22].

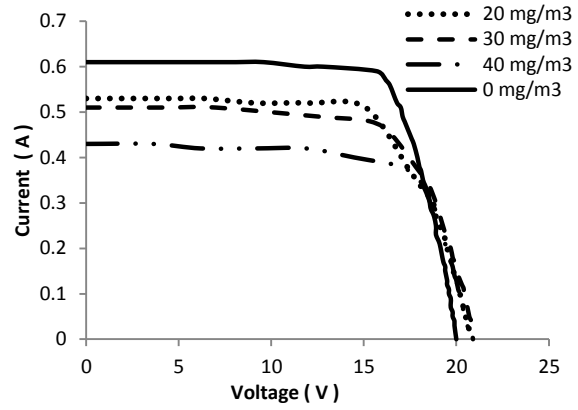


Figure 12: I-V curves of the PV module at different white dust densities.

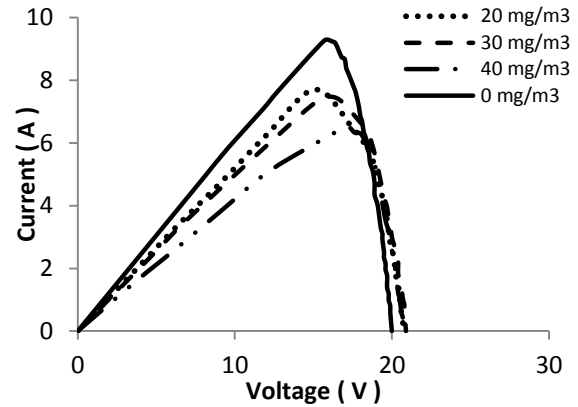


Figure 13: P-V curves of the PV panel at different white dust densities.

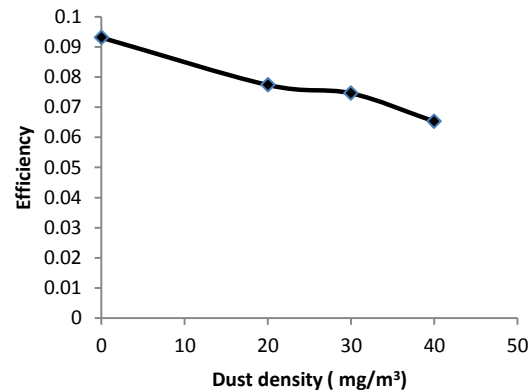


Figure 14: The efficiency of the PV module at different white dust densities.

3.3.4. Effect of wind speed on the PV module

In this section, the effect of wind speed on the PV performance by was studied. We take the PV data at 1m/s as a reference. Figures 15 and 16 show the effects of wind speed on the I-V and P-V curves, respectively. At 1m/s of wind speed the short circuit current (I_{sc}) and open circuit voltage were 0.6A and 17V, respectively. When the wind speed is increased to 2, 3, 4 and 5m/s, the short circuit current changed to 0.6, 0.59, 0.59 and 0.56A respectively. Conversely, the open circuit voltage (V_{oc}) was increased to 17.3, 17.8, 18.5 and 20.2V respectively. From this data, it can be concluded that I_{sc} slightly decreased by 1.48 % (1m/s) while V_{oc} was increased by 2.02 % (1m/s).

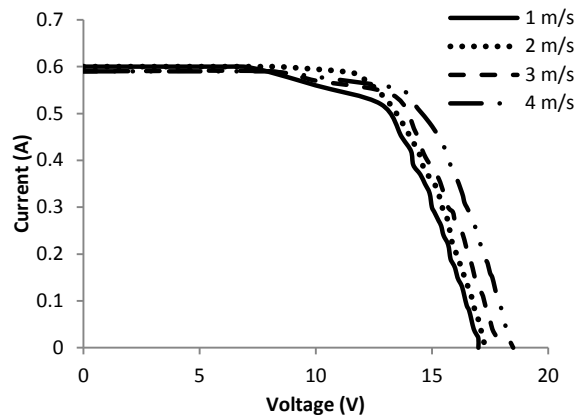


Figure 15: I-V curves of the PV panel at different wind speed.

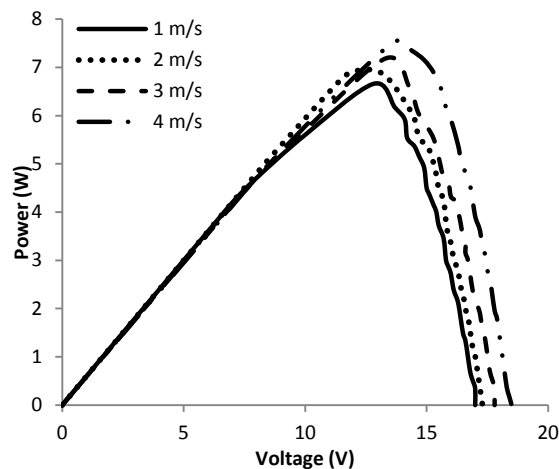


Figure 16: P-V curves of the PV panel at different wind speed.

On the other hand, at 1m/s of wind speed, the maximum power of the PV was 6.656W. In case of increasing wind speed to 2, 3, 4 and 5m/s, the maximum power increased to 6.902, 7.182, 7.535 and 8.064W, respectively. In other words, the maximum power and efficiency was increased by 3.6%, 7.9%, 13.2% and 21.1% for cases of 2, 3, 4 and 5m/s sequentially. In other word, the maximum power and efficiency of the PV was increased by 5% per 1m/s increase of wind speed (Figure 17). These results agreed well with the results of [6, 23, 24].

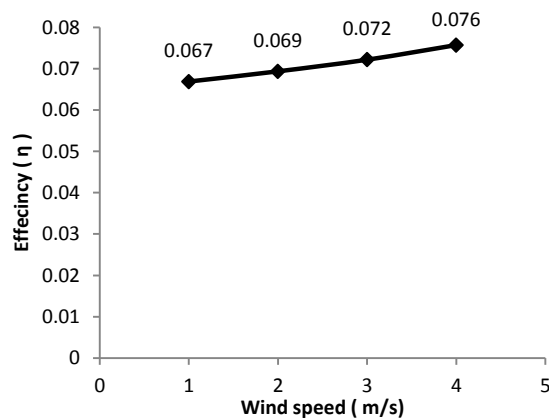


Figure 17: The efficiency of the PV module at different wind speed.

4. Conclusion

The effects of dust, wind speed and temperature on the mono-crystalline PV module were investigated at constant radiation ($G=1000\text{W/m}^2$). A series of experiments were conducted in order to investigate the effect of several types of dust. These were red soil, sand and white soil. The results showed that a significant effect was observed on both module current and short circuit current. However, they were dramatically decreased as the dust density increased. On the other hand, the dust density did not have a significant effect on the module maximum output voltage and the open circuit voltage. Moreover, a larger reduction in the PV performance was observed in the case of white soil dust, owing to its smaller particles, than sand or red soil. The effect of temperature on the PV module was also investigated. It was observed that the open circuit voltage (V_{oc}) was decreased by $4\%/5^\circ\text{C}$, while the short circuit current (I_{sc}) was slightly increased by $2\%/5^\circ\text{C}$. Consequently the maximum power (P_{Max}) and efficiency dramatically were decreased. In addition, when the effect of wind speed on the PV module was investigated it was found that the performance of the PV increased as the wind speed increased since the temperature of the PV was reduced.

5. Acknowledgments

The author would like to acknowledge the support and help of Eng. Mohammed Azzeh, Eng. Mohammed Khalefha, and Eng. Huda Jabarifor their contribution during the experiments work.

References

- [1] M. M. A. Al-Maghalseh, "The Impacts of Distribution Generators Size and Location on Power Efficiency and Voltage Profile in Radial LV Networks," *Advances in Science, Technology and Engineering Systems Journal*, vol. 3, pp. 276-283, 2018.
- [2] M. M. Al-Maghalseh and E. M. Maharmeh, "Economic and Technical Analysis of Distributed Generation Connection: A Wind Farm Case Study," *Procedia Computer Science*, vol. 83, pp. 790-798, 2016.
- [3] M. M. Al-Maghalseh, A. K. Abutemeha, and M. Iyadyyeh, "Modeling a hybrid system for electrical generation and wastewater treatment using photovoltaic and fuel cells," (in English), *Desalination and Water Treatment*, vol. 100, pp. 250-257, 2017.
- [4] M. M. Al-Maghalseh, "Evaluating the Reliability worth Indices of Electrical Medium Voltage Network: Case Study," *Procedia Computer Science*, vol. 130, pp. 744-752, 2018.
- [5] M. Al-Maghalseh and W. Saleh, "Design and cost analysis of biogas based power plant: Jenin perspective," in *Smart Cities: Improving Quality of Life Using ICT & IoT (HONET-ICT)*, 2017 14th International Conference on, 2017, pp. 31-35: IEEE.
- [6] M. Mani and R. Pillai, "Impact of dust on solar photovoltaic (PV) performance: Research status, challenges and recommendations," *Renewable and Sustainable Energy Reviews*, vol. 14, no. 9, pp. 3124-3131, 2010/12/01/ 2010.
- [7] A. Batra, A. Gupta, R. K. Pachauri, and A. Hussain, "Experimental Investigations on the Effects of Dust Fouling on PV Module," in *Proceeding of International Conference on Intelligent Communication, Control and Devices* :

- ICICCD 2016, R. Singh and S. Choudhury, Eds. Singapore: Springer Singapore, 2017, pp. 855-861.
- [8] G. M. Masters, *Renewable and Efficient Electric Power Systems*: Wiley, 2005.
- [9] S. Chander, A. Purohit, A. Sharma, Arvind, S. P. Nehra, and M. S. Dhaka, "A study on photovoltaic parameters of mono-crystalline silicon solar cell with cell temperature," *Energy Reports*, vol. 1, pp. 104-109, 2015/11/01/ 2015.
- [10] S. A. Sulaiman, H. H. Hussain, N. S. H. N. Leh, and M. S. I. Razali, "Effects of Dust on the Performance of PV Panels," *International Journal of Mechanical, Aerospace, Industrial, Mechatronic and Manufacturing Engineering* vol. 58, pp. 2028 - 2033, 2011.
- [11] M. M. Rahman, M. Hasanuzzaman, and N. A. Rahim, "Effects of various parameters on PV-module power and efficiency," *Energy Conversion and Management*, vol. 103, pp. 348-358, 2015/10/01/ 2015.
- [12] A. Alwaeli, *Effect of Tilt Angle and Temperature on PV Performance* vol. 113, 2017.
- [13] T. Nordmann and L. Clavadetscher, "Understanding temperature effects on PV system performance," in *3rd World Conference on Photovoltaic Energy Conversion*, 2003. Proceedings of, 2003, pp. 2243-2246 Vol.3.
- [14] F. A. Touati, M. A. Al-Hitmi, and H. J. Bouchech, "Study of the Effects of Dust, Relative Humidity, and Temperature on Solar PV Performance in Doha: Comparison Between Monocrystalline and Amorphous PVS," *International Journal of Green Energy*, vol. 10, pp. 680-689, 2013/08/09 2013.
- [15] S. A. M. Said, G. Hassan, H. M. Walwil, and N. Al-Aqeeli, "The effect of environmental factors and dust accumulation on photovoltaic modules and dust-accumulation mitigation strategies," *Renewable and Sustainable Energy Reviews*, vol. 82, pp. 743-760, 2018/02/01/ 2018.
- [16] S. Pulipaka and R. Kumar, "Analysis of soil distortion factor for photovoltaic modules using particle size composition," *Solar Energy*, vol. 161, pp. 90-99, 2018/02/01/ 2018.
- [17] A. Lay-Ekuakille, A. Ciaccioli, G. Griffio, P. Visconti, and G. Andria, "Effects of dust on photovoltaic measurements: A comparative study," *Measurement*, vol. 113, pp. 181-188, 2018/01/01/ 2018.
- [18] M. Chaichan and H. A. Kazem, *Effect of Sand, Ash and Soil on Photovoltaic Performance: An Experimental Study* vol. 1, 2017.
- [19] N. S. Beattie, R. S. Moir, C. Chacko, G. Buffoni, S. H. Roberts, and N. M. Pearsall, "Understanding the effects of sand and dust accumulation on photovoltaic modules," *Renewable Energy*, vol. 48, pp. 448-452, 2012/12/01/ 2012.
- [20] M. A. Kumar Tripathi, Ch.S.N. Murthy, Abhishek, "Experimental Investigation of Dust Effect on PV Module Performance," *Global Journal of Research In Engineering*, 2017-09-20 2017.
- [21] Z. A. Darwish, H. A. Kazem, K. Sopian, M. A. Al-Goul, and H. Alawadhi, "Effect of dust pollutant type on photovoltaic performance," *Renewable and Sustainable Energy Reviews*, vol. 41, pp. 735-744, 2015/01/01/ 2015.
- [22] M. Catelani, L. Ciani, L. Cristaldi, M. Faifer, M. Lazzaroni, and M. Rossi, "Characterization of photovoltaic panels: The effects of dust," in *2012 IEEE International Energy Conference and Exhibition (ENERGYCON)*, 2012, pp. 45-50.
- [23] T. Huld and A. Amillo, "Estimating PV Module Performance over Large Geographical Regions: The Role of Irradiance, Air Temperature, Wind Speed and Solar Spectrum," *Energies*, vol. 8, p. 5159, 2015.
- [24] D. Goossens and E. Van Kerschaver, "Aeolian dust deposition on photovoltaic solar cells: the effects of wind velocity and airborne dust concentration on cell performance," *Solar Energy*, vol. 66, pp. 277-289, 1999/07/01/ 1999.

Effect of Transverse Steady Magnetic Field on MHD Flow Under Free Convection Conditions in Vertical Microchannels

Mohammad A. Hamdan ^{*,a}, Anwar H. Al-Assaf ^b, Mohammad A. Al-Nimr ^c

^a The University of Jordan, Amman, Jordan

^b King Abdullah II Design and Development Bureau, Amman, Jordan

^c University of Science and Technology, Amman, Jordan

Received Feb 26, 2017

Accepted May 5, 2018

Abstract

Comsol software was used to investigate the effect of temperature jump and velocity slip on the hydrodynamic and thermal behavior of MHD flows under free convection conditions between parallel vertical plates and along a vertical plate. Further, the continuum model of fluid was used with Knudsen (Kn) number regime $0.001 < Kn < 0.1$, with the Maxwell slip velocity being applied along with the Smoluchowski temperature jump boundary on the solid-fluid surface interface.

It was found that the applied transverse magnetic produces Lorentz force tends to retard the flow velocity, which was found to be directly proportional with both the magnetic field number (N) and the Knudsen Number (Kn). This decrease in the flow velocity was recorded in the case of two parallel plates, while Lorentz force was found to decrease the thickness of the velocity boundary layer in the case of a single plate. Also, it was found that the increase in the magnetic field applied and the increase of Kn number lead to a decrease of the skin friction factor, Nusselt (Nu) number and the thickness of the velocity boundary layer. Finally, it was found that the applied magnetic field will cause an increase in the fluid temperature and hence both the friction coefficient factor and Nusselt number will be decreased by the increase of both Kn number and the magnetic influence number N.

© 2018 Jordan Journal of Mechanical and Industrial Engineering. All rights reserved

Keywords: Free convection, Knudsen number, Velocity slip, Lorentz force, Temperature jump, magnetic field.

1. Introduction

Microfluidics is one field of MEMS that deals with fluid flows in or around micro devices, and it can be found in a wide spectrum of applications. Microvalves, microducts, and micropumps are examples of such small devices involving the flow of liquids and gases. The increasing need of device miniaturization in fluid applications results in the need of a deep understanding of the fundamentals of fluid flow and heat transfer since it has been observed that flows differ from those in macroscopic machines, where the conventional flow models such as Navier-Stokes equations with no-slip boundary conditions on the fluid-solid interface are no more valid.

Magneto Fluid Dynamics (MFD) deals with the mutual interaction between conducting fluid flow and the applied magnetic field and hence such fluids are limited to liquid metals, plasmas, and strong electrolytes. Such interaction was found that the transverse magnetic field (B) affects the motion of the conducting fluid. This effect has been studied previously at the macro-scale level but not at the micro-scale level. The influence of magnetic field on fluid

dynamics and heat transfer in a conductive fluid is of interest in micro devices.

Recently and as a result of the increase interest in micro-flow area research, a significant number of publications on this subject had been published. Gad-el-Hak (1999),(2002) [1],[2] has published two papers, which presented an excellent state of the art review on the status of fluid flow phenomena related to micro devices. These papers concentrated on the use of MEMS as sensors and actuators for flow diagnosis and control. Furthermore, he concluded that that fluid flows in small devices may not be predicted from conventional flow models such as Navier-Stokes

On the other hand Gad El-Hak (2002) [2] presented a summary of the experiments that have been carried out to investigate the behavior of fluid flow in microchannels, over a large range of Reynolds numbers, geometries and experimental conditions, are presented in Table 6.3 of "The Handbook of MEMS".

Lauga (2005) [3], has conducted direct analytical simulation to investigate the performance of generic slip

* Corresponding author e-mail: mashamdan@yahoo.com

boundary conditions on the dynamics of the two – dimensional wake behind a circular cylinder.

Yu et al. (1995)[4] investigated a similar study of flows through micro tubes with variable diameters, extremely high Reynolds numbers for microscale conditions, up to 20,000 was obtained from this work

Haddad et al. (2006) [5] studied the fluctuating driving force frequency on basic gaseous micro-flows. It was found that the velocity slip and temperature jump increase with Knudsen number and /or the frequency of the driving force.

The dependency of velocity profiles on Knudsen number; during the transmission from smaller Knudsen number to a higher one was proved by Justyna and Steffen , (2007) [6]. It was also proved the non-dimensional wall velocity increases and the centreline velocity decreases.

In their study, Al-Nimr et al.(2010) [7] investigated the effect of velocity-slip boundary conditions on Jeffery-Hamel flow solutions using the first and the second order velocity slip models, the obtained results were compared with the no-slip mode. It was found that the obtained skin friction coefficient decreases with the Kn number.

Hamdan et al. (2010)[8] investigated the effect of second order velocity-slip/temperature-jump in micro channel flows. Also, they studied the effect of Knudsen number on first and second order velocity slip then compared this to the no slip condition.

Al-Nimr and Hader, (1999) [9] conducted an analytical study on MHD free convection flow in open –ended vertical porous channels, it was found that in under fully developed conditions, the volumetric flow rate reaches its maximum value and any further increase in the channel height will not lead to an increase in the volumetric flow rate. However, Nusselt number reaches its minimum limiting value and remains constant irrespective of any increase in the channel height.

Duwairi and Damseh (2004) [10] applied radiative vertical porous surface to investigate the Magnetohydrodynamic natural convection heat transfer from radiate vertical porous surfaces. They found out that the velocity and the heat transfer rates inside the boundary layer decreases with the magnetic field strength.

Mehmood, and Ali, (2006) [11] investigated the effect of slip condition of an unsteady MHD flow of a viscous fluid in planner channel. They found out that fluid slip at the lower wall caused the velocity at the wall to be increased. Furthermore, it was observed that the Hartmann number, the porosity parameter and the Grashoff number, decrease the slip at the wall, while the effect of the Peclet number is to strengthen the slip.

Muthuraj and Srinivas (2009) [12] conducted a work to study the influence of magnetic field and wall slip conditions on long wavy wall and steady flow between parallel flat wall and ?????. It was observed that increased suction parameter tended to decrease in fluid velocity.

Kalita (2012) [13] studied the effect of magnetic field on unsteady free convection MHD flow between two heated vertical plates, one of which is an adiabatic one. They found out that this effect of the magnetic field was of

maximum value at an angle of $\pi/2$ to the directions of the fluid and this decreases slowly as the angle decreases from $\pi/2$ to 0.

Hamdan et al (2015) [14] studied the effect of velocity slip and temperature jump on the hydrodynamic and thermal behaviors of MHD flows in the case of forced convection over flat plate, and in the case of forced convection between two parallel flat plates have been studied. It was found that the applied transverse magnetic produces Lorentz force that acts as an external body force tends to retard the flow velocity. Also, it was found that an increase in both the magnetic field applied and Kn number will decrease the skin friction factor, the Nusselt number, and also decrease the thickness of the velocity boundary layer.

In this work the effect of transverse steady magnetic field on the velocity slip and temperature jump of MHD flow will be studied for two different flow patterns in microchannel by implementing the first order slip/jump models. Those two cases are free convection over flat plate and free convection between two parallel flat plates.

2. Governing Equations

As stated, in this study the continuum model, which is based on continuity and momentum equations together with the energy will be used. Energy conservation principles with the two dimensional steady state assumption will add terms to both the momentum and energy equations due to the imposed magnetic field as shown in the following three equations:

$$\frac{\partial u}{\partial x} + \frac{\partial v}{\partial y} = 0 \quad (1)$$

$$\rho \left[u \frac{\partial u}{\partial x} + v \frac{\partial u}{\partial y} \right] = -\frac{\partial p}{\partial x} + \mu \frac{\partial^2 u}{\partial y^2} + g\rho\beta(T - T_\infty) - \sigma B^2 u \quad (2)$$

$$\rho c \left[u \frac{\partial T}{\partial x} + v \frac{\partial T}{\partial y} \right] = k \frac{\partial^2 T}{\partial y^2} + \mu \left(\frac{\partial u}{\partial y} \right)^2 + \sigma B_y^2 u^2 \quad (3)$$

2.1. Free Convection Flow over Flat Plate

The behavior of a free convection flow over a vertical flat plate will be investigated and analyzed under the presence of the transverse magnetic field B and with the assumption of the validity of steady Navier Stokes model with slip velocity and temperature jump on the surface – fluid interface as shown in figure 1.

Consider the following non-dimensional parameters

$$U = \frac{u}{u_\infty}, \theta = \frac{T - T_\infty}{T_w - T_\infty}, V = \frac{v}{u_\infty}, Y = \frac{yu_\infty}{\nu}, X = \frac{xu_\infty}{\nu}$$

$$\vec{B} = B_y \vec{j}$$

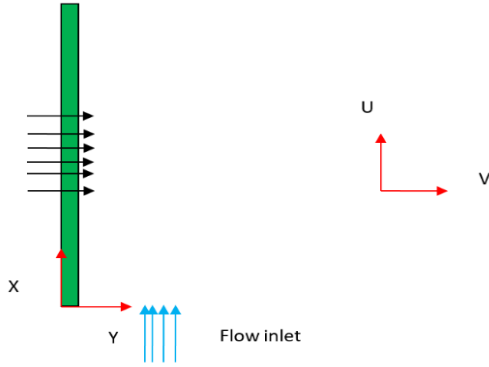


Figure 1: vertical plate setup

Where, U and θ are the non-dimensional velocity and temperature respectively, while u and T are the free stream velocity and temperature respectively, equations (1), (2) and (3) become respectively.

$$U \frac{\partial U}{\partial X} + V \frac{\partial U}{\partial Y} = 0 \tag{4}$$

$$U \frac{\partial \theta}{\partial X} + V \frac{\partial \theta}{\partial Y} = \frac{k}{\mu c} \frac{\partial^2 \theta}{\partial Y^2} + \frac{u_0^2}{c \Delta T} \left(\frac{\partial U}{\partial Y} \right)^2 + \frac{\sigma u_0 B^2 x_0}{\rho c \Delta T} U^2 \tag{5}$$

$$U \frac{\partial \theta}{\partial X} + V \frac{\partial \theta}{\partial Y} = \frac{1}{Pr} \frac{\partial^2 \theta}{\partial Y^2} + E_c \left(\frac{\partial U}{\partial Y} \right)^2 + RU^2 \tag{6}$$

Where

$$N_{\rightarrow} = E_c = \frac{u_0^2}{c(T_w - T_\infty)} \text{ and } R = \frac{\sigma B_y^2 \nu}{\rho c (T_w - T_\infty)}$$

Represent a system of non-dimensional equations that model the fluid flow over a vertical plate and can be solved simultaneously with the following boundary conditions:

1. At $X=0$ and any Y
 $U=0, V=0, \theta=0$
2. $Y \rightarrow \infty$ and any X
 $U=0$
3. $Y=0$ and any X

$$U(X, 0) = \left(\frac{2 - \sigma_u}{\sigma_u} \right) Kn \frac{\partial U}{\partial Y}(X, 0)$$

$$\theta(X, 0) = 1 + \left(\frac{2 - \sigma_T}{\sigma_T} \right) \left(\frac{2\gamma}{\gamma + 1} \right) \frac{1}{Pr} Kn \frac{\partial \theta}{\partial Y}(X, 0)$$

The friction factor is given by the formula

$$C_f = \left| \frac{\partial U}{\partial Y} \right|$$

While the Nusselt $Nu = \left| \frac{\partial \theta}{\partial Y} \right|$

2.2. Free Convection Flow Between Two Vertical Plates

The thermal behavior and the hydrodynamic behavior of a free convection flow between two parallel vertical plates will be investigated under the effect of a transverse magnetic field, this will be performed by incorporating the effect of the velocity slip and temperature jump on the fluid –surface interface. This case is presented in figure 2.

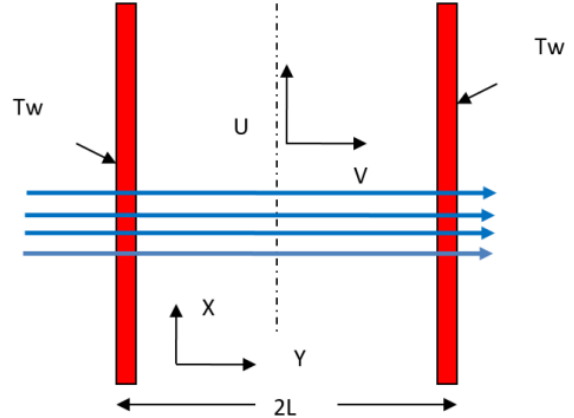


Figure 2: two vertical plates setup The governing equations of the system are:

$$\frac{\partial u}{\partial x} + \frac{\partial v}{\partial y} = 0 \tag{7}$$

$$\rho \left[u \frac{\partial u}{\partial x} + v \frac{\partial u}{\partial y} \right] = \mu \frac{\partial^2 u}{\partial y^2} + g \rho \beta (T - T_\infty) - \sigma B^2 u \tag{8}$$

$$\rho c \left[u \frac{\partial T}{\partial x} + v \frac{\partial T}{\partial y} \right] = k \frac{\partial^2 T}{\partial y^2} + \mu \left(\frac{\partial u}{\partial y} \right)^2 + \sigma B_y^2 u^2 \tag{9}$$

Assuming unidirectional flow, that is:

Applying it to equation (8), the left term will disappear and equation (8) will be reduced to the equation:

$$0 = \mu \frac{\partial^2 u}{\partial y^2} + g \rho \beta (T - T_\infty) - \sigma B^2 u \tag{10}$$

Also with the assumption that, $T = T(y)$ the energy equation (9) is reduced to:

$$0 = k \frac{\partial^2 T}{\partial y^2} + \mu \left(\frac{\partial u}{\partial y} \right)^2 + \sigma B_y^2 u^2 \tag{11}$$

Equations (7), (10) and (11) are combined and solved with the following two boundary conditions:

At $y=0$

$$\left. \begin{aligned} \frac{\partial u}{\partial y} &= 0 \\ \frac{\partial T}{\partial y} &= 0 \end{aligned} \right\} \tag{12}$$

And At $y=L$

$$\left. \begin{aligned} u(L) &= - \frac{(2 - \sigma_u)}{\sigma_u} \lambda \frac{\partial u}{\partial y} \\ T(L) - T_w &= - \frac{(2 - \sigma_T)}{\sigma_T} \frac{2\gamma}{\gamma + 1} \frac{\lambda}{pr} \frac{\partial T}{\partial y}(L) \end{aligned} \right\} \tag{13}$$

Furthermore, substituting the following dimensionless parameters:

$$\left. \begin{aligned} Y &= \frac{y}{L} \\ \theta &= \frac{T - T_\infty}{T_w - T_\infty} \\ U &= \frac{u}{u_0} \end{aligned} \right\} \quad (14)$$

$$\left. \begin{aligned} U(1) &= -\frac{(2 - \sigma_u)}{\sigma_u} kn \frac{\partial U}{\partial Y} (1) \\ \theta(1) &= 1 - \frac{(2 - \sigma_T)}{\sigma_T} \left(\frac{2\gamma}{\gamma + 1} \right) \frac{kn}{Pr} \frac{\partial \theta}{\partial Y} (1) \end{aligned} \right\} \quad (18)$$

3. Results and Discussion

In this work the commercial software COMSOL 3.5a is used to solve the above derived equations, this is done in conjunction with both the Multi-physics model and partial differential model. Both the vertical flat plate and the two vertical plates case will be taken individually.

Into the momentum equation (10) , the following will be obtained:

$$0 = \theta + \frac{\partial^2 U}{\partial Y^2} - NU \quad (15)$$

Also substituting the dimensionless parameters into the energy equation (11) to get:

$$0 = \frac{\partial^2 \theta}{\partial Y^2} + E \left(\frac{\partial U}{\partial Y} \right)^2 + FU^2 \quad (16)$$

Where $E = \frac{(T_w - T_\infty)L^4 \beta^2 \rho^2}{\mu k}$ and

$$F = \frac{\sigma B^2 u_0^2 L^2}{k(T_w - T_\infty)}$$

Equations (15) and (16) are solved using the following boundary conditions

At Y=0

$$\left. \begin{aligned} \frac{\partial U}{\partial Y}(0) &= 0 \\ \frac{\partial \theta}{\partial Y}(0) &= 0 \end{aligned} \right\} \quad (17)$$

At Y=L

3.1. Vertical flat plate

In this case the behavior of a steady free convection of a conducting fluid flow over a heated vertical flat plate is studied, with the effect of the transverse magnetic field for the slip/no slip, temperature jump and no temperature jump being taken into consideration.

In figure 3, the effect of the transverse magnetic field on the velocity profile within the hydrodynamic boundary layer is shown under the case of no slip (Kn=0). As indicated, the effect of the transverse applied magnetic field is to decrease the velocity profile, this is due to the creation of a retarding body force that acts in the opposite direction of the fluid. Finally, and as noted, this decrease in the flow increases with the value of N.

Applying the Maxwell boundary conditions on the plate –fluid interface and at the same time applying the transverse magnetic field the obtained velocity profile for different values of magnetic fields and different values of Kn number is presented in figures 4 through 6. As shown in these figures, the effect of increasing Kn number from 0.001 up to 0.1 on the velocity profile is to increase the velocity slip on the wall. Furthermore, the effect of increasing N of the velocity profile is to increase in the retardation of the velocity profile. This due creation of a retarding body force that acts in the opposite direction of the fluid.

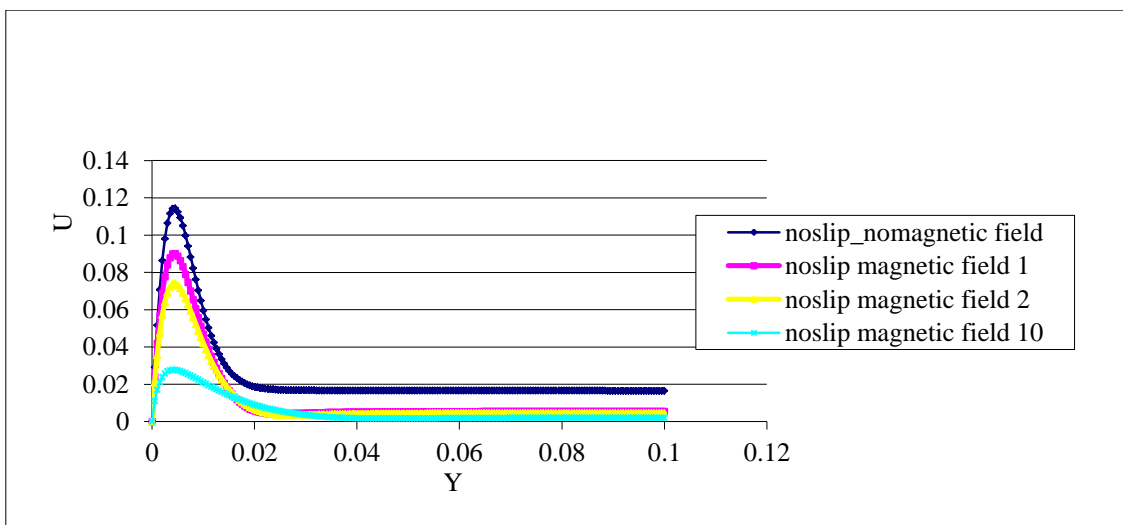


Figure 3: velocity profiles for Kn =0 and different values of N

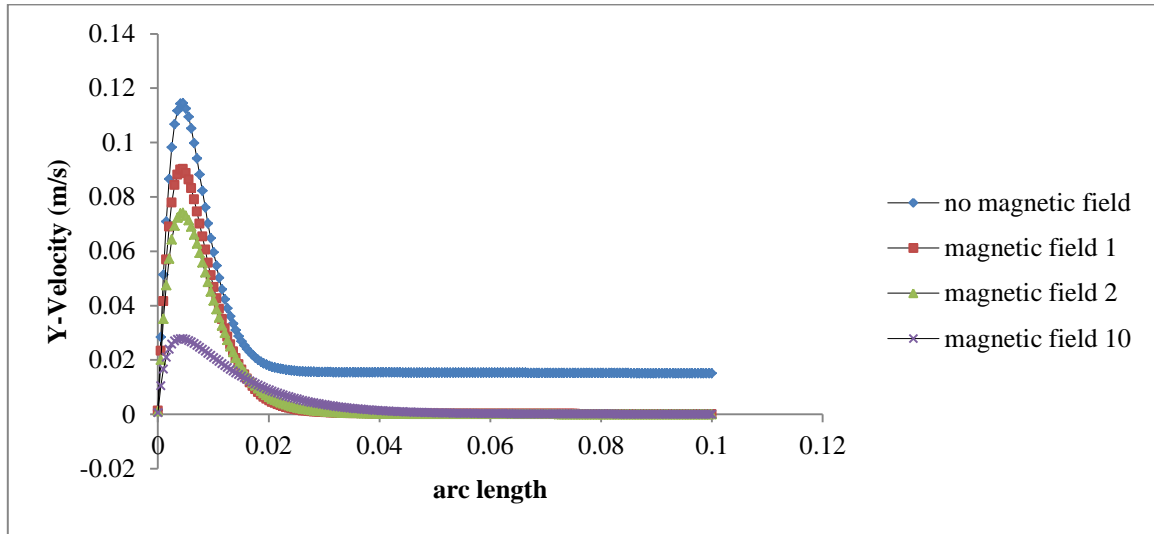


Figure 4: velocity profiles vertical plate $Kn=0.001$ different N values.

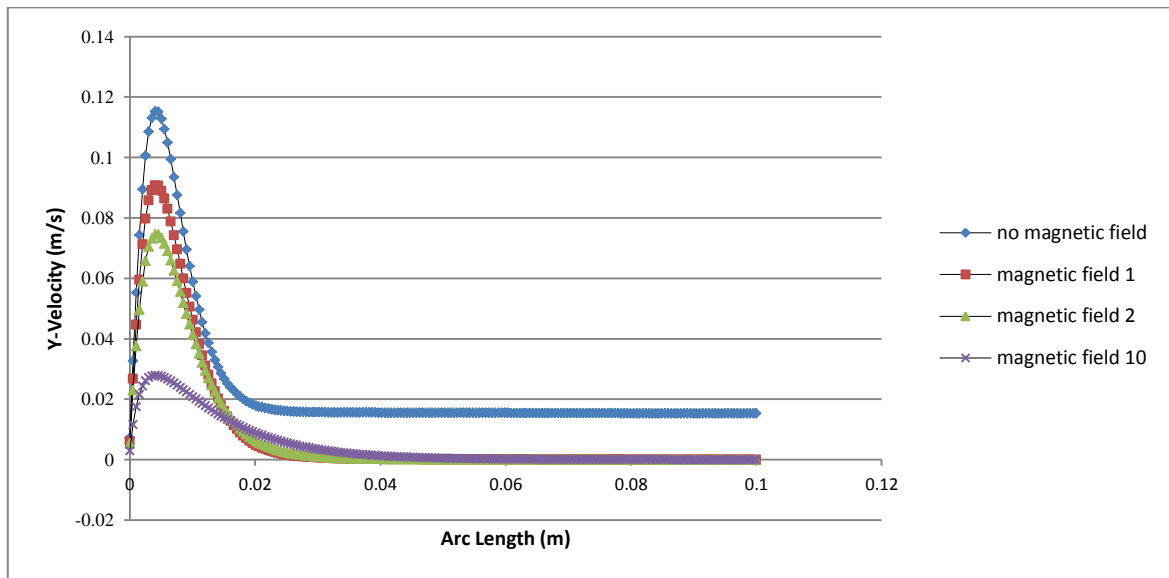


Figure 5: velocity profile for vertical plate for different N values at $Kn=0.01$

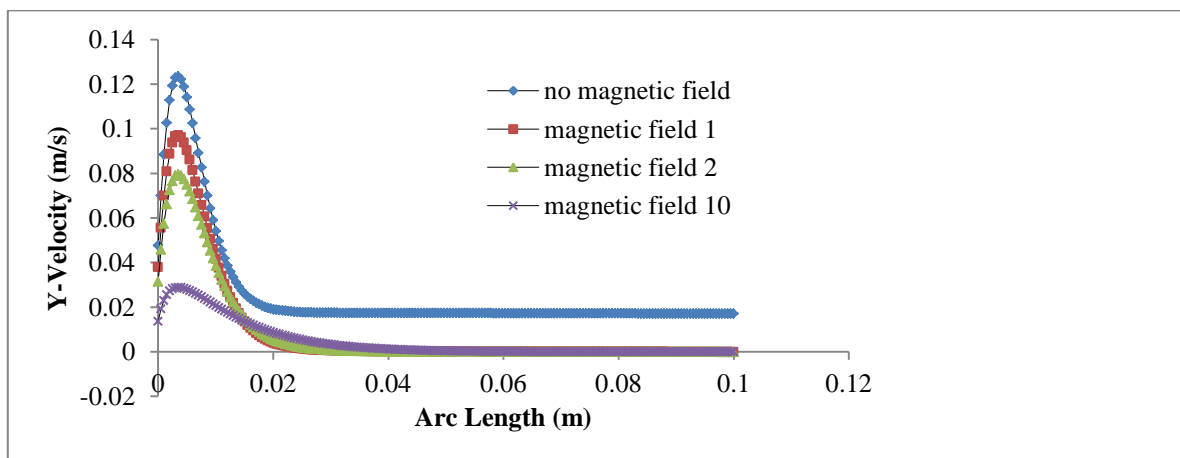


Figure 6: velocity profile for vertical plate for different N values at $Kn=0.1$

Figure 7 shows the temperature profiles under free convection conditions over vertical flat plate with different values of transverse magnetic field that is applied to the flow for the case of no jump ($Kn=0$). As indicated and in this figure, the temperature of the fluid increases with the magnetic field.

Figures 8 and 9 shows the temperature profiles under the conditions when the Smoluchowski boundary condition (Temperature jump) is applied on the fluid -plate

interface and for two values of Kn (0.001 and 0.1) along with different magnetic field values. It may be noted that the profile decreases rapidly in a direction away from the plate (in Y direction) as Y increases from zero value, and then, the rate decrease slows down significantly beyond, which the profile becomes independent of Y as it reaches zero value. It may be also noted that the temperature profile increases with N for any value of distance from the plate in Y direction.

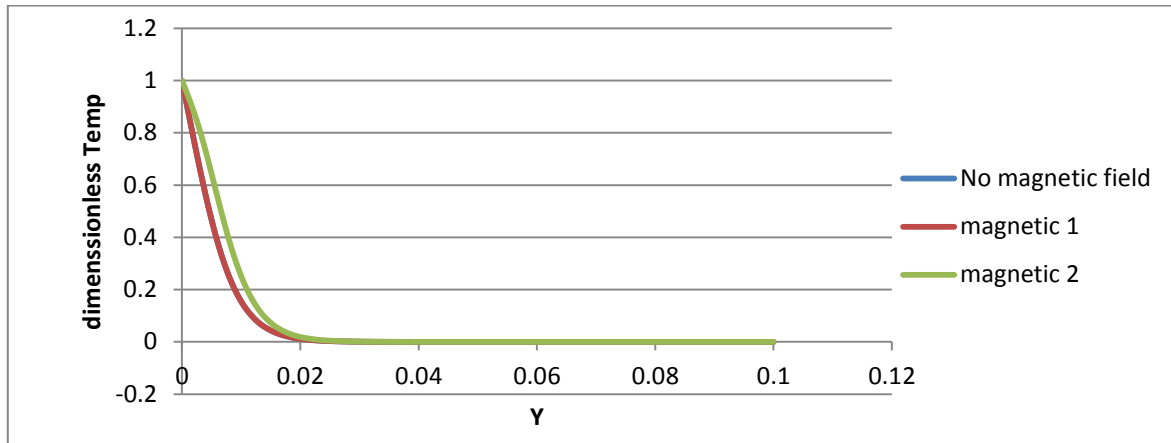


Figure 7: temperature profile over vertical plate with $Kn=0$ and different magnetic field

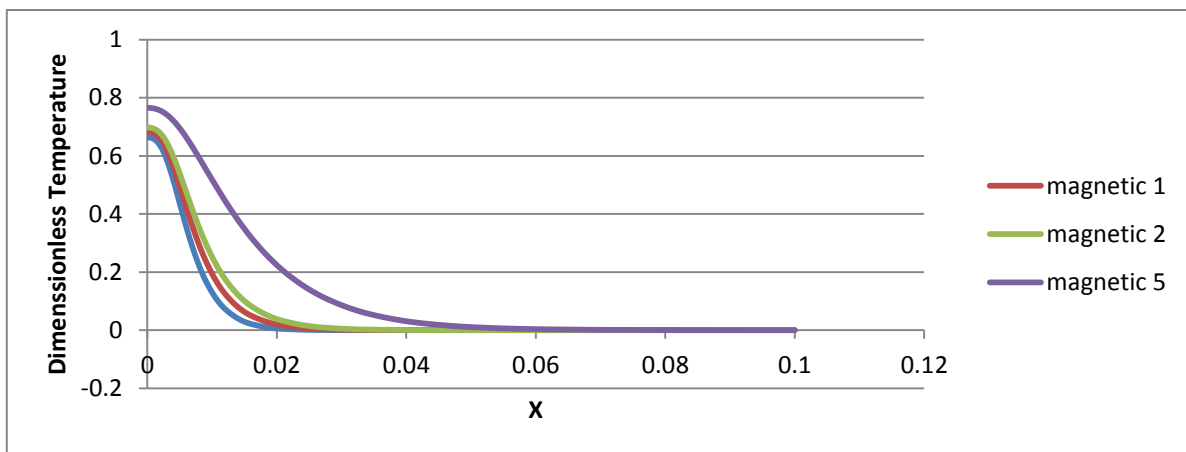


Figure 8: Temperature profiles for vertical plate with $Kn=0.001$ and different magnetic fields

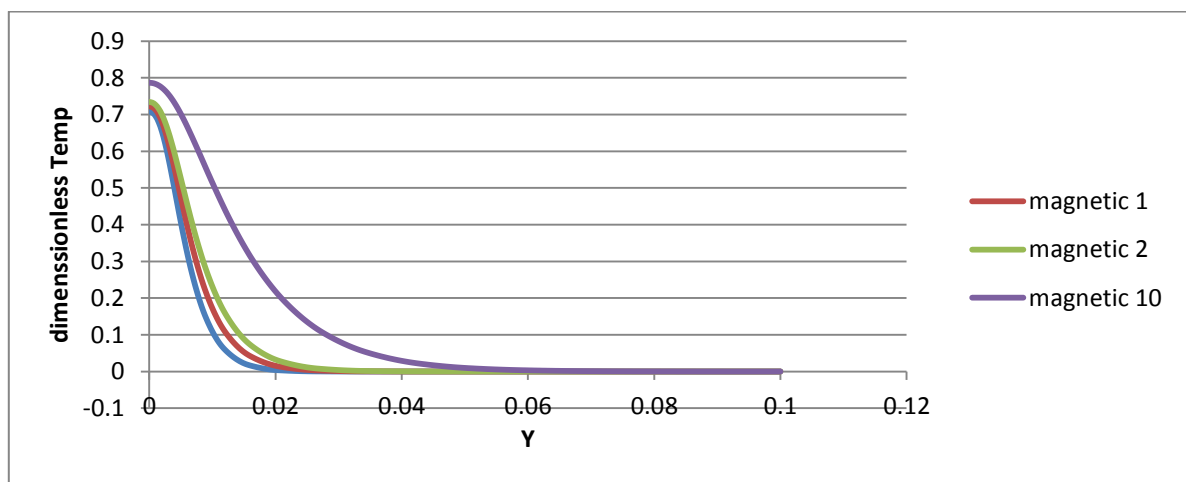


Figure 9: Temperature profiles for vertical plate with $Kn=0.1$ and different magnetic fields.

The variation in skin friction with the magnetic influence number is presented in Fig. 10 as indicated the skin friction decreases in the direction of flow along the plate (in x direction) at high rate initially; then, this decrease in rate starts to flatten as x approaches a constant value.

3.2. Free convection between two vertical plates

In this case the behavior of the steady free convection between two vertical plates was investigated under the effect of the transverse magnetic field and the Maxwell boundary conditions on the plates –fluid interface taking into consideration that the walls are non -conducting.

Starting with the conventional conditions of case of no slip condition. Figure 11 shows the effect of the transverse magnetic field applied on the fluid flow. As indicated and

as expected under the no slip conditions, the magnetic field as applied to the flow will tend to retard the flow.

The effect of the magnetic influence number on the velocity profile under different values of N and for the case when $Kn = 00.01$ is presented in figure 12. As it may be seen from this figure, the flow velocity retardation increases with the magnitude of the magnetic field. However, and under such conditions the slip velocity decreases as the magnetic field increases.

The effect of the transverse magnetic field on the temperature profile of a fluid between two vertical plates with $Kn = 0.001$ is shown in figure 13 below. It is clear that at any specified location between the plates, the temperature of the flow increases with the applied magnetic field.

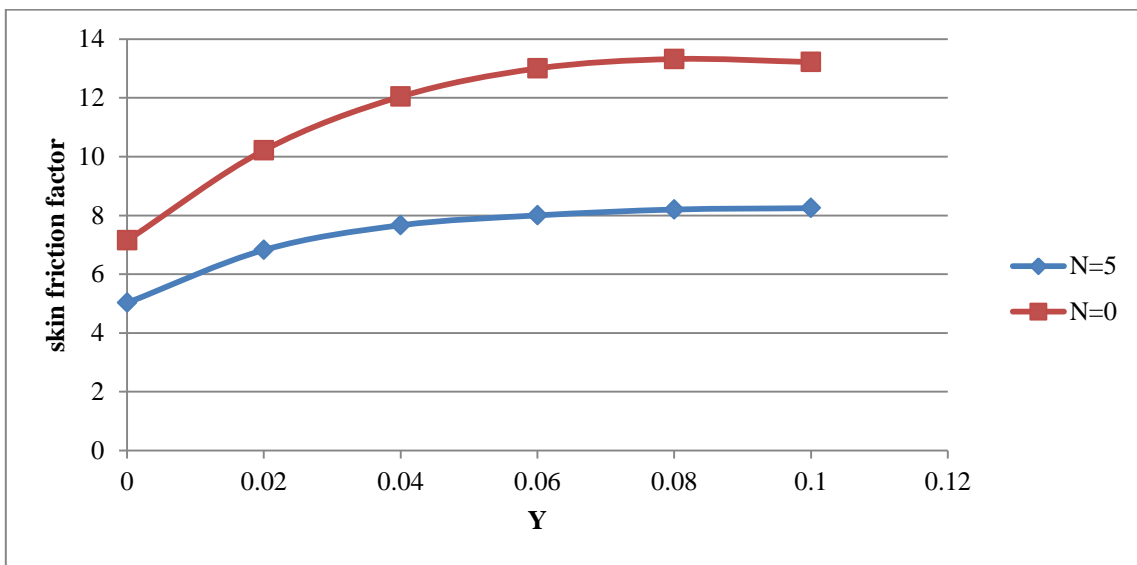


Figure 10: the effect of magnetic field on the skin friction value in a vertical

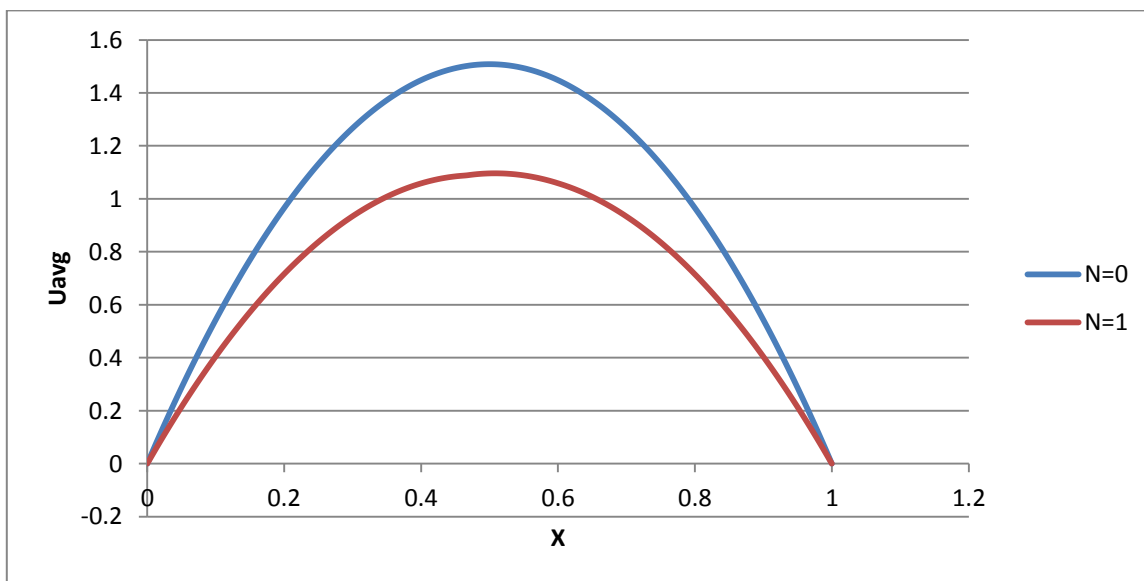


Figure 11: The effect of the transverse magnetic field on the flow velocity in the free convection between two parallel plates. $Kn=0$, $N=0$ and $N=1$

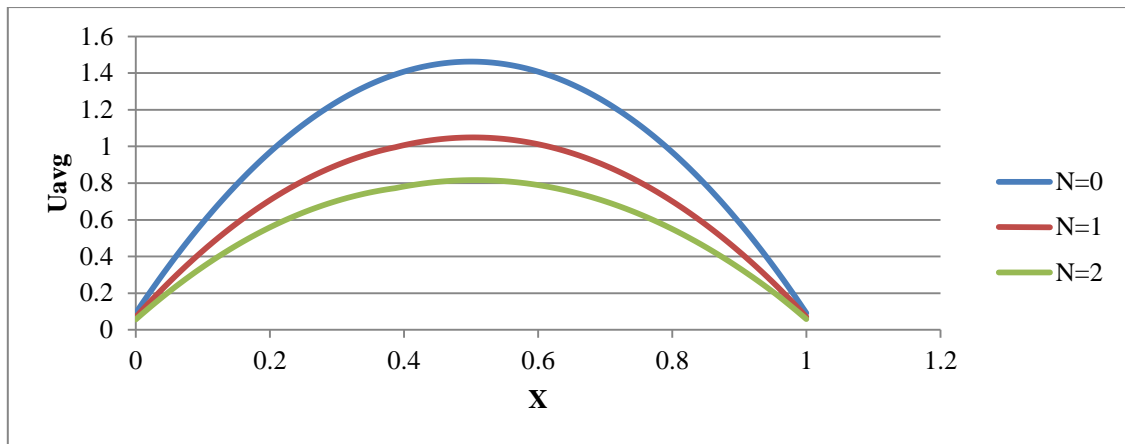


Figure 12: Velocity profile for free convection between two vertical parallel plates with $Kn=0.001$, $N=0$, $N=1$ and $N=2$

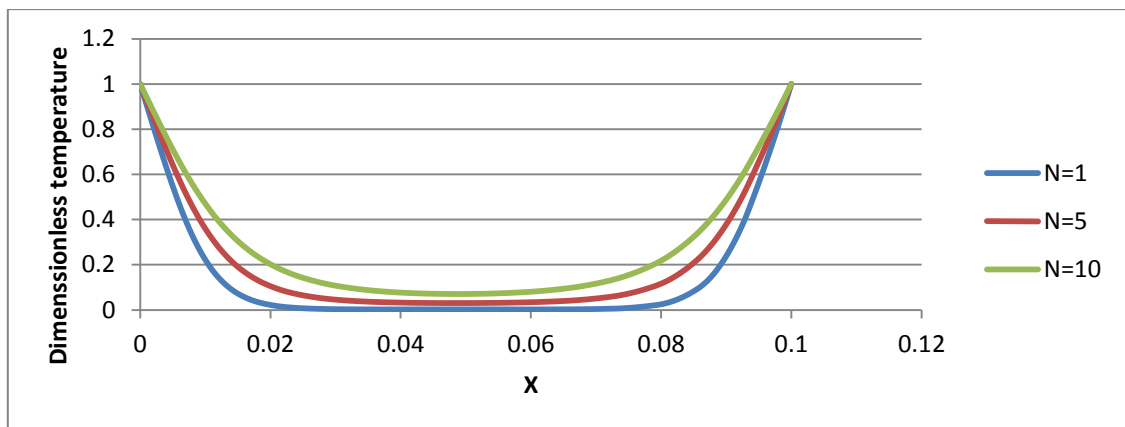


Figure 13: the effect of increasing the transverse magnetic field on the free convection velocity profile between two vertical plates with $Kn=0.001$

4. Conclusions

In this study the effect of induced magnetic field on hydrodynamic and thermal behaviors of MHD flows in the case of free convection have been studied. Four mathematical models that represent those cases have been developed; those are free convection over vertical flat plate, and free convection between two parallel vertical plates.

From this work, the following results may be concluded:

1. The applied transverse magnetic which produces Lorentz force that acts as an external body force tends to retard the flow velocity; this retardation was found to be directly proportional with both the magnetic field number (N) and the Knudsen Number (Kn).
2. The increase in the magnetic field applied and the increase of Kn number both will decrease the skin friction factor, the Nusselt number, and also decreases the thickness of the velocity boundary layer.

References

- [1] Gad-el-Hak, M. (1999), "The Fluid Mechanics of Micro devices - The Freeman Scholar Lecture", *Journal of Fluid Engineering*, Vol. 121, pp. 5-33.
- [2] Gad-el-Hak, M. (2002), "Flow Physics in Microdevices, Excerpted from Chapter 4 of The Handbook of MEMS", CRC Press, editor, CRC press, Boca Raton, Florida, 2002.
- [3] Lauga, E. (2005), "Microfluidics: The No-Slip Boundary Condition, Ch. 15 in Handbook of Experimental Fluid Dynamics", Editors: J. Foss, C. Tropea and A. Yarin, Springer, New-York.
- [4] Yu, D., Warrington, R., Barron, R., and Ameal, T., (1995), "An Experimental and Theoretical Investigation of Fluid Flow and Heat Transfer in Microtubes", *Proc. of ASME/JSME Thermal Engineering Joint Conf.*, March 19–24, Maui, HI, pp. 523–530.
- [5] Haddad, M., Al-Nimr, M. and Abuzaid, M., (2006), "Effect of periodically oscillating driving force on basic micro flows in porous media", *Journal of Porous Media*, Vol. 9(7), pp. 695-707.
- [6] Justyna Czerwińska and Steffen Jebauer, (2007), "Implementation of velocity slip and temperature jump conditions for microfluidic devices", IPPT PAN
- [7] Al-Nimr, M. A., Hammoudeh, Vladimir A. and Hamdan, M. A., (2010), "Effect of velocity-slip boundary conditions on Jeffery-Hamel flow solutions", *ASME J. Applied Mechanics*, Vol. 77, Issue 4, 0410101-410108
- [8] Hamdan, M. A., Al-Nimr, M. A. and Hammoudeh, Vladimir, (2010), "Effect of second order velocity-slip/temperature-jump on basic gaseous fluctuating micro-flows", *ASME J. Fluids Engineering*, Vol. 132(7), pp. 0745031-0745036.
- [9] Al-Nimr, M.A. and Hader, M.a., (1999), "MHD free convection flow in open -ended vertical porous channels", *Chemical Engineering Science*, Vol. 85(5), pp. 2517-2521.
- [10] Duwairi, H.M. and Damseh, A., (2004), "Magneto hydrodynamic natural convection heat transfer from radiate vertical porous surfaces", *Heat and Mass Transfer*, Vol. 40, pp. 787-792.

[11] Mehmood, A. and Ali, A. (2006) “The effect of slip condition on unsteady MHD oscillatory flow of a viscous fluid in planer channel”, Rom. Journ. Phys., Vol. 52, Nos. 1–2, pp. 85–91

[12] Mathura,R. and Srinivas,S. (2009) “Influence of magnetic field and wall slip conditions on steady flow between parallel flat wall and along wavy wall with soret effect” ,Journal of Naval architecture and Marine Engineering ,pp 63-71

[13] Bahskar. Kalita(2012) , “Magnetic field effects on unsteady free convection MHD flow between two heated vertical plates(one adiabatic)”,Adv.6 no 16, pp. 765-775.

[14] Mohammad A. Hamdan, Anwar H. Al-Assaf and Mohammad A. Al-Nimr (2015).”The Effect of Slip Velocity and Temperature Jump on the Hydrodynamic and Thermal Behaviors of MHD Forced Convection Flows in Horizontal Microchannels”. Iran. J. Sci. Technol. Trans. Mech. Eng. DOI 10.1007/s40997-016-0004-x

Nomenclature

NOTATION	DESCRIPTION	UNITS
a_0	Speed of sound	m/s
B	Magnetic field	Tesla
c	specific heat of the heat transfer fluid	J/kg °C
C	Constant of proportionality	Dimensionless
C_f	Friction Coefficient factor	Dimensionless
E	Electric field	V/m
F_e	Electric force	J/c
F_m	Magnetic force	N/A.m
g	Gravity accelaration	m/s ²
H	the magnetic field intensity	F m ⁻¹
h	Convective heat transfer coeffiecint	W/m ² K
J	Current density	A/m ²
J_c	Conduction current density	A/m ²
J_{ind}	Induced current	A/m ²
J_{trans}	Current due to macroscopic velocity	A/m ²
k	Thermal conductivity	W/(m.K)
k	Boltzman constant	J/K
Kn	Knudsen number	Dimensionless
M	mass	Kg
Ma	Mach number	Dimensionless
$M_{diffuse}$	Diffused momentum	Kg.m/s
M_{out}	Out momentum	Kg.m/s
$M_{specular}$	Specular momentum	Kg.m/s

M_{wall}	Momentum at wall	Kg.m/s
M_{in}	In momentum	Kg.m/s
N	Magnetic influence number	Dimensionless
n	Number density	#of molecules/m ³
Nu	Nusselt number	Dimensionless
R	Gas constant	Dimensionless
Re	Reynolds number	Dimensionless
Q_i	Energy of incoming molecules	J
Q_w	Reflected energy	J
T	temperature	K
T_∞	Temperature at inlet	K
T_s	Fluid temperature	K
T_w	Wall temperature	K
u	X velocity component	m/s
U	Internal energy,dimensionless velocity	J,dimensionless
u_m	Mean velocity	m/s
u_s	Slip velocity	m/s
u_∞	Velocity at inlet	m/s
v_0	Characterstic velocity	m/s
V	Velocity vector in the conductor	m/s
v	Dimensionless Y- velocity y-component of velocity	Dimensionless
W_{em}	Electromagnetic work	N/A.s
X	Dimensionless width	Dimensionless
Y	Dimensionless height	Dimensionless

GREEK NOTATIONS

β	Volumetric thermal coefficient	1/K
γ	Specific heat ratio	Dimensionless
λ_{mfp}	Mean free path	m
σ	Molecular diameter, electric conductivity	m
ν	Kinematic viscosity	m ² /s
σ_u	Momentum accomodation factor	Dimensionless
μ	Dynamic viscosity	N.s/m ²
ρ	density	Kg/m ³
σ_T	Temperature accomodation factor	Dimensionless
μ_0	magnetic field permeability	H m ⁻¹
θ	Dimensionless temperature	Dimensionless

Domains of Magnetic Moments of Two onboard Coils with Stable Damping of Microsatellite Angular Velocities

V.V. Lyubimov^{*}, S.V. Podkletnova

Department of Further Mathematics, Samara University, Samara, Russia

Received May 15 2018

Accepted 21 June 2018

Abstract

The present paper considers the problem of damping of microsatellite angular velocities. Two identical magnetic coils oriented in parallel to the axes of inertia of microsatellite are used as actuators. The aim of the paper is finding domains of the magnetic moments of coils ensuring asymptotically stable deceleration of microsatellite angular velocities. Lyapunov's second method is used to study the asymptotic stability of the microsatellite angular velocities. By analyzing the asymptotic stability condition, we have determined the domains of the magnetic moments of two onboard coils, which lead to stable a damping of the angular velocities. The calculation algorithm of the magnetic moments of coils ensuring asymptotic stability of the angular velocities is formulated.

© 2018 Jordan Journal of Mechanical and Industrial Engineering. All rights reserved

Keywords: *Microsatellite, Magnetic Coils, Stability Domain, Lyapunov's Method, Algorithm.*

1. Introduction

As is known, in the process of separating from a base spacecraft, microsatellites and nanosatellites receive a certain angular velocity. Besides, during the uncontrolled motion on the Earth orbit the satellites are affected by aerodynamic and gravitational moments, which can lead to the change of their angular velocity [1]. Note that satellite angular velocity can be changed at a high-speed collision with a particle of space debris [2]. Despite the presence of a significant amount of the perturbing factors, the solution of the flight target problem of modern satellites is based on the effective control of a satellite angular velocity. In particular, the problem of ensuring a given orientation of a satellite assumes a controlled reduction of its angular velocity to small quantities with subsequent stabilization of the small level of the angular velocity. In the recent years, significant information is accumulated about the controlled reduction of the satellite angular velocity by means of onboard magnetic coils [4-18]. However, the publications do not contain a solution to the problem of defining the magnetic moments domains of two onboard coils which ensure stable damping of the angular velocities. The aim of the presented work is to find the domains of magnetic moments of two coils that provide asymptotically stable reduction of the microsatellite angular velocity.

The research object in this paper is the controlled motion of a microsatellite around its center of mass. The microsatellite has the shape of a rectangular parallelepiped.

This form is the most efficient in terms of arranging equipment in the satellite [3].

Suppose that two fixed on board and oriented in parallel to microsatellite's axes of inertia electromagnetic coils are used as actuators. Two electromagnetic coils are sufficient for three-axis control of the microsatellite. Let us assume that the controlling moments from the interaction between the coils magnetic fields and the geomagnetic field make the main contribution to motion of the microsatellite around the center of mass. We use Lyapunov's second method to find the stability domains of the microsatellite relative motion. It is known, that mechanical moments from magnetic forces, gravity and aerodynamics are commensurable. However, with installation of strong onboard magnets and choosing a high orbit it is possible to obtain the mechanical moment from magnetic coils, which significantly exceeds the magnitudes of the mechanical moments of gravitational and aerodynamic forces [1]. In this case, we neglect the action of other force factors, such as gravitational or aerodynamic moments. The paper includes the following sections: introduction, condition of the asymptotic stability of the relative motion, stability domains of the relative motion, algorithm of finding of the magnetic moments, conclusion and references.

2. The condition of asymptotic stability of relative motion

The motion of a parallelepiped-shaped microsatellite around its center of mass is described by Euler's dynamic equations which in a vector form are:

$$J \cdot \frac{d\vec{\omega}}{dt} = \vec{M} \quad (1)$$

$$\text{where } J \text{ is the inertia tensor, } J = \begin{pmatrix} J_x & 0 & 0 \\ 0 & J_y & 0 \\ 0 & 0 & J_z \end{pmatrix},$$

J_x, J_y, J_z are the moments of inertia of the microsatellite relative to principal central axes Ox, Oy, Oz ; $\vec{\omega} = (\omega_x, \omega_y, \omega_z)$ is the vector of microsatellite angular velocity; $\omega_x, \omega_y, \omega_z$ are the projections of microsatellite angular velocity to the coordinate axes Ox, Oy, Oz ; \vec{M} is the vector of the controlling mechanical moment.

Assume that the microsatellite has the shape of a parallelepiped with the sides a, b and c , respectively, along the axes x, y and z . The principal central moments of inertia of such microsatellite in body-fixed coordinate system $OXYZ$ are:

$$\begin{aligned} J_x &= \frac{m}{12}(b^2 + c^2); \\ J_y &= \frac{m}{12}(a^2 + c^2); \\ J_z &= \frac{m}{12}(a^2 + b^2), \end{aligned} \quad (2)$$

where m is the mass of the microsatellite.

The kinetic energy of rotational motion of the microsatellite is:

$$V = \frac{1}{2} \cdot \vec{\omega}^T \cdot J \cdot \vec{\omega}. \quad (3)$$

The expression (3) can be considered as Lyapunov's function. In this case, according to Lyapunov's second method, the condition of the asymptotic stability of a stationary point $\omega_x = \omega_y = \omega_z = 0$ is:

$$\frac{dV}{dt} < 0. \quad (4)$$

Let us calculate the value of Lyapunov's function in a scalar form:

$$\begin{aligned} V &= \frac{m}{24} \cdot \left((b^2 + c^2) \omega_x^2 + (a^2 + c^2) \omega_y^2 + \right. \\ &\left. + (a^2 + b^2) \omega_z^2 \right). \end{aligned} \quad (5)$$

Differentiating function (5) with respect to the time of motion, we find the derivative of Lyapunov's function:

$$\begin{aligned} \frac{dV}{dt} &= \frac{m}{12} \cdot \left((b^2 + c^2) \omega_x \omega'_x + (a^2 + c^2) \omega_y \omega'_y + \right. \\ &\left. + (a^2 + b^2) \omega_z \omega'_z \right), \end{aligned} \quad (6)$$

where $\omega'_x = \varepsilon_x, \omega'_y = \varepsilon_y, \omega'_z = \varepsilon_z$ are the projections of angular acceleration of the microsatellite on the coordinate axes Ox, Oy, Oz .

The mechanical moment \vec{M} is calculated as follows [1]:

$$\vec{M} = \vec{L} \times \vec{H} = \begin{vmatrix} \vec{i} & \vec{j} & \vec{k} \\ L_x & L_y & L_z \\ H_x & H_y & H_z \end{vmatrix} \quad (7)$$

where \vec{L} is the vector of magnetic moment; \vec{H} is the geomagnetic field intensity vector; L_x, L_y, L_z are the magnetic moments of the coils oriented in the direction of corresponding principal axes; H_x, H_y, H_z are the projections of the geomagnetic field vector to coordinate axes Ox, Oy, Oz . From equality (7) we find the projections of the vector of the controlling mechanical moment:

$$\begin{aligned} M_x &= L_y H_z - L_z H_y; \\ M_y &= L_z H_x - L_x H_z; \\ M_z &= L_x H_y - L_y H_x. \end{aligned} \quad (8)$$

Substituting the magnitudes of the angular accelerations according to the equations (1) into the expression (6), we obtain:

$$\begin{aligned} \frac{dV}{dt} &= \omega_x (L_y H_z - L_z H_y) + \omega_y (L_z H_x - L_x H_z) + \\ &+ \omega_z (L_x H_y - L_y H_x). \end{aligned} \quad (9)$$

Ensuring asymptotic stability of the system requires fulfillment of inequality (4) what taking into account expression (9) is given by:

$$\begin{aligned} \omega_x (L_y H_z - L_z H_y) + \omega_y (L_z H_x - L_x H_z) + \\ + \omega_z (L_x H_y - L_y H_x) < 0. \end{aligned} \quad (10)$$

Here the components of angular velocity can be determined by means of angular velocity sensors. The components of the intensity vector can be calculated in one of several known ways as described in the studies [1], [6], [9], [16]. Let, for example, the components of the intensity

vector \vec{H} be calculated in the way described in the study [16]. In deducing these expressions, it is supposed that the geomagnetic field intensity is described by the

model of straight dipole [9]. Projecting the vector \vec{H} to the coordinate axes $OXYZ$, we get:

$$\begin{aligned} H_x &= H \cos \theta, H_y = -H \sin \theta \cos \varphi, \\ H_z &= H \sin \theta \sin \varphi, \end{aligned} \quad (11)$$

where $H = \frac{\mu_e}{r^3} (1 + 3 \sin^2 i \sin^2 u)^{1/2}$ is the module of intensity vector, $\mu_e = 7,87 \cdot 10^{15} (Tc \cdot M^3)$ is Earth's magnetic constant, i is the orbit inclination, u is the argument of a latitude, r is the distance from a microsatellite to the center of Earth, $r = R_e + h$; R_e is the Earth radius, θ is the nutation angle, φ is the precession angle.

The dynamical Euler's equations (1) are considered jointly with the kinematic equations that allow us to determine Euler's angles [16]:

$$\begin{aligned} d\theta / dt &= \omega_z \cos \varphi + \omega_y \sin \varphi + \tilde{\omega}_{YM} \sin \psi - \tilde{\omega}_{ZM} \cos \psi, \\ d\psi / dt &= (\omega_z \sin \varphi - \omega_y \cos \varphi) / \sin \theta - \\ &\tilde{\omega}_{XM} + \tilde{\omega}_{YM} \operatorname{ctg} \theta \cos \psi + \tilde{\omega}_{ZM} \operatorname{ctg} \theta \sin \psi, \\ d\varphi / dt &= \omega_x - d\psi / dt \cos \theta - \tilde{\omega}_{ZM} \sin \theta \sin \psi, \end{aligned} \quad (12)$$

where $\tilde{\omega}_{XM}$, $\tilde{\omega}_{YM}$, $\tilde{\omega}_{ZM}$ are the angular velocities of rotation of a magnetic coordinate system $OX_M Y_M Z_M$ around the fixed geocentric coordinate system $OX_e Y_e Z_e$;

$$\begin{aligned} \tilde{\omega}_{XM} &= (\dot{\Omega} + \dot{\alpha}_2) \cos \alpha_1, \\ \tilde{\omega}_{YM} &= -(\dot{\Omega} + \dot{\alpha}_2) \sin \alpha_1, \quad \tilde{\omega}_{ZM} = \dot{\alpha}_1. \end{aligned}$$

Herein the angular velocity $\dot{\Omega}$ determines the orbit precession. The angles α_2 and α_1 are determined from a solution of the differential equations:

$$\begin{aligned} \dot{\alpha}_1 &= \frac{3 \cos u \sin i (1 + \sin^2 i \sin^2 u)}{(1 - \sin^2 i \sin^2 u)^{1/2} (1 + 3 \sin^2 i \sin^2 u)} \dot{u}, \\ \dot{\alpha}_2 &= \frac{\cos i}{1 - \sin^2 i \sin^2 u} \dot{u}. \end{aligned}$$

The deduced inequality (10) allows to find a value of one of magnetic moments (for example L_x) if the values of two other moments are known (in our case L_y and L_z). Let us group the left side of inequality (10) relative to magnetic moments. As a result the condition of the asymptotic stability becomes:

$$\begin{aligned} L_x (\omega_z H_y - \omega_y H_z) + L_y (\omega_x H_z - \omega_z H_x) + \\ + L_z (\omega_y H_x - \omega_x H_y) < 0. \end{aligned} \quad (13)$$

At each instant of time inequality (13) describes a half-space of asymptotic stability of the system which schematically may be displayed, for example, in Figure 1 as the domain of space indicated by arrows. On the contrary, in front of the plane specified in Figure 1 there is a domain of instability. In the domain of system instability the following condition is fulfilled:

$$\begin{aligned} L_x (\omega_z H_y - \omega_y H_z) + L_y (\omega_x H_z - \omega_z H_x) + \\ + L_z (\omega_y H_x - \omega_x H_y) > 0. \end{aligned}$$

3. Stability domains of relative motion

Note that only two coils fixed parallel to the corresponding axes of inertia make it possible to achieve effective control in three channels of rotational motion. This conclusion follows from the system of equations (1). Indeed, zeroing of one of components of magnetic moment L_i ($i=x, y, z$) does not lead to zeroing of any of three mechanical controlling moments M_i in formula (8). Therefore, to save the electric energy of the microsatellite, we will use two instead of three on-board magnetic coils. In this case, one of the magnetic components (e.g. L_y) will be equal to zero.

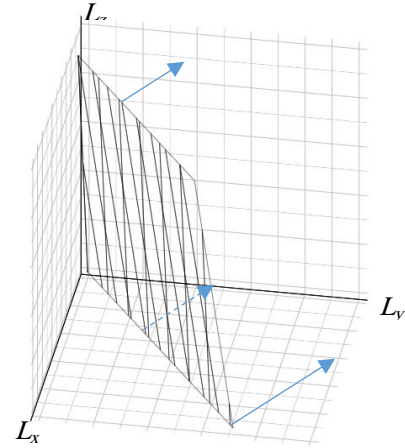


Figure 1. Domains of the asymptotic stability and instability of system with three magnetic coils in a satellite

Hence, the inequality (18) takes the form:

$$L_x (\omega_z H_y - \omega_y H_z) + L_z (\omega_y H_x - \omega_x H_y) < 0. \quad (14)$$

Inequality (14) allows to find possible values of one of magnetic moments (for example L_z) if the value of other moment is known (in our case L_x). In this case the domain of asymptotic stability is the half-plane. Indeed, the stability domain of the system lies under the straight line

$$L_x (\omega_z H_y - \omega_y H_z) + L_z (\omega_y H_x - \omega_x H_y) = 0, \text{ i.e. in}$$

the part of the plane, where the condition $L_x (\omega_z H_y - \omega_y H_z) + L_z (\omega_y H_x - \omega_x H_y) < 0$ is fulfilled. Here the domain of system instability is above the straight line

$$L_x (\omega_z H_y - \omega_y H_z) + L_z (\omega_y H_x - \omega_x H_y) = 0.$$

As the coils have own magnetic characteristics, let us set the limitations on the magnetic moments of coils:

$$\begin{aligned} \lambda_{1x} \leq L_x \leq \lambda_{2x}, \\ \lambda_{1z} \leq L_z \leq \lambda_{2z}, \end{aligned} \quad (15)$$

where $\lambda_{1x}, \lambda_{2x}, \lambda_{1z}, \lambda_{2z}$ are some constant positive values, which depend on physical characteristics of magnetic coils. At each instant of time an angular velocity sensor detects components of angular velocity of microsatellite. Let us assume that we know the value of the moment of the coil L_x and its axis is parallel to the axis x . It is necessary to find the limits in which the magnetic moment of the coil L_z must remain so that the system will be in stable equilibrium position. Without loss of generality, we separately consider two special cases.

In other words, we need to find out what maximal and minimal values of the magnetic moment L_x must be with limitative inequalities (14) and (15) being fulfilled. For example, it will graphically look like as shown in Figure 2. The domain of system stability lies under the boundary $L_x (\omega_z H_y - \omega_y H_z) + L_z (\omega_y H_x - \omega_x H_y) = 0$ between the lines $L_x = \lambda_{1x}$, $L_x = \lambda_{2x}$, $L_z = \lambda_{1z}$, $L_z = \lambda_{2z}$ i.e. in the shaded part of the plan

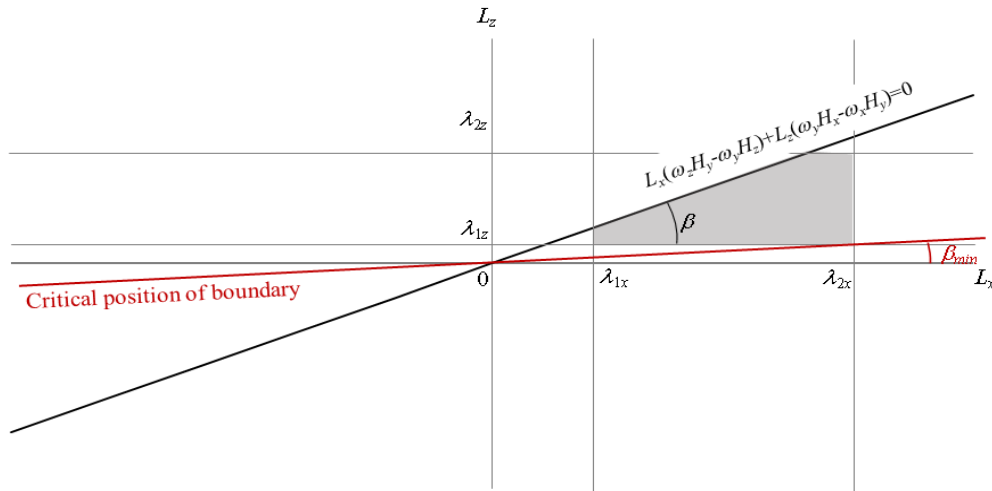


Figure 2. Domain of magnetic moments taking into account the limitations of system stability

When constructing stability domains the following question remains unresolved: at exactly which points the straight line

$$L_x (\omega_z H_y - \omega_y H_z) + L_z (\omega_y H_x - \omega_x H_y) = 0$$

intersects the lines $L_x = \lambda_{1x}$, $L_x = \lambda_{2x}$, $L_z = \lambda_{1z}$, and $L_z = \lambda_{2z}$. Indeed, there are several possible cases of intersections of these lines.

In Figure 2 the straight line $L_x (\omega_z H_y - \omega_y H_z) + L_z (\omega_y H_x - \omega_x H_y) = 0$ on the boundary of stability domain intersects the straight lines $L_x = \lambda_{1x}$ and $L_z = \lambda_{2z}$.

Let us consider critical positions of the line $L_x (\omega_z H_y - \omega_y H_z) + L_z (\omega_y H_x - \omega_x H_y) = 0$ in which at least at one point of the rectangle with the boundaries $L_x = \lambda_{1x}$, $L_x = \lambda_{2x}$, $L_z = \lambda_{1z}$, $L_z = \lambda_{2z}$ stability will remain. From inequality (14) we get

$$L_z (\omega_y H_x - \omega_x H_y) < -L_x (\omega_z H_y - \omega_y H_z). \tag{16}$$

If the following conditions are fulfilled

$$\omega_y H_x - \omega_x H_y > 0, \tag{17}$$

$$\omega_z H_y - \omega_y H_z < 0, \tag{18}$$

then from condition (16) we get

$$L_x < -L_z \cdot \frac{\omega_z H_y - \omega_y H_z}{\omega_y H_x - \omega_x H_y}, \tag{19}$$

that corresponds to the case presented in Figure 2.

If the following inequality is fulfilled

$$\omega_y H_x - \omega_x H_y < 0, \tag{20}$$

then the domain of stability is above the straight line $L_x (\omega_z H_y - \omega_y H_z) + L_z (\omega_y H_x - \omega_x H_y) = 0$.

Let us consider at first a case when inequalities (17) and (18) are fulfilled. Let us specify the angle β between the axis L_x and straight line $L_x (\omega_z H_y - \omega_y H_z) + L_z (\omega_y H_x - \omega_x H_y) = 0$ as shown in Figure 2. For distinctness we will assume that all the values λ_{1x} , λ_{2x} , λ_{1z} , λ_{2z} are positive. With the given

limitations the angle β may vary between 0 and $\frac{\pi}{2}$. Let

us begin to decrease the angle β , simultaneously rotating the line $L_x (\omega_z H_y - \omega_y H_z) + L_z (\omega_y H_x - \omega_x H_y) = 0$ around the origin of coordinates until the position where only one pair of possible values L_x and L_z is left with which the system remains in stable equilibrium position. The critical position of the boundary of the stability domain $L_x (\omega_z H_y - \omega_y H_z) + L_z (\omega_y H_x - \omega_x H_y) = 0$ is shown in Figure 3 with the red line. In critical position of the boundary $L_x (\omega_z H_y - \omega_y H_z) + L_z (\omega_y H_x - \omega_x H_y) = 0$ only one point of system stability is left.

Let us assume that a microsatellite has onboard magnetic coils with identical characteristics, then we obtain

$$\lambda_{1x} = \lambda_{1z} = \lambda_1, \lambda_{2x} = \lambda_{2z} = \lambda_2. \tag{21}$$

If the condition (21) and also the conditions specified earlier are fulfilled, then we obtain the graphic illustration of the problem represented in Figure 3.

At the moment when the boundary is in a critical position, the position of stable equilibrium of the system is determined only with one pair of magnetic moments of the coils, that is $L_x = \lambda_2$, $L_z = \lambda_1$. Let us begin to increase the angle β . While the straight line $L_x (\omega_z H_y - \omega_y H_z) + L_z (\omega_y H_x - \omega_x H_y) = 0$ is below the bisector of the first quadrant angle (see Figure. 3), the moment L_x may possess only a value from the interval $(\lambda; \lambda_2)$ where λ can be determined from the condition that the point $(\lambda; \lambda_1)$ belongs to the straight line $L_x (\omega_z H_y - \omega_y H_z) + L_z (\omega_y H_x - \omega_x H_y) = 0$. In this case the equality

$L_x(\omega_z H_y - \omega_y H_z) + L_z(\omega_y H_x - \omega_x H_y) = 0$ is fulfilled. Thus, while the angle $\beta < \frac{\pi}{4}$, then

$$-\lambda_1 \cdot \frac{\omega_y H_x - \omega_x H_y}{\omega_z H_y - \omega_y H_z} < L_x < \lambda_2. \quad (22)$$

At the same time inequality (19) must be fulfilled. As with the specified limitations the inequality $-\frac{\omega_z H_y - \omega_y H_z}{\omega_y H_x - \omega_x H_y} > 0$ is fulfilled, from inequality (22) it follows that

$$\lambda_1 \cdot \frac{\omega_y H_x - \omega_x H_y}{\omega_z H_y - \omega_y H_z} \cdot \frac{\omega_z H_y - \omega_y H_z}{\omega_y H_x - \omega_x H_y} < L_x < -\frac{\omega_z H_y - \omega_y H_z}{\omega_y H_x - \omega_x H_y} \cdot \lambda_2.$$

Hence we get

$$\lambda_1 < -\frac{\omega_z H_y - \omega_y H_z}{\omega_y H_x - \omega_x H_y} \cdot L_x < -\frac{\omega_z H_y - \omega_y H_z}{\omega_y H_x - \omega_x H_y} \cdot \lambda_2.$$

Then owing to the inequality

$$\lambda_1 < L_x < -\frac{\omega_z H_y - \omega_y H_z}{\omega_y H_x - \omega_x H_y} \cdot L_x < -\frac{\omega_z H_y - \omega_y H_z}{\omega_y H_x - \omega_x H_y} \cdot \lambda_2 \quad (23)$$

is true. Here we defined the angle β as an angle between the axis L_x and the straight line $L_x(\omega_z H_y - \omega_y H_z) + L_z(\omega_y H_x - \omega_x H_y) = 0$.

Hence it follows that the slope of the straight line $L_x(\omega_z H_y - \omega_y H_z) + L_z(\omega_y H_x - \omega_x H_y) = 0$ which is equal to $-\frac{\omega_z H_y - \omega_y H_z}{\omega_y H_x - \omega_x H_y}$ coincides with the tangent of the angle β , i.e.

$$\text{tg} \beta = \frac{\omega_y H_x - \omega_x H_y}{\omega_z H_y - \omega_y H_z}. \quad (24)$$

Then equality (23) is true while $\text{tg} \beta < \text{tg} \frac{\pi}{4} = 1$.

Hence it follows fulfillment of the condition

$$0 < \omega_y H_z - \omega_z H_y < \omega_y H_x - \omega_x H_y. \quad (25)$$

And then jointly with the inequality (23) we obtain

$$\lambda_1 < L_x < \frac{\omega_y H_z - \omega_z H_y}{\omega_y H_x - \omega_x H_y} \cdot L_x < \frac{\omega_y H_z - \omega_z H_y}{\omega_y H_x - \omega_x H_y} \cdot \lambda_2 < \lambda_2. \quad (26)$$

If β becomes greater than $\frac{\pi}{4}$ (see Figure 4) then the moment L_x can possess all possible values from λ_1 to λ_2 :

$$\lambda_1 < L_x < \lambda_2. \quad (27)$$

But at the same time inequality (19) must be fulfilled. As with the specified limitations the inequality

$-\frac{\omega_z H_y - \omega_y H_z}{\omega_y H_x - \omega_x H_y} > 0$ is valid, then from condition (27) it follows:

$$\frac{\omega_y H_z - \omega_z H_y}{\omega_y H_x - \omega_x H_y} \cdot \lambda_1 < \frac{\omega_y H_z - \omega_z H_y}{\omega_y H_x - \omega_x H_y} \cdot L_x < \frac{\omega_y H_z - \omega_z H_y}{\omega_y H_x - \omega_x H_y} \cdot \lambda_2.$$

When constructing stability domains the following question remains unresolved: at exactly which points the straight line $L_x(\omega_z H_y - \omega_y H_z) + L_z(\omega_y H_x - \omega_x H_y) = 0$ intersects the lines $L_x = \lambda_{1x}$, $L_x = \lambda_{2x}$, $L_z = \lambda_{1z}$, and $L_z = \lambda_{2z}$. Indeed, there are several possible cases of intersections of these lines.

In Figure 2 the straight line $L_x(\omega_z H_y - \omega_y H_z) + L_z(\omega_y H_x - \omega_x H_y) = 0$ on the boundary of stability domain intersects the straight lines $L_x = \lambda_{1x}$ and $L_z = \lambda_{2z}$.

Let us consider critical positions of the line $L_x(\omega_z H_y - \omega_y H_z) + L_z(\omega_y H_x - \omega_x H_y) = 0$ in which at least at one point of the rectangle with the boundaries $L_x = \lambda_{1x}$, $L_x = \lambda_{2x}$, $L_z = \lambda_{1z}$, $L_z = \lambda_{2z}$ stability will remain. From inequality (14) we get

$$L_z(\omega_y H_x - \omega_x H_y) < -L_x(\omega_z H_y - \omega_y H_z). \quad (16)$$

If the following conditions are fulfilled

$$\omega_y H_x - \omega_x H_y > 0, \quad (17)$$

$$\omega_z H_y - \omega_y H_z < 0, \quad (18)$$

then from condition (16) we get

$$L_z < -L_x \cdot \frac{\omega_z H_y - \omega_y H_z}{\omega_y H_x - \omega_x H_y}, \quad (19)$$

that corresponds to the case presented in Figure 2.

If the following inequality is fulfilled

$$\omega_y H_x - \omega_x H_y < 0, \quad (20)$$

then the domain of stability is above the straight line $L_x(\omega_z H_y - \omega_y H_z) + L_z(\omega_y H_x - \omega_x H_y) = 0$.

Let us consider at first a case when inequalities (17) and (18) are fulfilled. Let us specify the angle β between the axis L_x and straight line $L_x(\omega_z H_y - \omega_y H_z) + L_z(\omega_y H_x - \omega_x H_y) = 0$ as shown in Figure 2. For distinctness we will assume that all the values λ_{1x} , λ_{2x} , λ_{1z} , λ_{2z} are positive. With the given limitations the angle β may vary between 0 and $\frac{\pi}{2}$. Let us begin to decrease the angle

β , simultaneously rotating the line $L_x(\omega_z H_y - \omega_y H_z) + L_z(\omega_y H_x - \omega_x H_y) = 0$ around

the origin of coordinates until the position where only one pair of possible values L_x and L_z is left with which the system remains in stable equilibrium position. The critical position of the boundary of the stability domain

$L_x(\omega_z H_y - \omega_y H_z) + L_z(\omega_y H_x - \omega_x H_y) = 0$ is shown in Figure 3 with the red line. In critical position of the boundary $L_x(\omega_z H_y - \omega_y H_z) + L_z(\omega_y H_x - \omega_x H_y) = 0$ only one point of system stability is left.

Let us assume that a microsatellite has onboard magnetic coils with identical characteristics, then we obtain

$$\lambda_{1x} = \lambda_{1z} = \lambda_1, \lambda_{2x} = \lambda_{2z} = \lambda_2. \quad (21)$$

If the condition (21) and also the conditions specified earlier are fulfilled, then we obtain the graphic illustration of the problem represented in Figure 3.

At the moment when the boundary is in a critical position, the position of stable equilibrium of the system is determined only with one pair of magnetic moments of the coils, that is $L_x = \lambda_2$, $L_z = \lambda_1$. Let us begin to increase the angle β . While the straight line $L_x(\omega_z H_y - \omega_y H_z) + L_z(\omega_y H_x - \omega_x H_y) = 0$ is below the bisector of the first quadrant angle (see Figure. 3), the moment L_x may possess only a value from the interval $(\lambda; \lambda_2)$ where λ can be determined from the condition that the point $(\lambda; \lambda_1)$ belongs to the straight line $L_x(\omega_z H_y - \omega_y H_z) + L_z(\omega_y H_x - \omega_x H_y) = 0$. In this case the equality $L_x(\omega_z H_y - \omega_y H_z) + L_z(\omega_y H_x - \omega_x H_y) = 0$ is fulfilled. Thus, while the angle $\beta < \frac{\pi}{4}$, then

$$-\lambda_1 \cdot \frac{\omega_y H_x - \omega_x H_y}{\omega_z H_y - \omega_y H_z} < L_x < \lambda_2. \quad (22)$$

At the same time inequality (19) must be fulfilled. As with the specified limitations the inequality $-\frac{\omega_z H_y - \omega_y H_z}{\omega_y H_x - \omega_x H_y} > 0$ is fulfilled, from inequality (22) it follows that

$$\begin{aligned} & \lambda_1 \cdot \frac{\omega_y H_x - \omega_x H_y}{\omega_z H_y - \omega_y H_z} \cdot \frac{\omega_z H_y - \omega_y H_z}{\omega_y H_x - \omega_x H_y} < \\ & < -\frac{\omega_z H_y - \omega_y H_z}{\omega_y H_x - \omega_x H_y} \cdot L_x < -\frac{\omega_z H_y - \omega_y H_z}{\omega_y H_x - \omega_x H_y} \cdot \lambda_2. \end{aligned}$$

Hence we get

$$\lambda_1 < -\frac{\omega_z H_y - \omega_y H_z}{\omega_y H_x - \omega_x H_y} \cdot L_x < -\frac{\omega_z H_y - \omega_y H_z}{\omega_y H_x - \omega_x H_y} \cdot \lambda_2.$$

Then owing to the inequality

$$\lambda_1 < L_z < -\frac{\omega_z H_y - \omega_y H_z}{\omega_y H_x - \omega_x H_y} \cdot L_x < -\frac{\omega_z H_y - \omega_y H_z}{\omega_y H_x - \omega_x H_y} \cdot \lambda_2 \quad (23)$$

is true. Here we defined the angle β as an angle between the axis L_x and the straight line $L_x(\omega_z H_y - \omega_y H_z) + L_z(\omega_y H_x - \omega_x H_y) = 0$.

Hence it follows that the slope of the straight line $L_x(\omega_z H_y - \omega_y H_z) + L_z(\omega_y H_x - \omega_x H_y) = 0$ which is equal to $-\frac{\omega_z H_y - \omega_y H_z}{\omega_y H_x - \omega_x H_y}$ coincides with the tangent of the angle β , i.e.

$$\operatorname{tg} \beta = \frac{\omega_y H_z - \omega_z H_y}{\omega_y H_x - \omega_x H_y}. \quad (24)$$

Then equality (23) is true while $\operatorname{tg} \beta < \operatorname{tg} \frac{\pi}{4} = 1$.

Hence it follows fulfillment of the condition

$$0 < \omega_y H_z - \omega_z H_y < \omega_y H_x - \omega_x H_y. \quad (25)$$

And then jointly with the inequality (23) we obtain

$$\lambda_1 < L_z < \frac{\omega_y H_z - \omega_z H_y}{\omega_y H_x - \omega_x H_y} \cdot L_x < \frac{\omega_y H_z - \omega_z H_y}{\omega_y H_x - \omega_x H_y} \cdot \lambda_2 < \lambda_2. \quad (26)$$

If β becomes greater than $\frac{\pi}{4}$ (see Figure 4) then the moment L_x can possess all possible values from λ_1 to λ_2 :

$$\lambda_1 < L_x < \lambda_2. \quad (27)$$

But at the same time inequality (19) must be fulfilled. As with the specified limitations the inequality $-\frac{\omega_z H_y - \omega_y H_z}{\omega_y H_x - \omega_x H_y} > 0$ is valid, then from condition (27) it follows:

$$\frac{\omega_y H_z - \omega_z H_y}{\omega_y H_x - \omega_x H_y} \cdot \lambda_1 < \frac{\omega_y H_z - \omega_z H_y}{\omega_y H_x - \omega_x H_y} \cdot L_x < \frac{\omega_y H_z - \omega_z H_y}{\omega_y H_x - \omega_x H_y} \cdot \lambda_2.$$

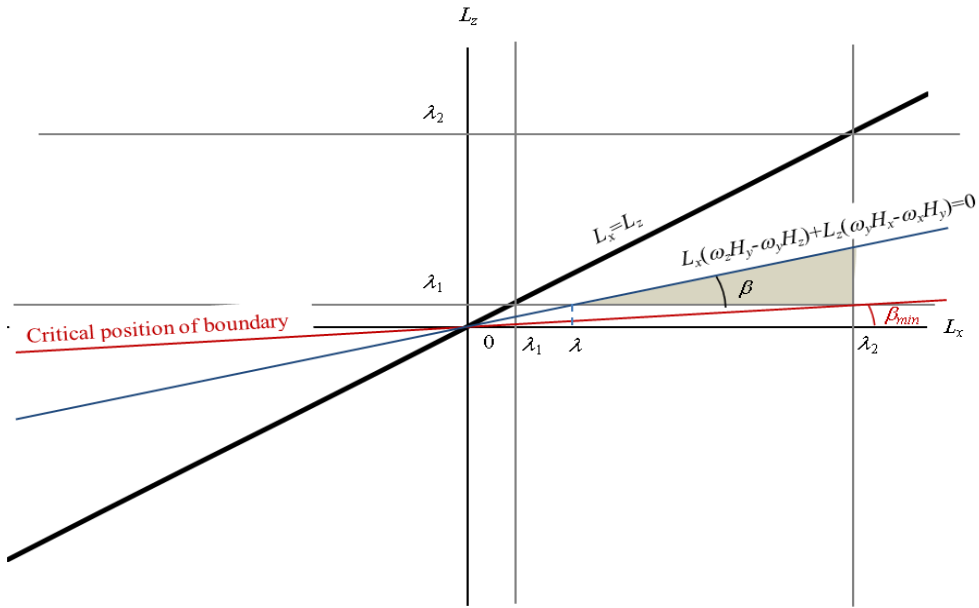


Figure 3. Stability domain with the angle $\beta < \frac{\pi}{4}$

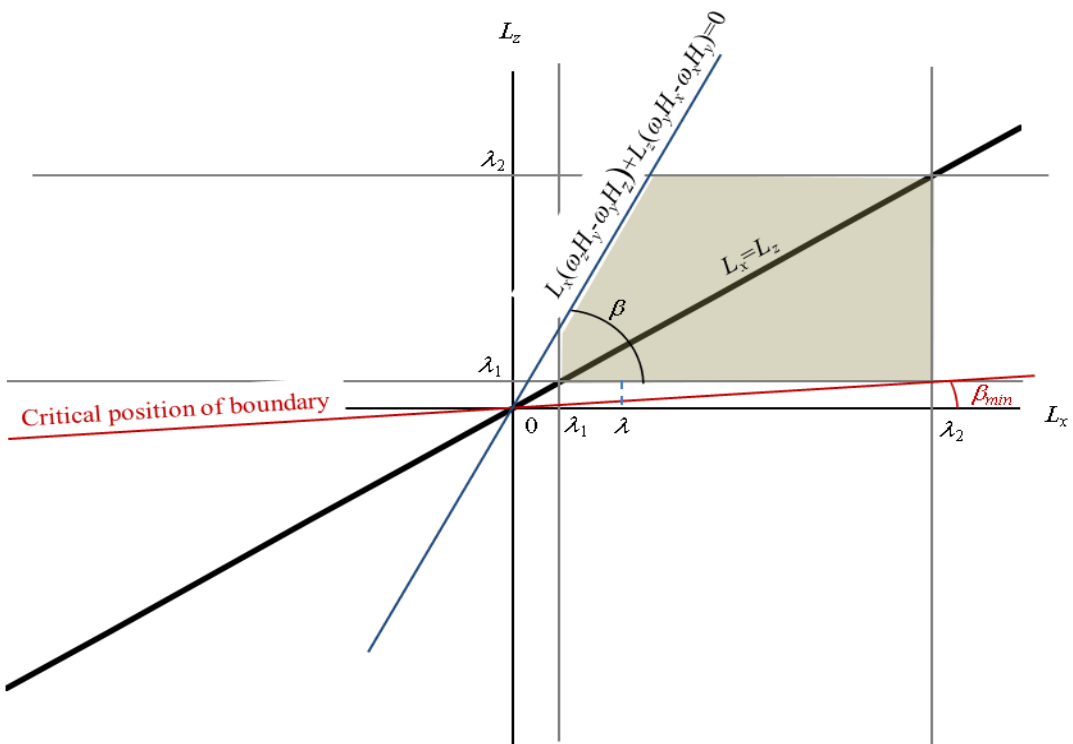


Figure 4. Stability domain in case of $\beta > \frac{\pi}{4}$

At the same time if the boundary of the domain is in a critical position, then the position of the stable equilibrium of the system is determined only by having one pair of values of magnetic moments on coils, that is $L_x = -\lambda_1$, $L_z = -\lambda_2$. Let us begin to decrease the angle β .

While the straight line $L_x(\omega_z H_y - \omega_y H_z) + L_z(\omega_y H_x - \omega_x H_y) = 0$ is below the bisector of the first quadrant shown in Figure 6 as thick straight line, the moment L_x can possess values from the interval $(-\lambda_x; -\lambda_1)$.

Here the value $-\lambda_x$ can be determined from the condition that the point $(-\lambda_x; -\lambda_2)$ belongs to the line $L_x(\omega_z H_y - \omega_y H_z) + L_z(\omega_y H_x - \omega_x H_y) = 0$. Then we get $\lambda_x = \lambda_2 \cdot \frac{\omega_y H_x - \omega_x H_y}{\omega_z H_y - \omega_y H_z}$. Thus, while $\beta > \frac{\pi}{4}$ the following inequality is valid

$$\lambda_2 \cdot \frac{\omega_y H_x - \omega_x H_y}{\omega_z H_y - \omega_y H_z} < L_x < -\lambda_1. \tag{33}$$

At the same time the inequality (19) must be fulfilled. As in the case of the limitation $-\frac{\omega_z H_y - \omega_y H_z}{\omega_y H_x - \omega_x H_y} > 0$, from inequality (33) it follows that

$$\begin{aligned} -\lambda_2 \cdot \frac{\omega_y H_x - \omega_x H_y}{\omega_z H_y - \omega_y H_z} \cdot \frac{\omega_z H_y - \omega_y H_z}{\omega_y H_x - \omega_x H_y} < \\ < -\frac{\omega_z H_y - \omega_y H_z}{\omega_y H_x - \omega_x H_y} \cdot L_x < \frac{\omega_z H_y - \omega_y H_z}{\omega_y H_x - \omega_x H_y} \cdot \lambda_1. \end{aligned}$$

Therefore, we get the inequality

$$-\lambda_2 < -\frac{\omega_z H_y - \omega_y H_z}{\omega_y H_x - \omega_x H_y} \cdot L_x < \frac{\omega_z H_y - \omega_y H_z}{\omega_y H_x - \omega_x H_y} \cdot \lambda_1.$$

Then owing to inequality (19) the following inequality is valid

$$-\lambda_2 < L_z < -\frac{\omega_z H_y - \omega_y H_z}{\omega_y H_x - \omega_x H_y} \cdot L_x < \frac{\omega_z H_y - \omega_y H_z}{\omega_y H_x - \omega_x H_y} \cdot \lambda_1. \tag{34}$$

The stability domain in this case is shown in Figure 6.

Thus, we defined the angle β as the angle between the axis L_x and the straight line

$L_x(\omega_z H_y - \omega_y H_z) + L_z(\omega_y H_x - \omega_x H_y) = 0$. As the slope of the straight line $L_x(\omega_z H_y - \omega_y H_z) + L_z(\omega_y H_x - \omega_x H_y) = 0$

which is equal to $-\frac{\omega_z H_y - \omega_y H_z}{\omega_y H_x - \omega_x H_y}$ coincides with the tangent of the angle β (24), inequality (34) is valid

while $\text{tg } \beta > \text{tg } \frac{\pi}{4} = 1$. Hence it follows that

$$\omega_y H_z - \omega_z H_y > \omega_y H_x - \omega_x H_y. \tag{35}$$

And then jointly with inequality (38) we get

$$-\lambda_2 < L_z < -\frac{\omega_z H_y - \omega_y H_z}{\omega_y H_x - \omega_x H_y} \cdot L_x < -\lambda_1. \tag{36}$$

As soon as β becomes less than $\frac{\pi}{4}$ (see Figure 7)

L_x can possess all possible values from λ_1 to λ_1 :

$$-\lambda_2 < L_x < -\lambda_1. \tag{37}$$

But at the same time the inequality (19) must be fulfilled. Moreover, jointly with inequality (37) owing to inequality (19) the following is true

$$-\lambda_2 < L_z < \frac{\omega_y H_z - \omega_z H_y}{\omega_y H_x - \omega_x H_y} L_x. \tag{38}$$

We note that inequality (38) is true while

$\text{tg } \beta \leq \text{tg } \frac{\pi}{4} = 1$, therefore

$$\frac{\omega_y H_z - \omega_z H_y}{\omega_y H_x - \omega_x H_y} \leq 1. \tag{39}$$

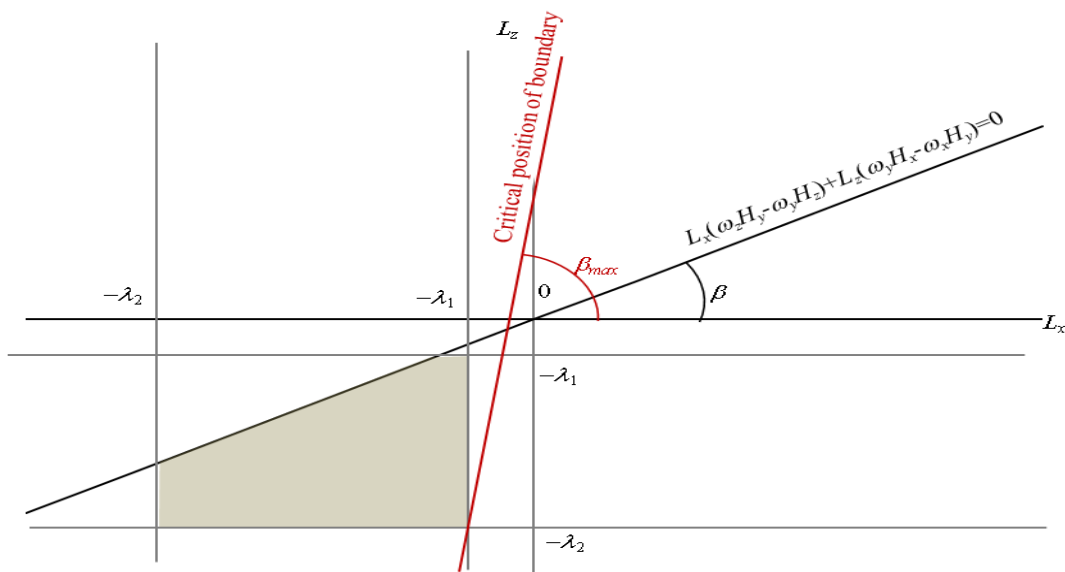


Figure 5. Graphical interpretation of the stability domain with using of two identical magnetic coils with negative values of magnetic moments

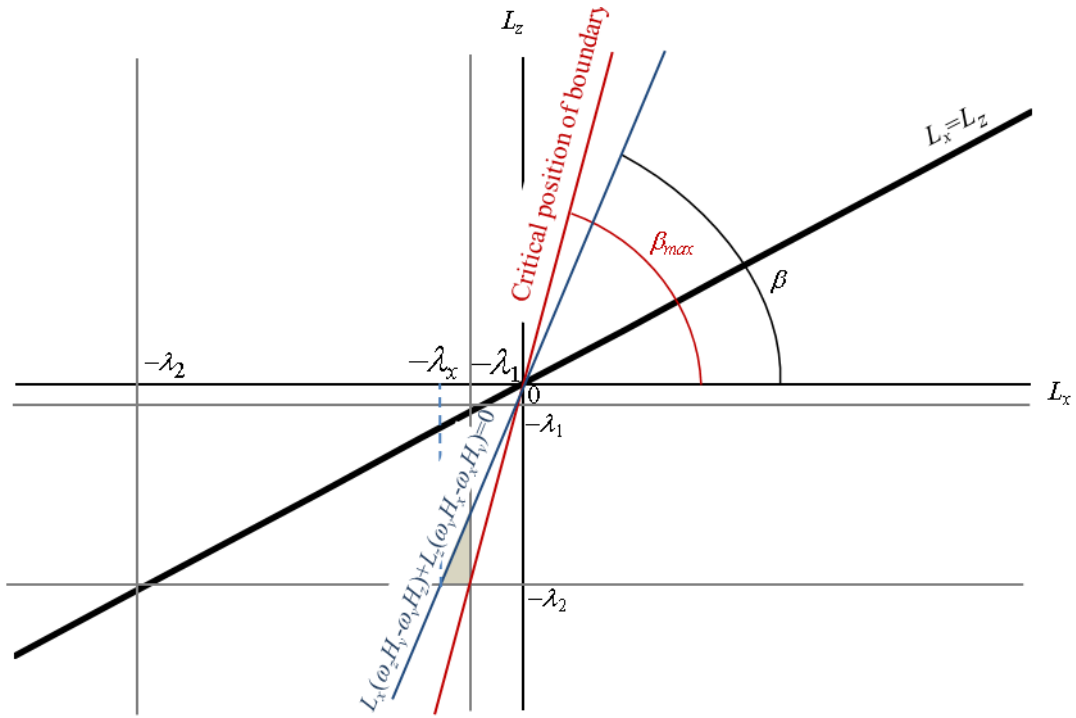


Figure 6. Stability domain in case of $\beta > \frac{\pi}{4}$ and negative values of magnetic moments

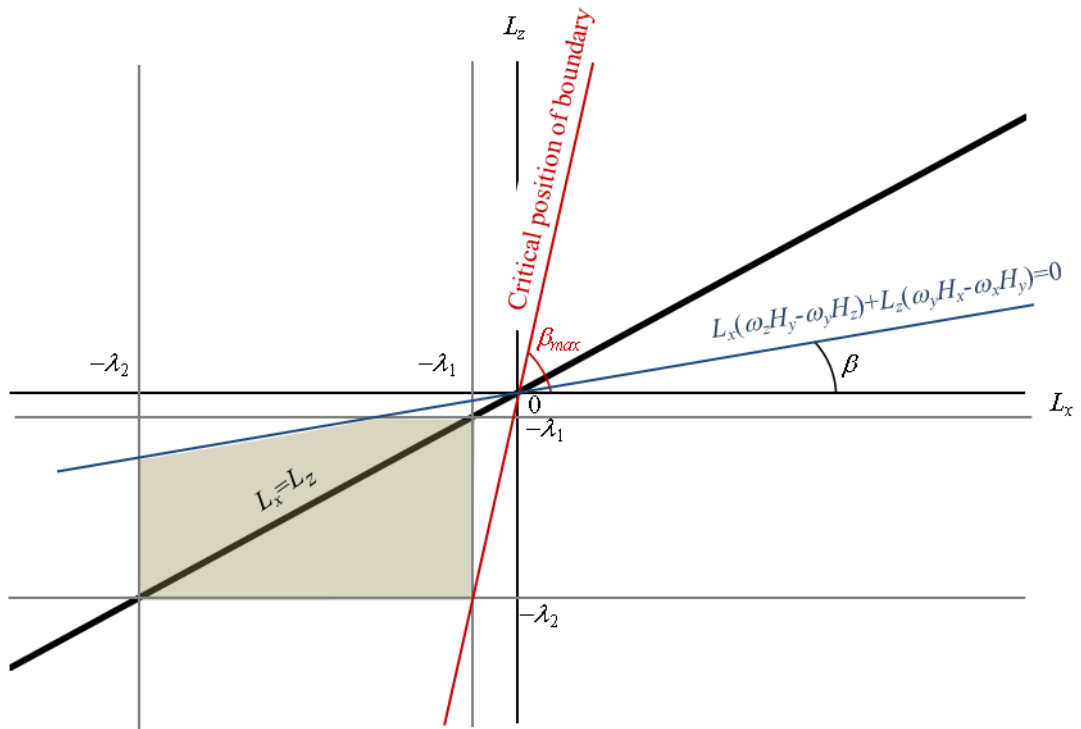


Figure 7. Stability domain in case of $\beta < \frac{\pi}{4}$ and negative values of moments of inertia

4. The algorithm of finding of the magnetic moments

The domains of magnetic moments of the microsatellite with the two onboard coils that ensure the asymptotic stability of the trivial solution $\omega_x = \omega_y = \omega_z = 0$ were determined. The study revealed the following characteristic cases of constructing the domains of magnetic moments.

1. When conditions (17) and (18) are fulfilled, in case inequality (25) is fulfilled and values of magnetic moments are positive, the asymptotic stability of the equilibrium position of the system requires the fulfillment of the inequality (26).

2. When conditions (17) and (18) are fulfilled, in case inequality (28) is fulfilled and values of magnetic moments are positive, the asymptotic stability of the equilibrium position of the system requires the fulfillment of the inequality (29).

3. When conditions (17) and (18) are fulfilled, in case the inequality (35) is fulfilled and values of magnetic moments are negative, the asymptotic stability of the equilibrium position of the system requires the fulfillment of inequality (36).

4. When conditions (17) and (18) are fulfilled, in case the inequality (39) is fulfilled and values of magnetic moments are negative, the asymptotic stability of the equilibrium position of the system requires joint the fulfillment of inequalities (37) and (38).

The found domains of stability of the system should be determined at each particular instant of the time of the microsatellite motion. Let us consider an algorithm of finding the magnetic moments what ensure damping angular velocities of a microsatellite with two onboard coils. The algorithm is presented in Figure 8. This algorithm contains the described above results of constructing of the asymptotic stability domains with numbers 1-4.

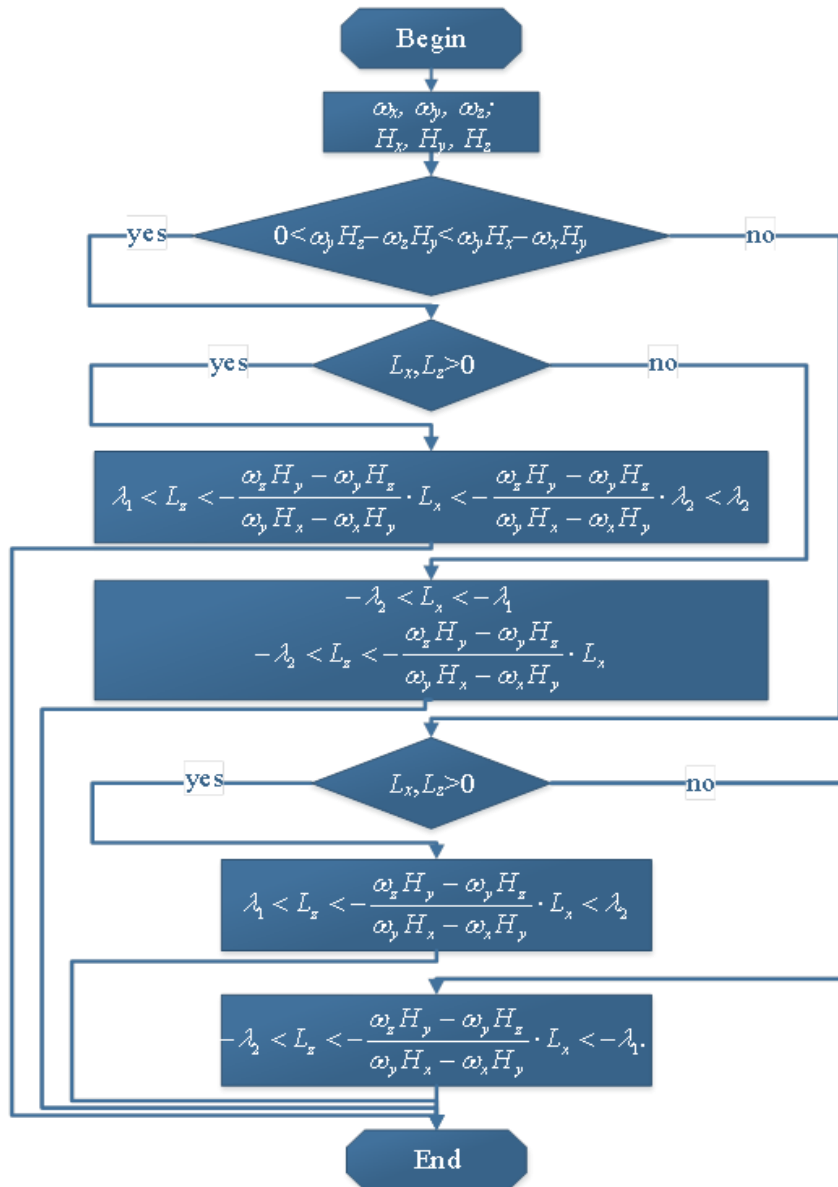


Figure 8. The algorithm of finding of the magnetic moments that ensure asymptotic stability of the system

5. Conclusion

The main problem considered in the paper is the calculation of domains of the magnetic moments of two onboard coils, which lead of stable damping of the microsatellite angular velocities. The paper is devoted to solving this problem. Application of Lyapunov's method allows us to obtain the conditions of asymptotic stability in the problem of controlled damping of angular velocity of the parallelepiped-shaped microsatellite with two onboard magnetic coils. The analysis of the stability conditions has determined the domains of the coils magnetic moments leading to the asymptotic stability of the system solution. This study considered a special case of the relation between the magnitudes of angular velocities and the magnitudes of the magnetic field intensities caused by fulfillment of the inequalities (17)-(18). Note that similar considerations are also possible to obtain the stability domains with other special limitations on the angular velocity and the intensity of the magnetic field. However, these results are beyond the scope of this paper, but can be considered in subsequent publications. It should be noted that the described angular velocity damping algorithm can be applied to modeling the rotational motion of new microsatellites or nanosatellites with the magnetic control system.

The domains of the asymptotic stability were obtained for a microsatellite in the form of a parallelepiped. However, similar stability domains can be defined for microsatellites of any other forms. It is necessary to recalculate the magnitudes of the principal central moments of inertia of the microsatellite by formulas (2). It should be noted that these results are valid for arbitrary initial angular velocities.

References

- [1] Beleckiy VV, Shentov AA. Rotational motion of a magnetized satellite. Moscow: Nauka; 1985.
- [2] A.V. Sedelnikov, "Evaluation of the level of microaccelerations on-board of a small satellite caused by a collision of a space debris particle with a solar panel". Jordan Journal of Mechanical and Industrial Engineering, Vol.11, No. 2, 2017, 121-127.
- [3] Vinnikov VV. The basics of designing electronic means. SPb.: SZTU publishing house; 2009.
- [4] V.V. Lyubimov, A.A. Osipov, N.D. Semkin, "Rotational Motion of a Nanosatellite Using Onboard Electromagnetic Coils after Collision with a Solid High-Speed Particle". 11th International Siberian Conference on Control and Communications, Omsk, Russia, 2004.
- [5] Maini AK, Varsha A. Satellite Technology: Principles and Applications. Chichester: John Wiley; 2007.
- [6] Kovalenko AP. Magnetic Spacecraft Control Systems. Moscow: Mashinostroenie; 1975.
- [7] Alpatov AP, Dranovskiy VI, Saltikov YD, Horoshilov VS. The dynamics of the spacecraft with the magnetic control systems. Moscow: Mashinostroenie; 1978.
- [8] A. Slavinskis, U. Kvell, E. Kulu, I. Sünter, H. Kuuste, S. Lätt, K. Voormansik, M. Noorma, "High spin rate magnetic controller for nanosatellites". Acta Astronautica, Vol. 95, No. 1, 2014, 218-226.
- [9] M.Yu. Ovchinnikov, V.I. Penkov, D.S. Roldugin, S.O. Karpenko, "Investigation of the effectiveness of an algorithm of active magnetic damping". Cosmic Research, Vol. 50, No. 2, 2012, 170-176.
- [10] M.Yu. Ovchinnikov, D.S. Roldugin, V.I. Penkov, "Three-axis active magnetic attitude control asymptotical study". Acta Astronautica, Vol. 110, 2015, 279-286.
- [11] Y. Yang, "Spacecraft attitude and reaction wheel desaturation combined control method". IEEE Transactions on Aerospace and Electronic Systems, Vol. 53, Issue 1, 2017, 286-295.
- [12] Y. Yang, "Controllability of spacecraft using only magnetic torques". IEEE Transactions on Aerospace and Electronic Systems, Vol. 52, No. 2, 2016, 954-961.
- [13] A.L. Rodriguez-Vazquez, M.A. Martin-Prats, F. Bernelli-Zazzera, "Spacecraft magnetic attitude control using approximating sequence Riccati equations". IEEE Transactions on Aerospace and Electronic Systems, Vol. 51, Issue 4, 2015, 3374-3385.
- [14] V.V. Lyubimov, S.V. Podkletnova, "Modeling the optimal reduction of the small angular velocity of a microsatellite using onboard magnetic coils". 10th International IEEE Scientific and Technical Conference Dynamics of Systems, Mechanisms and Machines, Dynamics, Omsk, Russia, 2016.
- [15] V.V. Lyubimov, S.V. Podkletnova, A.A. Osipov, "Simulating the process of microsatellite angular velocity decrease using various laws of electromagnetic coil control". 22nd Saint Petersburg International Conference on Integrated Navigation Systems, Saint Petersburg, Russia, 2017.
- [16] V.V. Lyubimov, "External stability of resonances in the motion of an asymmetric rigid body with a strong magnet in the geomagnetic field". Mechanics of Solids, Vol. 45, No. 1, 2010, 10-21.
- [17] V.V. Lyubimov, "Some features of disturbed rotational motion of a satellite with a strong onboard magnet". Russian Aeronautics, Vol. 52, No.2, 2009, 172-175.
- [18] V.V. Lyubimov, "Resonant mechanical moment during rotation of a microsatellite with a magnet and flywheels on board: Features, time interval, measurement methods". 24th Saint Petersburg International Conference on Integrated Navigation Systems, Saint Petersburg, Russia, 2017.

Embedded Wireless Testing System Applied in Coal Cutting Experiment

Chenxu Luo^{*}, Shuangxi Jing, Yu LIU, xiaoming HAN

School of Mechanical and Power Engineering, Henan Polytechnic University, Jiaozuo454000, China

Received APRIL 30 2018

Accepted JULY 26 2018

Abstract

The Study aims at finding solutions to the existing condition that is difficult to achieve the operation of the wire data transmission in the process of shearer cutting, which demands putting forward an embedded wireless testing system that meets 3D mechanical signal collection and transmission. Embedded signal acquisition and wireless data transmission are included by the test system. Signal acquisition device is used to get the three-dimensional force of shearer pick cutting coal and rock, the wireless data transmission was built based on the zigbee wireless technology and labview virtual technology. This system is utilized in the coal cutting test-bed (CTBCR), two sequential cylinder head with different cutting parameters were used in the cutting experiment. The results show that The relationship between the cutting force and the coal compressive strength, pick-tip cone angle, drum rotate speed, traction speed. Fluctuation in the cutting force has a linear relationship to coal compressive strength and traction speed. A plot of cutting force fluctuations versus the cutting thickness follows a sigmoidal curve. Based on the analysis of these test results a theoretical basis is supplied for design and effective use of shearer drums.

© 2018 Jordan Journal of Mechanical and Industrial Engineering. All rights reserved

Keywords: *Wireless transmission, embedded system, shearer pick, cutting force, cutting thickness.*

1. Introduction

When cutting the coal seam, the cutting pick of the shearer drum suffers a great impact and friction, which is a disadvantage for the shearer normal operation. The cutting load has a Significant influence on the shearer drum cutting specific consumption, cutting efficiency, dust quantity, stability and reliability^[1-2]. So the study on pick cutting force can provide relevant basis for the design of shearer drum. Scholars at home and abroad have done a large number of experiments on pick cutting force. Foreign representative is Nishimatsu who came from UK and Evans who came from Japan. They respectively established the pick cutting force formula according to the maximum tensile stress and maximum shear stress type^[3-4] But the formula design suits to coal cutting, and it has certain gap with the drum of shearer picks cutting^[5-7]. Xia Yimin etc.^[7-8] studied the dynamics of spiral cutting method based rock breaking, pointing out its load fractal in 2005. Li Xiaohuo etc.^[5-6] established different kinds of dynamic model: the cutting unit for continuous miner and drum type shearer, which provides the basis for the research, that numerical methods for solving continuous

miner cutting unit vibration state differential equation, under different working conditions and loading conditions of various mass, stiffness and damping factor of each part of the cutting unit vibration impact on the continuous miner in 2009. Domestic scholars researched on the pick not only the mechanical model was established, but also points out the influence parameters of the pick cutting force and its change rule^[8-9]. And that they all carried out in a straight line cutting conditions, it is different in terms of the actual working condition^[10-11]. Given the disadvantage of current test system based on the cable connection, it is hard to avoid cable layout complex, high cost, poor maintainability and system flexibility^[12-13], therefore, the solution is to use the wireless network test mode to build embedded wireless testing system, the cutting force signal is collected, then the wireless data was transferred to the PC, and carry on related research about dynamic performance^[14-16]. Related experiments were made based on the actual cutting condition. On the coal cutting test-bed, the embedded wireless testing system was used to study the influence on cutting load of cutting material parameters and the pick parameters. It can provide theoretical basis for designing a better pick cutting performance type cutting pick^[17-18].

* Corresponding author e-mail: xzhqingting@163.com.

2. Cutting test-bed based on coal

According to the theory of coal mining machine cutting coal and the similarity theory, the coal cutting force test-bed(Fig.1)and different types picks(Fig. 2) were developed, and the simulation of cutting coal seam was made^[19].

In order to meet with the actual condition in conformity with the drum shearer cutting coal and rock, propulsion cylinder working mesa translation as a cylinder along the axial movement was used, also using the pinion with rack drives the coal seam along with the radial feed movement to meet the drum cutting coal and rock movement. Cutting power of coal cutting test-bed is 15 kw, drum speed range is 0~200 r/min, the coal seam translational velocity is 0 ~ 10 m/min, translation range is 0 ~ 2.5 m,Cylinder of the hydraulic cylinder speed is 0~2 m/min, use the coal cutting test-bed to studying the related experiment^[20-21].



Figure 1: Coal cutting experiment and test system

2.1. The embedded wireless testing system

The function of the launcher based on wireless data transmission is acquisition, processing, and then making the electromagnetic wave signals emitted by wireless transmission. As shown in figure 3 embedded wireless testing system hardware block diagram. The wireless acquisition circuit design mainly includes the transformation of launcher amplifier circuit, filter circuit, A/D conversion circuit, single chip acquisition circuit and peripheral circuit, such as wireless transmitting and receiving modules. Single-chip microcomputer control A/D converter for the power supply voltage and the sensor signal acquisition and conversion, and the transformed signal digital should be processed and coded and then passed on to the wireless transmitting module for launching out.



Figure 2: Test picks

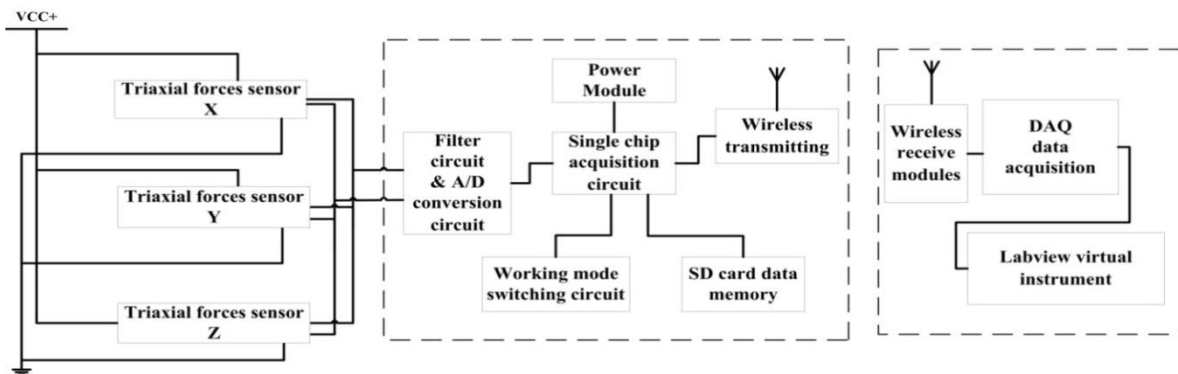


Figure 3: Embedded wireless testing system hardware diagram

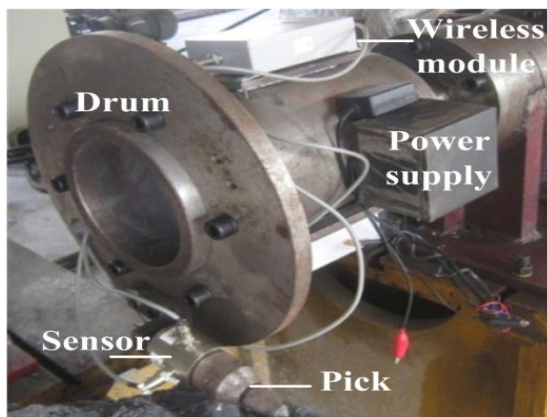


Figure 4: Pick sensor and wireless data transmission module



Figure 5: The Labview virtual acquisition signal display

PC is designed and produced based on the acquisition signal displayer of labview virtual instrument. As shown in Figure 5, the user interface is the visual display screen of the collected signals by this system, in this you can learn the shearer drum speed test facility, you can learn kinematics parameters such as feed speed of coal seam, you can also get the parameters under the condition of pick cutting three force.

3.3 Experimental study

3.1. The influence of coal compressive strength on the cutting force

According to the compressive strength of coal seam simulation similar standards, three kind of coal seams was made as shown in table 1. These single pick cutting experiments was carried out to research the influence of pick cutting load under different compressive strength of coal seam. Material parameters shown in table 1. And the drum cylinder speed is 60 r/min, the coal seam traction speed is 0.6m/min, drum diameter of 480mm, pick impact angle is 50°, inclination angle is 0°, pick

carbide tip diameter is 10mm, pick-tip cone angle 75°, pick-body cone angle 25°, pick body material is 40Cr, test time is 5 s. (corresponding to the five rotating cycle).

To get the cut load and volatility of pick in cutting different materials of coal seam conditions, three groups of test results about single cutting pick rotating 5 circumference cutting three types coal seam were analyzed as results listed in table 2. Among the load average is in the process of cutting pick cut coal seam (excluding no-load phase). Peak averages load is 5 cutting cycle of the average of the peak load, which indicates the impact of the cutting pick. Standard deviation represents the load fluctuation in the process of pick cutting coal seam; the greater the value shows, the more severe the load fluctuation is, it is not conducive to the stability of the whole machine. According to the results of statistical analysis, under the condition of the coal and rock material cutting, cutting pick cutting force and radial resistance all shown increasing trend with the increase of coal and rock compressive strength. Obviously the cutting material of cutting pick produce a great impact on the cutting force, the following have the specific analysis.

Table 1: Property parameters of experimental coal materials

Coal seam	Compressive strength	Friction coefficient	Poisson ratio	Density(kg/m ³)
Coal seam I	0.69	0.36	0.27	1414.64
Coal seam II	1.58	0.36	0.26	1563.53
Coal seam III	2.73	0.36	0.29	1608.56

Table 2: Statistics of cutting loads for different compressive strength coal

Compressive strength (MPa)	Mean cutting force (N)	Peak average cutting force (N)	Standard deviation	Mean radial resistance (N)	Peak average radial resistance (N)	Standard deviation
0.69	109.01	201.41	16.80	31.44	147.38	16.55
1.58	154.55	265.56	17.83	32.50	177.8	15.28
2.73	176.21	323.75	17.13	45.77	209.2	16.98

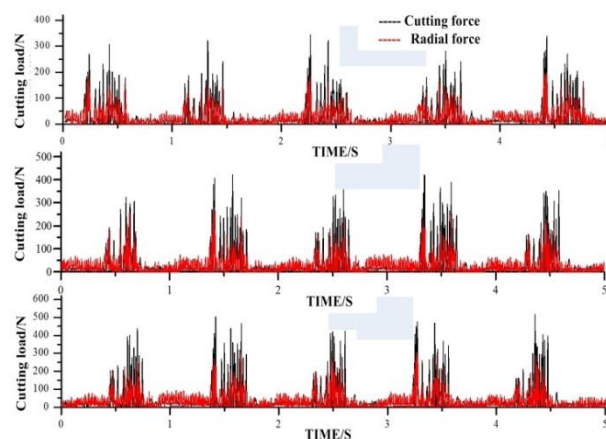


Figure 6: Mean cutting force of different compressive strength

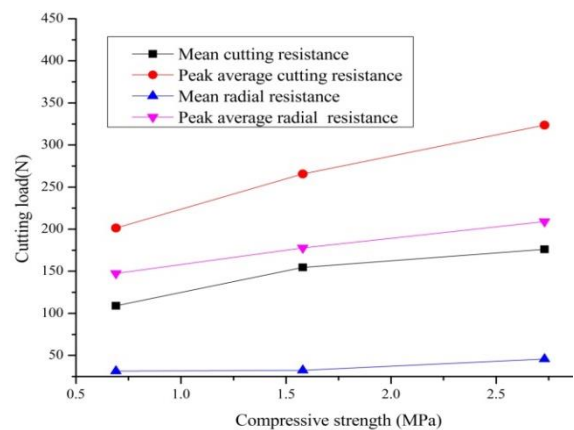


Figure 7: Relations of compressive strength and cutting force

Draw the curve of cutting load and compressive strength (fig.7). Seen from the results, with the increase of compressive strength, cutting force changes in the average peak average cutting force changes gently. Because the cutting average describes the average value of the load in the process of the interaction between cutting pick and coal seam. Cutting force peak means that in the process of cutting coal collapse fall down before cutting force rapid growth at the upper end of the maximum point of critical load. So the single peak load is difficult to fully describe the cutting broken rule, average analysis more accurate. Radial resistance changes with the compressive strength of trend is basically consistent with the cutting force, but the radial resistance on the amplitude is less than the cutting force. On the one hand, the traction speed in cutting process is far less than the linear velocity of top cutting gear pick, so in the process of rotary cutting, cutting load of the cutting pick instantaneous direction along the direction of cutting force component. On the other hand, on the direction of cutting force pick extrusion and impact crushing coal seam at the same time, but on the radial resistance direction is pure of extrusion, and the broken area is smaller. Combined with figure 6 and 7, it indicates that cutting load along with the change tendency of the compressive strength. There is a linear relationship

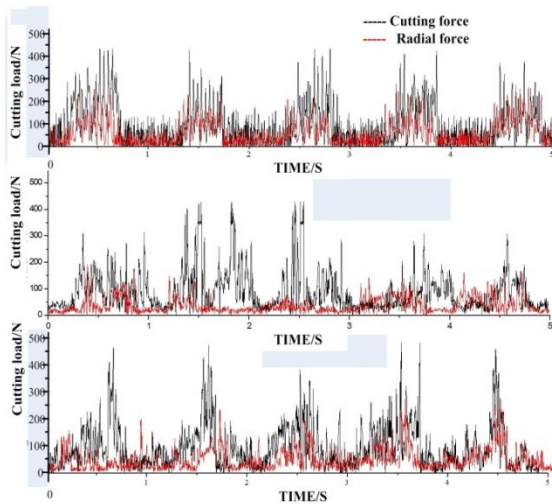


Figure 8: Cutting force graph of different pick-tip cone angles

between the coal strength and cutting force. However, the cutting force fluctuation which is coefficient of different coal and rock strength did not show the same distribution.

3.2. The influence of pick-tip cone angle on the cutting force

The size of the gear pick-tip cone angle determines the cut pick degree of the sharp knives, sharp cutting pick are more likely to pressure into the coal. Theory research results [22] have confirmed that the performance of sharp knives cutting coal is higher than a blunt tool, but it is not enough, so this section experimental study was carried on about the effect of different pick-tip cone angle on the cutting performance of coal seam. In order to study the influence of pick-tip cone angle on cutting force, respectively use 75°, 85° and 100° three types of pick-tip cone angle (as shown in figure 8. Cutting seam III, the drum cylinder speed is 60 r/min, the coal seam traction speed is 0.6m/min, drum diameter of 480mm, pick impact angle is 50°, inclination angle is 0°, pick carbide tip diameter is 10mm, pick-body cone angle 25°, pick body material is 40Cr, test time is 5 s. The pick cutting force domain curve as shown in figure 6, cutting force statistics as shown in table 3.

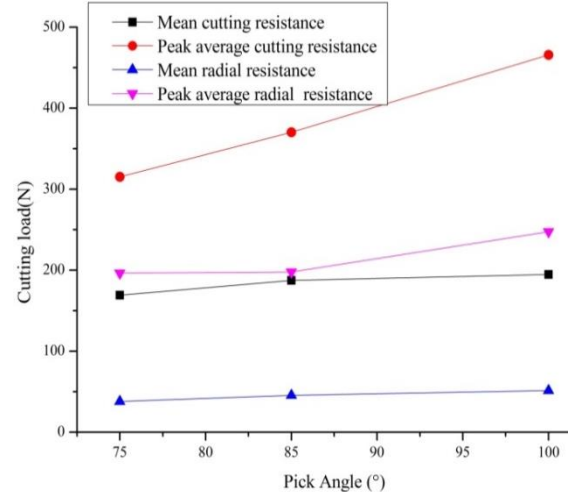


Figure 9: Relationship between pick-tip cone angle and cutting load

Table 3: Statistics of cutting loads for picks with different pick-tip cone angles

Pick-tip cone angle (°)	Mean cutting force (N)	Peak average cutting force (N)	Standard deviation	Mean radial resistance (N)	Peak average radial resistance (N)	Standard deviation
75°	169.01	315.11	17.13	37.83	196.21	16.98
85°	187.34	370.23	17.83	45.50	197.82	15.28
100°	194.55	465.64	16.80	51.44	247.4	17.55

Seen from table 3 and figure 9, the experimental study of the pick-tip cone angle, cutting load increases with the increase of pick-tip cone angle, but the change trend of volatility have no obvious regularity. So the size of the gear pick-tip cone angle has a great influence on the cutting pick cutting load, the specific analysis as following. Seen from the figure 9, with the increase of pick-tip cone angle, the cutting load peak average change obviously, the mean cutting load change quite gentle, This shows that the size of the pick-tip cone angle greatly influenced the cutting load peak and the coal spallation situation that appear in the process of cutting coal seam. The more smaller the pick-tip cone angle is, the more sharper the pick are, the more easier coal avalanche fall, the cutting load smaller.

In addition, when the pick-tip cone angle is greater, the probability of interference between pick body and the coal body of coal is also greater, and the friction resistance be greater too. As a result the cutting load is bigger. Therefore, when designing pick, when the shearer drum rotating speed, traction speed and pick impact angle established, in order to reduce the wear of pick quantity and improve the stress of the pick, we can design pick-tip cone angle according to this part of the test results coincide with the simulation results.

3.3. The influence of cutting movement parameters on cutting force

When the pick cutting pick rotary cutting, the motion parameters include: The rotation of the drum n and the coal

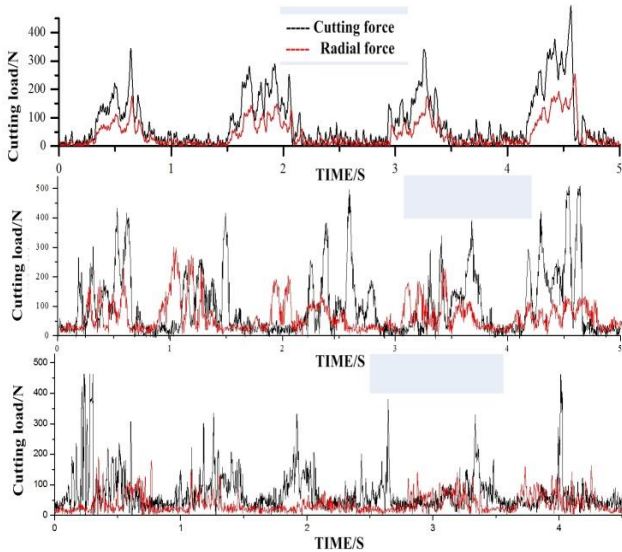


Figure 10: Time domain graph of cutting load with the drum rotating being 60r/min

seam movement speed v_q (traction speed). But, these two parameters can be represented by the maximum cutting thickness h_{max} , the conversion formula is:

$$h_{max} = 1000v_q / (nm) \tag{3}$$

In the formulam 3 is the number of cutting pick on each cutting line, When change the drum rotating speed or pulling speed, single pick chip thickness changes.

3.3.1. The influence of the drum rotate speed on pick cutting force

In order to study pick cutting load changes under different drum speed conditions, test condition is the drum diameter of 480mm, pick impact angle is 50°, inclination angle is 0°, pick carbidetip diameter is 10mm, pick-tip cone angle 75°, pick-body cone angle 25°, pick body material is 40Cr, test time is 5 s. drum speed respectively 40 r/min, 60 r/min and 80 r/min. In order to ensure maximum cutting thickness is 10 mm, respectively the corresponding coal seam traction speed is 0.4 m/min, 0.6 m/min, 0.8 m/min.

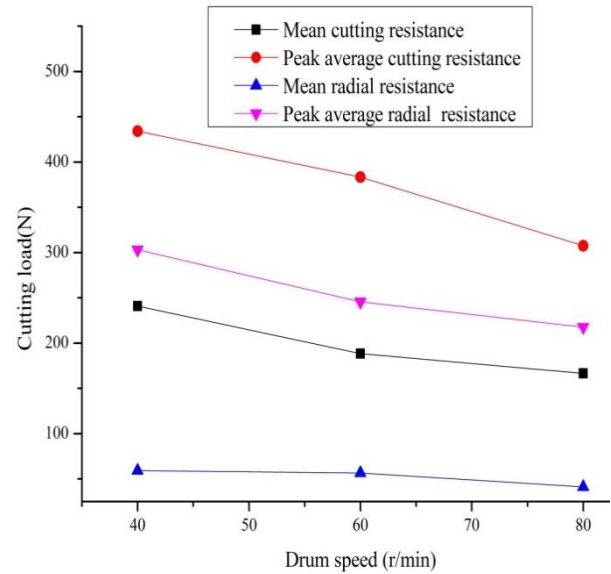


Figure 11: Relationship between drum rotating speed and cutting load

Table 4: Statistics of cutting load with different drum rotating speeds

Drum speed (r/min)	Mean cutting force (N)	Peak average cutting force (N)	Standard deviation	Mean radial resistance (N)	Peak average radial resistance (N)	Standard deviation
40	240.93	434	10.54	59.25	303	10.64
60	188.29	383.5	26.18	56.62	245.6	12.05
80	166.62	307.5	13.83	41.34	217.6	16.52

The domain waveform of the cutting load under different drum speeds in five cutting cycle time as shown in figure 10. Statistical analysis is carried on for the cutting load of three types single pick under different drum rotation speed condition and list in table 4. Draw the relation curve between cutting load and drum rotational speed (Fig.11). The above two type of fitting residual error are within the confidence region, fitting residual error within the confidence region, therefore, within the scope of the study the fitting change law correctly. As observed from the table 4 and figure 11, the cutting load is reduced with the increase of drum speed and it coincides with this formula obtained according to the theory of simulation results. The reasons for this situation is along with the rising of the drum rotating speed, instantaneous velocity of cutting pick increase when impact the coal and rock. Due to the required energy of coal and rock crushing is certain, so the cutting load reduce.

3.3.2. The influence of traction speed on pick cutting force

Shearer in the process of practical work, general drum rotating speed is constant, only by changing the traction speed

change cutting thickness, as the cutting thickness raises, coal cutting force raises. So shearer should reduce the traction speed when cutting hard coal, avoid machine overworked. When cutting soft coal can increase the traction speed in order to improve the productivity. In order to study pick cutting load under the condition of different traction speed and carry out three cutting test under the different traction speed. Test conditions shown as table 5.

The experimental study of this paper is aimed at single pick cutting, the cutting form is plane cutting when single pick cutting the smooth surface of coal seam. Plane cutting generated the coal debris in break toward two sides [7,19-21]. In the condition of laboratory is easier to realize cutting coal seam, So often use the cutting load of single pick and energy consumption under the condition of laboratory as the standard of cutting performance. The time domain waveform of cutting load under different traction speed in five cutting cycle is shown in figure 13. Under the condition of three different traction speed, carried on statistical analysis, the results listed in Table 6.

Table 5: Cutting parameters of different experimental conditions

Traction speeds (m/min)	Drum speed (r/min)	Pick-body cone angle (°)	Impact angles (°)	Cutting thicknesses (mm)	inclination angles (°)	Pick-tip cone angles (°)
0.3	60	25°	50°	5	0	75°
0.6	60	25°	50°	10	0	75°
0.9	60	25°	50°	15	0	75°



Figure 12: Presentation of different cutting thicknesses tests

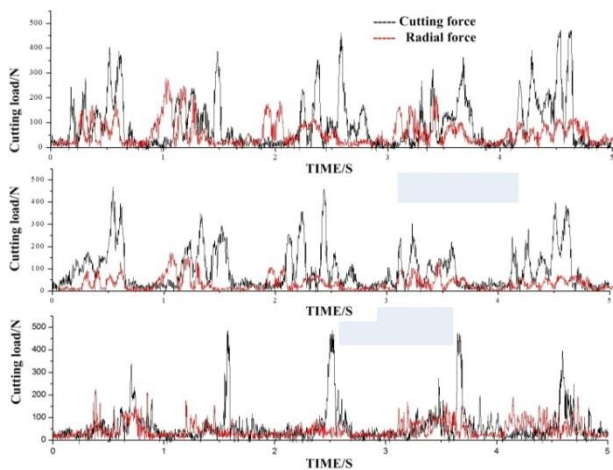


Figure 13: Time domain graph of cutting load with the traction speed being 0.6m/min

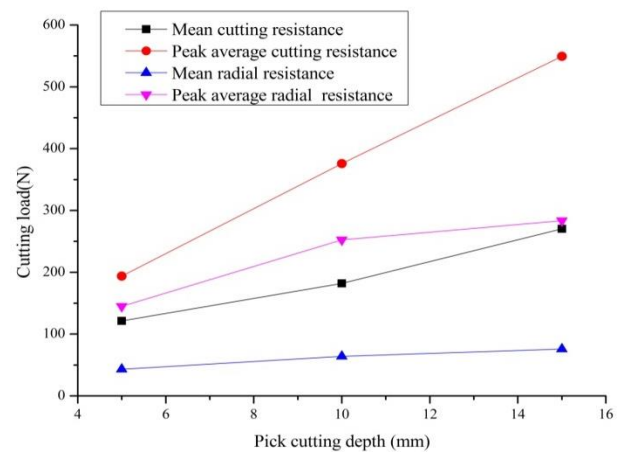


Figure 14: Relationship between cutting thickness and cutting load

Table 6: Statistics of cutting load with different drum traction speeds

Pick cutting thickness (mm)	Mean cutting force (N)	Peak average cutting force (N)	Standard deviation	Mean radial resistance (N)	Peak average radial resistance (N)	Standard deviation
5	121.49	193.9	13.29	43.15	145	18.63
10	182.03	375.7	12.65	64.13	252.5	13.21
15	270.48	549.5	14.71	75.96	283.5	16.23

Draw the relationship curve between the cutting load and cutting thickness (fig.14), According to the test results can be seen, cutting load increase with the traction speed increase, which coincide with the simulation results. Because this section drum rotating speed is constant, So the traction speed lead to cutting thickness increase, cutting thickness increases, the cutting load increase obviously. In addition, cutting the peak load is bigger than the average increase of cutting load average growth. The phenomenon generated by the following reason ,the increase of the pulling speed cause the increase of the cutting thickness, so the chip blocks of the corresponding caving are bigger , so from dense cores in the process of cutting to the coal caving the required cutting pick forces is bigger, so the peak load increase obvious.

4. Conclusion

- Under the working conditions, coal and rock cutting experiment is difficult to achieve cable data transmission. This device is designed to provide a scheme that can meet the data signal transmission. Experiment test system includes the design of the power supply circuit, signal amplification circuit, filter circuit, A/D conversion circuit, SCM (single chip micropyco) acquisition circuit, the design of the wireless communication module transmission circuit, and the design of the wireless receiver circuit.
- (2) In the scope of this experimental study, when cutting coal seam uses the larger alloy head, cutting pick can reduce the fluctuation of cutting load, and it can guarantee that the drum should run smoothly. With the increase of cutting thickness, the cutting energy consumption increases. As observed from maximum of cutting load and average cutting load, the cutting load increases with the increase of compressive strength.
- In the scope of this experimental study, with the increase of pick-tip cone angle cutting load showed a trend of increase, the cutting peak mean load change obviously. When pick-tip cone angle is smaller, coal avalanche fall is relatively easy, so cutting peak load is relatively smaller. The big pick-tip cone angle is good for pick cuts into the coal seam.
- When the drum at constant drum speed, the cutting load increases with the traction speed. The traction speed leads to the cutting thickness increase while the cutting thickness also increases, and consequently, the cutting force obviously increases. Along with the rising of the drum rotating speed, the rotary cutting pick has a large movement inertia according to the law of conservation of momentum, with the increase of kinetic energy transformation, as the coal seam is prone to be broken easier, so the cutting load reduces with the increase of drum rotation speed.

Acknowledgements

The authors are grateful for the funding of this work by the China Coal Industry Association Science and Technology Research Project (MTKJ2016-221) and Henan Province Science and Technology Development Research Project Fund (172102210021) and China Postdoctoral Science Foundation Funded Project (Project No. 2016M592289).

References

- S.Y. Liu, C.X.Luo, "Experimental modal research on the cutting system of EBZ-75 type boom-roadheader". *Applied Mechanics and Materials*,(2013)Vol.4: 278-280
- Chunsheng LIU, Degen LI, "Influence of Random Load on Mechanical Properties of Double- Drum Shearer". *Coal Mine Mechanical and Electrical*, (2012) Vol. 4:47-52
- Yimin XIA, Yingyong BU, Bowen LUO, Xuanyun QIN, Yuehong DENG, "Study on Fractal of Cobalt-rich Crusts Broken by Drum-type Mining Head". *Mining and Metallurgical Engineering*,(2005) Vol.25:9-11.
- C.X. Luo, H.X. Jiang, "Experimental Study on the Axial Force of Shearer Drum Cutting Coal and Rock". *Recent Patents on Mechanical Engineering*, Vol. 8 (2015) No. 1,268-234.
- C.X Luo, C.L Du, L.J Xu , K.H Zheng, "Fractal Distribution Studies of a Rotary Crushing Mechanism".*Recent Patents on Mechanical Engineering*, Vol. 7 (2014) No.1,798-785.
- H. Tuncdemir, N. Bilgin, H. Copur, C. Balci, "Control of rock cutting efficiency by muck size". *International Journal of Rock Mechanics & Mining Sciences*, (2008) Vol.45: 278-288.
- C. Balci, N. Bilgin, "Correlative study of linear small and full-scale rock cutting tests to select mechanized excavation machines". *International Journal of Rock Mechanics & Mining Sciences*, (2007)Vol.44: 468-476.
- B. Mishra, "Analysis of cutting parameters and heat generation on bits of a continuous miner-using numerical and experimental approach". Thesis, West Virginia University, (2007).
- Chun- hua WANG, Ren- zheng DING, Gui- xuan LI, et.al. "Simulation experimental on the deformation and destruction course of coal body under the function of pick cutting". *Journal of China Coal Society*, (2006) Vol. 31:121-124.
- Ajay Goyal, Suresh Dhiman, Shailendra Kumar, Rajesh Sharma, "A Study of Experimental Temperature Measuring Techniques used in Metal Cutting" *Jordan Journal of Mechanical and Industrial Engineering*, Vol.8 (2014) No. 2.
- X.P. Li, H. Guo, J.N. Liu, Y.L. Liu, "Dynamical characteristics of the linear rolling guide with numerical simulation and experiment". *Telkomnika*, Vol. 11(2013),Issue 1:436-442
- C.X. Luo, Z.T.Han, Y.Yuan, "Study on thermal-structural analysis for shearer ranging arm shell ". *Jordan Journal of Mechanical and Industrial Engineering*, Vol.9 (2015) No. 1.
- S.Y. Liu, C.X. Luo, "Vibration experiment of shearer walking unit". *Applied Mechanics and Materials*, Vol. 268, Issue 1, (2013) : 1257-1261.
- S.Y. Liu, C.L. Du, X.X. Cui, K.D. Gao, "Characteristics of different rocks cut by helical cutting mechanism". *Journal of Center South University*, Vol. 18 (2011) Issue 5, 1518-1524.
- S.Y. Liu, C.X. Luo, C.L. Du "Rotating mechanical stress and vibration measurement device". CN201210189314.1(2014)
- H.X. Jiang, C.L. Du, S.Y. Liu, "Numerical simulation of rock fragmentation process by roadheader Pick". *Journal of Vibroengineering*, Vol.15 (2013) Issue 4, 1087-1817.
- H.X. Jiang, C.L. Du, S.Y. Liu, "Nonlinear dynamic characteristics of load time series in rock cutting". *Journal of Vibroengineering*, Vol.16 (2014) Issue 1, 316-326.
- R. Zeng, C.L. Du. "Reasonable location parameters of pick and nozzle in combined cutting system". *Journal of Central South University of Technology*, Vol.21 (2014) Issue 3,1067-1076.
- M. Entacher, G. Winter, T. Bumberger, K. Decker, I. Godor, R. Galler, "Cutter force measurement on tunnel boring machines – System design", *Tunnelling and Underground Space Technology*, (2012) Vol. 31: 97-106.



الجامعة الهاشمية



المملكة الأردنية الهاشمية

المجلة الأردنية
للمهندسة الميكانيكية والصناعية

JJIMIE

مجلة علمية عالمية محكمة
تصدر بدعم من صندوق البحث العلمي

<http://jjmie.hu.edu.jo/>

ISSN 1995-6665

المجلة الأردنية للهندسة الميكانيكية والصناعية

مجلة علمية عالمية محكمة

المجلة الأردنية للهندسة الميكانيكية والصناعية: مجلة علمية عالمية محكمة تصدر عن
الجامعة الهاشمية بالتعاون مع صندوق دعم البحث العلمي في الأردن

هيئة التحرير

مساعد رئيس التحرير
الدكتور فارس العقلة
الدكتور أكرم السكر

رئيس التحرير
الدكتور علي جوارنه

الأعضاء

الأستاذ الدكتور ناصر الحنيطي
الجامعة الأردنية

الأستاذ الدكتور محمد أحمد حمدان
الجامعة الأردنية

الأستاذ الدكتور محمد هياجنة.
جامعة العلوم والتكنولوجيا الأردنية

الأستاذ الدكتور أمين الربيدي.
جامعة البلقاء التطبيقية

الأستاذ الدكتور سهيل كيوان
جامعة العلوم والتكنولوجيا الأردنية

الأستاذ الدكتور محمد الطاهات
الجامعة الأردنية

فريق الدعم

تنفيذ وإخراج

م . علي أبو سليمة

المحرر اللغوي

الدكتور بكر محمد بني خير

ترسل البحوث إلى العنوان التالي

رئيس تحرير المجلة الأردنية للهندسة الميكانيكية والصناعية

الجامعة الهاشمية

كلية الهندسة

قسم الهندسة الميكانيكية

الزرقاء - الأردن

هاتف : 00962 5 3903333 فرعي 4217

Email: jjmie@hu.edu.jo

Website: www.jjmie.hu.edu.jo